A STUDY ON
FLUID FLOW, HEAT TRANSFER, MORPHOLOGY AND MACROSEGREGATION IN CONTINUOUS CASTING OF STEEL

by

SHIV KUMAR CHOUDHARY

DEPARTMENT OF MATERIALS AND METALLURGICAL ENGINEERING
INDIAN INSTITUTE OF TECHNOLOGY, KANPUR
September, 1993

A STUDY ON
FLUID FLOW, HEAT TRANSFER, MORPHOLOGY AND
MACROSEGREGATION IN CONTINUOUS CASTING OF STEEL

A Thesis Submitted
in Partial Fulfilment of the Requirements
for the Degree of
DOCTOR OF PHILOSOPHY

by

SHIV KUMAR CHOUDHARY

to the

DEPARTMENT OF MATERIALS AND METALLURGICAL ENGINEERING

INDIAN INSTITUTE OF TECHNOLOGY, KANPUR

September, 1993

DEDICATED

TO

MY FATHER

CERTIFICATE

9/9/93

It is certified that the work contained in the thesis entitled **"A STUDY ON FLUID FLOW, HEAT TRANSFER, MORPHOLOGY AND MACROSEGREGATION IN CONTINUOUS CASTING OF STEEL"** by **Shiv Kumar Choudhary** has been carried out under our supervision and that this work has not been submitted elsewhere for a degree.

(D. Mazumdar)

Associate Professor

(A. Ghosh)

Professor

Department of Metallurgical Engineering

Indian Institute of Technology

Kanpur

ACKNOWLEDGEMENTS

LIST OF CONTENTS

LIST OF FIGURES

Figure	Title	Page

LIST OF TABLES

LIST OF SYMBOLS

Symbol

a : Billet size in the direction of X-axis (m)

A_P, A_E, A_W, A_N, A_S, A_B, A_T : Coefficients of the discretization equation

$A_{E,new}$ etc. : Modified coefficients of discretization equation after blockage ratio correction

A_{Eq} : Percentage of equiaxed zone area

b : Billet size in the direction of Y-axis (m)

BR_e, BR_w, BR_n, BR_s : Blockage ratios of various faces of velocity control volume

c : Specific heat of steel (J kg^{-1} ^{o}C)

C_0 : Initial concentration of solute in the liquid (wt. pct.)

$C_{c,0}$: Nominal carbon concentration of steel (wt. pct)

C_i : concentration of solute i at the location under consideration (wt. pct)

$C_{i,0}$: Nominal concentration of of solute i (wt. pct)

C_L : Equilibrium solute concentration in the liquid phase (wt. pct)

C_s : Equilibrium solute concentration in the solid phase (wt. pct)

$C_{s,0}$: Nominal sulphur concentration of steel (wt. pct)

$C_{c,s}$: Equilibrium carbon concentration of solid phase in the mushy zone (wt. pct)

$C_{c,L}$: Equilibrium carbon concentration of liquid phase in the mushy zone (wt. pct)

D_m : Diameter of the mould (m)

f_s : solid fraction in the mushy zone

$f_{s,t}, f_{s,b}$: Solid fraction at the top and bottom faces of a control volume respectively

g Acceleration due to gravity (m s^{-2})

Gr : Grashoff number

h_s : Spray heat transfer coefficient (W m^{-1} ^{o}C^{-1})

k_0 : Equilibrium partition coefficient

k_0^c : Equilibrium partition coefficient of carbon

k_{eff} : Effective partition coefficient

k_0^s : Equilibrium partition coefficient of sulphur

k_m : Mass transfer coefficient (m s^{-1})

K : Molecular thermal conductivity of steel (W m^{-1} ^{o}C^{-1})

K_{eff} : Artificial effective thermal conductivity of liquid (W m^{-1} ^{o}C^{-1})

$K_{eff,e}$ etc. : Effective thermal conductivity value at one face of a control volume (W m^{-1} ^{o}C^{-1})

K_t : The turbulent thermal conductivity (W m^{-1} ^{o}C^{-1})

L : Caster/domain length simulated (m)

L_m : Mould length (m)

L_s : Secondary cooling zone length (m)

$\dot{m}$: The mass flow rate of liquid steel (kg s^{-1}

p : Pressure (N m^{-2})

Pe : The Peclet Number

I_e etc. : Heat flux at one face of a control volume (W m^{-2})

I_m : Instantaneous mould heat flux (W m^{-2})

$\bar{I}_m$: Average mould heat flux (W m^{-2})

I_s : Heat flux at the cast surface (W m^{-2})

$q_x,\ q_y,\ q_z$	: Heat fluxes along X,Y, and Z coordinates (W m^{-2})
R	: Size/radius of billet (m)
Re	: Reynolds Number
r	: Radial distance (m)
r_0	: Pouring stream radius (m)
r_c	: Degree of carbon segregation
r_s	: Degree of sulphur segregation
S	: The source term in the discretization equation
S_P	: The slope of the linearized source term
S_U	: Constant part of the linearized source term
S_u	: Source term in the axial direction momentum balance equation (N m^{-3})
S_v	: Source term in the radial/ transverse direction momentum balance equation (N m^{-3})
T	: The temperature variable (^{0}C)
t	Time (s)
T_{liq}	: Liquidus temperature of steel (^{0}C)
t_m	: Dwell time of casting in the mould (s)
T_{sol}	: Solidus temperature of steel (^{0}C)
$T_P,\ T_E,\ T_W,\ T_N,\ T_S,\ T_B,\ T_T$	: Temperature at the various nodal points (^{0}C)
T_e etc.	: Temperature at one face of a control volume (^{0}C)
T_a	: Ambient temperature (^{0}C)
T_0	: The pouring/casting temperature (^{0}C)
T_s	: The cast surface temperature (^{0}C)
T_w	: Spray water temperature (^{0}C)
u	: Axial velocity component variable (ms^{-1})
U_{in}	: Velocity of the pouring stream at the entrance of the mould (m s^{-1})
U_0	: Casting speed (m s^{-1})
v	: Radial/transverse velocity

	component variable (m s^{-1})
X	: One of the transverse coordinate
X_{sl}	: Position of the solidification front from the axis of symmetry (m)
Y	: Another transverse coordinate
Z	: The axial coordinate

Greek letters

ΔT	: Super heat of liquid steel or Temperature difference (^{0}C)
ΔH_f	: Latent heat of solidification of steel (J kg^{-1})
$\Delta X, \Delta Y, \Delta Z$	: Length of control volume faces in three mutually perpendicular coordinate directions (m)
d_λ	: Dendrite arm spacing
α	: Index of coordinate system
α_L, α_s	: The slope of liquidus and solidus lines respectively in the iron-carbon equilibrium diagram
$\delta X_e, \delta X_w, \delta Y_n, \delta Y_s, \delta Z_t, \delta Z_b$	: Distance between the various nodes in three mutually perpendicular coordinate axes
β_L, β_s	: Intercepts of the liquidus and solidus lines respectively in the iron-carbon equilibrium diagram
β	: Coefficient of volumetric expansion of liquid steel (^{0}C^{-1})
ε	: Emissivity of the oxidized iron surface (= 0.85)
ε_0	: Rate of temperature change (^{0}C s^{-1})
ϕ	: General dependent variable (i.e. u, v, p or, T) of the discretization equation
$\phi_P, \phi_E, \phi_W, \phi_N, \phi_S$	: Values of ϕ at the various nodes in the general discretization equation
γ_L	: Volume fraction of liquid in the mushy zone

Γ_{eff}	: Effective thermal conductivity derived from the turbulence model (W m^{-1} ^{o}C^{-1})
λ	: Index of coordinate dimension (i.e. a 1-D, 2-D or, 3-D problem)
μ	: Molecular viscosity of liquid steel (kg m^{-1} s^{-1})
μ_{eff}	: Effective viscosity (kg m^{-1} s^{-1})
μ_t	: Turbulent viscosity (kg m^{-1} s^{-1})
ν_t	: Turbulent kinematic viscosity (m^2 s^{-1})
θ	: Temperature in absolute scale (^{o}K)
θ_0	: Pouring temperature in absolute scale (^{o}K)
θ_s	: Cast surface temperature in absolute scale (^{o}K)
θ_a	: Ambient temperate in absolute scale (^{o}K)
ρ	: Density of steel (kg m^{-3})
ρ_L	: Density of liquid phase (kg m^{-3})
ρ_s	: Density of solid phase (kg m^{-3})
σ	: Stefan - Boltzmann constant (5.67 x 10^{-8})
σ_t	: Turbulent prandtl number
ζ	: Flow parameter

Superscript

*	: Variable/parameters in their equivalent dimensionless forms

Subscript

E	: The east neighbouring nodal point (i.e. in the vertical/axial plane)
N	: The north neighbouring nodal point (i.e. in the transverse/radial plane)
P	: The central nodal point
S	: The south neighbouring nodal point (i.e. in the transverse/radial plane)
E	: The west neighbouring nodal point (i.e. in the vertical/axial plane)

A STUDY ON FLUID FLOW, HEAT TRANSFER, MORPHOLOGY AND MACROSEGREGATION IN CONTINUOUS CASTING OF STEEL

A Thesis Submitted
In Partial Fulfillment of the Requirements
for the Degree of

DOCTOR OF PHILOSOPHY

by

SHIV KUMAR CHOUDHARY

to the

Department of Materials and Metallurgical Engineering

Indian Institute of Technology, Kanpur
September, 1993

SYNOPSIS

Continuous casting (CC), is a process of casting molten metal continuously. It has over the years gained considerable importance in both ferrous as well as nonferrous metal industries. Because of several advantages, continuous casting is steadily replacing ingot casting throughout the world. Since 1980s, rapid developments in instrumentation and control systems, availability of superior quality materials, together with tremendous economic advantages of continuous casting led to its rapid adoption around the globe. Today, continuous casting is considered to be the most significant development of the recent decades in the field of iron and steelmaking . Of the total annual World production of about 800 million tons of crude steel, approximately 55 pct. is now-a-days continuously cast.

In India, continuous casting of steel made its inroad during 1960s. However, its present share is only about 35 pct. of approximately 17 million tons of crude steel produced in this country in 1992. Recognizing the global trend and the merits of continuous casting, India is trying to make major strides in this direction. The projected estimates of steel production is about 30 million tons of crude steel by 2000 A.D., and out of this, more than 90 pct. has been planned to be cast continuously. Therefore, in future, continuous casting will be the major route of steel casting in India. To meet such a challenging growth rate, considerable amount of indigenous research and development activities are clearly warranted. However, so far, efforts in this direction in India has not been adequate.

(In the present study, the following important aspects of continuous casting of steel have been selected for investigation:

(i)   mathematical modelling of heat transfer and solidification during continuous casting of steel,

(ii)   morphology and macrosegregation in continuously cast steel billets,

and (iii) correlations amongst the above to the extent possible.

The continuous casting process involves extraction of heat from the liquid steel. This consists of removal of superheat from the liquid steel entering the mould, latent heat released during solidification, and finally the sensible heat of the solidified metal. Heat is extracted from a solidifying casting by a combination of several coupled mechanisms such as,

(i)   convection and turbulent mixing in the liquid pool,

(ii)   conduction of heat in the solidified region,

(iii)   external heat transfer from the surface of the cast section by combined mechanism of conduction, convection, and radiation.

Broadly two different concepts have so far been applied to model the heat flow phenomena within the liquid pool, viz.

(i)   artificial effective thermal conductivity model

and   (ii)   conjugate fluid flow heat-transfer model.

The former class of model is based on the concept that convective and turbulent transport of heat in the liquid pool of a solidifying casting can be represented adequately, if the central core of the liquid metal is treated like a pseudo-solid having a relatively large thermal conductivity. While in the latter approach, the influence of fluid flow on convective and turbulent transport of heat is described relatively more precisely via the Navier-Stokes equation in conjunction with an appropriate thermal energy transport equation.

Of these two approaches, the former has been relatively more common. Model based on this approach leads to a single conduction type heat flow equation. In contrast, model based on conjugate fluid flow and heat transfer phenomena, though has a more fundamental basis, has been less common owing to the inherent difficulties in describing the fluid flow and the associated turbulence in the liquid pool of the solidifying casting. The latter approach also involves more extensive computational task as compared to the former.

In the present study, mathematical modelling was carried out by both the above mentioned approaches. Various assumptions were tested. Also, their predictions were compared with experimental measurements of shell thickness reported in literature.

Macrosegregation is inhomogeneity in chemical composition over a macroscopic area in cast products. Macroscopic transport of segregated liquid and crystals during solidification gives rise to the macrosegregated regions in cast sections. In continuously cast products a high degree of positive macrosegregation in the central region of cast section constitutes a major defect. This is known as 'centreline segregation'. Such chemical inhomogeneities due to macrosegregation are undesirable as they give rise to nonuniform mechanical properties and cracks in the finished product.

Equiaxed structure during solidification reduces the extent of centreline segregation by redistributing the segregated liquid more evenly in between the equiaxed dendrites. Therefore, morphology of solidification structure has a special significance in controlling the centreline segregation during continuous casting.

The thesis consists of five chapters. Chapter 1 briefly presents:

      (i)   importance and advantages of continuous casting of liquid steel and development of the process

      (ii)   a brief description of continuous casting of steel

      (iii) objective of the present study

      (iv) plan of work

Chapter 2 is concerned with heat flow model based on the concept of artificial effective thermal conductivity (K_{eff}). It starts with a review of literature on this topic. In the present study, a steady-state three-dimensional model has been developed. On the basis of available literature information, boundary conditions to the governing heat flow equation have been applied, and the equation was solved via the control volume based finite difference procedure. The model is sufficiently general and can be applied to various geometrical shapes of relevance to continuous casting of steel. Sensitivity of the predicted results to various numerical approximations including grid configurations, as well as to other modelling parameters such as axial conduction, mushy zone modelling procedure, choice of value of K_{eff} have been extensively studied. It has been shown that some assumptions and numerical procedures influence the computed results significantly. Finally, numerical predictions have been compared with three sets of experimental measurements reported in literature on shell thickness in industrial casters. In contrast to some earlier claims, these indicated only poor to moderate agreement between model prediction and experimental results.

Chapter 3 is concerned with mathematical modelling based on conjugate fluid flow - heat transfer approach. It starts with a review of literature on this topic. In the present study, a steady state, two dimensional mathematical model of continuous casting of steel has been developed. Governing fluid flow and heat transfer equations have been derived and a procedure for their non-dimensional representations outlined. The growth of

solidification front and its resultant influences on the fluid flow and heat transfer have been addressed, and a new calculation procedure for incorporating the solidification phenomena into the mathematical model has been proposed.

Control volume based finite difference procedure has been applied to solve the governing partial differential equations together with the associated boundary conditions, and towards this a computer program in FORTRAN-77 has been developed.

Adequacy of several key assumptions applied in deriving the mathematical model has been assessed. Towards this, modelling of turbulence, liquid steel flow in the mushy zone, thermal buoyancy, as well as heat flow across the meniscus have been studied computationally. It has been shown that except for approximations applied to the modelling of fluid flow in the mushy zone, predicted flow as well as temperature fields are relatively insensitive to the accurate modelling of fluid turbulence, heat flow across the meniscus etc..

Numerically predicted flow patterns in several billet casters have been assessed qualitatively against equivalent studies reported in the literature. Similarly, numerical predictions and reported experimental solidified shell thickness were compared for three different casting configurations. These in general demonstrated reasonable to good agreement between theory and experiment.

Chapter 4 deals with study of macrostructure and macrosegregation of continuously cast billet samples of low carbon steel collected from Tata Steel, Jamshedpur. It includes

an extensive literature review on the topic. Transverse sections of billets were examined. Macroetching revealed various zones. The equiaxed zone was mostly asymmetric around the billet centre. The area of equiaxed zone decreased with increase in tundish superheat. Samples for analyses of carbon and sulphur were collected by drilling at the billet centres as well as at the columnar-equiaxed transition (CET) boundaries, and analyzed by automatic carbon and sulphur determinator. Degrees of segregation of carbon and sulphur (r_c and r_s respectively) were correlated to each other both for the centres as well as for the CET boundaries of the billet sections. Correlation of r_c with r_s for the CET boundaries agreed closely with that predicted by Scheil's or modified Scheil's equation. Variations of r_c and r_s with fractional solidification, although did not agree with predictions of the above, were in qualitative agreement with actual macrosegregation data reported in literature.

Finally, attempts were made to correlate the experimental macrostructural and macrosegregation data with predictions based on conjugate fluid flow-heat transfer model. This was achieved for the CET boundaries. Since temperature of liquid steel could be measured only in tundish, the loss of temperature from the tundish to the mould was estimated for arriving at the correct pouring temperature for computation purposes. Results of this exercise demonstrated close agreement of predicted locations of CET boundaries with the measured values.

This is being taken as additional confirmation of the reliability of the conjugate fluid flow-heat transfer model developed during the present investigation. Therefore, it is

proposed that this model may also be employed to estimate size of equiaxed zone in continuous casting of steel.

Chapter 5 presents summary and conclusions as well as suggestions for further work.

CHAPTER 1

INTRODUCTION

Continuous casting (CC), is a process of casting molten metal continuously. It has over the years gained considerable importance in both ferrous as well as nonferrous metal industries. In steel plants, continuous casting provides the necessary link between steelmaking operations and final stages of rolling, by producing semi finished products such as, billets, blooms, and slabs. The major advantages of continuous casting process lie in the fact that it eliminates the conventional ingot casting thereby leading to[1,2] :

   (i)   higher yield (about 10-15 pct. increase),

  (ii)   increased productivity,

 (iii)   superior product quality,

  (iv)   lower capital and operating cost,

   (v)   reduced energy consumption due to elimination of soaking pits and primary rolling mill,

  (vi)   scope of more automation and better process control,

 (vii)   better working environment.

Evidences in literature indicate that the switching over from conventional to continuous casting operation can account for an energy saving of the order of 200 MJ per ton of finish steel[3]. Because of these distinct merits, continuous casting steadily replacing ingot casting throughout the world. Ste plants of the future, as it is readily evident will embo

primarily CC for casting molten steel.

1.1 DESCRIPTION OF CONTINUOUS CASTING OF STEEL

Fig.1.1 illustrates the major components of a typical modern continuous casting machine. A variety of designs has been commercialized and new innovations are taking place continually. Consequently, the salient features which are common to all designs are summarized below and shown in Fig.1.1.

Molten steel, tapped in a ladle or similar transfer vessel from steelmaking furnaces, is subjected to homogenization treatment by inert gas purging. Subsequently, it is subjected to secondary steelmaking treatments such as degassing, desulphurization etc. The extent of such treatment varies from plant to plant depending on the requirements and the facilities available. Finally, the ladle containing molten steel is brought to the CC shop for casting. Liquid metal from the ladle is poured slowly into a rectangular reservoir, known as tundish, located immediately above the casting machine. From the tundish molten steel is poured into one or more open-ended water-cooled copper mould (typically about 0.5 - 0.9m length). The flow of molten steel from the tundish to the mould is regulated by stopper rod or slide gate arrangements fitted to the bottom of the tundish.

To initiate a cast, a starter (i.e. dummy bar) is inserted through the bottom end of the mould so that it acts as a false bottom necessary for the casting operation to begin. Molten metal from the tundish is slowly poured into the mould up to a desired level, and immediately after that the dummy bar is gradually withdrawn. The rate of withdrawal of dummy bar (or solidified metal) must exactly match with the rate of pouring of liquid
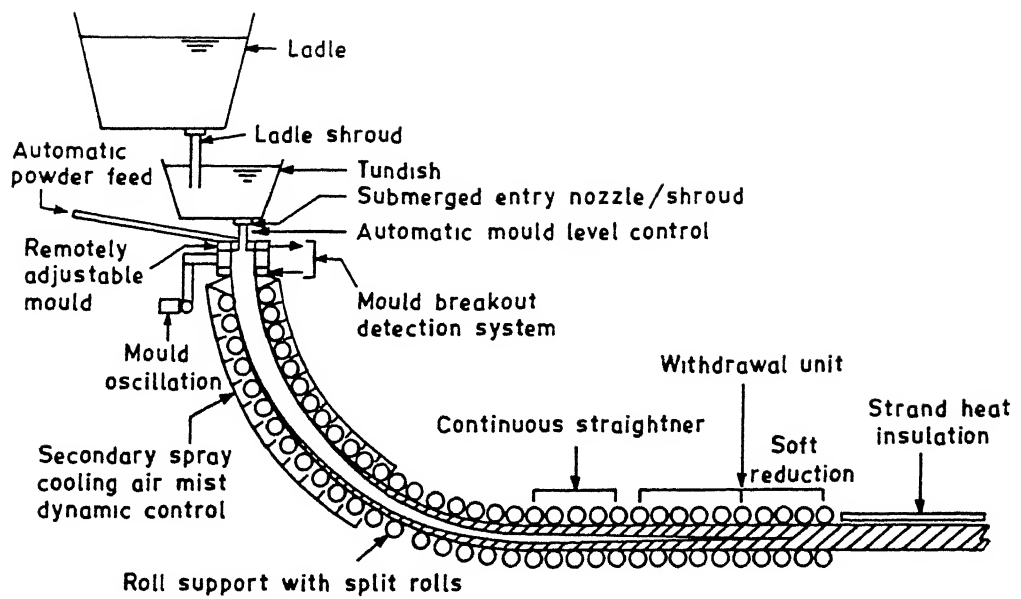
Fig. 1.1. Schematic of a typical slab casting machine.

steel for smooth operation. Uninterrupted pouring of liquid steel from the top and simultaneous withdrawal of cast section at the bottom of the mould gives rise to a situation in which the melt can be cast continuously in the form of one solid piece, which is subsequently cut into the desired lengths.

As the liquid metal enters the copper mould a thin solid layer, (i.e. the 'skin') is immediately formed due to the chilling action of water cooled mould wall. The solidified shell, because of solidification shrinkage, subsequently gets separated from the mould surface. To prevent sticking of the frozen solid shell to the mould wall, the latter is oscillated at a controlled rate during the casting operation. In addition to this, oils or low melting fluxes (i.e. mould powders) are introduced into the mould continuously to lubricate the mould wall and to facilitate easy withdrawal of the casting. Contraction in volume of the solid shell gives rise to the formation of air gap between the mould wall and the casting. Simultaneously, static pressure of liquid in the molten core pushes the shell to bulge outward and consequently tends to counteract the solidification shrinkage, and thereby reduce the gas width. The air gap increases with the progress of solidification along the mould length and constitutes about 70-80 pct. of the total resistance to heat flow in the mould/primary cooling zone.

Fig.1.2 schematically shows the phenomena occurring during continuous casting process. It may be noted that solidification is incomplete in the mould region. Therefore, the solidified skin must be sufficiently thick so as to withstand the ferrostatic pressure of the melt in the core of the casting. Immediately below the mould the casting is cooled by spraying water onto the
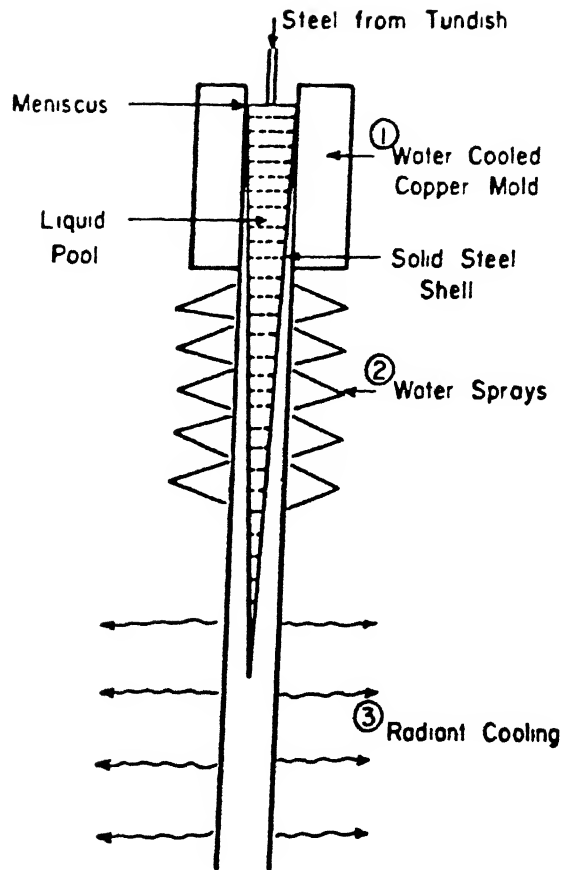
Fig. 1.2: Schematic of three zones of heat extraction during continuous casting of steel.

cast surface through a series of spray nozzles, to ensure complete solidification. This region in the CC machine is typically called the secondary cooling (or spray cooling) zone. There the casting is mechanically supported by a series of rolls (i.e. support rolls). During casting operation, the cast section is continuously withdrawn by withdrawal or pinch rolls, located outside the secondary cooling zone. Beyond the secondary cooling zone, the casting is cooled in the air mainly via radiation. This zone is therefore called the 'radiation cooling zone'.

1.2 DEVELOPMENT OF CONTINUOUS CASTING OF STEEL

The idea of continuous casting of steel was originally conceived by Sir Henry Bessemer during 1860s. He attempted to cast steel sheet continuously, though could not succeed because of inadequate technology and materials available at that time. By 1930s, continuous casting of nonferrous metals became feasible, and later proved quite successful. However, the high melting point, higher specific heat and lower thermal conductivity of steel were the main obstacles in the development of continuous casting technology for steel. The technology was first commercialized in Germany during 1943 and later adopted by a number of steel plants in Europe. The growth of CC, however, remained quite limited for sometime and as of 1975, only 5 pct. of the total World crude steel production was via continuous casting. Since 1980s, rapid developments in instrumentation and control systems, availability of superior quality materials, together with tremendous economic advantages of continuous casting led to its rapid adoption around the globe.

Today, continuous casting is considered to be the most

significant development of the recent decades in the field of iron and steelmaking . Of the total annual World production of about 800 million tons of crude steel, approximately 55 pct. is now-a-days continuously cast (Fig.1.3). In Western Europe it is above 70 pct., while in Japan, it is well above 90 pct.[3,4]. It is expected that in near future, practically 100 pct. of the total steel produced World wide will be continuously cast with few exceptions.

Intensive research and development activities in the area of solidification processing, equipment design, process upgradation, and automation etc. have played a vital role in bringing the continuous casting of steel to its present level. Research and development activities have primarily been directed towards productivity enhancement, quality improvement and energy saving. Such endeavor on the continuous casting of steel has led to a better understanding of the phenomena involved in CC and established the links between operation and cast quality, although much remains to be learned.

Towards the success of continuous casting technology, secondary processing (i.e. ladle metallurgy) of liquid steel has played an important role. Close control of superheat of liquid steel is one of the vital requirements for smoother operation and quality of the CC products. Such requirements can be conveniently achieved through both homogenization and proper ladle treatment. In continuous casting plants homogenization treatment of liquid steel is carried out on a routine basis. Moreover, secondary steel processing is required for controlling the oxygen level, inclusion float-out and modification. In addition, desulphurization, degassing, alloying, etc. during ladle
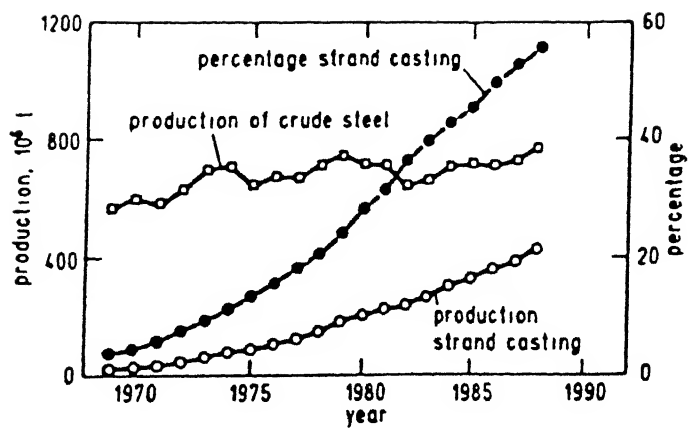
Fig. 1.3: Crude steel and CC production worldwide[3].

treatment have made it possible to cast almost all grades of steel through CC route successfully.

In India continuous casting of steel made its inroad during 1960s. However, its present share is only about above 35 pct. of approximately 17 million tons of crude steel produced in this country in 1992[5]. Recognizing the global trend and the merits of continuous casting, India is trying to make major strides in this direction. The projected estimates of steel production is about 30 million tons of crude steel by 2000 A.D.[6], and out of this, more than 90 pct. has been planned to be cast continuously. Therefore, in future, continuous casting will be the major route of steel casting in India. To meet such a challenging growth rate, considerable amount of indigenous research and development activities are clearly warranted. However, so far, efforts in this direction in India has not been adequate.

1.3 OBJECTIVE OF THE PRESENT STUDY

In the present study, the following important aspects of continuous casting of steel have been selected for investigation:

      (i) heat transfer and solidification phenomena during continuous casting of steel,

     (ii) morphology and macrosegregation in continuously cast steel billets,

and   (iii) correlation amongst the above to the extent possible and justified.

1.3.1   Heat Transfer and Solidification During Continuous Casting of Steel

The continuous casting process involves extraction of heat from the liquid steel. This consists of removal of superheat from the liquid steel entering the mould, latent heat released during solidification, and finally the sensible heat of the solidified metal. Heat is extracted from a solidifying casting by a combination of several coupled mechanisms such as,

(i)   convection and turbulent mixing, induced in the liquid pool by the momentum of the incoming pouring stream, as well as natural convection arising out of thermal gradients in the liquid region,

(ii)   conduction of heat in the solidified region,

(iii)   external heat transfer from the surface of the cast section by combined mechanism of conduction, convection, and radiation in the mould as well as the submould region.

Heat transfer plays a crucial role in the smooth and efficient operation of the continuous casting process. The productivity and the quality of CC products depend largely on the rate and the manner in which heat is extracted from the solidifying casting. Necessary minimum thickness of the solidified shell to avoid occurrence of break-outs in the submould region as well as the depth of the liquid pool relative to the metallurgical length of the casting machine depend predominantly on the heat transfer phenomena.

Recognizing the importance of heat transfer phenomena during continuous casting process, numerous studies have been carried

out in the past to improve upon the design and operation of CC machine and thereby to gain better understanding of the process fundamentals. Heat transfer phenomena have been extensively investigated theoretically. Several mathematical models have been developed to unscore various thermal phenomena encountered in continuous casting. Different approaches have been adopted and hence the models differ from one study to another in their treatment to describe the heat transfer processes within the liquid pool as well as across the surface of the solidified casting. Broadly two different concepts have so far been applied to model the heat flow phenomena within the liquid pool, viz.

(i) artificial effective thermal conductivity model[8-10] and (ii) conjugate fluid flow heat-transfer model[11,12].

The former class of model is based on the concept that convective and turbulent transport of heat in the liquid pool of a solidifying casting can be represented adequately, if the central core of the liquid metal is treated like a pseudo-solid having a relatively large thermal conductivity (e.g. approximately 5 to 10 times the molecular thermal conductivity of steel)[12]. While in the latter approach[11,12], the influence of fluid flow on convective and turbulent transport of heat is described relatively more precisely via the Navier-Stokes equation[13] in conjunction with an appropriate thermal energy transport equation.

Of these two approaches, the former has been relatively more common. Model based on this approach, as has been described in the subsequent chapters, leads to a single conduction type heat flow equation. In contrast, model based on conjugate fluid flow

and heat transfer phenomena, though has a more fundamental basis, has been less common owing to the inherent difficulties in describing the fluid flow and the associated turbulence in the liquid pool of the solidifying casting. The latter approach, as one might anticipate, involves more extensive computational task as compared to the former.

1.3.1.1 Plan of work for mathematical modelling of heat transfer

This includes,

(i) derivation of governing heat flow equations for the artificial effective thermal conductivity approach and the conjugate fluid flow – heat transfer approach,

(ii) development of flow charts and computer programs for the numerical solution of governing heat flow and/or fluid flow equations,

(iii) prediction of temperature and velocity profiles in billet casters,

(iv) prediction of thickness of solidified shell from temperature profile and comparison of the same with experimental measurements reported in the literature,

(v) testing of principal assumptions,

and finally,

(vi) assessment of the adequacies of the two modelling concepts with reference to the mathematical modelling of heat flow in continuous casting of steel.

1.3.2   Macrosegregation and Morphology in Continuously Cast Products

Macrosegregation is inhomogeneity in chemical composition over a macroscopic area in cast products. During continuous casting, solidifying dendrites reject solute elements (e.g. C,S,P,Mn etc.) at the solidification front and in the interdendritic regions. This leads to the gradual enrichment of residual liquid with progress of solidification. Macroscopic transport of segregated liquid and crystals during solidification gives rise to the macrosegregated regions in cast sections. In continuously cast products a high degree of positive macrosegregation in the central region of cast section constitutes major defect. This is known as 'centreline segregation'. Such chemical inhomogeneities due to macrosegregation are undesirable as they give rise to nonuniform mechanical properties and cracks in the finished product.

Equiaxed structure during solidification reduces the extent of centreline segregation by redistributing the segregated liquid evenly in between the equiaxed dendrites. Therefore, morphology of solidification structure has a special significance in controlling the centreline segregation during continuous casting. Low superheat casting and electromagnetic stirring promote equiaxed solidification and thereby reduce centreline segregation. Suction due to solidification shrinkage and bulging of strand between the support rolls have been identified as the main cause of flow of segregated liquid leading to centreline segregation. Adjustment of roll gap taper reduces the bulging before complete solidification, and thereby decreases the extent of macrosegregation. Also, soft reduction in the cross section of

slab during final stage of solidification has been found to be quite effective in controlling fluid flow in the mushy zone. In addition to these, several other techniques have been developed for controlling the centreline segregation in CC products.

In view of the adverse effect of centreline segregation on product quality in CC route, numerous studies have been carried out. As a result of these, it has now become possible to keep the segregation level below the desirable limit in common grade steels. However, for high grade steels (e.g. sour gas resistant steels) control of macrosegregation is relatively difficult. Therefore, macrosegregation is still a hot topic of research in the area of continuous casting.

1.3.2.1   Plan of work on macrosegregation and morphology

This includes,

(i)   collection of billet samples and relevant data from the CC shop of steel plant,

(ii) cutting thin sections from above billet samples, and polishing of cut cross-section (i.e. transverse section) for examination,

(iii) physical examination of transverse section in both unetched and etched condition to determine various morphological features,

(iv) chemical analysis of drilled samples to determine macrosegregation levels in transverse sections at the centreline as well as at the columnar-equiaxed transition boundary,

(v) Interpretation of results, including attempts for some correlation with studies on heat transfer.

1.4 PRESENTATION OF CHAPTERS IN THE THESIS

This investigation has been presented in the subsequent chapters of the thesis. Heat transfer study based on effective thermal conductivity model has been described in chapter 2. Study based on conjugate fluid flow-heat transfer model is described in chapter 3. Chapter 4 presents studies on morphology and macrosegregation. Literature review as well as summary and conclusions of study are presented in their corresponding chapters. Attempts have been made to make each chapter self contained. Chapter 5 presents summary and conclusions for the entire work.

CHAPTER 2

MATHEMATICAL MODELLING OF CONTINUOUS CASTING OF STEEL VIA ARTIFICIAL EFFECTIVE THERMAL CONDUCTIVITY APPROACH

2.1 INTRODUCTION

Heat transfer in the liquid region of a continuously cast section is relatively more complex than in the solidified region due to flow induced in the liquid pool via momentum of the pouring stream, by the buoyancy driven natural convection, and by the electromagnetic stirring, if present. Therefore, in addition to conduction, transfer of heat from the liquid to the solidified region takes place through bulk convection and turbulence. Exact modelling of heat transfer in the solidifying casting consequently requires prior knowledge of flow of liquid steel in the molten pool. This calls for the solution of complex turbulent fluid flow equations in conjunction with an appropriate equation of thermal energy transport.

To avoid the inherent complexities associated with the numerical solution of the turbulent fluid flow equations, convective as well as turbulent transport of heat have been either completely ignored[14] or the pool region assumed to be well mixed[7], in the earlier studies on heat transfer in continuous casting of steel. A somewhat realistic attempt was made subsequently by Mizikar[8], who took into account the enhanced heat transfer in the liquid due to convection by artificially increasing the thermal conductivity of the liquid pool. The

approach adopted by Mizikar to model the coupled effect of fluid convection and turbulence on heat transfer in such an ad-hoc manner has been termed in the literature[15] as the 'artificial effective thermal conductivity approach'. It has been argued[10,16] that such an adjustment of thermal conductivity values within the liquid pool (e.g. to account for the turbulence and convective heat transfer in the liquid) is not likely to affect the overall prediction of the rate of solidification and the temperature fields in CC, since convection predominantly affects the rate at which superheat is removed from the liquid steel, and typically, superheat constitutes only a small fraction of the total heat content (i.e. latent and sensible heat) of the liquid steel.

The artificial effective thermal conductivity model, originally proposed by Mizikar[8], is thus based on the key assumption that the convective and turbulent transport of heat in the liquid pool of a solidifying casting can be represented reasonably well, if the liquid core of the cast section is considered to be a pseudo-solid having a relatively large thermal conductivity value (viz., effective thermal conductivity) than that of the solidified steel. In essence, this implies that the governing equation describing the flow of heat within CC section will therefore be a pure conduction type equation. However, it is to be recognized here that the governing heat flow equation incorporating the effective thermal conductivity (K_{eff}) parameter, the numerical value for which was derived by Mizikar through force fitting the model predictions against those measured experimentally on a slab casting machine, lacks a sound fundamental basis. Indeed, so far there is no explicit evidence

in literature to establish that a large thermal conductivity value arbitrarily assigned to the liquid pool can in principle accommodate the effect of fluid motion and turbulence on heat transfer. Despite this limitation, the concept has been frequently applied by the several subsequent investigators[9,10,17], to investigate various thermal phenomena of relevance to continuous casting.

2.2 LITERATURE REVIEW

Several mathematical models[7-10] have been proposed so far to describe heat transfer and solidification phenomena in continuous casting of steel. Most of the models are based on the fundamental equation of heat conduction, and on empirical data to characterize the complex heat extraction processes across the surface of the cast strand in different cooling zones. The models however, often differ from one another in their treatment of the heat transfer in the liquid pool region.

The initial attempts on the mathematical modelling of continuous casting were made in the sixties. At that time good computer facility was almost practically non-existent. Therefore, investigators[7,9,18] mostly adopted analytical approach to solve the governing heat flow equation of continuous casting. Towards this, considerable idealization were made and the most simplified form of the heat flow equation was considered. One of such studies has been reported by Hills[7] who investigated the heat transfer and solidification in billet casting moulds. Hills[7] considered a unidirectional transient heat conduction equation as the governing equation of heat flow and applied integral profile

technique to solve the governing equation analytically. Conduction along the withdrawal direction was ignored and invariant thermophysical properties of steel were assumed. Molten steel was assumed to solidify as a pure metal (i.e. at fixed temperature), and furthermore heat conduction in the liquid region was neglected throughout the pool (i.e. well mixed pool region), so that the melt superheat and the latent heat release following solidification were uniform over the entire pool region. A constant mould heat transfer coefficient was assumed and applied as the required boundary condition at the mould metal interface.

In addition, Hills[7] performed experimental measurements of solidifying shell thickness over static moulds using the 'pour-out technique'. Predictions were compared with experimental measurements and reasonable agreements between the two have been reported. On the basis of mathematical modelling, Hills[7] also analyzed other experimental measurements reported in literature. In addition to these, a simple heat balance over the mould cooling water was carried out and a method to deduce the mould heat transfer coefficients suggested[7]. The mathematical model proposed by Hills; although was very simplistic, incorporates several unrealistic assumptions and thus, reliability of predicted results becomes an issue of concern.

In a subsequent study, Mizikar[8] took a relatively more realistic approach to simulate heat transfer phenomena in continuous casting and introduced the concept of an enhanced artificial thermal conductivity to account for the transport of heat in the liquid pool via convection and turbulence.

Mizikar[8] was also amongst the first to adopt a numerical method to solve the characteristic heat flow equation. The mathematical model proposed by Mizikar is essentially an unidimensional transient heat conduction equation applicable strictly to continuously cast steel slabs. An effective thermal conductivity value equal to 7 times the molecular thermal conductivity of steel at that temperature, was assigned to take care of the convection in the liquid pool region. Conduction of heat along the axial and one of the transverse directions (i.e. longer side) were neglected. Moreover, latent heat of solidification was taken into account by adjusting the specific heat value over the range of solidification temperatures. Explicit finite difference numerical method was adopted to solve the governing equation. The Savage-Pritchard correlation[19,20] was applied to estimate the mould heat flux, and incorporated in the model as an appropriate boundary condition across the mould wall.

Finally, predicted solidified shell thickness was compared with the experimentally measured data[8]. A reasonable agreement between the two has been reported. The appropriate value of the enhanced thermal conductivity, K_{eff}(i.e. = 7K), applied to the model was deduced by comparing numerical prediction with experimental measurements. Consequently, the value of K_{eff} in the liquid pool as suggested by Mizikar is in reality an empirical parameter. The model developed was further applied to process design and thus, some optimal set of cooling conditions (viz., an appropriate spray heat transfer coefficient value) in the secondary cooling zone was derived by assigning a desired slab surface temperature all along the spray lengths.

In a separate study, Mizikar[21] investigated experimentally the influence of spray water flux, spray pressure, spray nozzle types and their orientations on the cooling characteristics of CC slab in the secondary cooling zone. Heat transfer coefficients evaluated as a function of the spray variables were presented as nomograms. It was suggested that these heat transfer coefficient data can be applied to the mathematical model as the required surface boundary condition in the spray cooling zone. Consequently, detailed prediction of liquid pool profile, pool depth, surface temperature in the secondary cooling zone etc. can be estimated all along the descending cast strand. The data on heat transfer coefficient were however, limited to a few spray configurations only.

Gautier et.al[14] also proposed a similar type of model for predicting the thermal fields in continuously cast square billets. A transient heat conduction equation in terms of enthalpy, was considered as the governing heat flow equation. Although the model was developed in the cylindrical polar coordinate system, it was applied to predict the temperature fields in square billets,by reducing the latter to cylinders of equivalent surface area. In the liquid region convection was ignored completely, and thus, heat flow in the radial direction was considered solely by conduction. Furthermore, latent heat of solidification was estimated from the enthalpy-temperature relationship. For estimating the heat flux across the mould wall the mould was divided into two zones viz. the upper contact zone and the lower gap zone. In the upper contact zone heat flux was estimated from an empirical heat transfer coefficient data. In

the lower gap zone, gap width was estimated first by carrying out heat balance over the mould, and finally, an expression for the required mould heat flux was derived, assuming heat flow across the gap by conduction and radiation. Embodying the resultant mould heat flux expressions as the boundary condition, the governing heat flow equation was solved numerically by an explicit finite difference procedure. Surface temperatures at the mould exit of a billet caster were measured under a wide range of casting conditions via a two-color optical pyrometer and compared against the numerical predictions. The agreement between measurements and predictions has been reported to be satisfactory.

Perkins and Irving[17] extended the unidimensional heat flow model, reported by the previous investigators[8,14], further to the two dimensional situations and introduced other modifications, in an attempt to make it closer to the real continuous casting operation. The investigators applied their two dimensional, unsteady state heat conduction model to analyze the heat flow and solidification in bloom casters. Effect of mixing and convection was taken into account by increasing the thermal conductivity in the liquid region in a manner suggested by Mizikar[8]. Conduction along the axial direction was ignored and the latent heat release effect was incorporated by adjusting the specific heat in the mushy zone. For estimation of surface heat flux, as an appropriate boundary condition in the mould, Perkins and Irving[17] proposed a three zone heat extraction model for the mould region. In the upper zone a good contact between the strand and mould surface was assumed and a higher heat transfer coefficient value

applied to the mathematical model. Similarly, in the lowest zone radiation was assumed as the only mechanism of heat transfer and correspondingly, a constant lower heat transfer coefficient value was assigned there. In the intermediate zone, a linear interpolation of heat transfer coefficient between the values at the two extremities was considered. Both constant and variable thermophysical properties were assumed in the computational procedure, and various numerical techniques were employed to solve the governing heat flow equation. The predicted shell thickness and surface temperatures were validated against the corresponding plant scale measurements. The model was finally applied to optimize the bloom casting operation.

In their earlier study, Brimacombe et.al[9] have also applied the integral profile technique, originally used by Hills[7], to solve the governing heat flow equation (viz., unidimensional unsteady heat conduction with constant properties) of CC. Subsequently, based on the artificial effective thermal conductivity concept, Brimacombe and coworkers[10,22-24] carried out extensive heat transfer studies on continuous casting of steel. Liquid pool profile and surface temperatures in square billet casters were predicted numerically and compared with measured shell profiles. Reasonably good agreement was obtained only over the upper half of the mould while in the lower half and the upper spray regions the agreement was relatively less satisfactory and the measured shell thickness was in general greater than those calculated. Several factors were analyzed in order to explain this discrepancy. In this context, adequacy of several reported surface boundary conditions for the mould

region, including the time dependent heat flux correlation proposed by Savage and Pritchard[19,20] have been assessed. However, it was shown that the Savage-Pritchard correlation describes the heat flux across the mould wall fairly satisfactorily and therefore, can be universally applied as a reasonable surface boundary condition in the mathematical model (in the mould region). In addition, the investigators[10] also proposed a new correlation between average mould heat flux and the dwell time of casting in the mould. Furthermore, validity of the average mould heat flux correlation was verified with the measured mould heat transfer coefficient values of several continuous casting machines.

Lait and Brimacombe[22] in a subsequent study, solved almost a similar heat transfer model proposed earlier by Mizikar[8], using the explicit finite difference procedure. Both constant mould heat transfer coefficient as well as an empirical mould heat flux correlation were incorporated in the model as boundary condition. The model was applied to analyze the continuously cast stainless steel slab and low carbon steel billets. The predicted pool profiles were compared with the corresponding plant scale measurements. It has been reported that, while the agreement between theory and experiment for low carbon steel billets was quite reasonable, the same for the stainless steel slab was in general less satisfactory. In addition to this, the investigators[22] analyzed the validity of various assumptions viz., mode of latent heat release between liquidus and solidus, effective thermal conductivity values etc., incorporated in the model.

In a separate study, Brimacombe[10] modified the model[22] further and extended this to two dimensional situation in order to analyze the heat flow in square billet caster more accurately. In that study, value of effective thermal conductivity in the liquid was varied between 5 to 10 times the molecular thermal conductivity of steel at that temperature. The remaining features of the model were however essentially similar to those in the previous study[22]. The model was applied to design the mould and spray cooling configurations (mould length, spray length etc.) for square billet casting machines. Thus, correlations relating the working length of the mould, casting speed and shell thickness were proposed and necessary guidelines for designing the spray cooling zone to achieve the desired cooling conditions were also recommended[10].

The effective thermal conductivity approach, originally proposed by Mizikar[8], has also been applied to study several solidification related phenomena in CC. Recently, Laki et.al[25,26] have applied the concept to study the microstructural features such as the dendrite arm spacing and volume fraction of the delta ferrite in continuously cast stainless steel slab. The investigators[26] have also studied solidification in the meniscus region of a solidifying casting. Satisfactory agreements between numerical predictions and experimental observations have been reported.

Similarly, Mundim et.al[27] applied Crank-Nicholson finite difference scheme to analyze heat flow phenomena during slab casting. The model predictions were used to analyze the influences of various operating parameters such as melt

superheat, casting speed, steel composition, secondary cooling water flow rates etc., on the rate of solidification of liquid steel.

Although several mathematical model studies have been carried out using the concept of artificial effective thermal conductivity, only a few of them have reported a reasonable agreement between the experimental and the computed results throughout the pool region. By and large, correspondence between theory and experiments were somewhat acceptable only in the upper pool region[10] (i.e. the mould region). Disagreement in the lower part (viz., the submould region) has sometimes been attributed to the error associated with the measurements as well[10,20-24].

Recently, Lahiri[28] has suggested, on the basis of mathematical analysis, that the value of effective thermal conductivity in the liquid pool should be at least 43 times the molecular thermal conductivity of liquid steel. This finding[28], however, is in much contrast to the equivalent previous claims of 5 to 10 times of the molecular thermal conductivity[10]. Similarly, Mazumdar et.al[15,29] have reported significant discrepancy between their model predictions and experimental data in literature on shell thickness. Using a two dimensional pseudo steady state heat flow model, the investigators[15] analyzed heat flow and solidification phenomena mathematically in two different square billet casting operations. Based on the fundamental analysis, Mazumdar[29], however, attempted to explain the possible cause of such discrepancy between prediction and measurements, and attributed these to the basic assumption of the modelling[8,10] itself (i.e prescription of a unique value of effective thermal

conductivity throughout the liquid region to account for the bulk motion and turbulent convection on heat transfer). Mazumdar[29], went on to propose that a single value of the artificial effective thermal conductivity, although widely accepted, is physically unrealistic and consequently, not adequate enough to describe realistically the heat flow in various industrial continuous casting process.

Considering such divergent views expressed by the previous investigators as well as the present world wide interest in an effective alternative approach of modelling, it is naturally important to assess the adequacy of the effective thermal conductivity based model as applied to the mathematical modelling of continuous casting of steel.

Some assessment of the mathematical model studies have been attempted by earlier investigators[10,22,29]. However, these were quite limited in their scope (viz., unidimensional model, model specific to a particular casting configuration etc). Moreover, sensitivity of numerical parameters on computed results were not assessed. In the present study, therefore, the evaluation of modelling procedure based on effective thermal conductivity approach has been carried out in a much more comprehensive fashion as compared to those carried out earlier. The salient features of the present investigation are noted below.

(i) A steady state three dimensional heat flow model of continuous casting has been considered, and a computational procedure developed for solving the same.

(ii) The generalized heat flow model developed in this study can be applied to the analysis of practically all continuous

casting configurations (billets (square and round), bloom and slab).

(iii)   The influence of various numerical approximations and parameters on computed results were assessed rigorously.

2.3 FORMULATION OF THE GOVERNING EQUATION FOR THE PRESENT STUDY

2.3.1   Assumptions in Modelling

Heat flow during continuous casting of billets, blooms slabs etc. involves several complex phenomena such as: solidification of molten steel over a range of temperature, non-planer or wavy solidification front due to non-equilibrium conditions (e.g. rapid rate of growth, jerky withdrawal of casting strand etc.) at the solid - liquid interface, segregation of solute elements (e.g. C,S,P,Mn, etc.) resulting into changes in morphology (i.e. columnar-equiaxed transition), shrinkage in the volume upon solidification and so on. Moreover, cooling below the solidus temperature is associated with solid-state phase transformations and volume contraction etc.. Finally, bulging of strand between the support rolls in the secondary cooling zone and bending of strand etc. are likely to introduce considerable amount of complexity to any rigorous mathematical analysis of heat transfer phenomena during continuous casting of steel. Consequently, in order to describe heat flow within the solidifying strand during continuous casting mathematically, following simplifying assumptions have been incorporated in the present heat transfer model.

(i)   Effect of fluid turbulence and convection on heat transfer has been taken into account by artificially increasing the thermal conductivity in the liquid pool region.

(ii) Solidification is essentially under equilibrium condition.

(iii) Solidification front is flat or planer with respect to the adjacent liquid.

(iv) Dimension of the cast section remains fixed throughout the process (i.e. bulging and volume contraction etc. are ignored).

(v)   Meniscus surface is flat (i.e. no surface disturbance and melt level fluctuation in the mould).

(vi) Invariant density and specific heat of steel.

(vii) Except for the latent heat release, heat effects associated with other phase transformation reactions (e.g. δ-ferrite $\longrightarrow$ austenite, austenite $\longrightarrow$ pearlite etc.) have been neglected.

(viii) Effect of segregation, mould oscillation, bending of strand etc. have been ignored.

(ix) Due to symmetry of heat flow in square sections (e.g. billet), only a quadrant of its cross-section has been considered for the heat flow flow analysis. For slab, a semi-infinite geometry has been assumed and heat flow through its narrow face has been ignored. Similarly, for cylindrical billet, heat flow has been assumed to be

independent of the θ-direction (i.e. $\partial T/\partial\theta = 0$) (see later).

2.3.2 Governing Heat Flow Equation

Heat flow in the solidifying strand in CC is essentially multidimensional. Thus, appropriate heat balance under steady state conditions over a small volume element in the system (Fig.2.1), in cartesian coordinate, can be represented in terms of the following partial differential equation:

$$\rho c U_o \left(\frac{\partial T}{\partial Z}\right) = \frac{\partial}{\partial Z}\left(K_{eff}\frac{\partial T}{\partial Z}\right) + \frac{\partial}{\partial X}\left(K_{eff}\frac{\partial T}{\partial X}\right) + \frac{\partial}{\partial Y}\left(K_{eff}\frac{\partial T}{\partial Y}\right) + S$$

$$(W\ m^{-3})$$

$$...(2.1)$$

The term on the L.H.S. of Eq.(2.1) represents heat flow in the axial (i.e. withdrawal) direction (Z) due to the bulk motion (U_o) of the descending strand. The first term on R.H.S. is a conduction term in axial direction, whereas the second and the third term represent conduction of heat along the transverse plane (viz., X and Y directions respectively). ρ, c, K_{eff} and S are density, specific heat and effective thermal conductivity of steel. S is a source term.

In the previous studies[8,10,22-24] the effective thermal conductivity (K_{eff}) values in the liquid pool was varied arbitrarily between 5-10 times (mostly 7 times) of the molecular thermal conductivity of steel. In the present study also, the value of K_{eff} in the liquid region (i.e. where $T \geq T_{liq}$) has been assumed, as a first approximation, to be equal to 7 times the
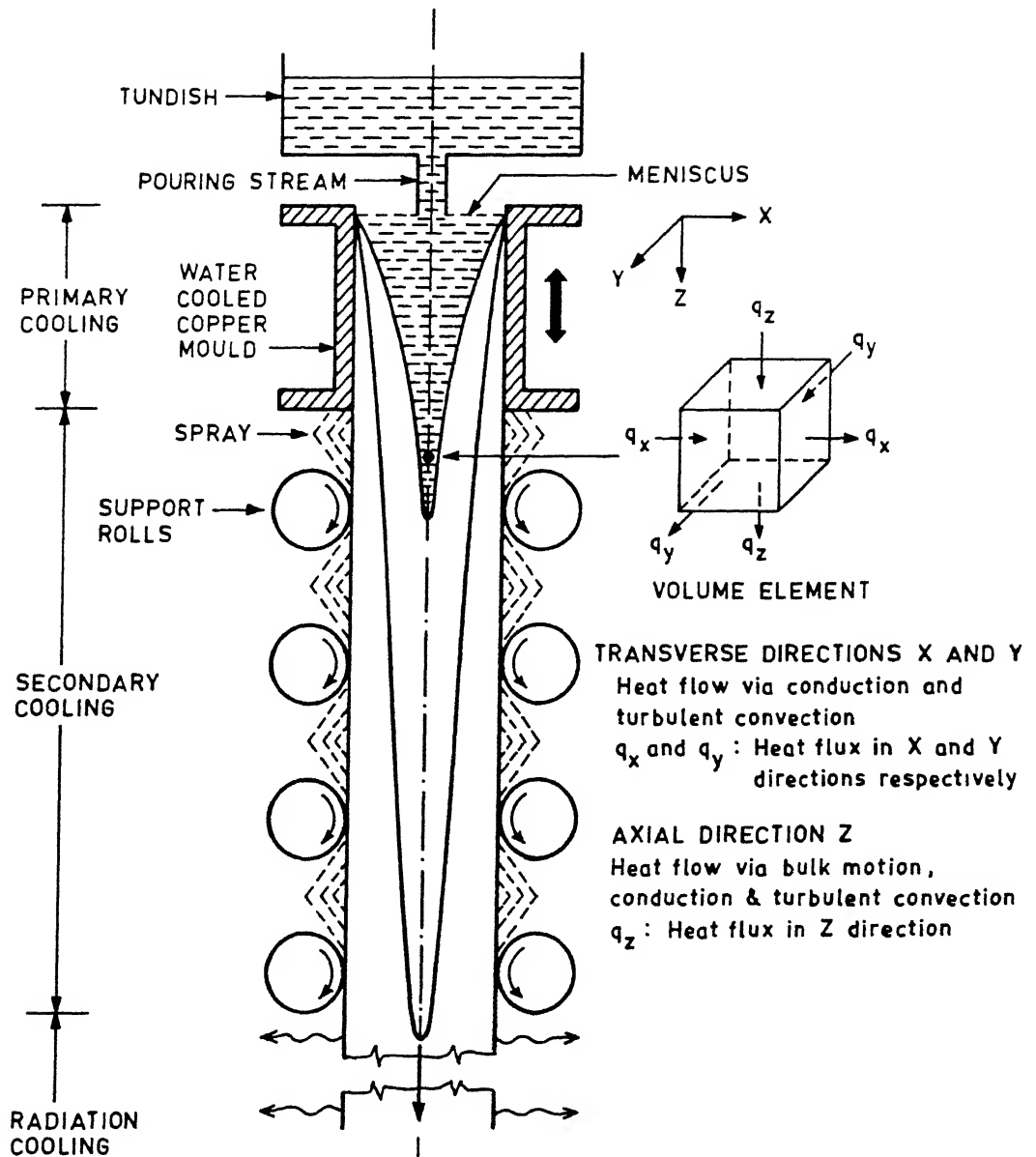
Fig. 2.1.   Schematic of a typical continuous casting operation; also a three dimensional volume element in the casting strand illustrating the concept of heat balance applied to derive Eq. 2.1.

molecular thermal conductivity of steel. In the solid region
however, K_{eff} was considered to be equal to the thermal
conductivity (K) of steel at that temperature. Similarly, in the
mushy zone, in general the continuum approach has been considered
and the mixture rule [viz., $K_{mush} = f_s K + (1 - f_s) K_{eff}$, where f_s
is the fraction of solid], applied to estimate the relevant
effective thermal conductivity value.

2.3.3   Modelling of Axial Heat Conduction Term in the Governing Equation

Because of relatively lower thermal conductivity
of steel than other common metals such as Aluminium etc. and
faster casting speed, previous investigators[8,10,22-24] have
ignored the heat conduction along the axial direction and thus,
neglected the $\frac{\partial}{\partial Z}(K_{eff} \frac{\partial T}{\partial Z})$ term in the governing equation
(Eq.(2.1)). Since the exact influence of axial conduction on
overall heat flow have so far not been demonstrated explicitly,
therefore in the present work, an axial conduction term has been
included in Eq. 2.1. Incorporation of this term in the governing
equation, as one might anticipate, would require two boundary
conditions along the Z coordinate axis. Thus, one of the
boundaries e.g., the meniscus from region outside the pouring
stream, can either assumed to be at the prescribed temperature
(i.e. T_0) or regarded as completely insulated (i.e. zero heat
flux across the boundary). At the outflow boundary, zero axial
temperature gradient is commonly applied boundary condition.
However, for a short domain length the axial temperature gradient

may not be equal to zero, and hence, the imposed boundary condition may not be a realistic one. To take care of this, the outflow boundary was considered to be located far away from the inlet boundary so that a zero heat flux condition in the former is physically valid. Consequently, in the present study, a sufficiently longer casting strand (at least 5m) was considered as the appropriate calculation domain and zero axial temperature gradient was prescribed at the exit as the relevant boundary condition. These will be discussed in detail in a subsequent section.

2.3.4 Modelling of Latent Heat Release Effect

In the governing heat flow equation (Eq. (2.1)), the rate of latent heat release per unit volume (S) during solidification constitutes a heat source term. During solidification, latent heat (ΔH_f) is released between the liquidus and the solidus temperatures (i.e. in the mushy zone). Since ΔH_f for liquid-solid transformation of steel is significant (Table 2.2), therefore, modelling of the latent heat release effect is critical for the accurate prediction of the rate of solidification and the overall temperature field in CC. The mushy zone, where the latent heat is released, however, involves several complex phenomena such as segregation of solute elements, dendrite growth, columnar-equiaxed transition, flow through complex inter dendritic channels etc., and it is not known to what extent these factors affect the mode of latent heat release during the solidification of steel. Consequently, some idealization have been made to describe 'S' mathematically. To

this end, in a most simplified approach, the specific heat of steel has been increased linearly in between the liquidus and solidus temperatures to account for the latent heat release[8]. In some other studies[10], a known enthalpy-temperature relationship has been applied to the heat flow equation to take into account the effect of latent heat. Alternatively, in the mushy zone the latent heat release can be computed from the distribution of solid fraction (f_s) assuming equilibrium solidification of steel[25,26]. In the present study also, the last approach has been adopted and thus, the volumetric rate of latent heat release has been expressed as:

$$S = \rho U_0 \Delta H_f \frac{\partial f_s}{\partial Z} \qquad (Wm^{-3}) \qquad \qquad ...(2.2)$$

where ΔH_f is the latent of fusion of steel

The term ($\partial f_s / \partial Z$) represents change in solid fraction (f_s) with progress of solidification in a volume element (see later) during its descend through an incremental distance (ΔZ) in the axial direction. The solid fraction can be estimated from the relevant portion of iron-carbon equilibrium diagram (Fig.2.2). At any temperature (T) between the liquidus and solidus temperatures, for a given initial carbon (C_0) content in steel, solid fraction (f_s) can be estimated by applying Lever rule to the iron-carbon diagram as follows:

$$f_s = (C_L - C_0)/(C_L - C_s) \qquad \qquad ...(2.3)$$

Liquid composition (C_l) and corresponding solid carbon contents
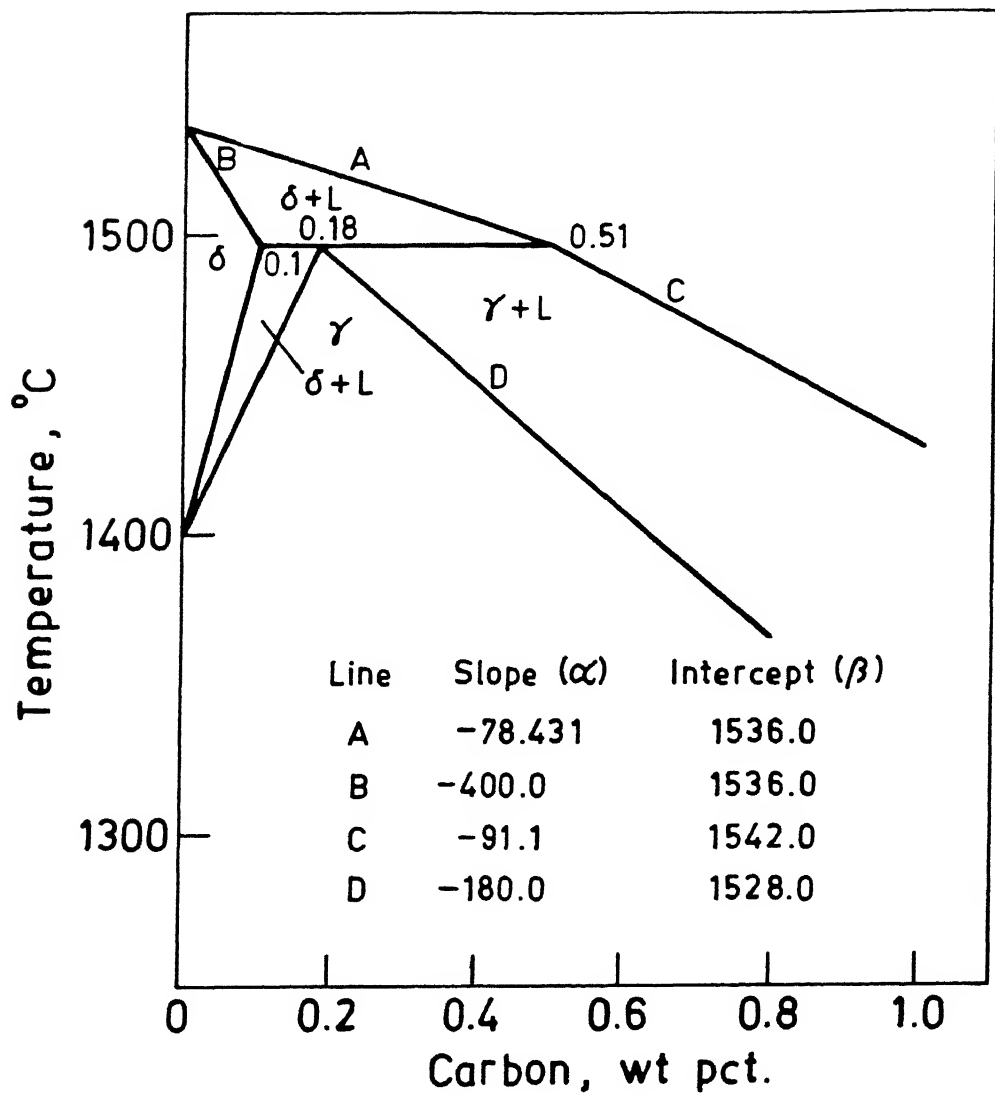
Fig. 2.2. Relevant section of the idealised iron-carbon equilibrium diagram.

(C_s) in Eq.(2.3) have been deduced from the following expressions, assuming a linear variation of liquidus and solidus temperatures with pct.C in the phase diagram (Fig.2.2).

$$C_L = (T - \beta_L)/\alpha_L \qquad \qquad \ldots(2.3a)$$

and $\qquad C_S = (T - \beta_S)/\alpha_S \qquad \qquad \ldots(2.3b)$

where α's and β's are the slopes and intercepts of respective liquidus and solidus lines in Fe-C diagram (Fig.2.2).

2.3.5 Boundary Conditions

A schematic representation of the calculation domain and the relevant boundary conditions have been presented in Fig.(2.3). These are summarized below mathematically as :

(i) at the meniscus (Z=0)

    (a) inside the pouring stream
       $0 \leq X \leq r_0$ and/or $0 \leq Y \leq r_0$, $\qquad T = T_0 \qquad \ldots(2.4a)$

    (b) outside the pouring stream
       $r_0 < X \leq a/2$ and/or $r_0 < Y \leq b/2$, $\quad q_z = 0 \qquad \ldots(2.4b)$

(ii) at the outflow boundary (Z=L)

    $0 \leq X \leq a/2$ and/or $0 \leq Y \leq b/2$, $\quad \partial T/\partial Z = 0 \quad \ldots(2.5)$

(iii) at the axis of symmetry and/or central plane

$$X=0, \ 0 \leq Y \leq b/2, \ 0 \leq Z \leq L, \quad \partial T/\partial X = 0 \left.\begin{array}{c} \\ \\ \end{array}\right\}$$

$$\qquad \qquad \qquad \qquad \qquad \qquad \qquad \qquad \qquad \qquad \ldots(2.6)$$

$$Y=0, \ 0 \leq X \leq a/2, \ 0 \leq Z \leq L, \quad \partial T/\partial Y = 0$$

(iv) at the cast surface,

$$X=a/2, \ 0 \leq Y \leq b/2, \ 0 \leq Z \leq L, \quad q_s = -K \left.\frac{\partial T}{\partial X}\right|_{X=a/2}$$
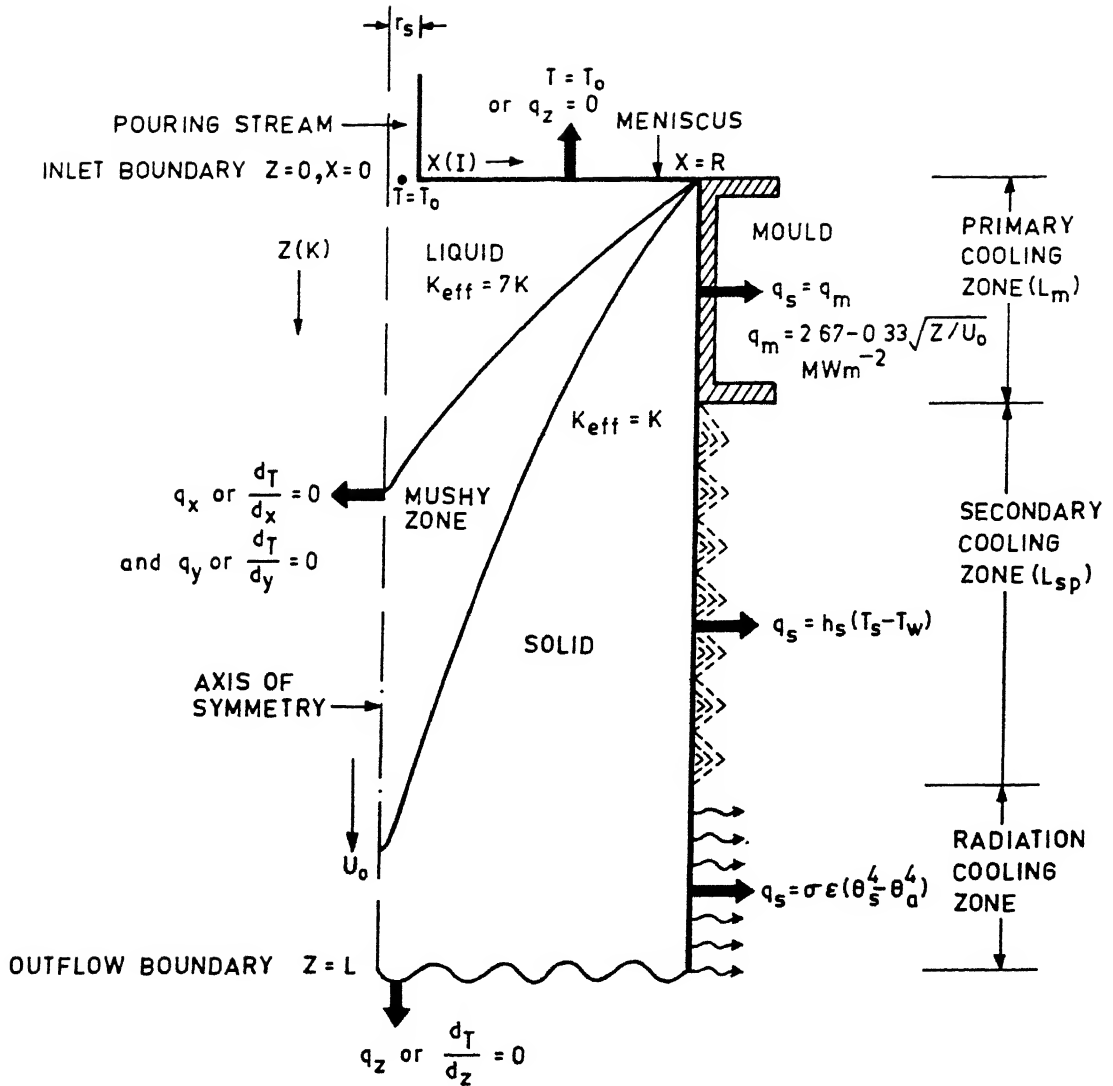
Fig. 2.3. Schematic of the calculation domain in two dimension and the associated boundary conditions applied to solve Eq. 2.1.

$$Y=b/2, \quad 0 \leq X \leq a/2, \quad 0 \leq Z \leq L, \qquad q_s = - K \left. \frac{\partial T}{\partial Y} \right|$$

$$...(2.7)$$

The boundary condition (i) originated from the fact that the temperature inside the pouring stream was assumed to be the same as the pouring or casting temperature (T_o) of the steel. Outside the pouring stream, melt surface was assumed to be covered with an insulating slag layer. Therefore, heat flux in this region across the meniscus can be assumed to be zero. Far away from the meniscus, the out flow boundary has been considered and the normal temperature gradient at this boundary was prescribed to be zero (i.e. b.c.(ii)). Across the central plane, due to symmetrical heat flow in all directions, zero normal temperature gradients was assumed (i.e. b.c. (iii)). At the cast surface, extraction of heat from the surface is complicated by the formation of an insulating air gap between the cast and the mould surfaces. Air gap constitutes about 70-80 pct.[16,24] of the total heat transfer resistances in the mould. The gap characteristics are complex and often unknown. Heat flux at such a boundary has been estimated either from the empirical data of mould heat transfer coefficient or via semi-empirical correlations. In this regard, the Savage-Pritchard correlation[20] for the instantaneous mould heat flux has been reported to give a fairly reasonable estimate of the mould heat flux and it has been applied by many previous investigators[10,22]. In the present study also the Savage-Pritchard correlation[20] has been adopted to deduce the instantaneous mould heat flux (q_m).

Thus, q_s (Eq.(2.7)) can be quantified in the mould region ($0 \leq Z \leq L_m$, $L_m < L$) as :

$$q_s = q_m = \left[2.67 - 0.33 \sqrt{t} \; \right] \times 10^6 \qquad \ldots(2.8)$$

or, $\quad q_m = \left[2.67 - 0.33 \sqrt{Z/U_0} \; \right] \times 10^6 \qquad \ldots(2.8a)$

where t is time in seconds.

In the secondary cooling zone ($L_m < Z \leq L_s$, $L_s < L$), heat extracted from the surface of the casting is predominantly by impinging water sprays. Therefore, the surface heat flux (q_s) can be expressed by the following expression :

$$q_s = h_s \; (T_s - T_w) \qquad \ldots(2.9)$$

Similarly, in the radiation cooling zone ($L_s < Z \leq L$), heat loss from the casting to the surrounding is purely by radiation and hence, surface heat flux can be approximated by the following expression:

$$q_s = \sigma\varepsilon \; (\theta_s^4 - \theta_a^4) \qquad \ldots(2.10)$$

The governing equation together with the boundary conditions summarized above represent the complete mathematical description of heat flow in CC, which on solution would provide a complete three dimensional temperature field. Consequently, solid shell thickness, surface temperature etc., in the cast section in the different cooling zones i.e. mould, spray and radiation, can be conveniently estimated.
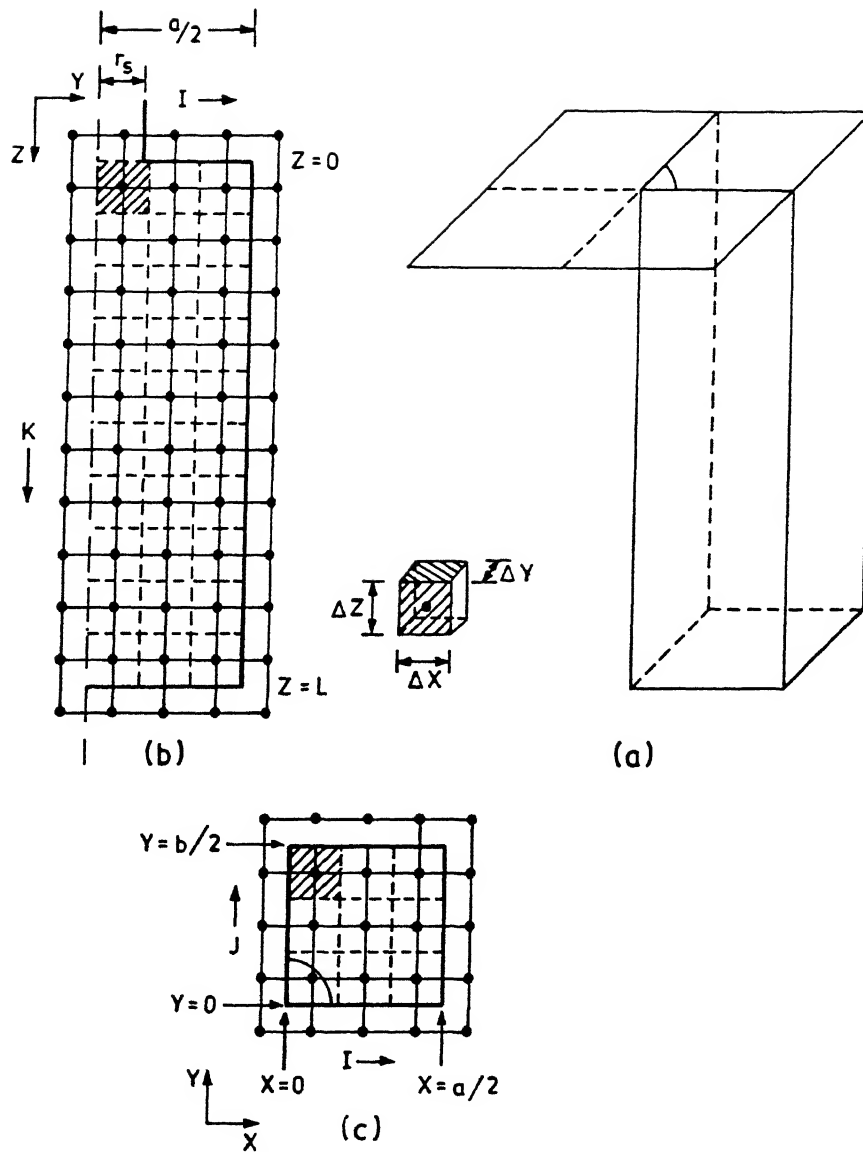
Fig. 2.4. Schematic of grid distribution in (a) one quarter of a square billet (b) the central vertical plane and (c) a transverse plane.
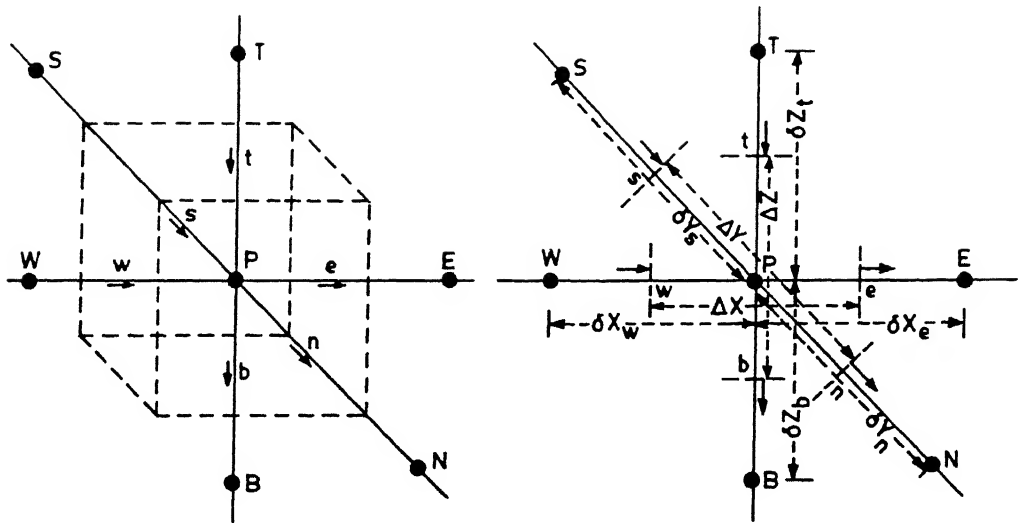
Fig. 2.5.   A typical three dimensional control volume in cartesian coordinate system.

wise profile of the dependent variable (i.e. T) between the nodal points has been assumed. The numerical integration procedure involved deriving the volume integral of each terms of Eq.(2.1) over the control volumes under consideration (e.g. P in Fig.2.5), which leads to the following expression:

$$\int_t^b \int_s^n \int_w^e \left(U_0 \rho \ c \left(\frac{\partial T}{\partial Z} \right) \right) dx \ dy \ dz \ = \ \int_t^b \int_s^n \int_w^e \left(\frac{\partial}{\partial Z} \left(K_{eff} \ \frac{\partial T}{\partial Z} \right) \right) dx \ dy \ dz$$

$$+ \int_t^b \int_s^n \int_w^e \left(\frac{\partial}{\partial X} \left(K_{eff} \ \frac{\partial T}{\partial X} \right) \right) dx \ dy \ dz \ + \ \int_t^b \int_s^n \int_w^e \left(\frac{\partial}{\partial Y} \left(K_{eff} \ \frac{\partial T}{\partial Y} \right) \right) dx \ dy \ dz$$

$$+ \int_t^b \int_s^n \int_w^e S \ dx \ dy \ dz \qquad \qquad \qquad ...(2.11)$$

In Eq.(2.1) it is readily seen that along the X and Y directions, there are only second order derivatives (i.e. the elliptic terms). Numerical integration of these derivatives can be more conveniently carried out and represented as follows:

$$\int_t^b \int_s^n \int_w^e \left(\frac{\partial}{\partial X} \left(K_{eff} \ \frac{\partial T}{\partial X} \right) \right) dx \ dy \ dz \ + \ \int_t^b \int_s^n \int_w^e \left(\frac{\partial}{\partial Y} \left(K_{eff} \ \frac{\partial T}{\partial Y} \right) \right) dx \ dy \ dz$$

$$= \ \left[K_{eff} \ \frac{dT}{dX} \right]_w^e \Delta Y \ \Delta Z \ + \ \left[K_{eff} \ \frac{dT}{dY} \right]_s^n \Delta X \ \Delta Z$$

$$= \ [- q_e + q_w] \ \Delta Y \ \Delta Z \ + \ [- q_n + q_s] \ \Delta X \ \Delta Z$$

$$= \ \frac{K_{eff,e}}{\delta x_e} (T_E - T_P) \ \Delta Y \ \Delta Z \ + \ \frac{K_{eff,w}}{\delta x_w} (T_P - T_W) \ \Delta Y \ \Delta Z$$

$$+ \frac{K_{eff,n}}{\delta y_n} (T_N - T_P) \, \Delta X \, \Delta Z \; + \; \frac{K_{eff,s}}{\delta y_s} (T_P - T_S) \, \Delta X \, \Delta Z$$

$$\ldots (2.12)$$

In the axial direction, Z, however, in addition to the usual second order derivatives, there is a first order derivative associated with the bulk motion term (i.e. parabolic term) as well. Consequently, a procedure such as the fully implicit marching integration, can not in principle be applied to numerically integrate the derivatives along the Z coordinate[30]. It would have been possible if there would have been the first order derivative only in Eq.(2.1) (i.e. zero axial conduction)[8,10]. Thus, the first order and second order derivatives in the Z-direction were tackled by considering the former as a convection and the latter one as a diffusion term. These terms were then numerically integrated using the concept as applied to a combined convection-diffusion problem proposed by Patankar[30], as follows:

$$\underbrace{\int_t^b \int_s^n \int_w^e \left(U_0 \, \rho \, C \left(\frac{\partial T}{\partial Z} \right) \right) dx \, dy \, dz}_{\text{bulk convection term}} - \underbrace{\int_t^b \int_s^n \int_w^e \left(\frac{\partial}{\partial Z} \left(K_{eff} \, \frac{\partial T}{\partial Z} \right) \right) dx \, dy \, dz}_{\text{diffusion / conduction term}}$$

$$\ldots (2.13)$$

$$= (\rho C U_0 T_b - \rho C U_0 T_t) \, \Delta X \, \Delta Y \; - \; \left[K_{eff} \, \frac{\partial T}{\partial Z} \right]_t^b \Delta X \, \Delta Y$$

$$\ldots (2.14)$$

In the CC situation, the Peclet number $\left(Pe = \rho C U_0 / (K/\delta)\right)$ is much larger than unity (i.e. a convection dominated case). Therefore, upwind difference scheme (UDS)[30] was employed to define the convective contribution and the routine central difference scheme (CDS)[30] for the diffusive (or conductive) contribution to heat transfer. These concepts transform Eq.(2.14) in the following form:

$$\rho C U_0 (T_P - T_T) \Delta X \Delta Y - \frac{K_{eff,b}}{\delta Z_b}(T_B - T_P) \Delta X \Delta Y$$

$$+ \frac{K_{eff,t}}{\delta Z_t} (T_P - T_T) \Delta X \Delta Y \qquad \ldots (2.15)$$

Finally, numerical integration of source term (S) yields:

$$\int_t^b \int_s^n \int_w^e \left(\rho U_0 \Delta H_f \left(\frac{\partial f_s}{\partial Z}\right)\right) dx\ dy\ dz = \rho U_0 \Delta H_f \left[f_s\right]_t^b \Delta X \Delta Y$$

$$= \rho U_0 \Delta H_f \left[f_{s,b} - f_{s,t}\right] \Delta X \Delta Y$$

$$\ldots (2.16)$$

Substituting, the various terms after integration in Eq.(2.11), and rearranging, the following discretization equation can be derived for the governing heat flow equation:

$$A_P T_P = A_B T_B + A_T T_T + A_E T_E + A_W T_W + A_N T_N + A_S T_S + S_U \ldots (2.17)$$

A_P in Eq.(2.17) represents the center point (i.e. P) coefficient of the discretization equation and is defined as:

$$A_P = A_B + A_T + A_E + A_W + A_N + A_S - S_p \qquad \ldots (2.18)$$

In Eqs.(2.17) and (2.18) the coefficients, A_B, A_T, contain the contributions of both bulk convection and diffusion from the neighbouring top and bottom control volumes (i.e. B and T) to the dependent variable (T_P) at a given central node P. Whereas, the other coefficients, e.g. A_E, A_W, etc., contain only diffusion contribution of the neighbouring control volumes (i.e., E, W, etc.) to the center point temperature, T_P. The appropriate expressions for various coefficients can be summarized as:

$$A_T = (\rho C U_0 + \frac{K_{eff,t}}{\delta Z_t}) \; \Delta X \; \Delta Y \qquad \ldots(2.19)$$

$$A_B = \frac{K_{eff,b}}{\delta Z_b} \; \Delta X \; \Delta Y \qquad \ldots(2.20)$$

$$A_E = \frac{K_{eff,e}}{\delta X_e} \; \Delta Y \; \Delta Z \qquad \ldots(2.21)$$

$$A_W = \frac{K_{eff,w}}{\delta X_w} \; \Delta Y \; \Delta Z \qquad \ldots(2.22)$$

$$A_N = \frac{K_{eff,n}}{\delta Y_n} \; \Delta X \; \Delta Z \qquad \ldots(2.23)$$

$$A_S = \frac{K_{eff,s}}{\delta Y_s} \; \Delta X \; \Delta Z \qquad \ldots(2.24)$$

S_U in equation (2.17) represents the constant part of a general linearized source (viz., $S = S_U + S_p T_P$). In the portion of the domain containing mushy zone, S_U was set equal to the discretized latent heat source term [i.e. rate of latent heat evolution in a given control volume], which is defined as :

$$\int_t^b \int_s^n \int_w^e S \; dx \; dy \; dz = S_U = \rho \; U_0 \Delta H_f \left(f_{s,b} - f_{s,t} \right) \; \Delta X \; \Delta Y \quad \ldots(2.25)$$

Evidently, for the present problem, S_P was considered to be zero.

Thus, in a system of n control volumes, n numbers of similar algebraic equations (viz., Eq.(2.17)) were obtained via the above mentioned discretization procedure. Also, since the discretization equations were obtained from the same governing equation (i.e. the energy balance equation Eq.(2.1)), the former therefore embodied the same conservation principle as the latter one. It is interesting to note here that this is an important feature of the control volume based numerical procedure in contrast to the routine Taylor series based numerical procedure (e.g. finite difference technique). The control volume face conductivities (e.g. $K_{eff,t}$, $K_{eff,b}$ - -,etc.) can be computed taking either arithmetic or harmonic mean (interpolation) of the relevant conductivity values prevalent at the adjacent nodal points. As seen from Eqs. (2.19) through (2.24), coefficients of discretization equations were computed on the basis of the conductivity values at control volume face as well as the geometrical features, the latter essentially deduced from the grid layout applied to the numerical solution scheme.

Prior to the solution of the discretization equations the boundary conditions were also transformed into equivalent numerical form. For implementation of boundary conditions numerically, only those control volumes located at the domain boundaries were considered[30,31]. Discretization equations are derived via the same above mentioned procedure. In essence, implementation of boundary conditions were the modification of either A_P and/or S_U terms of the discretization equations of the boundary control volumes.

To illustrate this further, Fig.2.6 schematically presents

the heat flow situation at the boundaries in a 2D calculation domain (i.e. transverse-X and axial-Z directions only). The boundary conditions to the energy balance equations in transverse direction as has been mentioned earlier were specified via the surface heat flux expression (e.g. Eqs.(2.7)-(2.10)). Thus, integration of the X-directional heat conduction term of the governing partial differential equation for the boundary control volume (Fig.2.6(a)) yielded:

$$\int_t^b \int_s^n \int_w^e \left(\frac{\partial}{\partial X} \left(K_{eff} \frac{\partial T}{\partial X} \right) \right) dx\ dy\ dz = \left[K_{eff} \frac{dT}{dX} \bigg|_e + K_{eff} \frac{dT}{dX} \bigg|_w \right] \Delta Y\ \Delta Z$$

$$= \left[- q_e + q_w \right] \Delta Y\ \Delta Z \qquad \ldots (2.26)$$

noting that at the domain boundary :

$$q_e = known = q_s \qquad \ldots (2.27)$$

(e.g. for the mould region, q_s is prescribed via the mould heat flux expression q_m, (Eq.(2.8)). Thus, following the procedure outlined above it can be shown that, integration of the governing equation around the near surface nodal points (except the corners) leads to a discretization equation of the type:
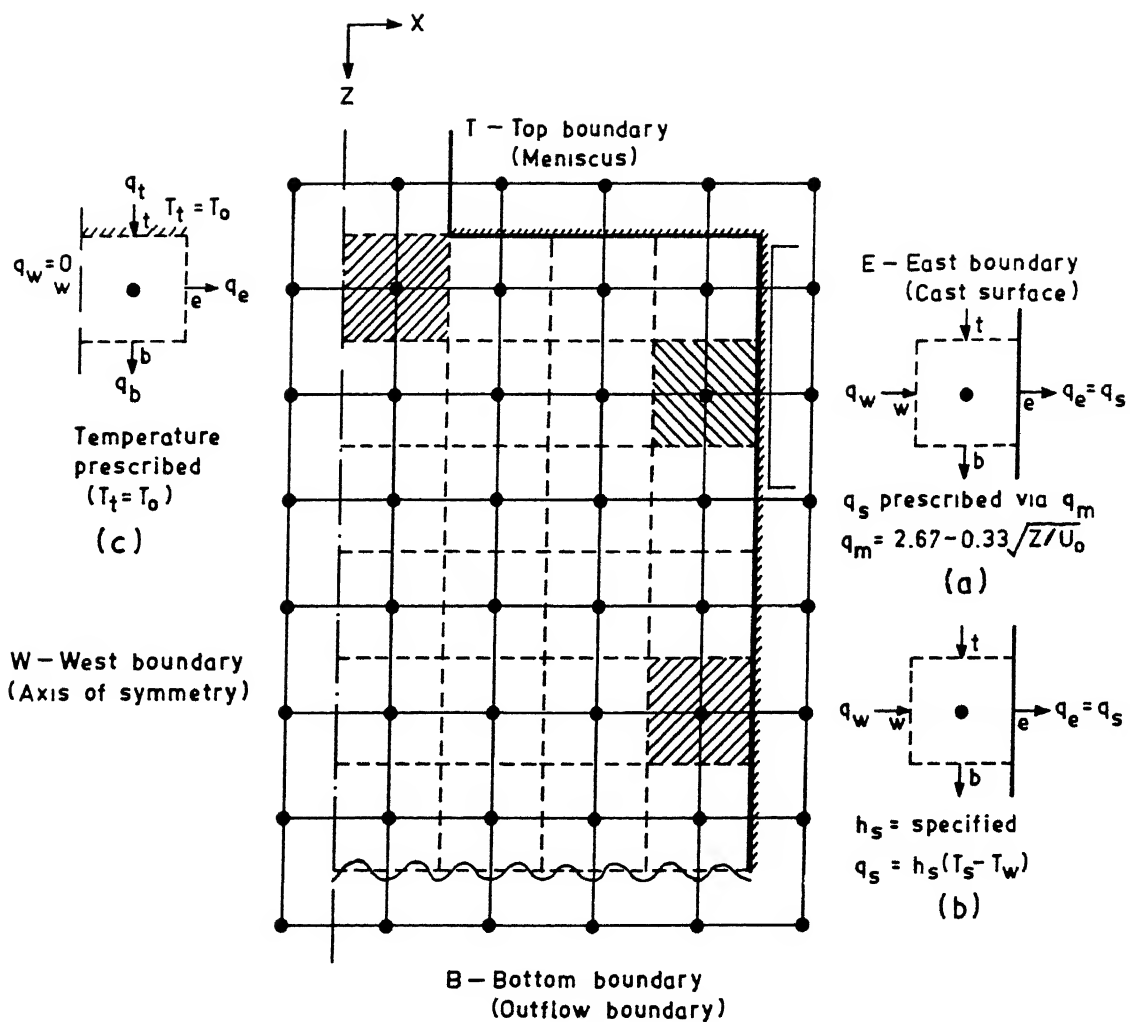
Fig. 2.6. Typical boundary control volumes in a
2D calculation domain.

$$A_P T_P = A_B T_B + A_T T_T + A_W T_W + A_N T_N + A_S T_S + \left(S_U - q_s \, \Delta Y \, \Delta Z \right)$$

$$\ldots (2.28)$$

in which, $\qquad A_P = A_B + A_T + A_W + A_N + A_S$

For the secondary cooling zone, during each iteration, surface temperatures (T_S) of the cast section have been estimated first via proper extrapolation (higher or lower order methods, detailed later) of computed internal temperature fields, and subsequently, surface heat fluxes (q_s) were estimated (Fig.2.6b) and substituted in Eq.(2.28). After taking into account the effect of surface boundary condition via modifying the S_U term as mentioned above, it is readily seen that the east neighbor 'E' (Figs.2.6a and 2.6b) has no role to play and thus, is isolated from the calculation scheme.

Similarly. the prescribed temperature (T_o) inside the pouring stream (Eq.(2.4)) has been taken into account by redefining the S_U and S_P terms, in the discretization equation of the control volumes lying in the immediate vicinity of the meniscus (Fig.2.6c), as follows :

$$A_P T_P = A_B T_B + A_E T_E + A_W T_W + A_N T_N + A_S T_S + \left(S_U + A_T . T_o \right)$$

$$\ldots (2.29)$$

Similarly, it can be shown that the zero heat flux or zero temperature gradient at the axis of symmetry (Eq.(2.6)), outflow boundary (Eq.(2.5)), and at the meniscus (Eqs.(2.4 and 2.4a)) can be conveniently incorporated considering the coefficients, $A_W = 0$, $A_B = 0$, and $A_T = 0$ respectively, in the discretization

equations of the respective west, bottom, and top boundary control volumes of the domain (Fig.2.6).

After incorporating the boundary conditions, via the above mentioned procedures, the resultant set of discretization equations were solved using the well known Tri-Diagonal Matrix Algorithm (TDMA) adopting a line by line solution procedure. In this, a particular grid line, say in Z-direction, is chosen and assuming the dependent variable (T) to be known (viz., guessed) in the X and Y directions, the problem is essentially reduced to a pseudo one dimensional situation and subsequently solved by the TDMA . This was applied to all the grid lines in one direction and the entire process was repeated for the other two space directions to obtain a tentative distribution of the 3D-temperature field. This typically constituted one iteration. The total number of iterations required was decided by the convergence criteria adopted, which in the present study was defined according to:

$$\sum \sum \sum \left\{ A_p T_p - \left(\sum A_{nb} T_{nb} + S_U \right) \right\} \leq 10^{-4} \qquad \ldots(2.30)$$

in which,

$$\sum A_{nb} T_{nb} = A_B T_B + A_T T_T + A_E T_E + A_W T_W + A_N T_N + A_S T_S$$

$$\ldots(2.31)$$

The triple sum in Eq.(2.30) represents the summation over the entire volume (e.g. the calculation domain). A typical under relaxation factor of 0.2 on the dependent variable has been employed in all the computations to achieve/enhance the convergence.

2.4.2   The Computer Program

For the numerical solution of the present problem, a general computer program in FORTRAN 77 and in double precision has been developed. The program is so written that three dimensional computations (3-D) as well as those in 2-D and 1-D can also be performed by manipulating certain key parameters. Furthermore, an interesting feature of the present computer program has been that, the same program can also be used for computations in cartesian as well as in the cylindrical polar coordinate systems. The transformation from one coordinate system to another or from one geometry to another can be illustrated by considering a general form of the heat conduction equation presented in Section 2.3.2:

$$\rho c U_0 \left(\frac{\partial T}{\partial Z}\right) = \frac{\partial}{\partial Z}\left(K_{eff} \frac{\partial T}{\partial Z}\right) + \frac{1}{\lambda_1} \frac{\partial}{\partial X}\left(\lambda_1 K_{eff} \frac{\partial T}{\partial X}\right) + \lambda_2 \frac{\partial}{\partial Y}\left(K_{eff} \frac{\partial T}{\partial Y}\right) + S$$

$$...(2.32$$

in which, λ_1 has been defined as an <u>index of coordinate system</u> and λ_2 as <u>index of coordinate dimension</u>.

(i) if, $\lambda_1=1$ and $\lambda_2=1$;   Eq.(2.32) becomes a 3-D heat conduction equation in cartesian coordinate, applicable to heat flow during billet casting

(ii) if, $\lambda_1=1$ and $\lambda_2=0$;   gives 2-D heat conduction equation in cartesian coordinate, applicable for slab caster

(iii) if, $\lambda_1=r=X$ and $\lambda_2=0$;   represents heat flow in 2-D cylindrical polar coordinate, applicable to round/axisymmetric billet caster.

As mentioned already, all the above three types of typical casting geometries have been simulated computationally in the present study.

The computer program consists of several subroutines or module for each specific operation. Flow chart of the program is shown in Fig.2.7. A typical computation is initiated with specifying the coordinate system and dimension (i.e. 3-D or 2-D and cartesian or cylindrical-polar). Relevant data and grids in various directions are specified. Geometric quantities, viz. distance between nodes and control volume faces, area of control volume faces and their volumes etc., are computed and conditions at each nodes are initialized. Subsequently, the following sequence of operations are carried out during each iteration till a converged solution obtained.

   (i) The thermophysical properties are updated in subroutine PROPS,

  (ii) coefficient of discretization equations are calculated in subroutine CALCT,

 (iii) boundary conditions are incorporated in subroutine BOUND,

  (iv) coefficients of discretization equations, are reassembled in subroutine CALCT,

   (v) the system of discretization equations are solved via TDMA in subroutine LISOLV,

  (vi) solid-fraction at various locations computed in subroutine FEC,

 (vii) surface temperature is estimated from the predicted internal temperature field,
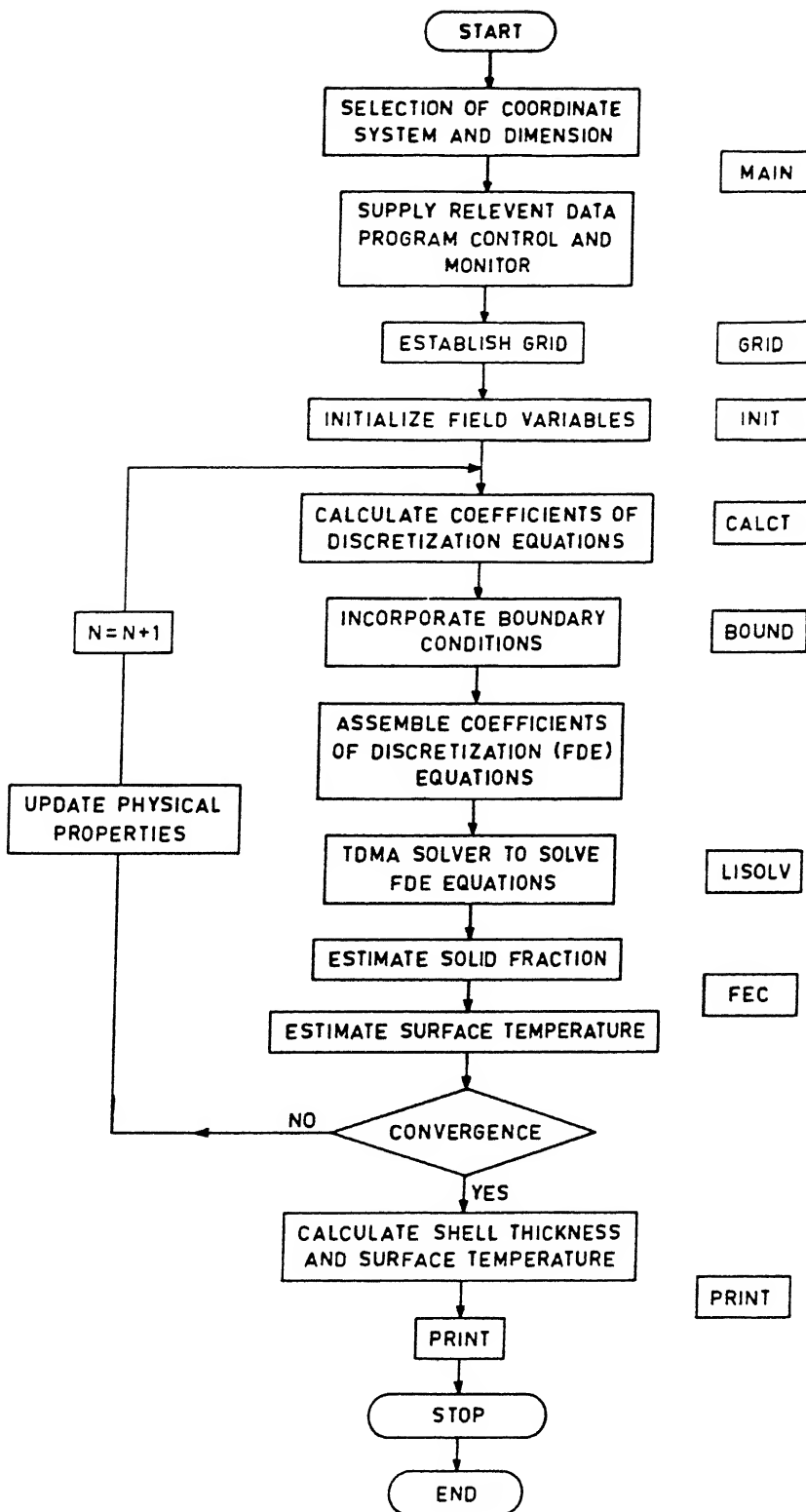
Fig 2.7. Flow chart of computer program for the model based on effective thermal conductivity concept.

(viii) the above mentioned steps (i) through (iv) are repeated till a converged solution is obtained,

(ix) from the converged solution (i.e. the temperature field) final cast surface temperature and shell thickness, for various axial positions, are estimated,

(x) relevant out put data are printed in subroutine PRINT.

All computations were carried out on the HP-9000 super mini computer available at I.I.T. Kanpur. As summarized in the subsequent sections, relevant data of actual CC operation were taken from literature, for carrying out numerical computations and their subsequent validation with experimental measurements.

2.5 RESULTS AND DISCUSSIONS

2.5.1 Sensitivity of Computation to the Choice of Grid Distribution

A variety of grid systems were employed in order to arrive at the practical grid independent solutions. Figures 2.8 and 2.9 respectively show the variations of shell thickness and midface surface temperature with distance below the meniscus for the various grid configurations tested. These further show that 25 x 40 and 25 x 80 produced almost identical estimates of
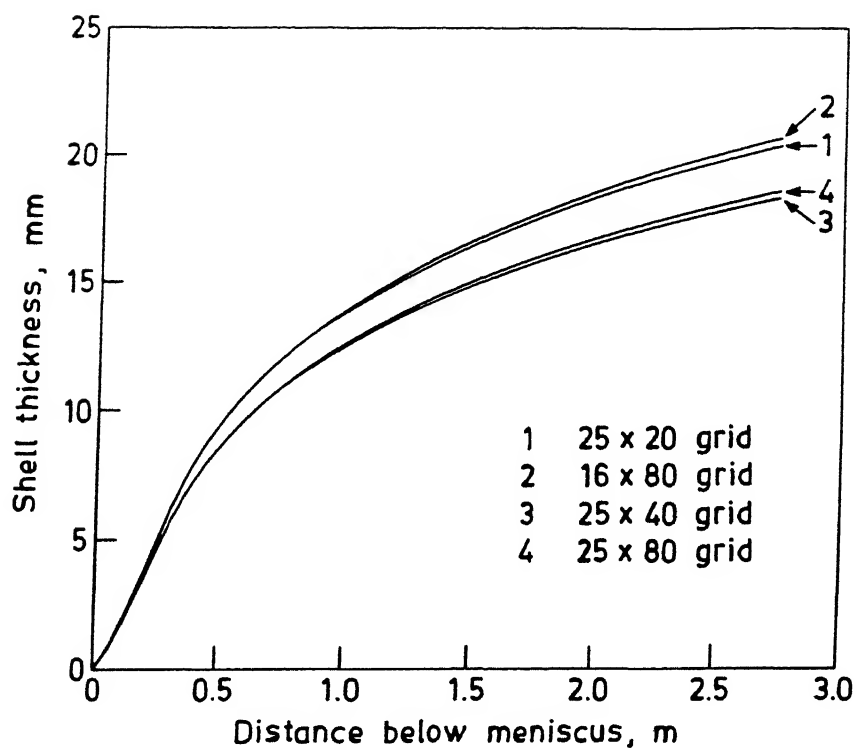
Fig. 2.8. Variation of shell thickness with distance below meniscus for different grid configurations (data set 4, table 2.1).
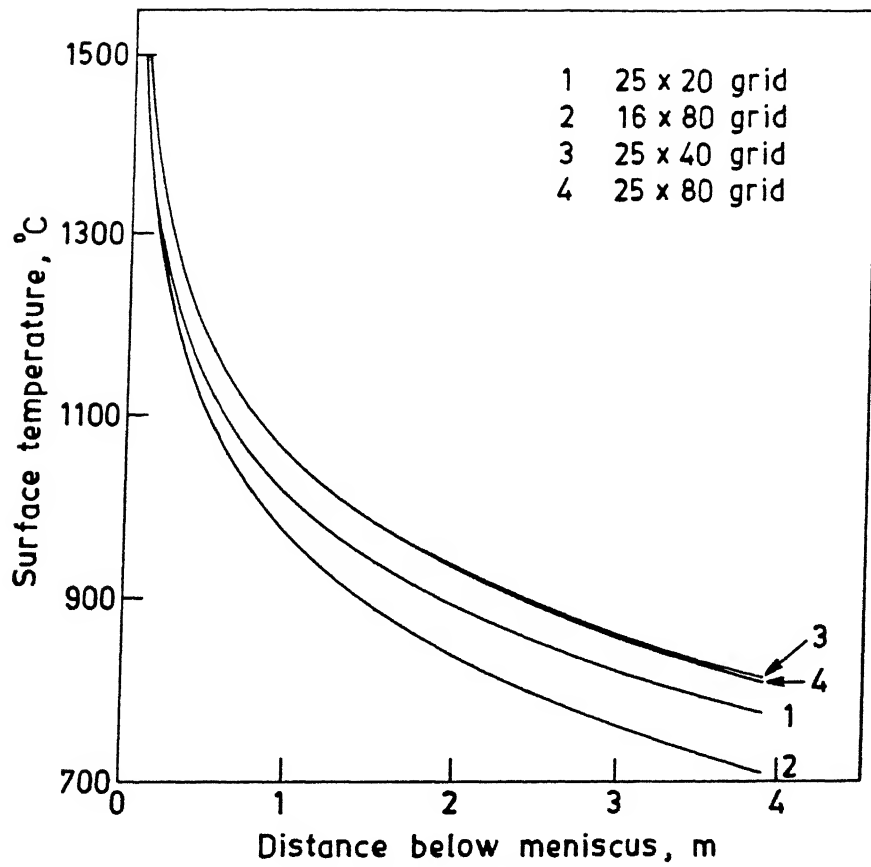
Fig. 2.9. Variation of surface temperature with distance below meniscus for different grid configurations (data set 4, table 2.1).

both shell thickness as well as surface temperature. However, minor differences existed between 25 x 20 and 25 x 80 grids or for 16 x 40 and 25 x 40 grids. These appear to indicate that for 25 x 40 grids the solution became nearly grid independent. However, the solution, as reflected from these figures seem to be relatively more sensitive to the number of grid points along the transverse directions, which is evident from the differences indicated between predictions derived via 16 x 80 and 25 x 80 grid systems. Other grid configurations (viz., 12 x 80, 18 x 80, 25 x 100 etc.) were also tried. However, 25 x 40 grid configuration, equivalent to a grid spacings of 3 mm in the transverse and 50 mm in the axial direction, was found to be satisfactory for arriving at grid independent solutions from a practical stand point. Consequently, similar grid spacings (e.g. transverse $\cong$ 3mm and axial $\cong$ 50 mm) as those corresponding to 25 x 40 grid systems were employed in all subsequent calculations reported.

2.5.2 Influence of Various Numerical Approximations on the Computed Results

2.5.2.1 Arithmetic mean vs. harmonic mean approximation for estimating the control volume face thermal conductivity

Before computations with actual CC data are carried out, and the results compared against the experimental measurements, influence of various numerical approximations on the predicted results were rigorously assessed. In the present

study, as has been mentioned already, liquid region was assumed to have a higher thermal conductivity (seven times the molecular thermal conductivity, K) than that of the solidified region. Similarly, the temperature dependent thermal conductivity of steel led to a highly nonuniform distribution of thermal conductivity in the calculation domain. While thermal conductivity values were known only at the grid points, calculation of coefficients of discretization equation (Eqs.(2.18)-(2.23)) required thermal conductivity values to be known at the mid positions between the nodal points (i.e. at the control volume faces). Consequently, it was necessary that proper interpolation techniques were applied to estimate thermal conductivity at the control volume face from those of the adjacent nodal points.

In the present study, control volume face conductivities were computed via (i) arithmetic mean and (ii) harmonic mean approximation procedures[30]. For a given control volume face (say 'e' in Fig.2.5), midway between the nodes (i.e. P and E), arithmetic mean approximation[30] gives the following value of control volume face conductivity:

$$K_{eff,e} = \frac{1}{2} (K_{eff,P} + K_{eff,E}) \qquad \qquad ...(2.33)$$

In contrast, harmonic mean approximation for the same provides:

$$K_{eff} = \frac{2 \, K_{eff,P} \times K_{eff,E}}{\left[K_{eff,P} + K_{eff,E}\right]} \qquad \qquad ...(2.34)$$
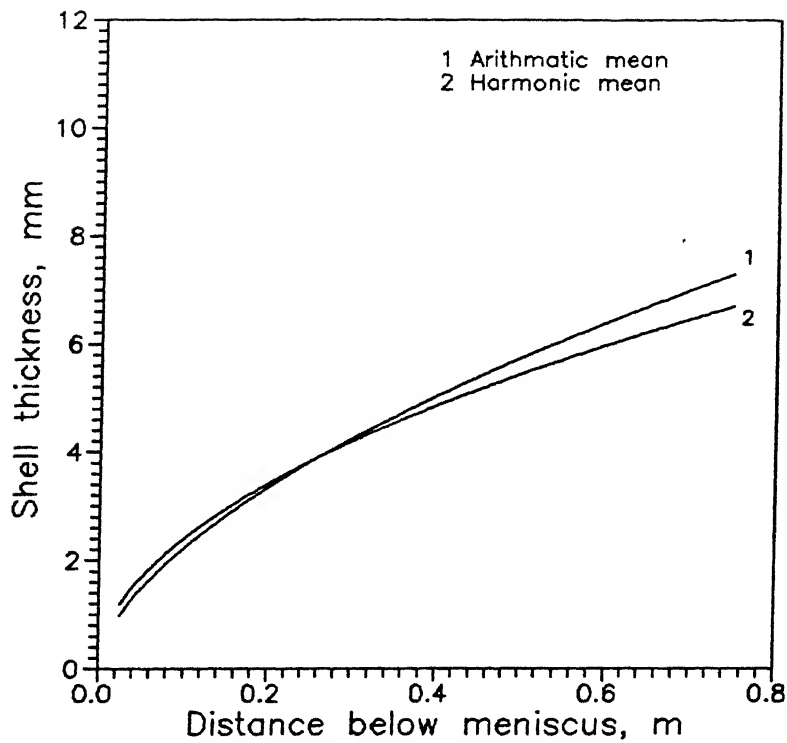
Fig.2.10: Effect of arithmatic mean and harmonic mean approximation techniques (e.g. for control volume face conductivity) on predicted shell thickness in a square billet[22].

(conditions of computations are summarized in Table 2.1)
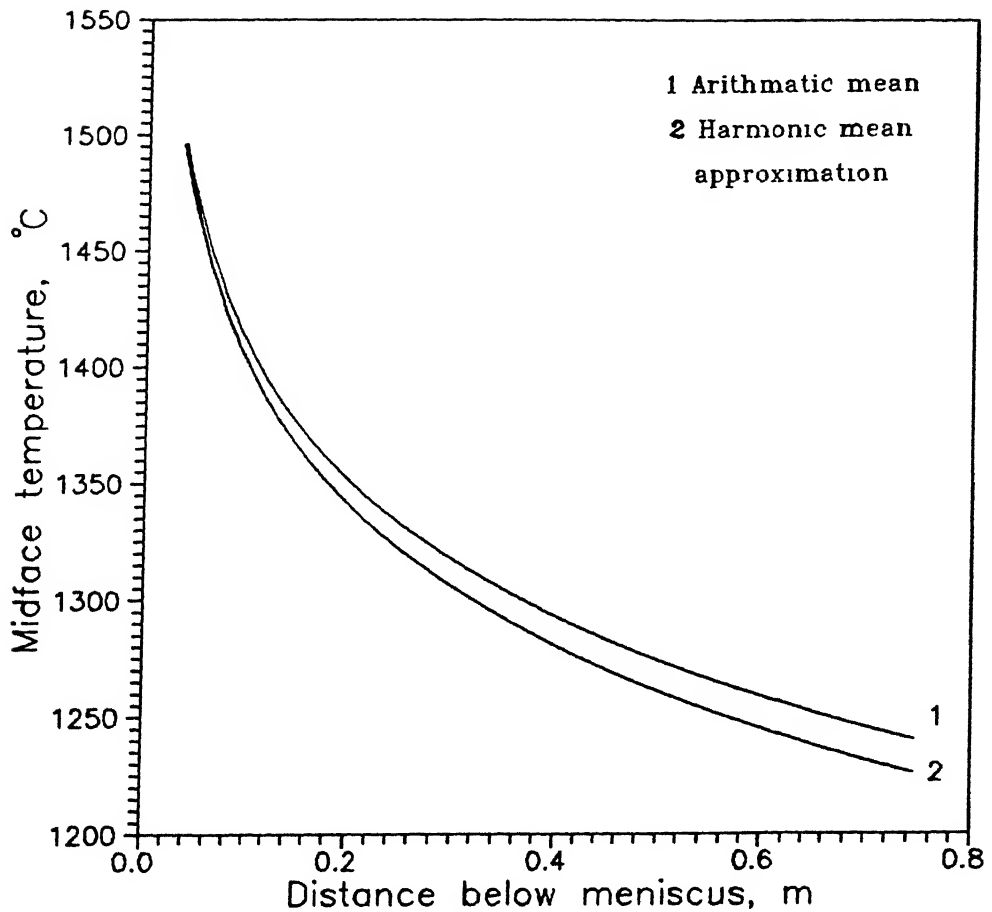
Fig.2.11: Effect of arithmatic mean and harmonic mean approximation
(e.g., for control volume face conductivity) on predicted
midface temperature in a square billet

(data set 2, Table 2.1)

Figs. 2.10 and 2.11 respectively present the variation of computed shell thickness and surface temperatures derived via arithmetic and harmonic mean approximation techniques. Despite wide variation of thermal conductivity in the calculation domain, these show practically negligible differences and indicate that the two procedures provide practically identical estimates. Therefore, from the view point of relative simplicity the arithmetic mean interpolation procedure has been adopted for all subsequent computations.

2.5.2.2 Lower order vs. higher order interpolations for estimating surface temperatures

As shown in Fig.2.6, at the cast surface, there is no grid point and hence cast surface temperature has to be calculated from the predicted internal temperature fields via some suitable interpolation techniques. Similarly, in the secondary cooling zone, the boundary condition at the cast surface has been prescribed via the heat transfer coefficient (h_s) and the spray water temperature (T_w). In order to calculate the surface heat flux (q_s) via Eq.(2.9), surface temperatures, at various positions in the spray cooling zone, have to be estimated first from the computed internal temperature field during each iteration. Therefore, accurate estimation of the surface temperature is critical for the reliability of the predicted results. The surface temperatures can be estimated from the internal temperature field using either the lower order or the higher order boundary treatments[32].
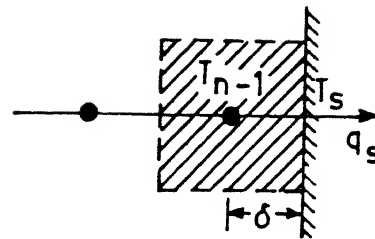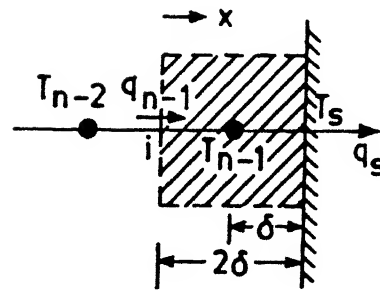
Fig. 2.12. Boundary control volumes considered for (a) lower order and (b) higher order interpolation methods for estimating cast surface temperature.

In the lower order interpolation procedure, for example, surface temperature or surface heat flux is estimated on the basis of a single nodal point temperature adjacent to the domain boundary (see Fig.2.12(a)). Thus, on the basis of such considerations,

$$q_s = \frac{K_s}{\delta} \left(T_{n-1} - T_s \right)$$

or, $$T_s = T_{n-1} - \frac{\delta}{K_s} q_s \qquad \qquad \ldots (2.35$$

On the other hand, the higher order interpolation takes into account two successive internal nodes adjacent to the strand surface boundary (Fig.2.12(b)) for estimation of the relevant surface temperature or heat flux[32] as follows :

$$q_s = 4 \frac{K_s}{\delta} \left(T_{n-1} - T_s \right) - 3q_{n-1} \qquad \ldots (2.36)$$

in which,

$$q_{n-1} = \frac{K_i}{\delta} (T_{n-2} - T_{n-1}) \qquad \ldots (2.37)$$

As is well known, the higher order interpolation technique is likely to provide relatively more accurate values of the surface temperature , since this takes into account the influences of other neighbouring nodes and consequently, makes the energy balance physically more meaningful.

Fig.2.13 presents the midface temperature variations along the axial direction, as estimated via the two interpolation procedures. There, the higher order interpolation method is seen to predict somewhat higher surface temperature (about 4 pct.)
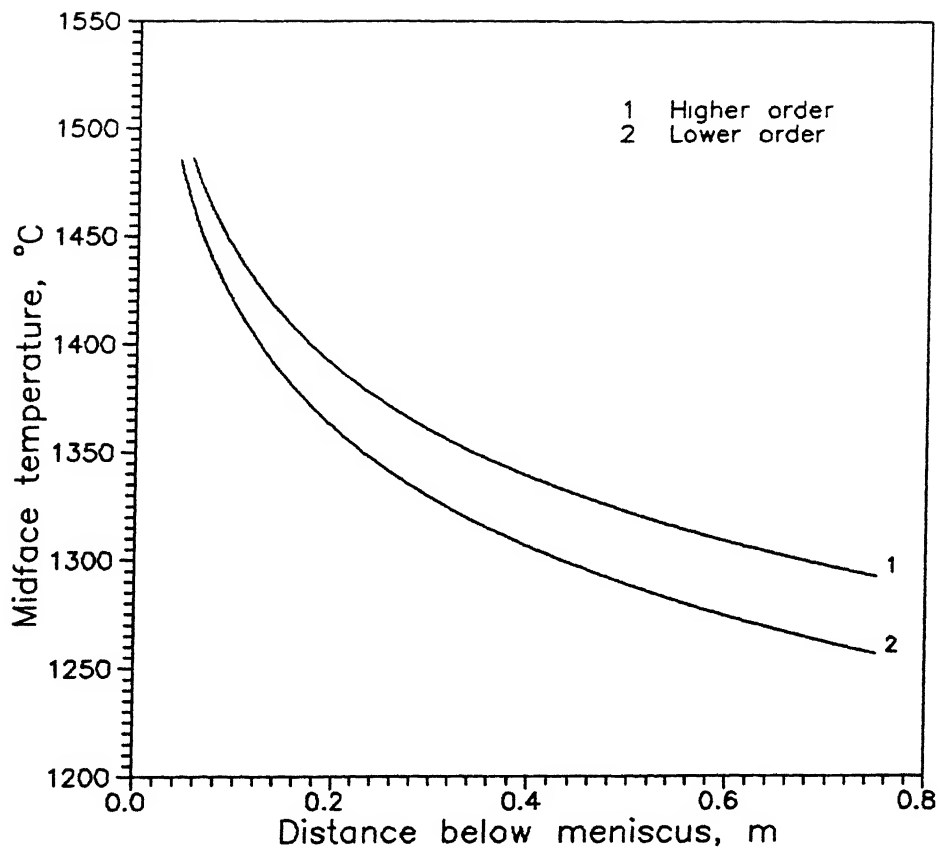
Fig.2.13. Effect of higher order and lower order interpolation techniques on predicted midface temperature in a square billet[22].

throughout the strand as compared to its lower order counterpart. Despite such marginal differences, the higher order interpolation technique has been considered in the present work since it is physically more realistic than the lower order method.

2.5.2.3 Influence of different numerical integration procedure for the mould heat flux expression

As pointed out earlier, the instantaneous heat flux expression represented via Eq.(2.8) has been applied as a prescribed surface boundary condition in the mould region. In order to estimate the rate of heat extraction, the heat flux expression has to be integrated numerically over the control volume faces at the cast surface boundary (Fig.2.14). For a given control volume P, as shown in Fig.2.14, the heat flux expression can be integrated numerically via the following procedures:

$$\int_t^b \int_s^n \int_w^e q_m \, dx \, dy \, dz = \Delta X \, \Delta Y \int_t^b q_m \, dz \qquad (2.38)$$

in which, $\Delta X \, \Delta Y$ represents the control volume face area on which the heat flux q_m is assumed to prevail.

Furthermore,

$$\int_t^b q_m \, dz = \int_t^b \left(2.67 - 0.33\sqrt{Z/U_0} \right) dZ \times 10^6$$

$$\dots (2.39)$$
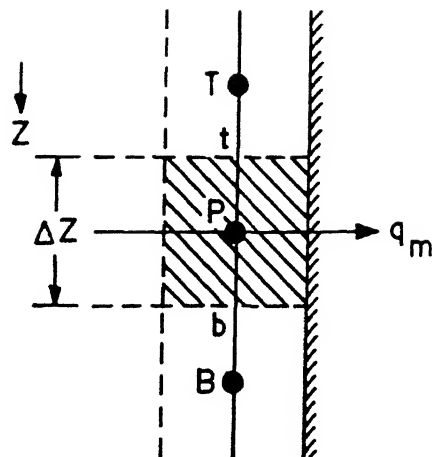
Fig. 2.14. A 2D representation of a typical boundary control volume in the central vertical plane of a square billet.

The net heat flux can then be estimated on the basis of:

(i)   solely the location of central nodal point P (referred to as route-1), i.e., in terms of the instantaneous distance (Z_P). Equation (2.40) then becomes:

$$\int_t^b q_m \, dz = \left(2.67 - 0.33\sqrt{Z_P / U_0} \right) \Delta Z \quad x \ 10^6$$

$$\ldots(2.40)$$

or, (ii) locations of either top or the bottom faces of the control volume P.

Estimation of the heat flux based on the top face of control volume gives (i.e. route-2).

$$\int_t^b q_m \, dz = \left(2.67 - 0.33\sqrt{Z_t / U_0} \right) \Delta Z \quad x \ 10^6$$

$$\ldots(2.41)$$

In terms of a pseudo time coordinate, the above mentioned estimates of heat flux values can be seen to be explicitly defined in terms of the previous time step value. Similarly, those estimated on the basis of bottom (or the leading) face alone means that the flux is estimated solely on the basis of the current time step value (referred to as route-3). Thus, the corresponding integration procedure of the mould heat flux expression yields the following expression :

$$\int_t^b q_m \, dz = \left(2.67 - 0.33\sqrt{Z_b / U_0} \right) \Delta Z \quad x \ 10^6$$

$$\ldots(2.42)$$
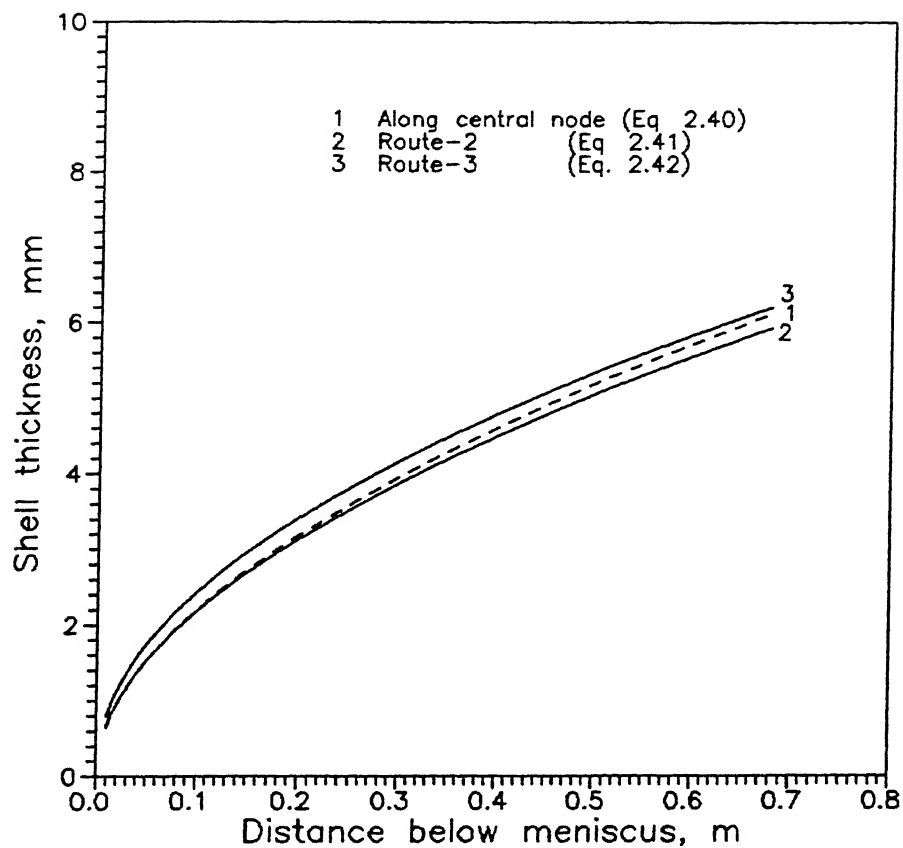
Fig.2.15: Effect of different integration routes applied to the mould heat flux expression on predicted shell thickness in a square billet caster[22].

(conditions of computations are summarized in Table 2.1)

In view of routes 2 and 3, route-1 can be visualized to be a combination of route 2 and 3, and therefore can be considered to be analogous to a semi-implicit or semi explicit estimation of the integrated heat flux.

In the present study, instantaneous mould heat flux was evaluated via all the three above mentioned numerical integration procedures. Predicted results thus obtained were presented in terms of variation of shell thickness with distance below meniscus in Fig.2.15, Very little differences, have resulted from these three considerations as is evident from Fig.2.15. From a theoretical point of view, average distance between the two control volume faces (i.e. route-1) is more realistic. Therefore, on the basis of Fig.2.15, route-1 was employed in all subsequent computations for integrating the instantaneous mould heat flux expression.

2.5.3 Influence of Axial Conduction on the Computed Results

In the previous studies[8,10,14,22], conduction of heat in the axial direction has been assumed to be negligible. It has been considered in general that relatively higher withdrawal rate of casting and lower thermal conductivity of steel makes the term $U_o \frac{\partial}{\partial Z}\left(\rho CT\right)$ in Eq.(2.1) dominant in comparison to the corresponding conduction term along the same (e.g. axial) direction. However, in the present study the axial conduction term has been incorporated in the governing equation to test directly the validity of such an assumption. Thus, to assess the sensitivity of the axial heat conduction term in Eq.(2.1),
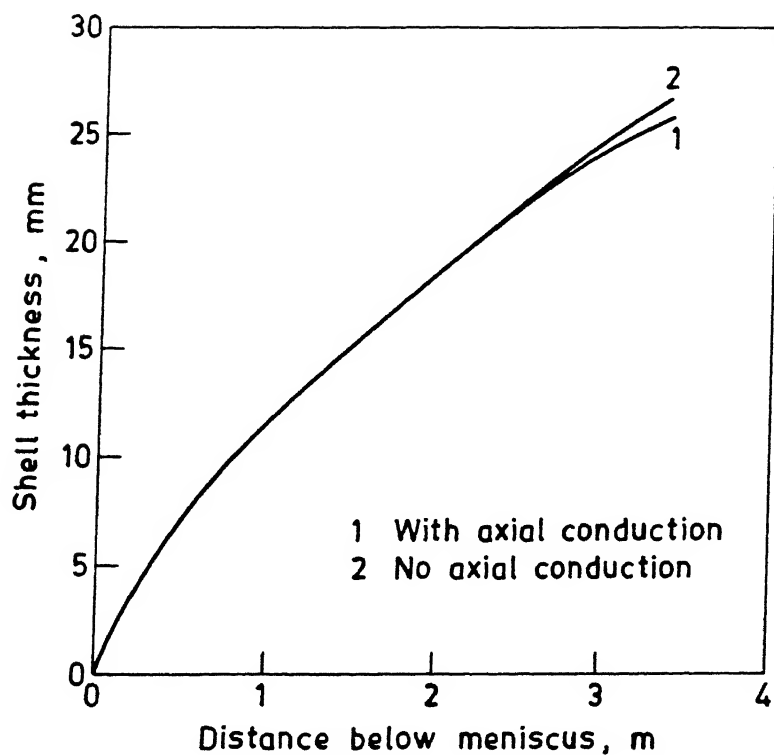
Fig. 2.16. Influence of axial conduction term in the governing heat flow equation on predicted shell thickness
(data set 4, table 2.1).
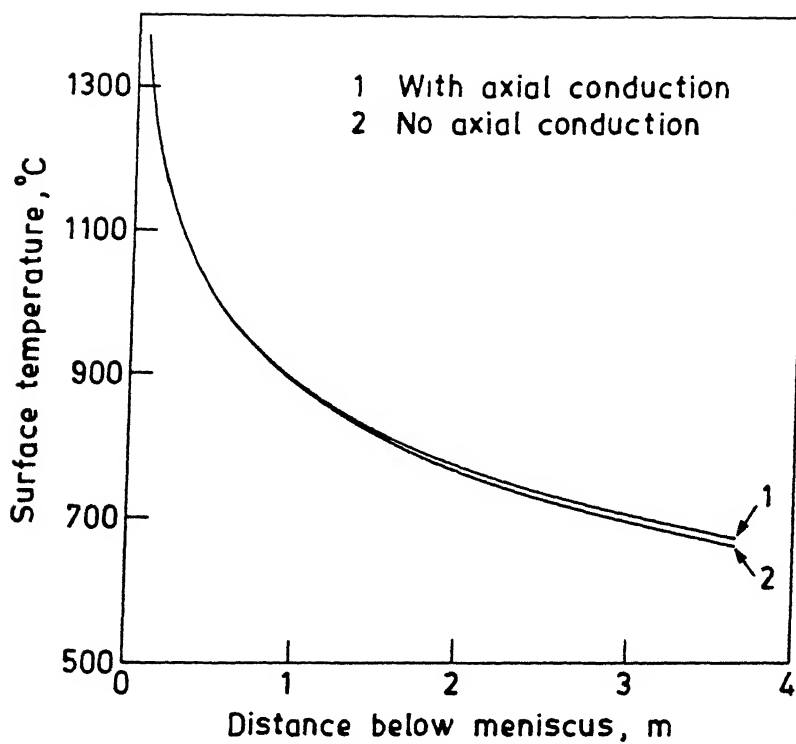
Fig. 2.17. Influence of axial conduction term in the
governing heat flow equation on predicted
temperature
(data set 4, table 2.1).

calculations were carried out by ignoring axial conduction altogether as well as considering axial conduction in the numerical calculation procedure. Results thus obtained are summarized in Figs.2.16 and 2.17 which show only marginal influences of the axial conduction term on the resultant predicted shell thickness and surface temperature. On the basis of these, it can therefore be concluded that axial conduction of heat has no significant role to play so far as transport of heat in CC is concerned.

2.5.4 Influence of Modelling Procedures Applied to Approximate Heat Conduction in the Mushy Zone

In some of the earlier studies[8,10,22], from the view point of heat flow, mushy zone has been considered as a solid region and thus, the effective thermal conductivity (K_{eff} = 7K) value was assigned only to the completely liquid region (i.e. where $T > T_{liq}$). However, the characteristics of mushy zone is somewhat different from either the complete liquid or solid regions. Lait et.al[22] have studied the influence of incorporating the mushy zone in the liquid region (i.e. K_{eff} = 7K assigned in the regions $T \geq T_{sol}$) as well. About 6 pct. overall increase in the shell thickness for plain low carbon steel billet has been reported from such consideration. Some other investigators assumed the thermal conductivity of mushy zone to vary with fraction of liquid at various positions in this zone[25,26]. In the present study both the previously mentioned approaches were considered to assess directly the influences of specific modelling procedures applied to the mushy zone on overall
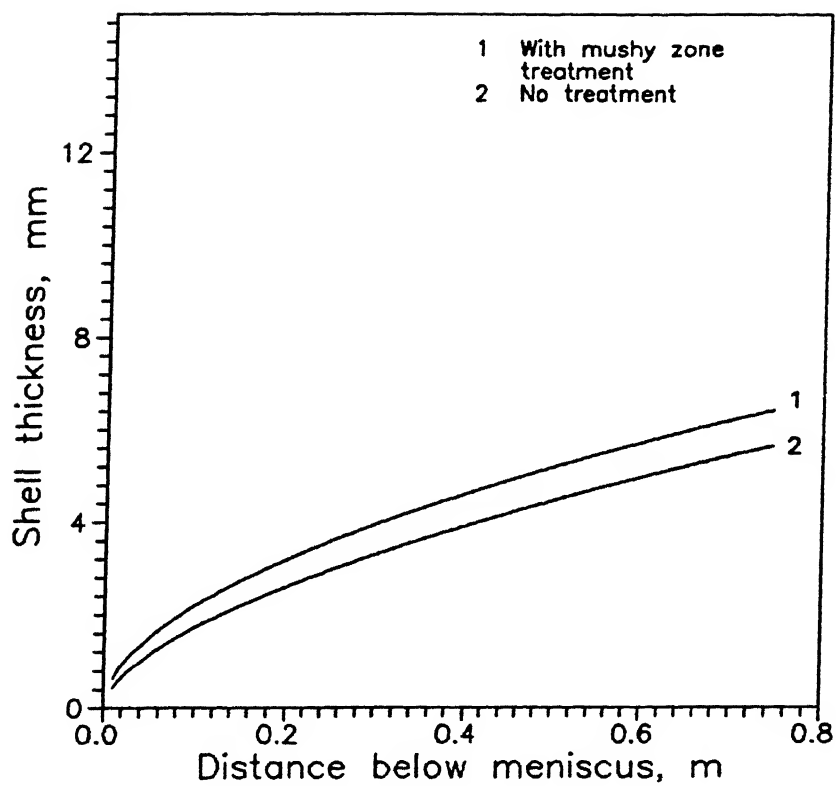
Fig.2.18: Influence of mushy zone treatment on predicted shell thickness in a square billet caster

(data set 2, Table 2.1)
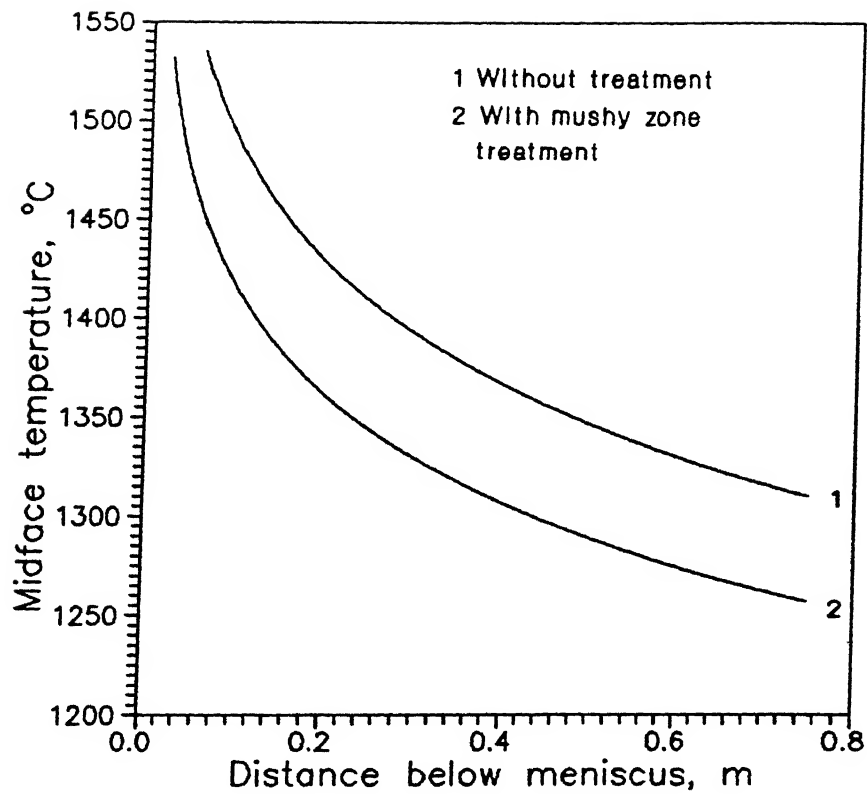
Fig.2.19: Influence of mushy zone treatment on predicted midface temperature of a square billet .

(data set 2, Table 2.1)

predicted heat transfer rates. The mushy zone treatment, in principle therefore, refers to the estimation of thermal conductivity in the two phase region via the following expression, based on the popular mixture model:

$$K_{mush} = Kf_s + (1 - f_s) K_{eff} \qquad \qquad ...(2.43)$$

In another set of computation $K_{eff} = 7K$ (i.e. without treatment) has been assigned throughout the regions above the solidus temperature (i.e. $T > T_{sol}$) of steel. This corresponds to a procedure where mushy zone has been essentially treated as a liquid.

The results derived on the basis of two such considerations have been presented in Figs.2.18 and 2.19. From these, it is at once evident that the estimates of shell thickness while are essentially similar, some differences (about 4-5 pct.) between the respective estimates of mid-face temperature exist (Fig.2.19). Theoretically, treating the mushy zone as a mixture of solid and liquid appears to be a relatively better approximate, and hence this concept was applied to all subsequent computations.

2.5.5   Influence of Values of Mould Heat Flux on the Computed Results

2.5.5.1   Instantaneous vs. average mould heat flux expressions as the surface boundary condition in the mould region

In the present study, as mentioned earlier, the Savage-Pritchard[20] correlation (Eq. 2.8) for the instantaneous

mould heat flux has been applied as the surface boundary condition in the mould region. Lait et.al[22] have also proposed another correlation based on the Savage-Pritchard correlation for estimating the average mould heat flux. Validity of the average mould heat flux correlation has been demonstrated by the same investigators[10] through comparison with industrial experimental data on a wide range of continuous casting machines. According to Lait and co workers[22], the average mould heat flux ($\bar{q}_m$) can be correlated with the average mould dwell time (t_m) of the casting via the following expression:

$$\bar{q}_m = [2.69 - 0.223 \sqrt{t_m}] \times 10^6 \qquad \ldots(2.44)$$

in which, the dwell time t_m is defined according to:

$$t_m = \frac{L_m}{U_0} \qquad \ldots(2.45)$$

The sensitivity of the computed results to the choice of the heat flux expressions viz., Eq.(2.8) and (2.45) as surface boundary condition in the mould region has been investigated and the results thus obtained are shown in Fig.2.20, where estimates of two sets of shell thickness have been directly compared. Evidently, no significant difference was found between the two sets of estimates. Since the instantaneous mould heat flux expression is physically more meaningful, consequently this can be considered to be more appropriate in the numerical solution scheme.
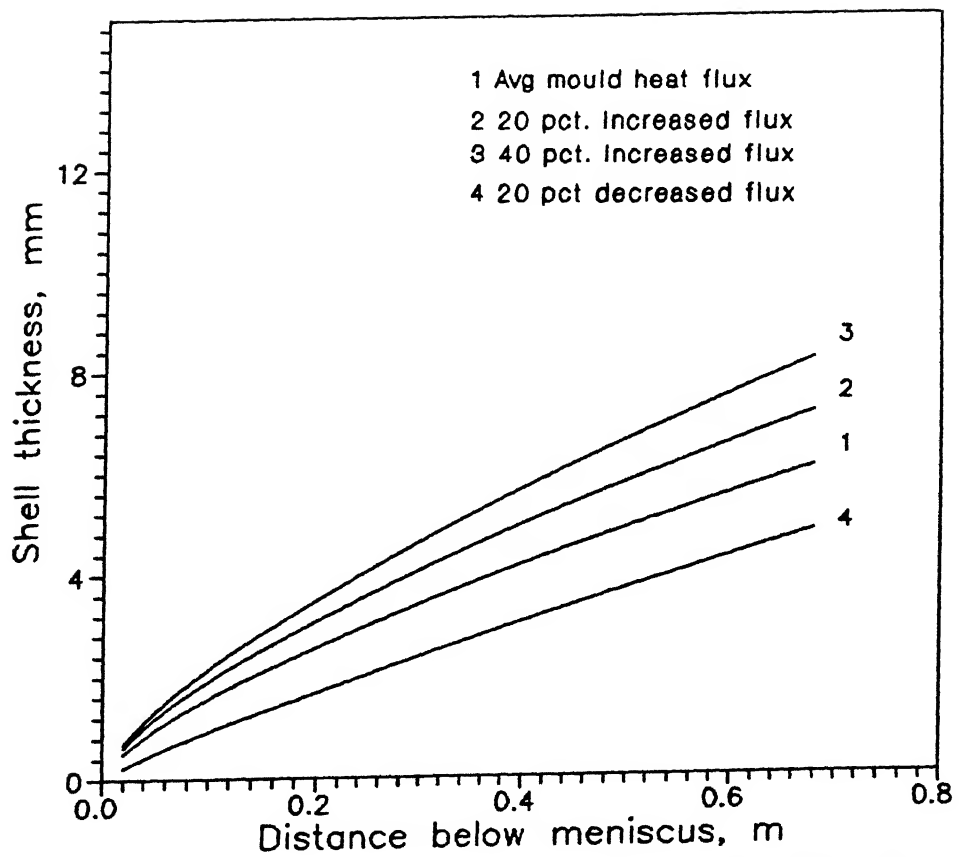
Fig.2.21. Influence of arbitrarily varying the mould heat flux value   on the predicted shell thickness in a square billet

(data set 2, Table 2.1)

2.5.5.2 Confidence limit of mould heat flux expression and its likely influence on the accuracy of computed results

Based on several measurements on industrial billet and slab casters, the mould heat flux correlations have been shown to be within a scatter of ±50 pct.[10,22]. Calculations have been consequently carried out by arbitrarily changing the average mould heat flux value up to about ± 40 pct., and results thus obtained are presented in Fig.2.21. It is evident from the figure that the actual limit of confidence of the mould heat flux has an important bearing on the overall predicted results and thus, is expected to affect the overall accuracy of numerical computation considerably.

2.5.6 Sensitivity of Computation to the Choice of Effective Thermal Conductivity Values

In the artificial effective thermal conductivity model, as proposed originally by Mizikar[8], the effective thermal conductivity value applied (i.e. K_{eff}) to the liquid region has been an empirically fitted parameter. Furthermore, there is at present no evidence of any fundamental nature for the selection of an appropriate K_{eff} value for varying casting configurations. Mizikar deduced the K_{eff} value empirically by matching a set of theoretical predictions with the corresponding measurements on an industrial slab caster, and found that $K_{eff} = 7K$ in the liquid pool of a typical slab caster provides reasonably good agreement between theory and experiments. Brimacombe and coworkers[10] applied K_{eff} value equal to 5-10 K in their studies. However, the

value of $K_{eff} = 7K$ in the liquid has been more frequently employed by the subsequent investigators, to account for the turbulent and convective transport of heat in the liquid pool region of a solidifying casting. Contrary to all these, in a recent study, Lahiri[28] on the basis of purely theoretical considerations has suggested that the value of K_{eff} should be at least 43K. In view of a wide range of K_{eff} values suggested in the literature, an attempt has been made to assess the sensitivity of computation to the choice of an appropriate value of the K_{eff} in the liquid pool, so that industrial conditions can be effectively simulated. In this connection, values of K_{eff} selected were 1K, 7K, 12K and above 30K for · numerical computation.

A typical slab caster was selected for the numerical calculation with the above mentioned values of K_{eff}. In slab caster, liquid pool typically is relatively more wide and the pool depth consequently is shallower than billet or bloom casters. Therefore, the effect of turbulence and convection is expected to be more pronounced in slab than those in other configurations. Fig.2.22 presents estimates of shell thickness for various K_{eff} values, which illustrates that the shell thickness did not vary much if the K_{eff} is varied between 1K and 7K. However, there is significant influence on shell thickness when K_{eff} value was arbitrarily increased to 12K. It has also been observed that a K_{eff} value above 30K did not give any solidification at all in the mould region. Equivalent results for a square billet caster are also presented in Fig.2.23. This however, showed that the differences between predictions via K_{eff}
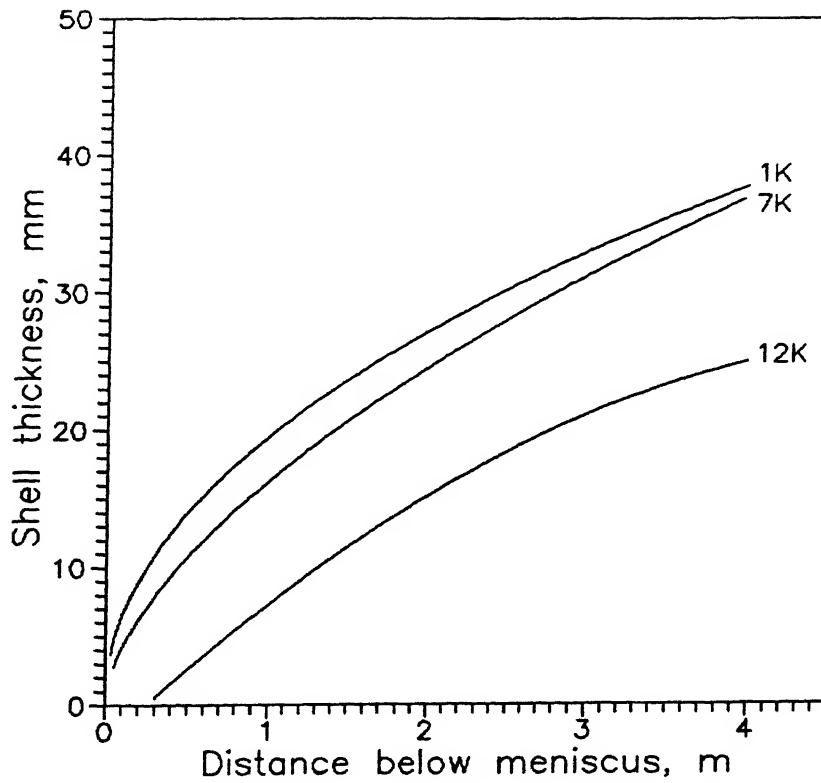
Fig. 2.22: Influence of different effective thermal conductivity values on predicted shell thickness of a slab caster[27] (data set 3, Table 2.1)
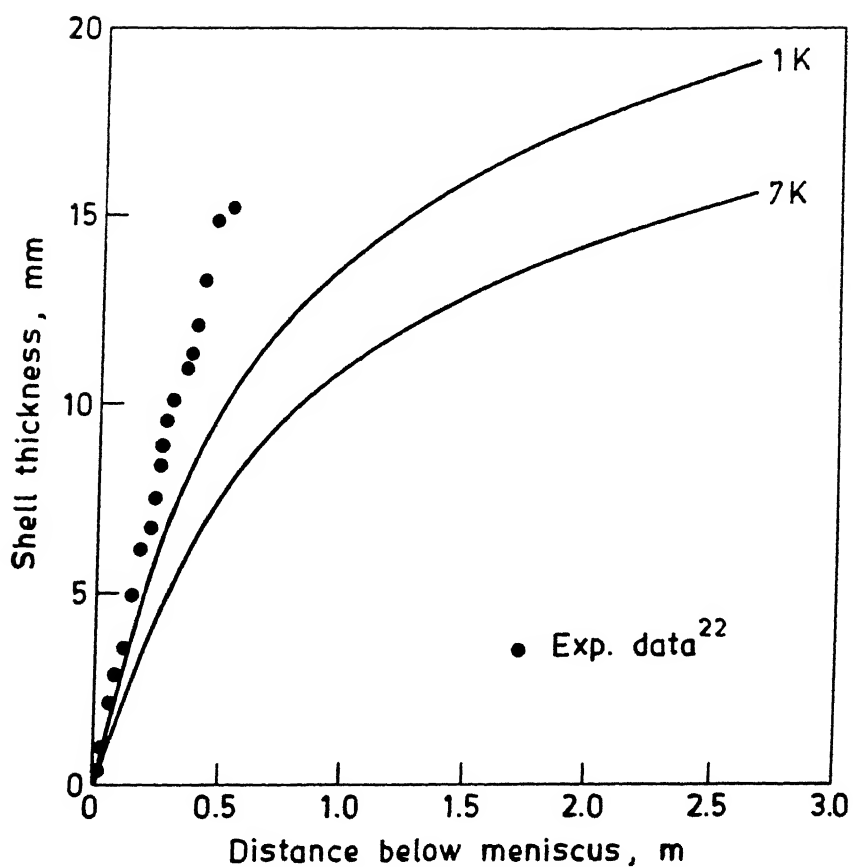
Fig. 2.23. Present estimates of solid shell thickness in a billet caster for different effective thermal conductivity values and their comparison with experimental measurements[22] (data set 1; table 2.1).

= 1K and K_{eff} = 7K were somewhat more pronounced than those observed in slab caster (viz., Fig.2.22).

The trend in results reflected by the choice of different K_{eff} values, as presented in Figs.2.22 and 2.23 can however, be rationalized as follows. The overall heat flux at any location in the transverse direction, say X, can be expressed by the following relationship.

$$q_X = - K_{eff} \frac{dT}{dX} \qquad \ldots(2.46)$$

For Fig 2.22 or 2.23, heat flux at the boundary is the same for all the curves for the mould region. Therefore the internal temperature distribution would depend on the magnitude of assumed K_{eff} value. For lower K_{eff} values (e.g. 1K) relatively large temperature gradients and for higher K_{eff} (e.g. 12K) values more uniform and hence less temperature gradient are to be expected within the liquid metal pool. Therefore, if the K_{eff} is arbitrarily made much larger, the transverse or radial variation of temperature from the center line (nearly equal to the pouring temperature) can be expected to be only marginal. Thus, for K_{eff} = 12K, little difference in predicted temperatures between meniscus and any other locations in the mould region has been observed. Consequently, such redistribution of temperature produces very little shell in the mould. In contrast, at K_{eff} = 1K, from a similar stand point, predicted temperature difference between meniscus and elsewhere was much larger, and thus, relatively more solidification (e.g. more shell thickness) is observed computationally.

K_{eff} is an adjustable parameter and there is little information based on which this can be assigned appropriate value (only scope is trial and error). Consequently, the most popular and widely applied value (viz., K_{eff} = 7K) has been adopted in the present study for computations. It may be stated that this choice was quite reasonable as well from the point of view of Fig. 4.23, and the preceding discussions of the same.

2.5.7 Comparison of Results with Experimental Data from Literature

In order to validate the mathematical model and thus to test the adequacy of the model developed, comparisons have been made between predicted results and corresponding experimental measurements reported in literature. Figs.2.24 and 2.25 present the computed solid shell profiles for two different square billet casters. Relevant data employed to these computations have been obtained from the reported studies by Lait et al[22]. These authors carried out extensive measurement of pool profiles by radioactive tracer technique on industrial casters. Table 2.1 presents the data employed to deduce the results shown in Figs.2.24 and 2.25. However, some of the useful information such as melt superheat and spray heat transfer coefficient, are not available in Ref.23. Therefore a typical superheat value of 25^{0}C was employed in computation of results presented in Figs.2.24-2.25. Because of uncertainty in the values of spray heat transfer coefficient, comparisons have been restricted to the mould region only, although the secondary cooling zone was also included (with an estimated heat transfer coefficient data)
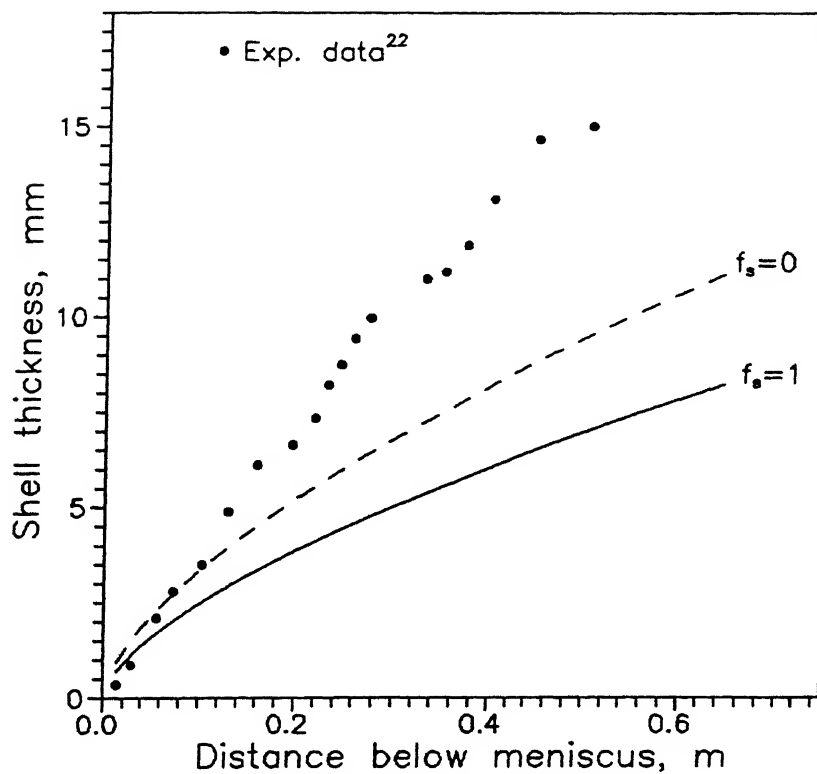
Fig. 2.24: Comparison between the predicted and experimental shell thickness of a typical square billet caster (conditions as in ref. 22 for 0.14 m sq. billet).
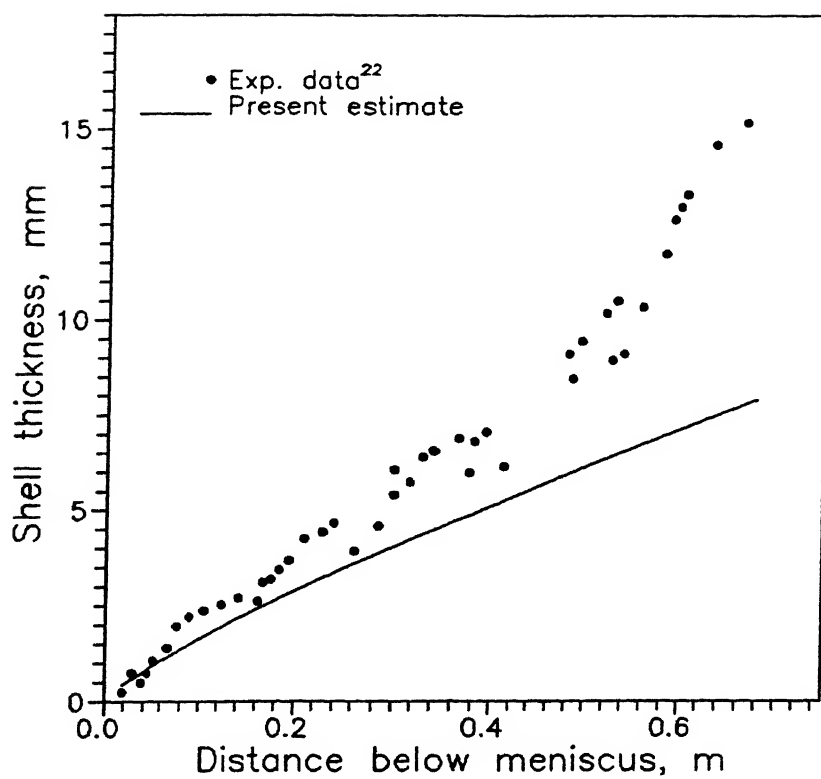
Fig. 2.25: Comparison between the predicted and experimental shell thickness for a typical square billet caster (conditions as in ref. 22 for 0.133 m sq. billet).

in the numerical solution scheme. It is important to note here that in view of negligible axial conduction (as has been shown already), inclusion of secondary cooling zone in the computation is not likely to affect the predicted results in the mould region. Thus, Figs.2.24 and 2.25 show that the overall agreement between the experimental and predicted data is somewhat poor and less satisfactory than those suggested earlier[10,22]. The agreement between theory and experiment was however reasonable in the upper mould region alone.

In Fig.2.26 another set of experimental data for a typical round billet caster reported by Ushijima[33], have been presented along with the present theoretical estimates. Fairly reasonable agreement for the upper pool region (i.e. mould) is demonstrated in the plot. Whereas, in the submould region, significant discrepancy between the experimental and predicted data is evident. As mentioned already, discrepancy between prediction and observation can be attributed to the experimental technique (in this case, visual observations) as well as to the mathematical modelling concepts applied. Towards this, it is important to mention here that Asai and Szekely[11] have demonstrated good agreement with the observation reported by Ushijima[33] via their fluid flow based heat transfer model. Hence it cannot be stated that the discrepancy illustrated in Fig.2.26 is due to heat transfer coefficient value employed in the present investigation.

As a final point, it is to be mentioned here that none of the earlier studies attempted to examine the issues of sources of uncertainty in the numerical calculation procedure. However, as the present study has indicated that the numerical approximations
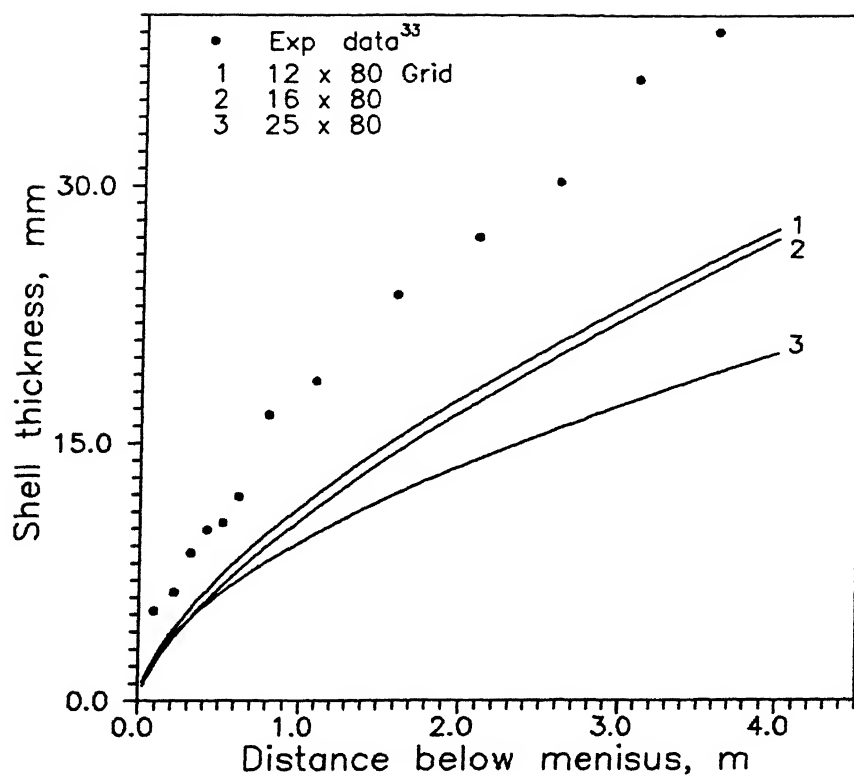
Fig. 2.26: Comparison between predicted shell thickness for various grid configurations and corresponding experimental measurements of a typical round billet caster[33](conditions as in ref.11).

applied have considerable bearing on the accuracy of the predicted results. Similarly, in no studies reported so far, the issue of grid independent solution has been addressed.

To illustrate this point further, in Fig.2.26 predictions based on 12x40 and 16x80 grid systems have also been included in addition to those derived via 25x40 grid system. With reference to Fig.2.26, it is important to note that prediction of shell thickness are relatively more sensitive to grid distribution in the transverse/radial direction. This is to be expected since variation of thermal properties are relatively more steep in the transverse direction than are in the longitudinal direction/withdrawal direction. Considering the pouring temperature as a reference, immediately below the meniscus the thermal field derived via a fine grid system is expected to be relatively more close to the reference temperature than those deduced via a sparse grid system. Since a higher temperature field results in a low solidified shell thickness and vice versa, consequently, it is seen in Fig.2.26 that with the increase in grid configuration in any direction, the shell thickness decreases. Similarly, predicted surface temperature derived from internal temperature field is also expected to be somewhat greater for finer grid system, leading to different heat flux ($=h\Delta T$) values at the cast surface for the two grid systems. Consequently, the influence of grid distribution is seen to be relatively more pronounced in the secondary cooling zone than in the mould region.

Figure 2.26 appears to indicate that as the grid configuration applied became more and more sparse, the prediction

tends to come closer to the observation, and this apparently suggests that reasonable to excellent agreement exists between theory and experiments. Nevertheless, as has been discussed already, the numerical results, unless are independent of nodal configuration, have no validity and hence comparison of such results with experiments have in reality, no meaning.

Hence, in Fig.2.26 comparison of experimental measurement is meaningful only with curve 3 (24x40 grid), for which the solution was found to be grid independent. This shows that agreement between predictions and experimental data are poor. The authors have already discussed it. It may be due to uncertainties in experimental data or inadequacy of mathematical models based on effective thermal conductivity concept. It is possible that both of these are contributing partly to discrepancy. It is not possible to make any more definite statement without further studies.

2.6 SUMMARY AND CONCLUSIONS

Based on the concept of artificial effective thermal conductivity approach a steady state 3D heat flow model of CC has been developed. Control volume based finite difference procedure has been employed for the numerical solution of the governing heat flow equation. A general computer program, which incorporates Tri Diagonal Matrix Algorithm (TDMA) for the solution of discretization equation, has been developed in FORTRAN 77. The program is so written that computations in cartesian as well as in cylindrical polar coordinate systems can be performed in both 2-D and 3-D. Before carrying out any

comparison between theory and experiments, sensitivity of numerical solution to grid configuration and various numerical approximations in the calculation procedure, have been analyzed. Validity of various assumptions in the modelling has also been tested and finally, the computed results thus obtained have been compared with experimental measurements reported in literature.

The present study has revealed that the axial conduction term has a minor role to play so far as the modelling of overall heat flow in CC is concerned. Numerical solution has been found to be relatively more sensitive to the choice of grid configurations in the transverse direction. Similarly, procedures applied to model heat flow in mushy zone as well as the surface boundary condition in the mould were found to affect the predictions somewhat. In order to select a proper K_{eff} value and test its sensitivity to computed results, values of K_{eff} were varied over a wide range. Finally it was decided to take K_{eff} =7K for further computations.

Model predictions have been assessed against three sets of experimental data for round and square billet casters. However, in most of the cases the overall agreement between predictions and experimental measurements of shell thickness were not found to be satisfactory. Validity of other assumptions such as, equilibrium solidification of steel, constant thermophysical properties, have been already established by the previous investigations.

Considering all the points mentioned above, it appears that the concept of artificial effective thermal conductivity as applied to the liquid pool to account for the effect of fluid

convection and turbulence on heat transfer, is not adequate enough to describe various thermal phenomena in CC realistically. To test this hypothesis further, in the next chapter a relatively more fundamental model based on the concept of conjugate fluid flow and heat transfer has been presented.

Table 2.1:   Data of CC used in the present computation

Parameter	Data Set-1 [ref.22]	Data Set-2 [ref.22]	Data Set-3 [ref.27]	Data Set-4 [ref.33]
Cast geometry	square	square	slab	round
Cast size (m x m)	0.14	0.133	0.25	0.115
Mould length (m)	0.51	0.685	0.6	0.5
Casting speed (m s^{-1})	0.0254	0.044	0.0125	0.0317
Steel carbon (pct.)	0.1	0.1	0.14	0.1
Melt superheat* (^{o}C)	25	25	25	25
Solidus temp. (^{o}C)	1496	1496	1496	1496
Liquidus temp. (^{o}C)	1529	1529	1526	1529
Spray heat transfer coefficient (W m^{-2} ^{o}C^{-1})	–	–	–	1079.45**

* - estimated
** - source: ref.[11]

Table 2.2:   Thermophysical properties of steel* used in

computation

Density	kg m^{-3}	7400
Latent heat of solidification	J kg^{-1}	271954
Specific heat	J kg^{-1} ^{o}C^{-1}	682
Thermal conductivity	W m^{-1} ^{o}C^{-1}	34.6 & 15.89+0.011T**

* -   source: Physical Constants of Some Commercial Steels at Elevated Temperatures, Ed. The British Iron and Steel Research Association, Butterworths Scientific Pub., London, 1953.

** - source: Ref.[8]

CHAPTER 3

MATHEMATICAL MODELLING OF HEAT TRANSFER IN CONTINUOUS CASTING OF STEEL VIA CONJUGATE FLUID FLOW AND HEAT TRANSFER APPROACH

3.1 INTRODUCTION

Continuous casting of steel involves coupled fluid flow and heat transfer phenomena. Thermal energy from/within the molten core of a solidifying casting is transported by turbulent mixing, convection, as well as by the molecular thermal diffusion (viz., conduction). The rate of this turbulent convective transport of heat is governed principally by the kinetic energy of the pouring stream as well as by the buoyancy induced natural convection.

Therefore, from a fundamental point of view, detailed mathematical modelling of the continuous casting process necessitates solution of fluid flow equations concurrently with an appropriate heat transfer equation. Thus, the mathematical model reported in the present chapter has been referred to as the conjugate fluid flow and heat transfer model of continuous casting process. The model, in its detailed form as will be outlined subsequently, involves solutions of five or six coupled, nonlinear and multidimensional partial differential equations and thus, involves a more complex computational task than those

reported earlier in Chapter 2. Nevertheless, the model having a rigorous fundamental basis, is expected to provide relatively more accurate description of the relevant phenomena associated with the continuous casting operation[11,12].

Thus to investigate various thermal phenomena (e.g., heat flow and solidification) during continuous casting of steel, a mathematical model based on the conjugate fluid flow and heat transfer approach has been developed in the present study. Towards this, relevant previous work, derivation of the governing equations of fluid flow and thermal energy transport, numerical solution procedure together with the adequacy of numerical predictions with reference to the reported plant scale measurements are described in the subsequent sections of the text.

3.2 LITERATURE REVIEW

Although conjugate fluid flow - heat transfer model has a sound fundamental basis, the approach has so far been relatively less frequently adopted by the researchers investigating mathematically heat transfer related phenomena in CC. According to the present author, the inherent computational complexity associated with the model (e.g. numerical solution of turbulent Navier-Stokes equation together with thermal energy transport) appears to be one of the principal reasons for such an observation. Thus, so far, only few investigators[11,12] have reported studies based on the concept of conjugate fluid flow and heat transfer. Remaining of the studies are either exclusively on heat transfer[21-24] (i.e., via artificial effective thermal

conductivity approach) or purely on fluid flow[34] in CC.

The very first study that took into account the possible interactions between fluid flow and heat transfer in CC, has been reported by Szekely and Stank[35]. In their study, the investigators[35] adopted the general approach of Mizikar[8] (viz., effective thermal conductivity model) with a major modification of assigning a definite flow pattern in the molten pool to deduce the convective heat flow terms in the governing equation. The investigators, considered the following three cases in their heat flow calculations :

(i) potential flow of fluid in the liquid pool was assumed and the velocity field was deduced from the inlet velocity of the pouring stream as source,

(ii) a high effective thermal conductivity in the liquid pool was assumed to account for the convection and turbulence within the pool, and

(iii) complete lateral mixing in the pool was assumed.

The results of computations for the three idealized flow conditions mentioned above, were finally compared with each other. It has been reported that the liquidus and solidus profiles remained almost insensitive to the choice of any of the three types of flow conditions. This illustrates an apparent independence of solidification from the flow field in the liquid pool. However, the rate of release of superheat was found to depend markedly on the flow field in the molten pool. In the same study, the investigators[35] also carried out a theoretical analysis for the dispersion of tracer in the pool region and have

reported that the mixing and flow field within the pool play a significant role in the floating out of the inclusion particles from the melt during continuous casting operation.

The study by Szekely and Stank[35], although based on a simplified approach of fluid flow analysis in CC, nevertheless, represents an oversimplification of the actual process. Thus, their model is not likely to be adequate enough to predict the actual flow field and its associated influence on heat transfer in CC.

In a subsequent study, Szekely and Yadoya[36] developed a model from a more fundamental considerations. They considered turbulent flow in the molten pool and applied conservation equation for mass, momentum, and energy, to predict the turbulent flow field, temperature field and tracer dispersion respectively in the upper pool region (i.e., the mould region). In addition, they carried out extensive water model studies[37,38] and compared the theoretical predictions of the velocity field with the results of water model experiments.

Szekely and Yadoya[36] essentially considered steady state, two dimensional fluid flow and heat transfer in cartesian as well as cylindrical polar coordinates. The investigators[36] assumed turbulent flow in the liquid pool and used the equivalent stream function/vorticity - transport equations for computing the flow field in the pool region. Furthermore, the spatial distribution of turbulent viscosity was deduced from the Kolmogorov-Prandtl mixing length model[39,40]. To avoid computational complexity, these investigators[36], however, ignored the solidification phenomena and its influence on the pool hydrodynamics. Thus,

there was no latent heat release term and instead, a viscous dissipation term in addition to the standard convection and turbulent diffusion terms, was considered in the governing thermal energy balance equation. Finally, a general material conservation equation was employed for predicting the distribution of tracer concentration in the liquid pool region. For a given set of casting conditions, the set of governing partial differential equations were solved iteratively using the finite difference numerical procedure, and embodying a prescribed inlet conditions (viz., known pouring temperature and inlet velocity of stream) together with a prescribed heat flux at the mould wall as boundary conditions. Finally, the predicted velocity fields were compared with the results of water model study and a reasonably good agreement (qualitative only) between predictions and experimental measurements was demonstrated. The predicted temperature fields and tracer concentration profiles were also found to be quite consistent with those observed in the water model study[36].

Szekely and Yadoya[36], however, did not take into account the influence of heat transfer (viz., solidification and mushy zone formation) on fluid flow and consequently, the results reported are somewhat oversimplified and hence to some extent physically unrealistic. Nonetheless, the investigations[35-38] provided the necessary guidelines for further development of a more realistic model. The effort of Szekely and Yadoya can be considered to be a pioneer undertaking as this was the first detailed reported study involving application of the theory of fluid flow and turbulent transport to metallurgical systems, particularly in continuous

casting.

In a later study, Asai and Szekely[11] made further improvements in the model reported by the earlier investigators[35,38], by taking into account the effect of solidification (i.e., latent heat release) and the mushy zone formation on the pool hydrodynamics and the resultant energy transport in CC. The investigators[11] applied their model to analyze fluid flow and heat transfer in various billet casters and validated their model against the actual plant scale measurements reported in literature[33].

Asai and Szekely[11] considered a steady state two dimensional fluid flow and heat transfer situation and accordingly, developed a model in cylindrical polar coordinate system. For the velocity field calculation, stream function and vorticity transport equations were considered. Further, Kolmogorov-Prandtl mixing length model[39,40], with some modifications, was applied to deduce the turbulent viscosity in the pool. Resistance to flow produced by the solid matrix in the mushy zone was taken into account by assuming its viscosity to be 20 times the molecular viscosity of steel. In the computation of temperature field, latent heat of solidification, released in the mushy zone, was estimated from the corresponding change in the solid fraction assuming equilibrium solidification of steel. The governing fluid flow equations together with energy balance equations were solved using the finite difference procedure and for the two distinct sets of input conditions considered. Velocity fields, spatial distribution of turbulence kinetic energy and temperature fields

were predicted. Solidification profiles thus estimated from the predicted temperature fields were compared with corresponding experimental measurements reported in the literature[33]. Predicted and the measured shell thicknesses were mostly found to be in reasonable agreements with each other.

In addition to these, computed velocity fields and effective viscosity were subsequently applied to calculate the transient distribution of tracer concentration and trajectory of inclusion particles within the liquid pool. Towards this, an appropriate transient material conservation equation was considered in the numerical calculation procedure. However, agreement between theoretically estimated and experimentally measured mixing rates were in general less satisfactory. In contrast to this, the computed trajectory of the inclusion particles within the pool was found to be quite consistent with the general expectations.

In a more recent study, Flint and coworkers[12] developed a steady state three dimensional conjugate fluid flow – heat transfer model applicable to the mould region of a continuous slab caster. These investigators assumed turbulent flow in the liquid pool, and considered mass, momentum, and enthalpy balance equations to compute the velocity, pressure, and temperature fields. The turbulent properties in the liquid region were estimated from the k-ε model. Latent heat released during solidification, and resistance to fluid flow in the mushy zone were taken into account by incorporating appropriate source terms in the governing fluid flow and heat transfer equations (e.g. momentum sink and latent heat source terms respectively). These source terms were assumed to be dependent on the liquid fractions

in the mushy zone. Scheil's equation[41] was applied to calculate the local liquid fractions in the mushy zone, and using the numerical procedure proposed by Voller and Prakash[42], above mentioned source terms were estimated for the numerical computations of velocity and temperature fields. These investigators used TEACH-T code of Gosman and Ideriah[43] to solve the governing equations and associated boundary conditions. They[12] analyzed the influence of various numerical parameters on the computed results, and reported that the numerical parameters such as grid configuration, discretization technique, value of turbulence model empirical constants, method of treating the wall drag, and the input turbulence level, have significant effects on the model predictions.

Flint and coworkers[12] have also reported comparisons between the 2D and 3D fluid flow - heat transfer models as well as the effective thermal conductivity and fluid flow - heat transfer models. Two dimensional model was found to give poor quantitative predictions of fluid flow and flow-induced shell growth in the mould in comparison with the 3D model. Similarly, the effective thermal conductivity model was found to be less satisfactory than fluid flow heat transfer model.

Influence of some of the operating parameters of slab casting such as, superheat of liquid steel, casting speed, and submerged entry nozzle (SEN), on the predicted velocity and temperature fields were also studied by Flint and coworkers[12]. Finally, the model predictions were validated against the experimental observations made on a full-scale water model.

3.3 FORMULATION OF TRANSPORT EQUATIONS FOR THE PRESENT STUDY

3.3.1 Assumptions in Modelling

In deriving the governing fluid flow and heat transfer equations, the following assumptions were incorporated in the mathematical model.

(a) Momentum and heat transfer have been assumed to be essentially a steady state, two dimensional phenomena with reference to an axisymmetric continuous casting operation. Thus, for cartesian coordinate system, fluid flow and heat transfer were analyzed only in the central vertical plane of the cast section. Also, due to the symmetry of the configuration chosen, velocity and temperature fields were computed only in one half section of the chosen central vertical plane.

(b) While considering the mathematical simulation in cartesian - coordinate system, influence of one of the two transverse directions (i.e. y-direction) on the predicted velocity and temperature fields were neglected (i.e. no influence of corner region). Thus, for continuous casting of rectangular cross-sections (e.g. billets), phenomena at the mid face and the corresponding central vertical plane has been taken into account. Similarly, for cylindrical polar coordinates (e.g. round billets), influence of θ - direction was ignored.

(c) Solidification front was assumed to be planer with respect to the adjacent liquid. Also, the influence of movement of solidification front on flow field in the pool was ignored as a first approximation.

(d) Flow in the liquid pool has been assumed to be induced by the momentum of the incoming pouring stream as well as by the

thermal buoyancy (i.e. natural convection phenomena). Influence of other secondary factors such as bulging, suction due to solidification shrinkage etc., were ignored.

(e) Only the perfectly vertical cast section has been considered as the calculation domain (i.e. no influence of strand bending or the curvature effect) for necessary mathematical simulation.

(f) Effect of mould oscillation has been ignored.

In addition to these, most of the assumptions made during the study on artificial effective thermal conductivity approach (viz., Chapter 2, Section 2.3.1) were also made applicable to the present study. Therefore, these are not reproduced here.

3.3.2 Governing Equation of Fluid Flow Within the Liquid Pool and Boundary Conditions

The flow field within the liquid pool of a solidifying section must satisfy the mass conservation (i.e. continuity) and the momentum conservation equations. The governing fluid flow equations, therefore, for a two dimensional, steady state, incompressible, turbulent flow may be expressed by the following general partial differential equations.

Equation of continuity,

$$\frac{\partial u}{\partial Z} + \frac{1}{\alpha}\frac{\partial}{\partial X}\left(\alpha v\right) = 0 \qquad \qquad \ldots(3.1)$$

Equation of motion in axial direction,

$$\frac{\partial}{\partial Z}\left(\rho uu\right) + \frac{1}{\alpha}\frac{\partial}{\partial X}\left(\alpha\rho uv\right) = -\frac{\partial p}{\partial Z} + \frac{\partial}{\partial Z}\left(\mu_{eff}\frac{\partial u}{\partial Z}\right) + \frac{1}{\alpha}\frac{\partial}{\partial X}\left(\alpha\ \mu_{eff}\frac{\partial u}{\partial X}\right)$$

$$+ S_u \qquad \qquad \ldots(3.2)$$

where, axial momentum source term per unit volume is,

$$S_u = \frac{\partial}{\partial Z}\left(\mu_{eff}\frac{\partial u}{\partial Z}\right) + \frac{1}{\alpha}\frac{\partial}{\partial X}\left(\alpha\ \mu_{eff}\frac{\partial v}{\partial Z}\right) - \rho g\beta(T - T_0)$$

$$...(3.3)$$

Equation of motion in transverse/radial direction,

$$\frac{\partial}{\partial Z}\left(\rho uv\right) + \frac{1}{\alpha}\frac{\partial}{\partial X}\left(\alpha\rho vv\right) = -\frac{\partial p}{\partial X} + \frac{\partial}{\partial Z}\left(\mu_{eff}\ \frac{\partial v}{\partial Z}\right) + \frac{1}{\alpha}\frac{\partial}{\partial X}\left(\alpha\ \mu_{eff}\ \frac{\partial v}{\partial X}\right)$$

$$+ S_v \qquad\qquad ...(3.4)$$

where, radial momentum source term per unit volume is,

$$S_v = \frac{\partial}{\partial Z}\left(\mu_{eff}\ \frac{\partial u}{\partial X}\right) + \frac{1}{\alpha}\frac{\partial}{\partial X}\left(\alpha\ \mu_{eff}\ \frac{\partial v}{\partial X}\right) + \mu_{eff}\ (v/X^2)$$

$$...(3.5)$$

The parameter 'α' appearing in Eqs.(3.1) through (3.5), is a scaling factor (e.g. to be visualized as an index of coordinate system), which is unity for the cartesian coordinate (applied to the analysis of square billets), and ($\alpha = x = r$) for the cylindrical polar coordinate (for analysis of round billet) systems. Furthermore, for the Cartesian coordinate system, the quantity ($\mu_{eff}v/x^2$) in Eq. (3.5) is set equal to zero.

In Eqs.(3.1) through (3.5), μ_{eff} is the effective viscosity which is defined as the sum of the molecular and turbulent contributions to the viscosity, i.e.,

$$\mu_{eff} = \mu + \mu_t \qquad\qquad ...(3.6)$$

The turbulent viscosity (μ_t) in Eq.(3.6) is not a physical property of the fluid and instead, is largely determined by the nature of flow.

In Eq.(3.3), the source term (S_U) in the axial momentum balance equation contains $[-\rho g\beta(T-T_0)]$ term. This takes into
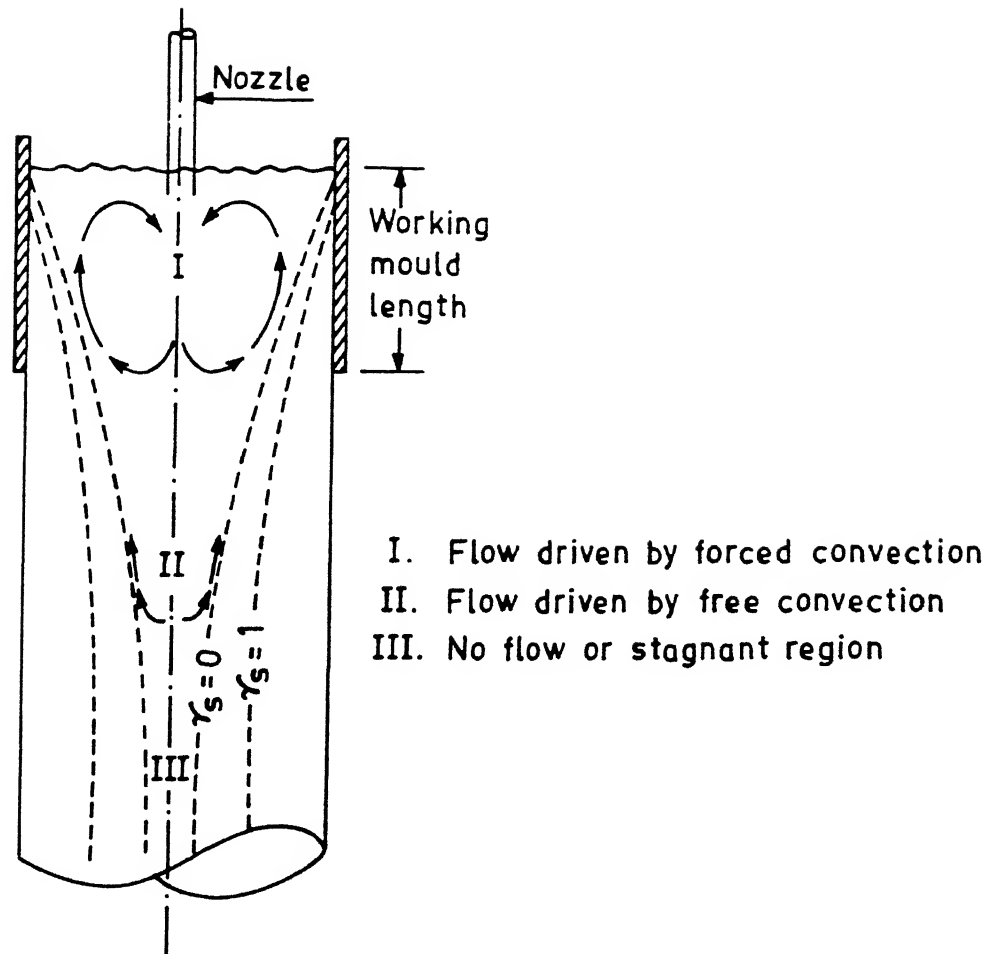
Fig. 3.1. Schematic of the flow pattern in the liquid pool of a continuously cast billet.

account the influence of buoyancy force (i.e. Boussinesq source term[13]), generated by the difference in density due to difference in temperature (i.e. natural convection) within the liquid pool of a solidifying casting (Fig. 3.1). In none of the earlier studies on continuous casting, influence of buoyancy on the flow of liquid steel within the pool has been been taken into account. However, as the literature indicates[23,24], flow in the lower pool region is expected to be influenced by the buoyancy and in view of these, thermal buoyancy has been included in the momentum balance equation along the axial direction in the present study.

Inside the liquid pool there are temperature gradients along the axial as well as the radial directions. Due to this, the density of liquid steel increases gradually as it moves form the hotter to the cooler region within the liquid pool, and therefore, have more and more tendencies to settle down during its descent through the pool. Therefore, the buoyancy force in the present investigation has been considered to act in the same direction as that of gravity (i.e. axial direction).

Boundary Conditions:

The boundary conditions assumed for the momentum balance equations (3.1 - 3.5) are:

(a) At the meniscus ($Z = 0$),

    (i) inside the pouring stream,

$$0 \leq X \leq r_0, \quad u = U_{in} \quad \text{and} \quad v = 0 \qquad \ldots (3.7)$$

    (ii) outside the pouring stream,

$$r_0 < X \leq R, \quad u = 0 \quad \text{and} \quad \frac{\partial v}{\partial Z} = 0 \qquad \ldots (3.8)$$

(b) At the exit or outflow boundary (Z = L),

$$0 \leq X \leq R, \qquad \frac{\partial u}{\partial Z} = 0 \text{ and } \frac{\partial v}{\partial Z} = 0 \qquad \ldots (3.9)$$

(c) At the axis of symmetry (X = 0),

$$0 \leq Z \leq L \qquad \frac{\partial u}{\partial X} = 0 \text{ and } \frac{\partial v}{\partial X} = 0 \qquad \ldots (3.10)$$

(d   At the side wall (i.e., mould wall) (X=R),

$$0 \leq Z \leq L, \qquad u = U_{in} \text{ and } v = 0 \qquad \ldots (3.11)$$

A schematic diagram of calculation domain and the relevant boundary conditions are shown in Fig.3.2. The inlet velocity of the pouring stream (Eq.(3.7)) was derived from the global continuity, setting (cross sectional area of nozzle x inlet velocity of the stream) equal to (cross sectional area of the mould x casting speed). At the meniscus and the axis of symmetry, no normal velocity components may exist. Therefore, these were set equal to zero at these locations. Similarly, At all the solid surfaces (i.e., mould wall and solidification front) fluid motion ceases to zero. Further, the entire domain moves with a bulk motion (U_o). Therefore, at the mould wall, the solidification front as well as in the completely solidified region, the axial velocity component (u) was set equal to the casting speed, whereas, the corresponding radial velocity component was assigned zero values. The exit or outflow boundary was assumed to be located far away from the meniscus (preferably in a completely solidified region) so as to keep the influence of out flow boundary on the predicted upstream flow field to a minimum. Thus, the gradients of both axial and radial velocity components were set equal to zero at the chosen exit boundary. The selection of an appropriate outflow boundary and the associated computational
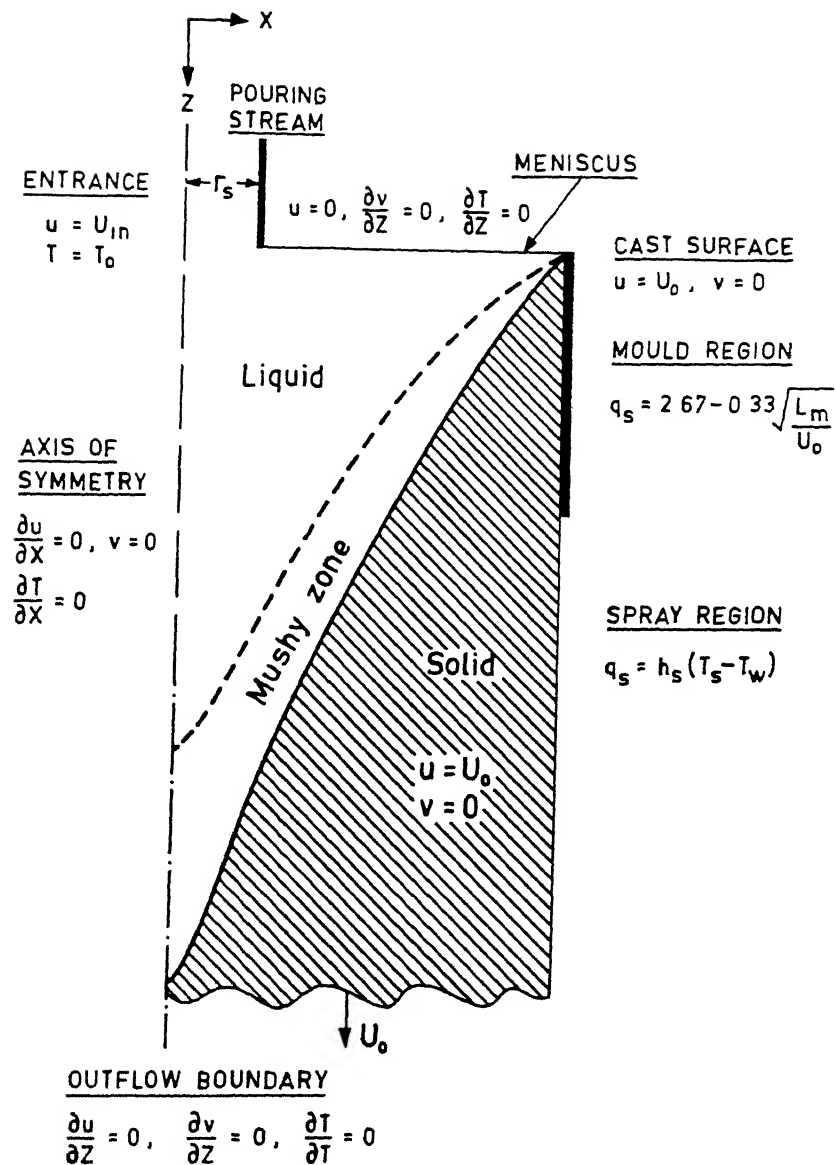
Fig. 3.2. Schematic representation of the 2-D calculation
domain and the boundary conditions applied
in the computation of velocity and temperature
fields.

implications of the same are discussed in detail in a later section.

3.3.3   Modelling of Turbulence Within the Liquid Pool

The diffusion terms embodying effective viscosity (μ_{eff}) in the momentum balance equations (Eqs.(3.2)-(3.5)), takes into account the influence of turbulent and viscous dissipation of momentum within the liquid pool. As mentioned already, the effective viscosity which is the sum of molecular and turbulent viscosity (i.e. $\mu_{eff} = \mu + \mu_t$), is strongly position-dependent, and is largely determined by the nature of hydrodynamics and turbulence present in the system. Various types of turbulence models are available in literature[44,45] for estimating the turbulent viscosity. For example, the well known K - ε model[44] is generally accepted to give a proper representation of turbulence in the high Reynolds number recirculatory flow systems. Similarly, as pointed out already, the Kolmogorov-Prandtl mixing length model can also be applied to derive the turbulent viscosity in the liquid region[11]. Towards this, it is important to note here, that theoretical as well as water model studies on CC have revealed that within the upper pool region only, the flow is predominantly turbulent and recirculatory[36,37]. In contrast, turbulence is practically insignificant in the lower pool region (Fig.3.1). Therefore, in the computational scheme, it would be more realistic to apply a turbulence model to the upper pool region only and practically consider laminar flow conditions in the lower submould region. However, as is well known, it is difficult to apply the K - ε or in fact, any other differential

turbulence model (one equation or two equation models) selectively in specific regions due to the following constraints.

(i) Outflow boundary is not known *a-priori*. Therefore, specification of boundary conditions on the turbulence parameters (say K and ε) to any arbitrarily chosen outflow boundary is difficult,

(ii) Since nature of the flow is considerably different in the upper and lower pool regions if we consider turbulent flow to be confined to the mould region only, it is difficult even then to apply any first or higher order turbulence model selectively in the mould region due to the imposed uncertainty in the value of turbulence parameter at the mould exit (no boundary condition can in principle be applied on the dependent variables at the mould exit since the latter truly is not a physical outflow boundary).

(iii) At the solidification front and in the mushy zone, the governing turbulence transport equations (say K and ε equations) will require considerable modifications. However, presently, nothing is known on this issue.

Consequently, considering the complexity of the pool hydrodynamics and the associated nonlinearity of the equations dealing with conjugate fluid and heat flow, it was decided to evaluate the turbulent properties in the liquid pool using some simplified model rather than a more rigorous and advanced differential model of turbulence (e.g., the K - ε model). In this context, applicability of the Pun - Spalding formula[46,47] of average effective viscosity to the present situation was analyzed critically. The Pun - Spalding formula is based on the

Prandtl mixing length model of turbulence and was originally developed for the analysis of flow in the centrally fired axisymmetric combustion chambers[47]. In principle the Pun-Spalding formula can also be applied to the other equivalent systems involving flows dominated by inertia force, in sudden expansion type geometries. The formula, though not quite conceptually applicable, has been applied successfully to the study of inertia dominated flows in the gas stirred ladle systems[48,49].

In CC, discharge of liquid steel from the pouring nozzle to the mould is conceptually analogous to the flow through a sudden expansion, such as the one considered by Pun and Spalding[46,47]. This follows since the flow particularly, in the mould region, is dominated by inertia force (e.g., entry Reynolds number at discharge nozzle varies typically between 5×10^4 to 9×10^4). Therefore, as a first approximation, average effective viscosity was calculated for the mould region only using the Pun - Spalding formula[46,47], which in the present investigation can be represented in the following form:

$$\mu_{eff} = A \ D_m^{2/3} \ Z_m^{-1/3} \ \rho^{2/3} \ (\dot{m} \ U_{in})^{1/3} \qquad \ldots (3.12)$$

In Eq. (3.13), A is a dimensionless empirical constant (= 0.012)[46,47], and $\dot{m}$ is the mass flow rate of steel and is estimated via the following expression:

$$\dot{m} = (\pi \ r_0^2) \ \rho \ U_{in} \qquad \ldots (3.13)$$

In the submould region, somewhat less turbulence has been

assumed and hence, the effective viscosity in this zone was arbitrarily set to only about 30 - 50 pct. of the mould effective viscosity values. The sensitivity of the predicted flow and temperature fields to the choice of the effective viscosity value will be addressed rigorously in Section 3.5.2.

3.3.4 Governing Equation of Heat Flow and Boundary Conditions

The governing equation of heat flow expresses the conservation of thermal energy over a volume element within the system. For a steady state, two dimensional heat flow situation during continuous casting, the appropriate thermal energy balance equation can be represented by the following general expression:

$$\frac{\partial}{\partial Z}\left(\rho C U_0 T\right) + \frac{\partial}{\partial Z}\left(\rho C u T\right) + \frac{1}{\alpha}\frac{\partial}{\partial X}\left(\alpha \rho C v T\right) = \frac{\partial}{\partial Z}\left(\Gamma_{eff}\frac{\partial T}{\partial Z}\right)$$

$$+ \frac{1}{\alpha}\frac{\partial}{\partial X}\left(\alpha \ \Gamma_{eff}\frac{\partial T}{\partial X}\right) + S \qquad \qquad ...(3.14)$$

The first term on the L.H.S. of Eq. (3.14) represents heat flow in the axial (withdrawal) direction (X) due to the bulk motion (U_0) of the descending strand. Whereas, the second and the third terms are the convection terms due to velocity components u and v respectively. On the R.H.S., the first and the second term represents conduction of heat along the axial (X) and the radial (Y) directions respectively, and S is the latent heat source term defined as:

$$S = \rho \ U_0 \Delta H_f\left(\frac{\partial f_s}{\partial Z}\right) \qquad \qquad ...(3.15)$$

similarly, the effective thermal conductivity in Eq.(3.14) is defined as:

$$\Gamma_{eff} = K + K_t/\sigma_t \qquad \qquad ...(3.16)$$

Furthermore, in Eq.(3.16) σ_t is the turbulent Prandtl number and is defined as :

$$\sigma_t = \alpha_t/\nu_t = \frac{\text{turbulent thermal diffusivity}}{\text{turbulent momentum diffusivity}} \qquad ...(3.17)$$

For most of the turbulent flows, $\sigma_t \simeq 1$. However, a typical value of $\sigma_t = 0.7$ for liquid steel, has been used by Asai and Szekely[11] in their studies. Assuming $\sigma_t \simeq 1$ i.e., $\alpha_t = \nu_t$, it is readily seen that:

$$K_t/\rho C = \mu_t/\rho$$

or, $$K_t = \mu_t C$$

Since $$\mu_{eff} \propto \mu_t$$

Therefore, $$\Gamma_{eff} = K + \mu_{eff} C \qquad \qquad ...(3.18)$$

It may be noted that the energy balance equation is applicable to each zone in continuous casting, viz. liquid, mushy zone, and the solidified region. Furthermore, the derivative $(\partial f_s/\partial Z)$ appearing in Eq.(3.15) is by definition zero everywhere except in the mushy zone viz., ($T_{sol} < T < T_{liq}$). In the solidified region the velocity components (u and v) become zero and thus, a pure conduction like equation results for the solidified region from Eq.(3.14), with additional contribution due to bulk motion (or casting speed) of the descending strand. However, in the

liquid pool, heat is transferred by convection (i.e due to fluid velocity components u and v) and turbulent conduction only, and the bulk motion contribution in the liquid core is zero. Therefore, in the regions $T > T_{sol}$ the energy balance equation (Eq.(3.14)) becomes analogous to the momentum balance equations viz. Eqs. (3.2) and (3.4).

In the present investigation, latent heat released during solidification has been evaluated from the solid fractions in the mushy zone assuming equilibrium solidification of steel. Procedure for the estimation of latent heat release from the relevant equilibrium phase diagram (Fig.2.2) has already been described in Section 2.3.4, and is therefore not reproduced here.

The boundary conditions applied to Eq.(3.14) were also exactly identical to those considered for the effective thermal conductivity model. For clarity of presentation, temperature as well as the velocity boundary conditions are shown in Fig.3.2, and are also stated below.

(a) At the meniscus (Z = 0),

(i) inside the pouring stream,

$$0 \leq X \leq r_0, \qquad T = T_0 \qquad \qquad ...(3.19)$$

(ii) outside the pouring stream,

$$r_0 < X \leq R, \qquad \partial T/\partial Z = 0 \quad \text{or} \quad q_z = 0 \qquad ...(3.20)$$

(b) At the exit boundary (Z = L),

$$0 \leq X \leq R, \qquad \partial T/\partial Z = 0 \qquad \qquad ...(3.21)$$

(c) At the axis of symmetry (X = 0),

$$0 \leq Z \leq L, \qquad \partial T/\partial X = 0 \qquad \qquad ...(3.22)$$

differential equations and the associated boundary conditions to their equivalent dimensionless forms prior to carrying out any detailed computations. As is well known, in the dimensionless form the system of equations become essentially scale free, and hence the chances of accumulated error in the predicted result are less. In addition to these, the orders of magnitude of various terms in the non-dimensional partial differential equations become comparable to one other and therefore, influence of any particular parameter on the computed results can be conveniently estimated/studied.

In the nondimensionalization procedure, the following dimensionless variables were defined.

(i)   dimensionless space variables

$$z^* = Z/R$$
$$x^* = X/R$$

(ii)   dimensionless velocity components

$$u^* = u/U_{in}$$
$$v^* = v/U_{in}$$

(iii)   dimensionless pressure variable

$$p^* = p/(\rho U_{in}^2)$$

(iv)   dimensionless temperature variable

$$T^* = T/T_0$$

and finally,   (v)   the relevant dimensionless groups,

Reynolds Number (Re) $= \rho U_{in} R/\mu_{eff}$

Peclet Number (Pe) $= \rho C U_{in}/(\Gamma_{eff}/R)$

Thus, the fluid flow equations and the associated boundary conditions in dimensionless form (say in cartesian coordinate

system) can be conveniently presented as:

Equation of continuity

$$\frac{\partial u^*}{\partial Z^*} + \frac{\partial v^*}{\partial X^*} = 0 \qquad \qquad \ldots(3.26)$$

Equation of motion in axial direction

$$\frac{\partial}{\partial Z^*}\left(u^* u^*\right) + \frac{\partial}{\partial X^*}\left(u^* v^*\right) = -\frac{\partial p^*}{\partial Z^*} + \frac{\partial}{\partial Z^*}\left(\frac{1}{Re}\frac{\partial u^*}{\partial Z^*}\right)$$

$$+ \frac{\partial}{\partial X^*}\left(\frac{1}{Re}\frac{\partial u^*}{\partial X^*}\right) + S_u^* \qquad \ldots(3.27)$$

where, axial momentum source term per unit volume

$$S_u^* = \frac{\partial}{\partial Z^*}\left(\frac{1}{Re}\frac{\partial u^*}{\partial Z^*}\right) + \frac{\partial}{\partial X^*}\left(\frac{1}{Re}\frac{\partial v^*}{\partial Z^*}\right) - Rg\beta T_0 (T^* - 1)/U_{in}^2$$

$$\ldots(3.28)$$

Equation of motion in transverse/radial direction

$$\frac{\partial}{\partial Z^*}\left(u^* v^*\right) + \frac{\partial}{\partial X^*}\left(v^* v^*\right) = -\frac{\partial p^*}{\partial X^*} + \frac{\partial}{\partial Z^*}\left(\frac{1}{Re}\frac{\partial v^*}{\partial Z^*}\right)$$

$$+ \frac{\partial}{\partial X^*}\left(\frac{1}{Re}\frac{\partial v^*}{\partial X^*}\right) + S_v^* \qquad \ldots(3.29)$$

where, transverse/radial direction momentum source term per unit volume

$$S_v^* = \frac{\partial}{\partial Z^*}\left(\frac{1}{Re}\frac{\partial u^*}{\partial X^*}\right) + \frac{\partial}{\partial X^*}\left(\frac{1}{Re}\frac{\partial v^*}{\partial X^*}\right) \qquad \ldots(3.30)$$

The corresponding boundary conditions applied to the momentum balance equations in dimensionless form are:

(a) At the meniscus ($Z^* = 0$)

    (i) inside the pouring stream

$$0 \leq X^* \leq r_0^*, \quad u^* = 1 \quad \text{and} \quad v^* = 0 \qquad \ldots(3.31)$$

(ii) outside the pouring stream

$$r_0^* < X^* \leq 1, \quad u^* = 0 \quad \text{and} \quad \partial v^*/\partial z^* = 0 \quad \ldots (3.32)$$

(b) At the exit boundary $(z^* = L^*)$

$$0 \leq X^* \leq 1, \quad \partial u^*/\partial z^* = 0 \quad \text{and} \quad \partial v^*/\partial z^* = 0 \quad \ldots (3.33)$$

(c) At the axis of symmetry $(X^* = 0)$

$$0 \leq z^* \leq L^*, \quad \partial u^*/\partial X^* = 0 \quad \text{and} \quad v^* = 0 \quad \ldots (3.34)$$

(d) At the side wall (i.e., mould wall) $(X^* = 1)$

$$0 \leq z^* \leq L^*, \quad u^* = U_0 \quad \text{and} \quad v^* = 0 \quad \ldots (3.35)$$

Similarly, the energy balance equation and associated boundary conditions in the dimensionless form become as follows:

$$\frac{\partial}{\partial z^*}\left(U_0^* \, T^*\right) + \frac{\partial}{\partial z^*}\left(u^* T^*\right) + \frac{\partial}{\partial X^*}\left(v^* T^*\right) = \frac{\partial}{\partial z^*}\left(\frac{1}{Pe}\,\frac{\partial T^*}{\partial z^*}\right)$$

$$+ \frac{\partial}{\partial X^*}\left(\frac{1}{Pe}\,\frac{\partial T^*}{\partial X^*}\right) + S^* \quad \ldots (3.36)$$

In Eq.(3.36), S^* is the dimensionless latent heat source term, and is defined as:

$$S^* = \frac{U_0^* \, \Delta H_f}{C \, T_0} \left(\partial f_s / \partial z^*\right) \quad \ldots (3.37)$$

The corresponding dimensionless temperature boundary conditions are:

(a) At the meniscus $(z^* = 0)$

(i) inside the pouring stream

$$0 \leq X^* \leq r_0^*, \quad T^* = T_0^* \quad \ldots (3.38)$$

(ii) outside the pouring stream

$$r_o^* < X^* \leq 1, \qquad \partial T^*/\partial Z^* = 0 \qquad \ldots(3.39)$$

(b) At the exit boundary ($Z^* = L^*$)

$$0 \leq X^* \leq 1, \qquad \partial T^*/\partial Z^* = 0 \qquad \ldots(3.40)$$

(c) At the axis of symmetry ($X^* = 0$)

$$0 \leq Z^* \leq L^*, \qquad \partial T^*/\partial X^* = 0 \qquad \ldots(3.41)$$

(d) At the cast surface ($X^* = 1$)

(i) mould region

$$-0 \leq Z^* \leq L_m^*, \quad q_m^* = \frac{1}{\rho C U_{in} T_0}(2.67 - 0.33\sqrt{Z/U_0}) \times 10^6 \qquad \ldots(3.42)$$

(ii) secondary cooling zone,

$$L_m^* < Z^* \leq L_s^*, \quad q_s^* = \frac{h_s}{\rho C U_{in}}(T_s^* - T_w^*) \qquad \ldots(3.43)$$

(iii) radiation cooling zone

$$L_s^* < Z^* \leq L^*, \quad q_s^* = (\sigma \varepsilon \theta_0^4/\rho C U_{in} T_0)(\theta_s^{*4} - \theta_a^{*4}) \qquad \ldots(3.44)$$

in which, $\qquad \theta_0 = T_0 + 273$

3.3.6   Modelling of Fluid Flow in the Mushy Zone

Computation of velocity field within the mushy zone is much more complex than in the bulk liquid steel, as the mushy zone typically involves flow through complex interdendritic channels. Furthermore, flow is also induced in the mushy zone by suction caused by the solidification shrinkage. In addition, rejection of solute elements by the solidifying dendrites into

the interdendritic spaces (i.e. microsegregation phenomena) poses additional complications.

To take into account the exact influence of all these factors in the theoretical analysis of fluid flow and heat transfer in the liquid pool, considerable difficulties (fundamental as well as computational) were anticipated. Consequently, an ad-hoc simplified approach has been considered to model the fluid flow in the mushy zone. Towards this, it is important to mention here that Asai and Szekely[11] considered the increased resistance to flow produced by the solid matrix in the mushy zone by increasing the liquid steel viscosity by a factor of 20 in the mushy zone. The investigators[11] derived this factor from a typical viscosity-temperature correlation reported in the literature[50]. In the present study, the same assumption was made for simulating the possible influence of mushy zone on the resultant fluid flow. However, as will be described subsequently, influence of other choices of mushy zone viscosity on the predicted flow and temperature fields were also studied computationally.

3.3.7   Choice of the Outflow Boundary

Typically, the axial gradients of the dependent variables are assumed to be zero (Eq.(3.21)) at the exit plane (e.g. the outflow boundary), at which a fully developed flow situation must truly exist. Thus, with such a constraint at the outflow boundary, it was observed that no meaningful solution (i.e. realistic velocity field) could be obtained if the outflow boundary is placed anywhere arbitrarily. It was also found that

the erroneous/unrealistic positioning of the outflow boundary leads to uncertainty in the boundary conditions at the exit plane and consequently, in turn produces unrealistic prediction.

In billet casters, pool depth often extends much below the cast strand, and flow reversal is significant even in the lower portion of the liquid pool. Hence, the imposed zero gradient boundary conditions at any arbitrarily chosen outflow boundary may not be a realistic one, unless the chosen exit plane lies in the completely solidified region. Thus, due care was taken in all computations to ensure that exit plane was located far enough downstream in the completely solidified region, so as not to influence the upstream results. Thus, in the computations reported subsequently, the exit plane was considered to be located at 10 m downstream of the inlet plane.

3.4 NUMERICAL SOLUTION OF THE GOVERNING PARTIAL DIFFERENTIAL EQUATIONS

3.4.1 Numerical Solution Procedure

Numerical solution of the governing fluid flow and heat transfer equations were carried out by the popular TEACH-T computer code, originally developed by the Computational Fluid Dynamics research group at the Imperial College, London. However, as will be discussed below, the original TEACH-T code was considerably modified before it was used in the present numerical investigation.

The TEACH-T code is based on the control volume based finite difference numerical procedure and incorporates formulations

based on the primitive variables (u,v, and p), instead of the retrieved stream function and vorticity[43,51]. The SIMPLE (Semi Implicit Method for Pressure-Linked Equations) algorithm, originally developed by Patankar and Spalding[30], is applied to numerically solve the pressure-velocity coupling in the governing fluid flow equations. The computer code is suitable for axisymmetric, two dimensional, turbulent or laminar recirculating flow calculations with variable thermophysical properties. Furthermore, it can solve the set of governing partial differential equations in Cartesian or cylindrical polar coordinate systems. The K-ε model of turbulence has been embodied in the code for the computation of turbulence parameters. The overall structure of the code is modular, thus enabling any dependent variables to be removed or added at will.

For the flow field calculations staggered grids were employed for its special attributes[30,51], where, the scalar variables (i.e. P and T) were specified at the central nodal point of the control volumes, and the vectors (i.e. u and v) were located on the cell interfaces (as opposed to centers). Figs.(3.3) and (3.4) present schematic of grid distribution and various types of control volumes respectively, considered in the present computational work. The relevant governing equations were integrated over their respective control volumes to yield a system of discretization or finite difference equations. The procedures of discretization of the governing partial differential equation has already been described in detail in chapter 2 of the present work, and therefore, are not reproduced here. In essence a general variable ϕ (say u,v, or T) at any
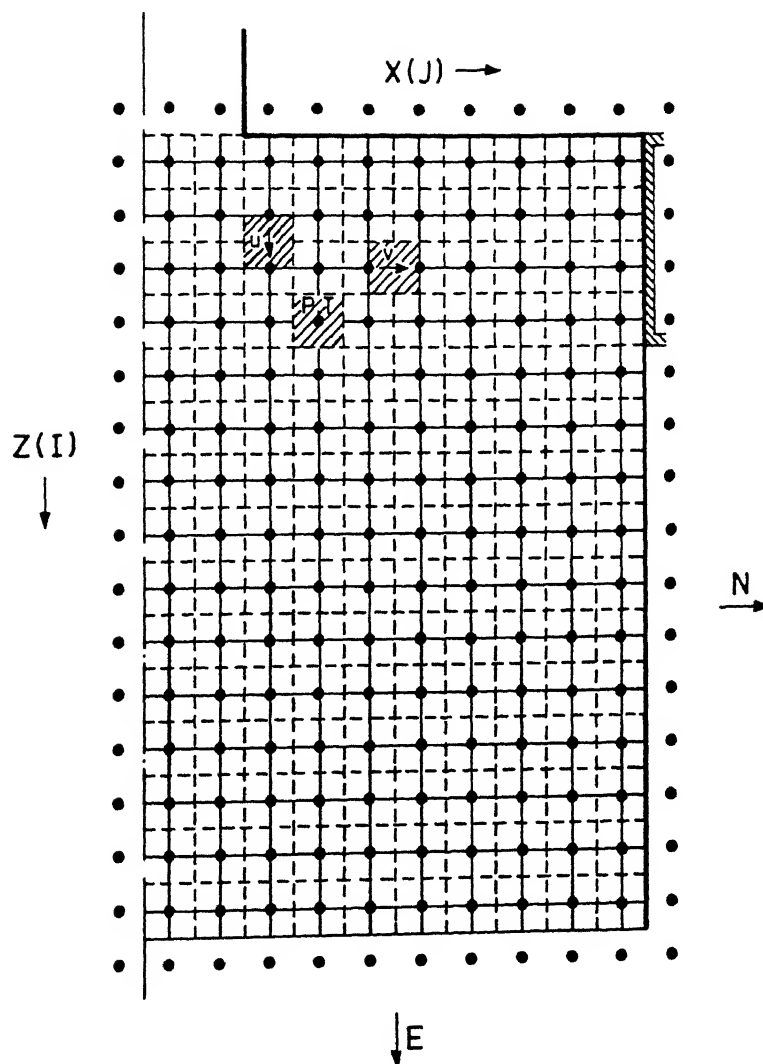
Fig. 3.3. Schematic of the grid layout and control volumes for vector (u & v) and scalar (P & T) variables.

(a)

Control volume for
scalar variables (i.e P & T)

(b)

Control volume for
axial velocity component (U)

(c)

Control volume for
radial velocity component
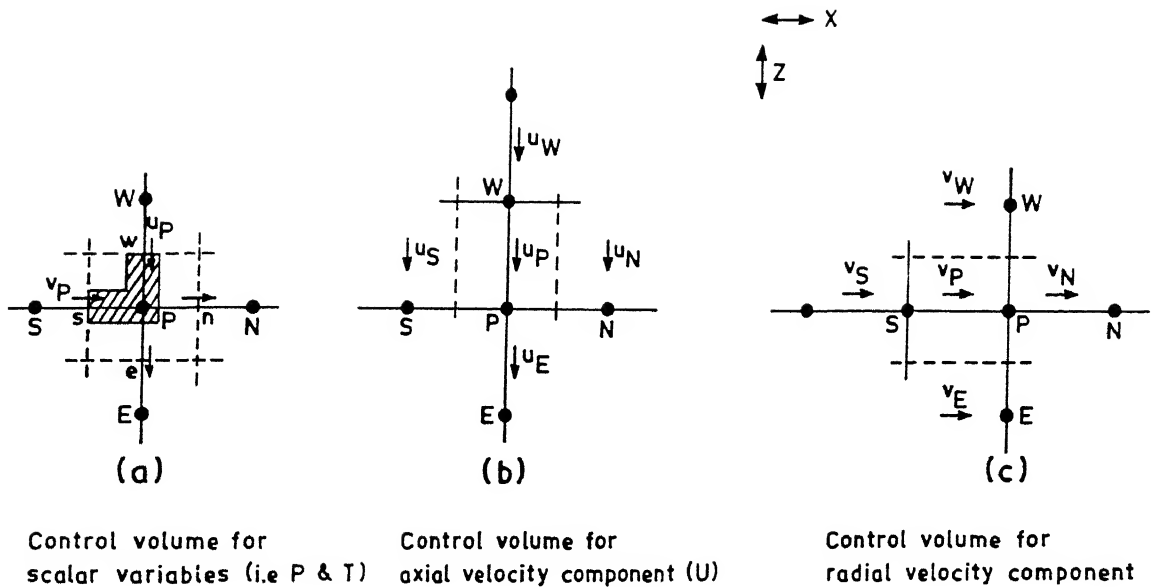
Fig. 3.4. Schematic of three typical control volumes for scalar (i.e. P & T) and vector (u & v) variables employed in the numerical computation scheme.

nodal point P (Fig.3.4) can be represented in terms of its neighbour point coefficients (E, W, N and S) via the following discretization equation:

$$A_P \phi_P = A_E \phi_E + A_W \phi_W + A_N \phi_N + A_S \phi_S + S_U \qquad \ldots(3.45)$$

in which, $A_P = A_E + A_W + A_N + A_S - S_P$

In Eq.(3.45), A's are the coefficients of discretization equation embodying the combined influence of both convection and diffusion contributions to ϕ_p by the neighbouring grid points, while S stands for the 'source term' as defined in Eqs. (3.2) and (3.4). Again, linearization of S can be accomplished, as in Eq.(3.45) by using the variable ϕ as follows:

$$S = S_U + S_P \phi_P \qquad \ldots(3.46)$$

In Eq.(3.46), S_U and S_P are the two functions which depend on the particular ϕ variable concerned.

During the discretization procedure, transport properties (e.g. viscosity and conductivity) at the control volume faces were estimated via a more accurate harmonic mean interpolation method[30,51]. However, in computational fluid dynamics, a realistic representation of the convection and diffusion terms is essential to the accuracy and convergence or even stability of the iterative calculation scheme. Therefore, the hybrid difference scheme[51] was incorporated in the computation scheme for representing the combined convective and diffusive contribution of momentum and heat from the neighboring control volumes to the central ones. The set of discretization equations were solved iteratively by the well known Tri-Diagonal Matrix

Algorithm (TDMA) incorporating an efficient line by line solution procedure[51]. To this end, routine underrelaxation practice to the dependent variables was applied. The underrelaxation practice applied together with the scope of convergence/convergence criterion adopted in the present study are discussed in the relevant subsequent section.

3.4.2 Numerical Procedure for Incorporating the Influence of Solidifying Shell on Fluid Flow and Heat Transfer

The velocity components (i.e., u and v) are zero at the solidification front, while the entire domain is moving with casting speed (U_o). Therefore, in the numerical solution procedure applied to the fluid flow equations, the axial velocity component u was set equal to the casting speed U_0 and the radial velocity component v was set equal to zero at the solidification front as well as in the entire solidified region. Mathematically, these conditions on the governing fluid flow equations can be expressed as,

$$T \le T_{sol} \quad \text{or,} \quad X_{sl} \le X \le R, \quad u = U_o, \quad v = 0 \qquad \ldots (3.47)$$

The restrictions imposed by Eq. 3.47 provides a realistic description of bulk motion of the descending strand with respect to the fluid flow in the molten pool in continuous casting.

The numerical procedure for prescribing these conditions, within the solidified region as well as at the solidification front, therefore, should be such that the solution procedure is able to reflect the exact prescribed values of velocity

components in these regions. To this end, there are two numerical techniques available[52,30]. Of these, the first[30] involves artificially assigning a very high values (say 10^{30}) of viscosity in the solidified region together with the desired values at the solidification front. This procedure, however, rests on the ability of the numerical procedure to handle a large step change in the values of transport coefficient (e.g. effective viscosity etc.). In this context, harmonic mean interpolation for estimation of transport coefficients at the cell interfaces has been found to be the most appropriate[30]. The other procedure[52], called the 'cell porosity' or 'blockage ratio' technique, involves blocking off preferentially those control volumes lying in the inactive zone (i.e. solidified region) so that only the remaining control volumes form the active domain for the computation of flow field. In the present study, the latter procedure has been employed to take into account the influence of the growing shell on the fluid flow and thus on the turbulent convective transport of heat. It is to be emphasized here that both these techniques are expected to provide identical estimates of flow parameters in the calculation domain.

In the cell porosity method, for each control volume face, a blockage ratio (from 0 to 1) was defined. Thus, for the control volume face lying fully in the solidified region (i.e. completely blocked to flow), blockage ratio was defined as unity. Similarly, for the face lying completely in the liquid region, blockage ratio was set equal to zero. Those control volume faces which are cut by the solidification front (i.e. only partially in the solidified region), blockage ratios were estimated from

the fraction of the area of control volume face blocked by the solid. During each iteration, position of solidification front for each axial station was derived from the predicted temperature field and a smooth curve fitted through the loci of the solidification front. Subsequent to this, the positions of intersection of the fitted curve (e.g., numerical solidification front profile) and all the relevant control volume faces were computed. From these, blockage ratios of the various faces of control volume were calculated. Intersection of a radial velocity control volume and the solidification front together with the procedure used for the evaluation of the blockage ratio is illustrated schematically in Fig.3.5.

Subsequent to the calculation of blockage ratio, the original coefficients of the discretization equation (Eq.(3.45)), i.e., A_E, A_W, etc., were modified as according to:

$$
\left.
\begin{aligned}
A_{E,new} &= (1-BR_e)A_E \\
A_{W,new} &= (1-BR_w)A_W \\
A_{N,new} &= (1-BR_n)A_N \\
A_{S,new} &= (1-BR_s)A_S
\end{aligned}
\right\} \qquad \ldots (3.48)
$$

where, BR's are the blockage ratios (or (1-BR) is the cell porosity) for the four faces of any two-dimensional control volume.

When all the blockage ratios for a control volume were 1 (i.e. in the completely solidified region), all the neighbouring coefficients of the discretization equation became zero, and hence, the grid node became completely isolated from its neighbors. The value of a variable ϕ at such a node could then be

SOLIDIFICATION FRONT*

$X_{SL,w}$

$\longrightarrow$ N

LIQUID REGION

$Z(I)$
$(I,J-1)$

s

$V(I,J)$

w

n

(I,J)

FULLY SOLIDIFIED REGION

$X(J-1)$ e $X(J)$

$X_{SL,e}$

ΔX

BLOCKAGE RATIOS OF c.v. FACES

face 's' $BR_s = 0$ Liquid region

face 'n' $BR_n = 1$ Fully blocked

Partially blocked faces :

face 'w' $BR_w = 1 - \dfrac{X_{SL,w} - X(J-1)}{\Delta X}$

face 'e' $BR_e = 1 - \dfrac{X_{SL,e} - X(J\ 1)}{\Delta X}$
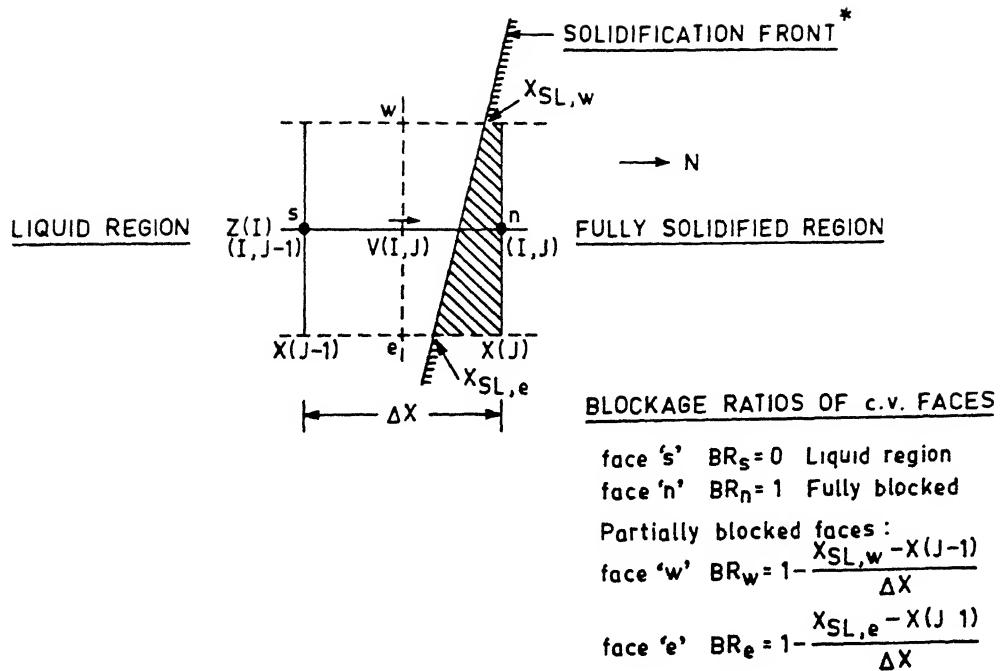
* Deduced via curve fitting through
a set of solidus temperatures

Fig. 3.5. Schematic of a typical radial velocity control volume located in the vicinity of the solidification front and evaluation of blockage ratios for various control volume faces.

fixed at any desired value, $\phi_{P,desired}$ (for example, $U = U_0$ and $v = 0$ at the nodes just on the solidification front or in the solidified region for the present case) by redefining the components of the source term in the discretization equation as :

$$S_U = 10^{30} \times \phi_{P,desired}$$

and

$$S_P = -10^{30} \qquad \left.\right\} \qquad \ldots(3.49)$$

With such a prescription, Eq.(3.45) reduces to

$$-S_P \phi_P \cong S_U$$

or,

$$\phi_P = -S_U/S_P = \phi_{P,desired} \qquad \left.\right\} \qquad \ldots(3.50)$$

Such a technique allowed the value of the dependent variable to be fixed whereever needed. Thus, during each iteration, the velocity equations were solved by assigning $u=U_0$ and $v = 0$ in the completely solidified region. Subsequently, the temperature equation was solved, in which the velocity components u and v were both set equal to zero in the solidified region in order to eliminate completely the thermal convection terms in the governing heat flow equation. Similarly, in the solid region, true value of thermal conductivity of steel was applied when solving for the temperature field.

3.4.3 The Computer Program

As mentioned already, the TEACH-T computer code was employed for the computation of flow field in the present study. However, the original computer code was modified

extensively with the addition of few more subroutines and several other features for numerical solution of governing fluid flow and heat transfer equations. The following modifications have been incorporated in the original TEACH-T code:

(1) The TEACH-T code is capable of computing only the laminar or turbulent flow fields. Thus, for the temperature field calculations, a separate subroutine was developed and incorporated in the code so that convective turbulent heat transfer problem can also be solved numerically.

(2) For the calculation of solid fraction distribution in the mushy zone and the associated rate of latent heat release, a separate subroutine has been developed and added to the computer program.

(3) A separate subroutine for the computation of pool profile has also been developed and incorporated.

(4) A numerical procedure for estimating the blockage ratios has been incorporated via a separate subroutine.

(5) The average effective viscosity formula of Pun and Spalding[46] has been applied as an alternative to the K-ε turbulence model.

In addition to these, for the implementation of boundary conditions, the original subroutine PROMOD (which contains all relevant boundary conditions) has also been modified considerably in accordance with the specification of the present problem. Also, a separate module for the relevant temperature boundary conditions was incorporated in the PROMOD subroutine.

All the four new subroutines mentioned above, were separately developed and tested against standard input data,

before incorporating into the original TEACH-T program. Detailed flow chart of the modified TEACH code applied to the present investigation is illustrated in Fig.3.6. Prior to initiating the actual computations for the data set presented in Table 3.1, both uniform as well as non uniform grids of different configuration were tried in an attempt to establish practical grid independent solutions. Towards this, for a typical cylindrical billet[30], 200 x 18 grids and for square billets[23] 200 x 24 grids (Table 3.1), were found to give satisfactory results. This corresponds to grid spacing of approximately 50 mm and 3.5 mm in the axial and transverse directions respectively. All computations were performed on mini-super CONVEX computer available at I.I.T. Kanpur. A convergence criterion of maximum normalized residual ($= 5 \times 10^{-5}$) was set on all variables, which for a general variable ϕ is defined mathematically as :

$$\text{Residual} = A_P \phi_P - \left(A_E \phi_E + A_W \phi_W + A_N \phi_N + A_S \phi_S + S_U \right)$$

$$\text{Normalized Residual} = \left[\sum \sum (\text{Residual}) \right] / (\text{Total input momentum/heat})$$

$$\dots (3.51)$$

Each computation was carried out till the absolute sum of residuals on u,v, mass continuity, and T all fell below their stipulated values (i.e. the prescribed maximum normalized residual value). The data applied to the numerical computations are presented in Tables 3.1 and 3.2 respectively.
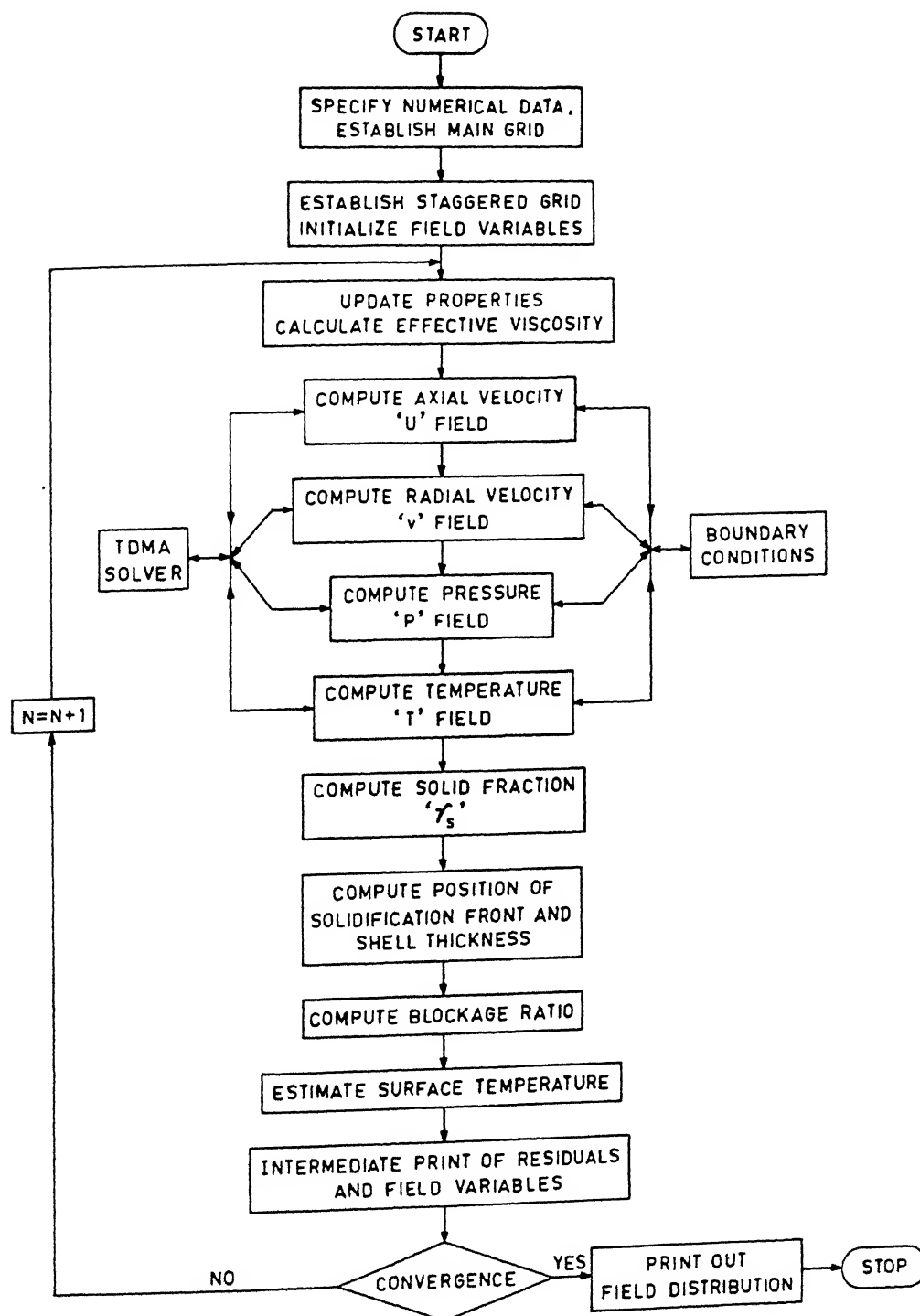
Fig 3.6 Flow diagram of the model applied to the numerical computation of velocity and temperature fields in continuous casting process

3.5 RESULTS AND DISCUSSION

3.5.1 Some Considerations on the Scope of Convergence of a Multidimensional Coupled Fluid Flow Heat Transfer Problem

As mentioned already and illustrated in the preceding sections, the fluid flow and heat transfer equations describing the present problem are highly nonlinear in nature. The source terms, some of the boundary conditions, together with variable thermo-physical properties are in general seen to contribute to the nonlinearity. In addition to these, mutual coupling between fluid flow and heat transfer equations through the buoyancy term in the axial momentum equation and the presence of solidified shell in the calculation domain lead to some severe nonlinearity in the present problem. As a result of these inherent complexities, numerical solution of the set of partial differential equations presented considerable difficulties in arriving at a converged solution.

Initially, several trial executions were carried out with original (i.e. dimensional) forms of the momentum and energy balance equations, and these failed to produce any meaningful solution. Subsequently, it was observed that non-dimensionalization of the governing equations somewhat enhanced the scope of arriving at the converged solution. Through extensive computational trials it was further observed that convergence could be obtained only for a narrow range of value of the relaxation parameters (on u, v, and T respectively). This latter parameter and hence convergence was found to be sensitive

to the particular set of input conditions as well as the grid configurations applied. On the basis of computational trials made during the initial stage of the study, the following observations were made:

(i) Underrelaxation of the dependent variables was important, and the choice of values of underrelaxation parameter was found to be critical from the view point of arriving at the converged solution.

(ii) The value of underrelaxation parameter on a given dependent variable was not unique but was a function of grid layout and hence, for any given set of grid configuration chosen, it was to be determined through numerical trial and error.

(iii) The maximum number of iteration (or the computational work) that was required for arriving at converged solution was a function of both grid layout and the value of relaxation parameter applied.

Thus, for each individual problem that is to be solved, a large number of initial numerical trials have to be conducted. This, according to the present investigator, appears to be a major limitation in the application of turbulent fluid - heat flow concept to the continuous casting of steel.

Intermediate results obtained during computations indicated that the magnitude of dependent variables fluctuated over a wide range before reaching the final converged solution. The extent of fluctuations in the dependent variables (i.e., dimensionless axial velocity component and temperature) with the progress of iteration is shown in Figs. 3.7 and 3.8 respectively. These clearly demonstrate the extent of the associated complexities
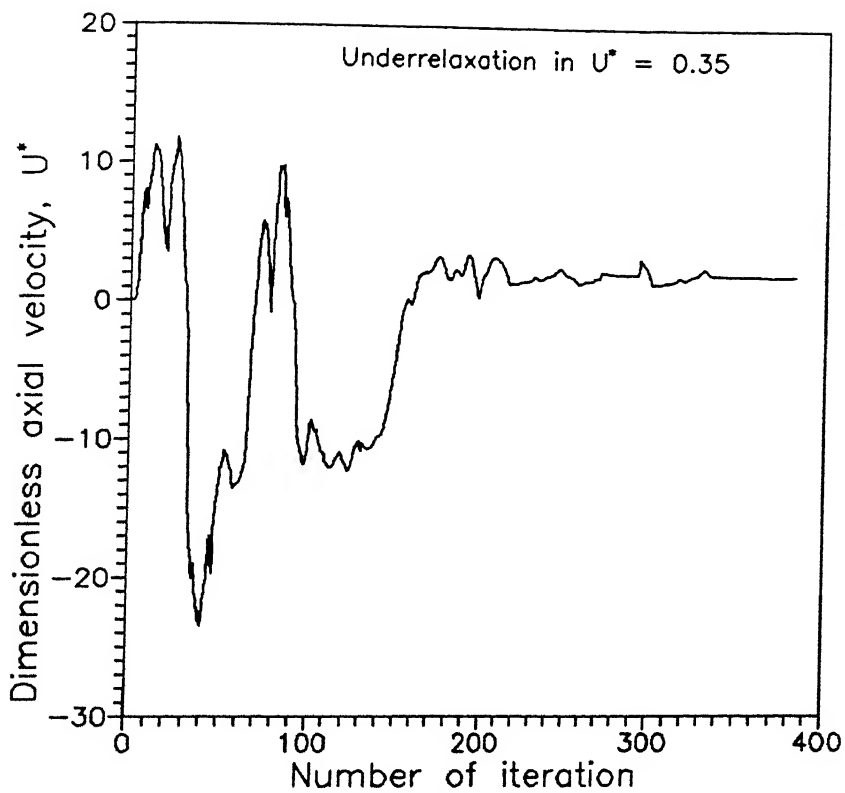
Fig. 3.7: Variation of the dimensionless axial velocity component at a monitoring location (i.e. r=0.005 m, Z=0.1 m) with the progress of iteration.
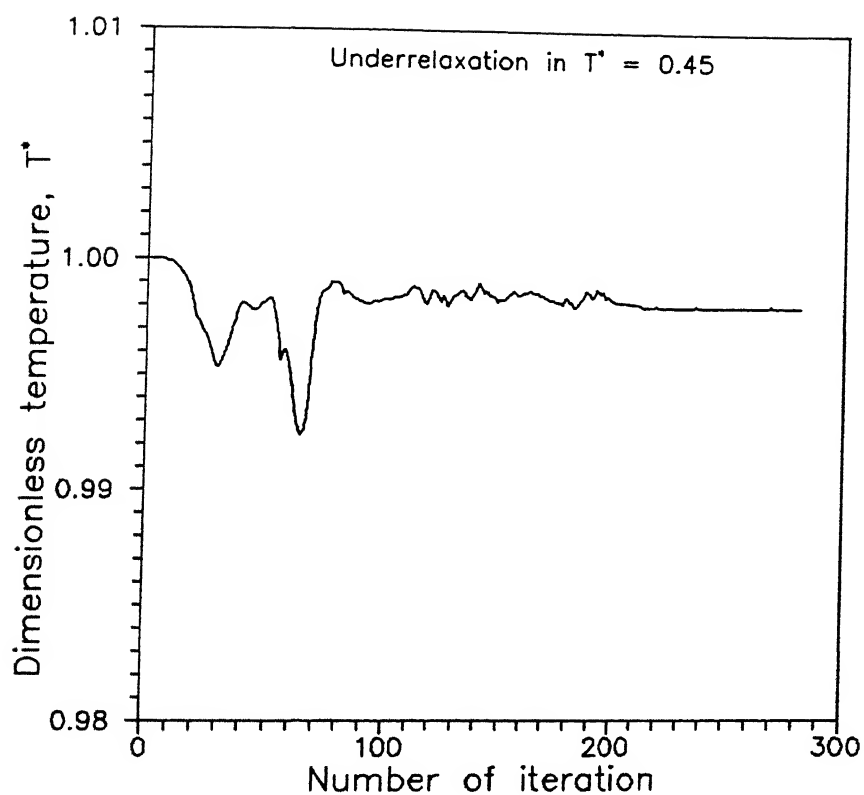
Fig. 3.8: Variation of the dimensionless temperature at a monitoring location (i.e., r=0.005 m, Z=0.1 m) with the progress of iteration.

involved in the numerical solution of the present problem which is essentially due to the coupling of fluid flow, heat transfer, solidification phenomena.

3.5.2 Sensitivity of Computations to the Choice of Effective Viscosity Value

The Reynolds number at the liquid steel inlet/nozzle was estimated to be of the order of 10^4 or greater. Therefore, the flow in the liquid pool, particularly in the mould region, can be safely considered to be turbulent. To this end, any appropriate turbulence model can be applied in order to estimate the required turbulent properties within the system. However, estimation of effective viscosity or as a matter of fact any other turbulence parameter in the liquid pool using a rigorous turbulence model (e.g. the K - ε model) may not be appropriate for the present problem due to the reasons described already in section (3.3.3). Therefore, as mentioned before, the Pun - Spalding formula[46] (Eq.(3.12) was applied to estimate the average effective viscosity in the liquid pool for the mould region only.

The expression in Eq.(3.12) indicates that μ_{eff} increases with increase in the rate of kinetic energy (i.e. $\dot{m}U_{in}^2$) conveyed to the liquid pool by the incoming pouring stream. Also, μ_{eff} increases with increase in the mould diameter (D_m) and decreases with any increase in the mould length (L_m). Theoretical as well as experimental studies[12,35-37] on CC indicate that turbulent flow is confined only in the upper liquid pool region of the solidifying casting. Consequently, in the present investigation,
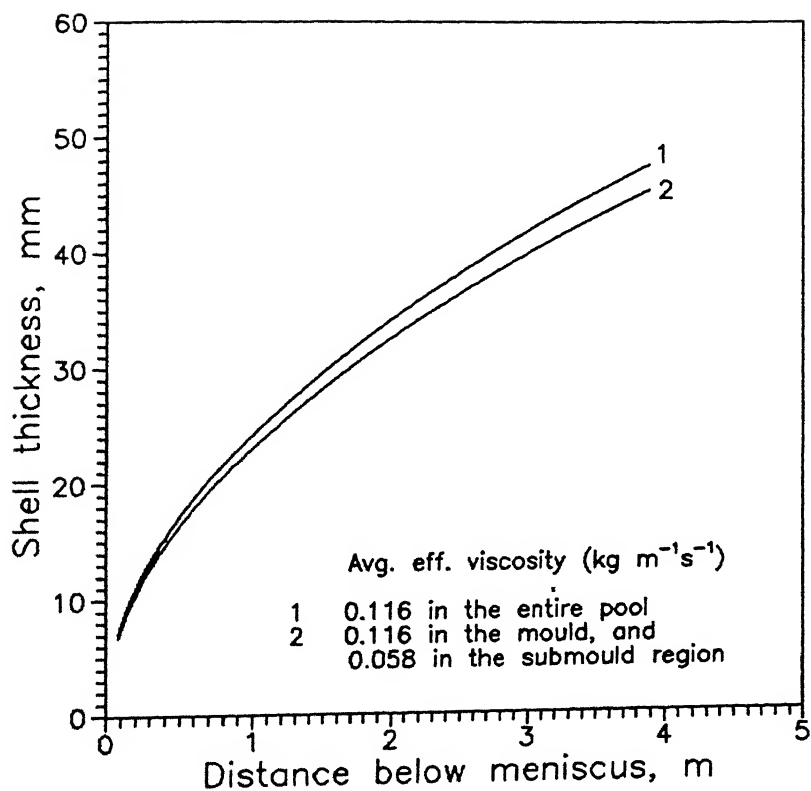
Fig. 3.9: Influence of average effective viscosity values in the mathematical model on the computed shell thickness.

the Pun-Spalding formula[46] was applied to the mould region and thus, effective viscosity was estimated from the dimensions of the mould assuming negligible distortion in the pool geometry (i.e., in the pool diameter) by the thickness of the solidified shell. Furthermore, in the submould region arbitrarily, somewhat less turbulence was assumed and towards this, approximately 50 - 70 pct. lower effective viscosity value than those estimated via Eq.(3.13) for the mould was prescribed in the submould region. It is to re-emphasized here that no differential model of turbulence can be so conveniently applied over the entire liquid pool, as it is possible with a bulk average turbulence model (Eq.(3.12)).

Thus, the influence of prescribing the same μ_{eff} value throughout the pool and a 50 pct. reduced μ_{eff} value in the submould region, on the numerically predicted shell thickness is shown in the Fig.3.9. This clearly indicates that the assumption of different turbulence levels in the submould region does not affect the overall heat transfer rates significantly. The present analysis thus revealed that the exact modelling of turbulence phenomena is relatively less critical for predicting the temperature fields and solidification phenomena in CC.

3.5.3 Modelling of Flow in the Mushy Zone and Its Influence on the Computed Results

For the temperature field calculations, transfer of heat in the mushy zone has been considered to take place by the convection and the molecular conduction. Whereas, for the velocity field calculation, resistance to the bulk flow of fluid

imparted by the solidifying dendrites in the mushy zone was taken into account by artificially increasing the viscosity of the mushy zone. As described already, Asai and Szekely[11] assigned a value of viscosity in the mushy zone 20 times larger as compared to that of liquid steel. As a first approximation, in the present study as well, the same procedure has been applied and the same value has been prescribed to the viscosity of liquid in the mushy zone. However, it is important to assess the sensitivity of overall predictions to the choice of other possible values of mushy zone viscosity.

Fig.3.10 shows the influence of various values of prescribed mushy zone viscosity on the predicted shell thickness. These show that over a narrow range (i.e. 20 - 30 times) the overall influence was only marginal, whereas over a somewhat wider range (i.e. 20 - 60 times), the mushy zone viscosity affected the shell growth relatively significantly, particularly, in the lower pool region. Such behaviour can be attributed to a gradually reduced bulk flow in the mushy zone with increased viscosity, leading to a decreased convective transport of heat. Consequently, decreased shell thickness was predicted with increasing mushy zone viscosity. Since lower in the pool the mushy zone becomes gradually thicker, the effect was found to be relatively more pronounced in the lower part of the liquid pool (Fig.3.10).
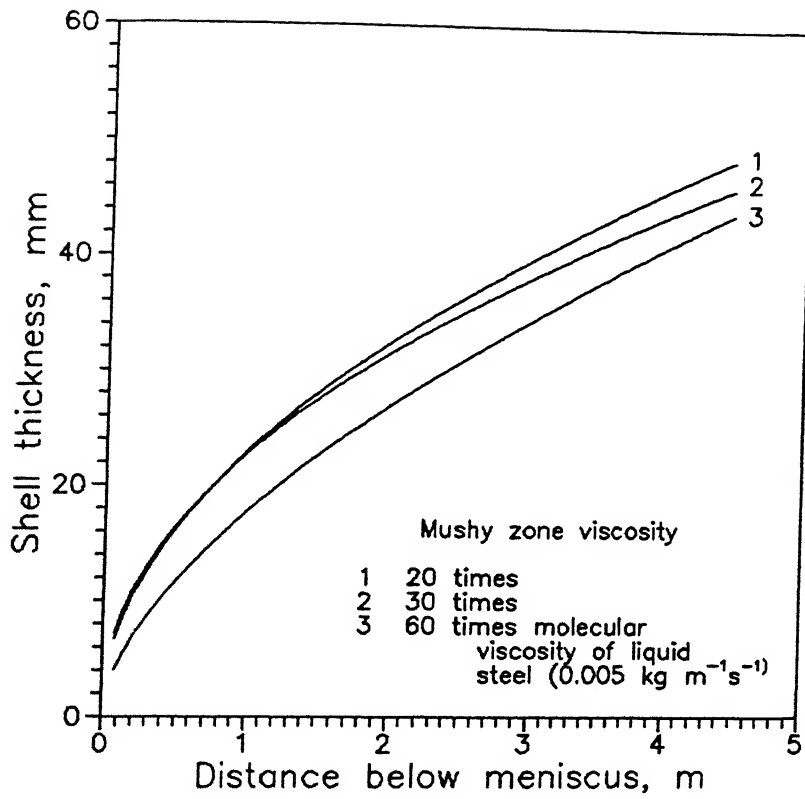
Fig. 3.10: Influence of mushy zone viscosity value on the predicted shell profile.

3.5.4 Influence of Thermal Buoyancy Force on the Computed Results

In the previous theoretical studies[11,12,37] on fluid flow, the influence of thermal buoyancy force has not been taken into account, although buoyancy at the first sight appears to be one of the principal driving forces for liquid steel flow, particularly, in the relatively stagnant lower pool region. In the present study, an attempt has been made to quantify the influence of buoyancy on the numerical predictions by incorporating a buoyancy force term (e.g. $-\rho_o g\beta(T-T_o)$) into the axial direction momentum equation (Eqs.(3.2) and (3.3)).

The value of the coefficient of volumetric expansion (β), embodied in the expression of buoyancy, is not readily available for liquid steel in the literature[54,55]. Therefore, an estimated[54] value of $\beta = 0.001\ ^0C^{-1}$ was used in all numerical computations to deduce the buoyancy force originating from temperature gradients in the liquid pool. To assess the sensitivity of β (the value of which as applied to the present investigation has some uncertainty) and hence the thermal buoyancy on the computed results, few calculations with other possible values of β were also carried out. Influence of different values of coefficient of volumetric expansion on the estimated shell thickness is presented in Fig.3.11. The predicted shell profiles (Fig. 3.11) revealed that the buoyancy induced natural convection in the liquid pool has practically negligible influence on the overall heat transfer and solidification phenomena in CC.
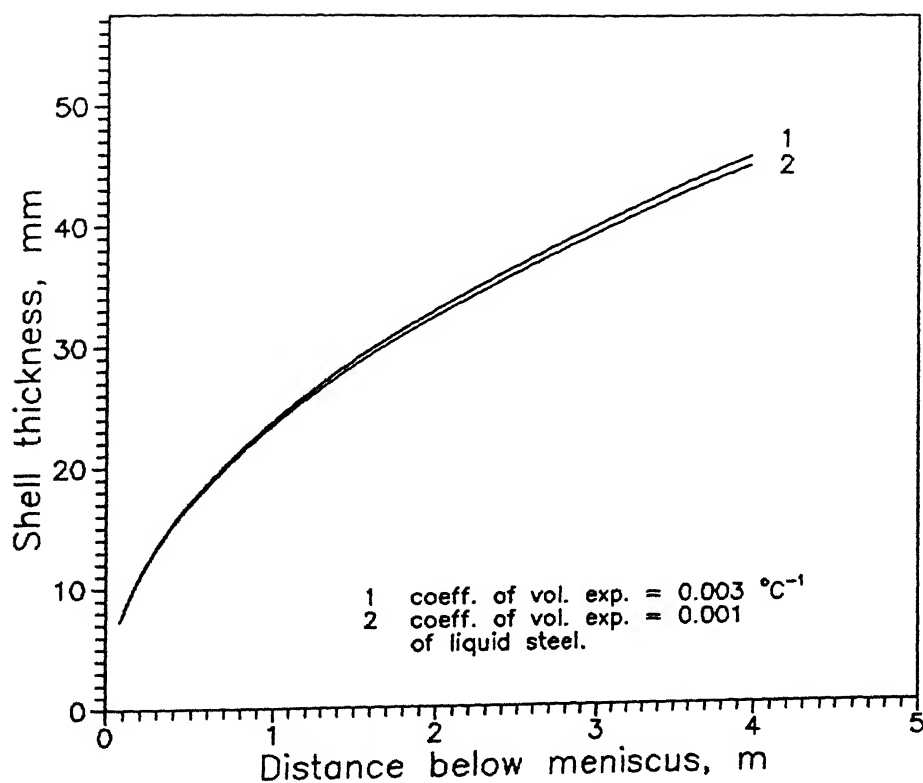
Fig. 3.11: Influence of thermal buoyancy force term in the axial direction momentum balance equation on the predicted shell profile.

3.5.5 Role of Prescribed Temperature vs. Insulated Surface, Out Side the Pouring Stream, as Meniscus Boundary Conditions

The objective of the present exercise was to evaluate the appropriateness of the above mentioned boundary conditions as applied to solve the governing heat flow equations and consequently, to investigate their resultant influence on the computed results. As illustrated already, in the first type of boundary condition, temperature inside the pouring stream was specified by prescribing the casting temperature (T_o), whereas, outside the pouring stream, the melt surface was assumed to be covered with an insulating slag layer and consequently, the normal gradient of temperature (i.e. the heat flux) was assumed to be zero. In the other type of boundary condition, casting temperature was prescribed throughout the entrance boundary (e.g. on the meniscus, from the line of symmetry to mould wall). The influence of these two types of boundary conditions on the computed results are illustrated in Fig.(3.12) where the variation of shell thickness with distance below meniscus is presented. There, it is at once evident that both type of free surface boundary conditions produce practically identical results. This clearly suggests that either of the boundary conditions can be applied to the governing heat flow equation for estimating temperature fields and the resultant solid shell profiles in CC billets. These obviously correspond to situations in which there is minimal or no submergence of the inlet nozzle below the meniscus.
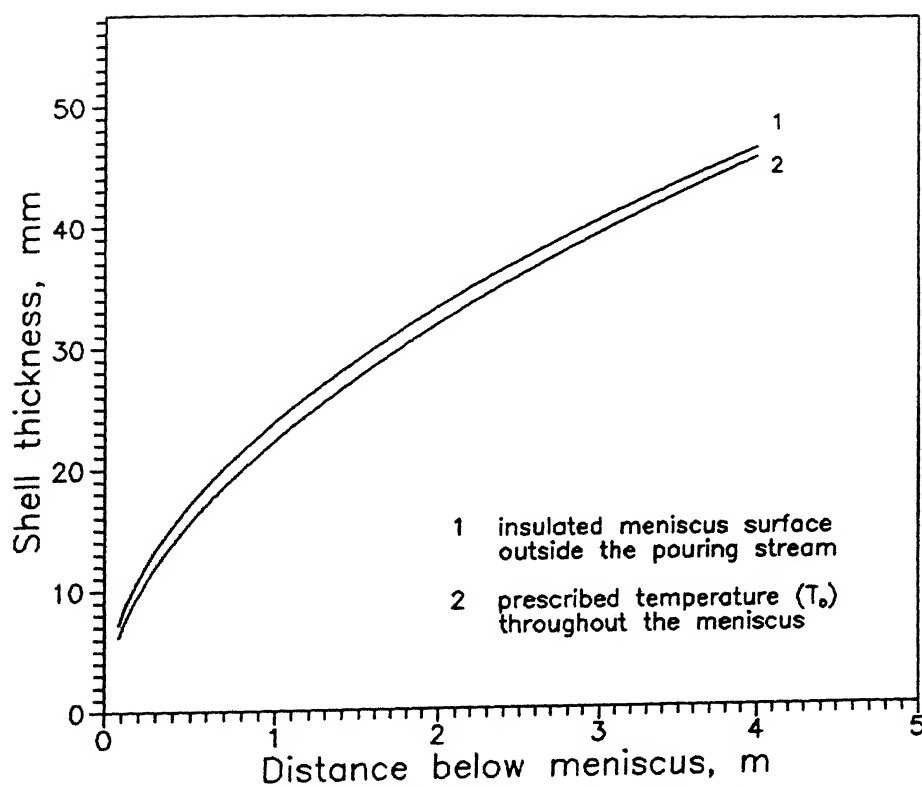
Fig. 3.12: Influence of two different types of meniscus boundary conditions (applied to the temperature equation) on the predicted shell profile.

3.5.6   Predicted Flow Field Within the Liquid Pool of Solidifying Castings

Theoretical studies[11,36] as well as high temperature experimental study[23,24] on flow field in the liquid pool of CC have revealed that the liquid pool can be divided into two principal regions; an upper region in which turbulent recirculatory flow is essentially induced by the momentum of the incoming pouring stream, and a lower region in which the liquid is relatively stagnant with natural convection and solidification shrinkage providing the main driving force for liquid steel flow. Radio active tracer measurements[23] on a typical billet caster have appeared to suggest that the flow was predominant (i.e. the well mixed) only in the upper pool region (i.e. up to a depth of about 3m), whereas, significant portion of the liquid pool was relatively stagnant. Similarly, water model study also appears to indicate[36] that the depth to which the upper well mixed region extends below the meniscus depends on the nozzle type, pouring rate and section size. In billet casting, with straight-bore nozzles, maximum penetration depth has been reported to be around 4 to 6 times the mould width[36]. Furthermore, with straight-bore nozzles, the flow of liquid steel is downward in the center of the billet due to the action of the input stream and upward (i.e. reverse flow) near the solidification front[11,34]. On the other hand, the flow pattern in the mould with a submerged multi-hole nozzle consists of two distinct recirculating loops for each hole; one stream flowing upward (rotating clockwise) towards the meniscus while, the other flowing downward (rotating anti clockwise). In general, with radial flow multi-hole nozzles,
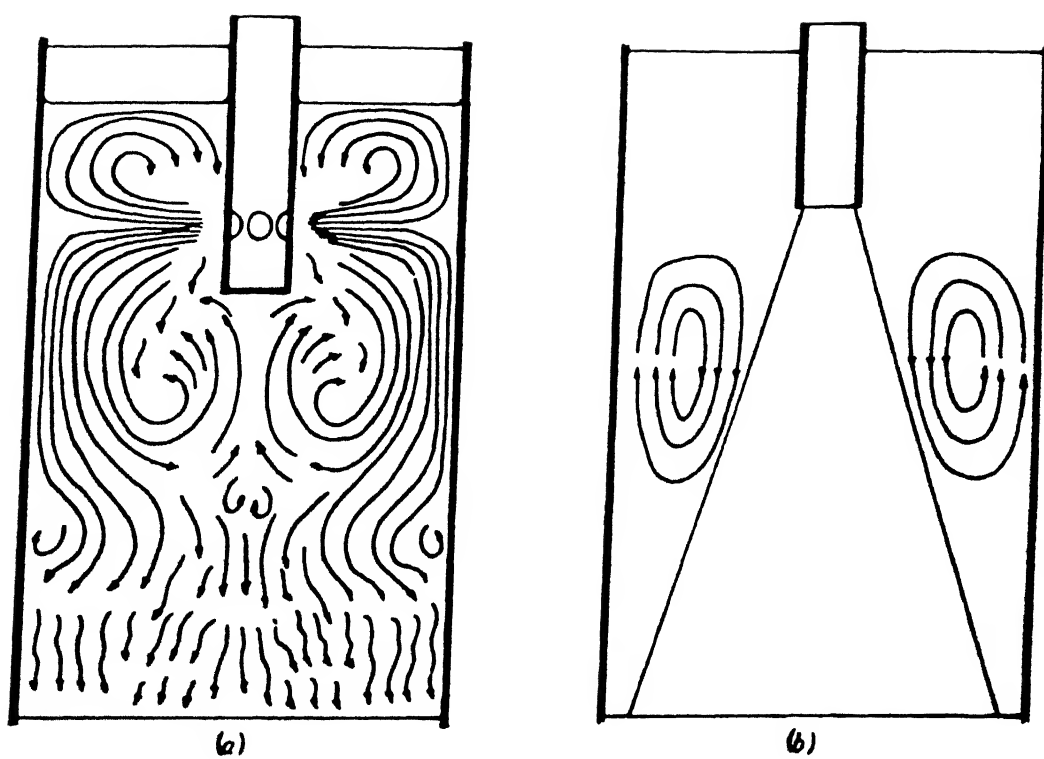
Fig. 3.13: Schematic representation of the flow field with (a) radial flow nozzle and (b) straight bore nozzle.

the upper region of good mixing becomes much smaller. Consequently, details of flow can be expected to be intricately related to the nozzle configurations applied to the CC operation. Schematic representation[36] of flow fields with radial flow nozzle and straight-bore nozzle are shown in Fig.3.13.

In the present study, flow fields have been computed for straight nozzle with no submergence. This in principle corresponds to open stream casting. Relevant numerical data for computations are presented in Tables 3.1 and 3.2. Computed velocity fields at the central vertical plane in round and square billets casters are presented in Figs. 3.14 through 3.16. There, for the sake of clarity only a portion of the central vertical plane is shown. These illustrate that the flow is predominantly in the axial (downward) direction in the central core of the billet section, whereas, the flow is directed vertically upward (reverse flow region) adjacent to the solidification front. However, very close to the solidification front flow is almost insignificant. Furthermore, recirculation zone is seen only in the upper pool region only. It was found to confined only up to 1 to 1.4 m pool depth. Beyond 3 m pool depth flow was almost insignificant. In the absence of any detailed earlier equivalent study no extensive comparison can be drawn with the present set of computed results, although the general nature of the computed velocity field appears to be consistent with those reported in literature[12,35,36].

Inlet Velocity = 1.05 (m/sec)
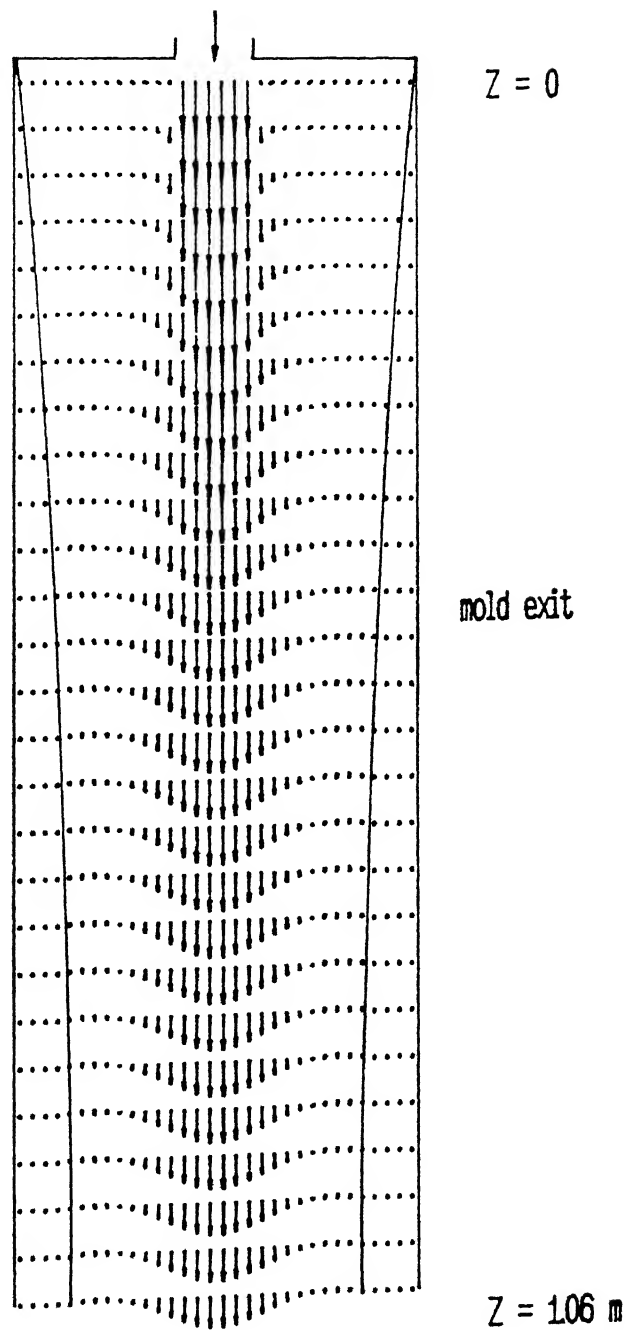
Fig. 3.14: Computed two dimensional flow field in a typical round billet[33] (data set 3, Table 3.1).

Inlet Velocity = 1.014 (m/sec)

Z = 0

mold exit

Z = 1.325 m
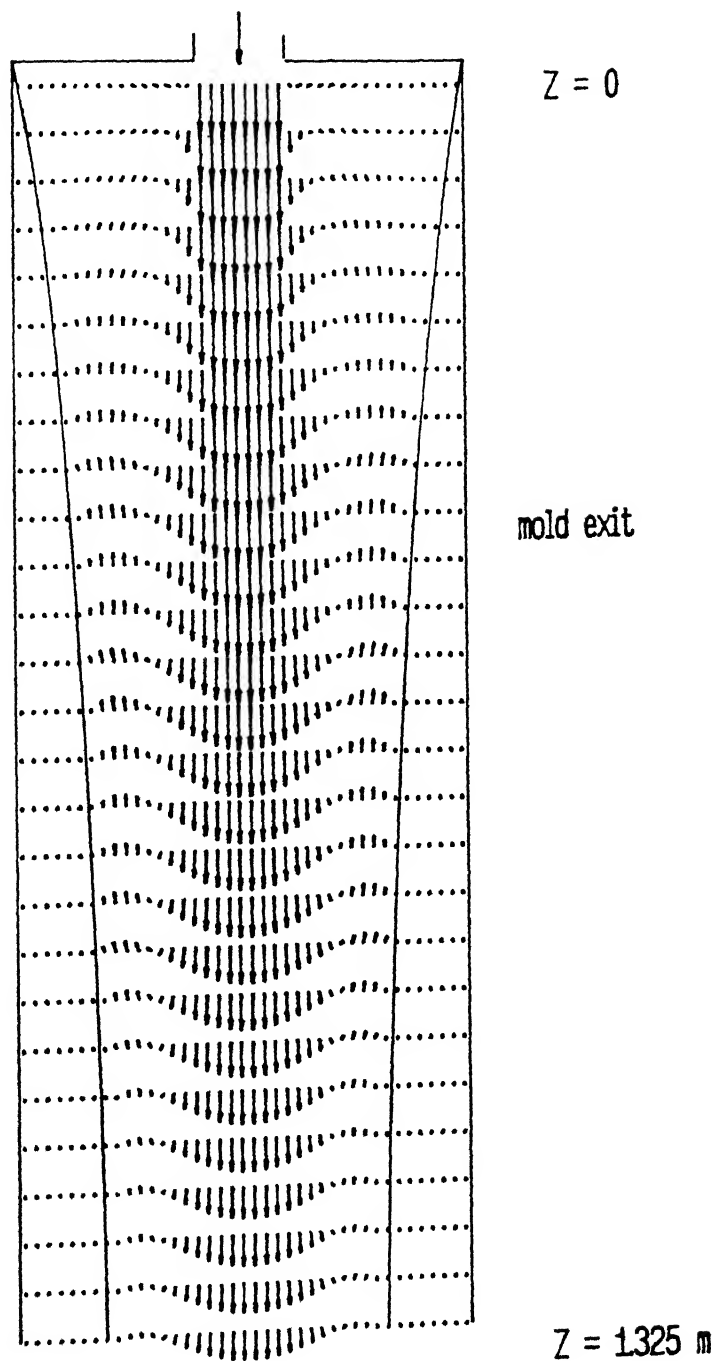
Fig. 3.15: Computed flow field in the central vertical plane of a typical square billet[22] (data set 1, Table 3.1).

Inlet Velocity = 1.585 (m/sec)

Z = 0

mold exit

Z = 1325 m
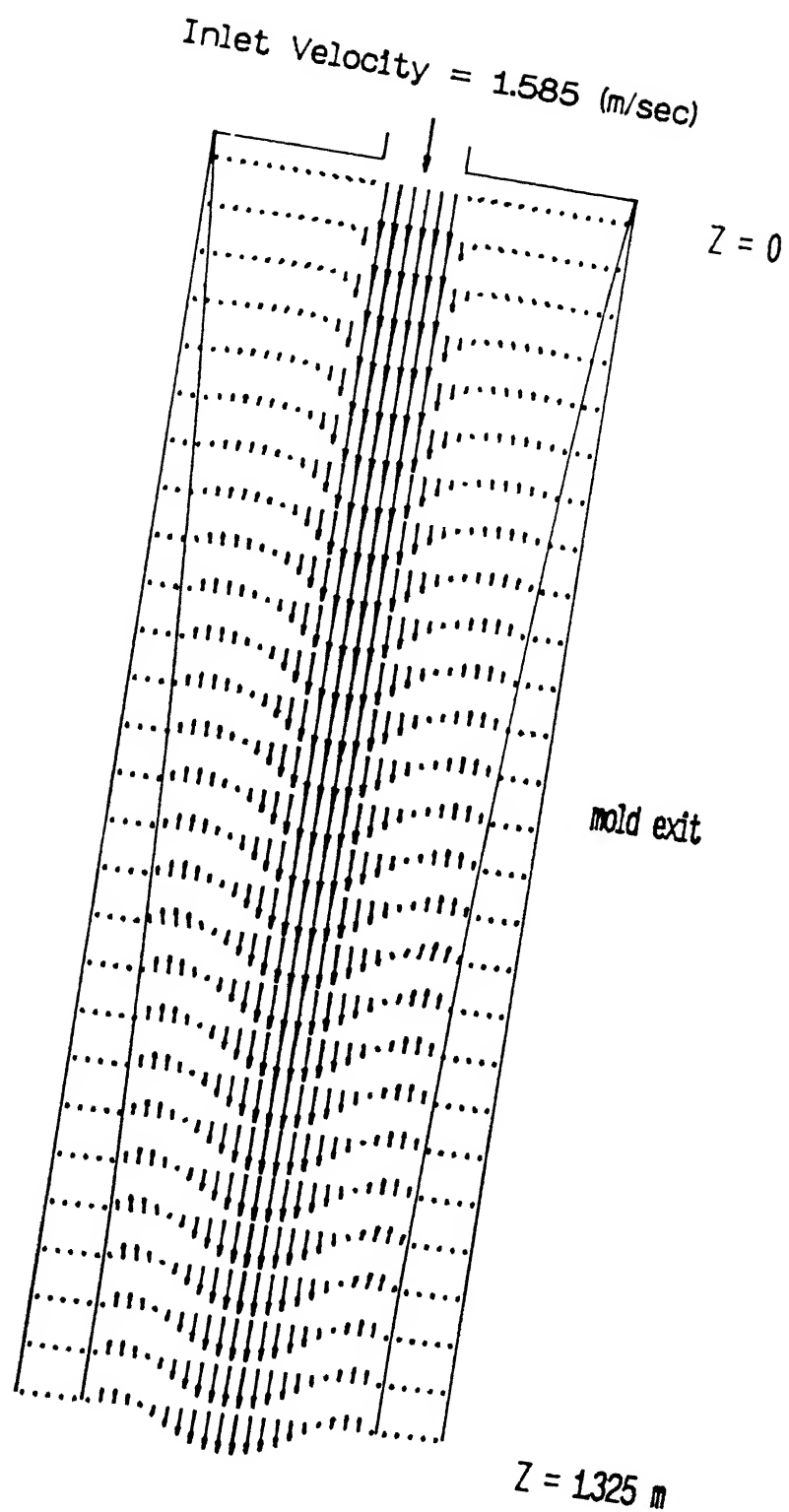
Fig. 3.16: Computed flow field in the central vertical plane of a typical square billet[22](data set 2, Table 3.1).

3.5.7   Comparison of Numerical Predictions with Reported Experimental Measurements

Solidified shell profiles for various casters (viz., Table 3.1) were derived from the corresponding predicted temperature fields (see the flow diagram of the computer program). As shown in Fig.3.17, the predicted shell thickness revealed a discontinuous growth of shell along the casting direction. This discontinuity in shell growth may be attributed to the thermal instability prevalent at the solidification front leading to uneven growth of shell during the casting process. It is also not unlikely that such a behaviour to some extent may also be due to relatively coarse grid (spacing 40-50 mm) applied in the axial (Z) direction in the numerical computations. To assess these, attempts were made to refine the grid configurations. This however, had only limited success from the view point of convergence, because of the reasons enumerated already. Thus, calculations were carried out with an optimum grid configuration and relaxation parameters, derived by trial and error, for each individual casting configuration (Table 3.1)

Fig. 3.17 shows computed shell thickness as function of distance below meniscus for a round billet[33]. Since computed data points exhibit some scatter, it was decided to smoothen the curve by regression analysis. The resulting best fit curve was employed for subsequent discussions.

Figures.3.18 through 3.20 present comparison between the predicted shell thickness and corresponding experimental measurements reported in literature[22,33]. Reasonably good agreement all along the pool depth, in all the three types of
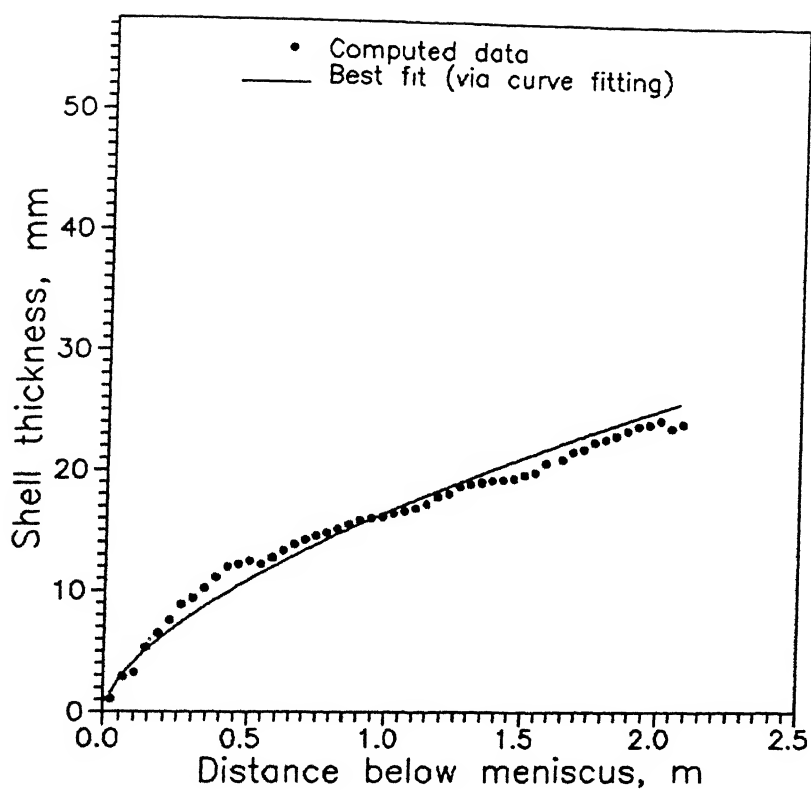
Fig. 3.17: Comparison between the computed shell thickness and the corresponding best fit curve for a typical round billet[33] (data set 3, Table 3.1).
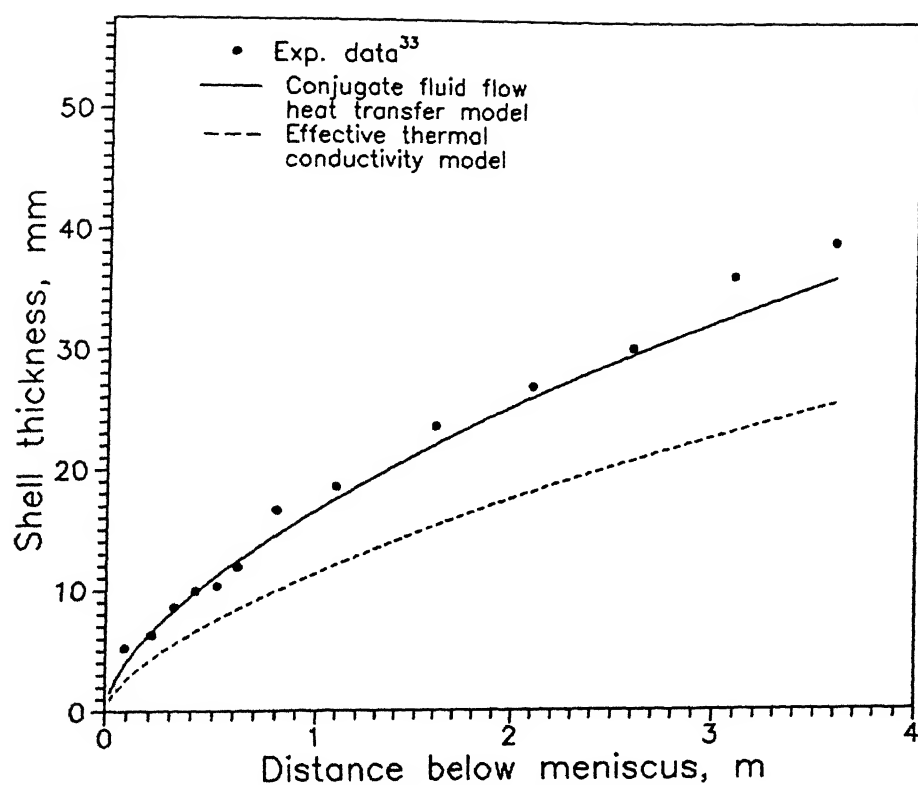
Fig. 3.18: Comparison between the present estimates of
the shell thickness and the corresponding
experimental measuremant of a typical round
billet caster[33] (conditions as in ref.11)
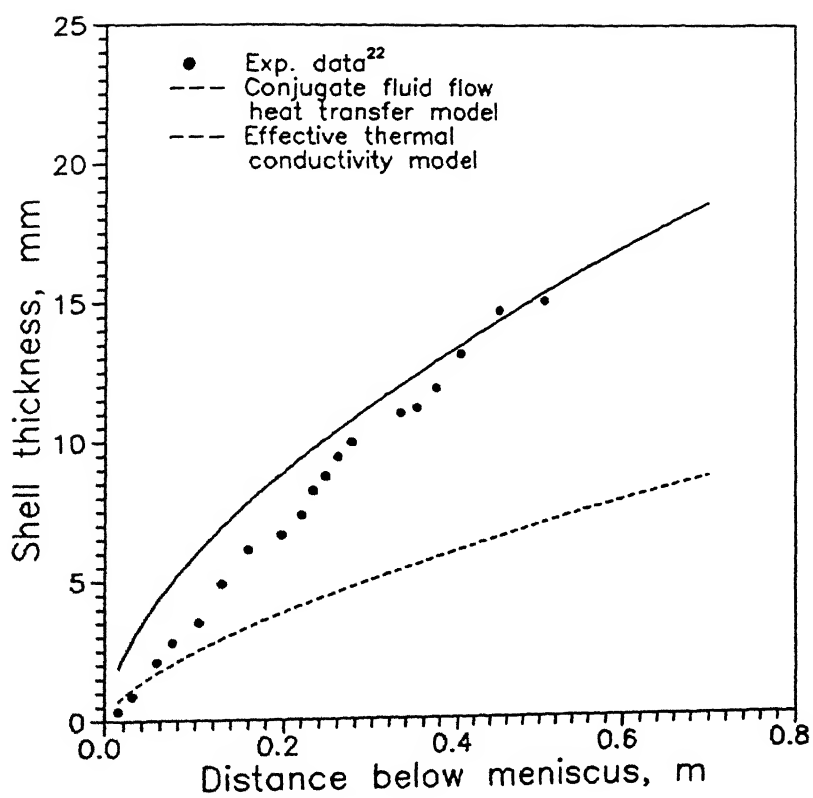
Fig.3.19: Comparison between the present estimates of the shell profile and the corresponding experimental measurement of a typical square billet caster[22]. (data set 1, Table 3.1)
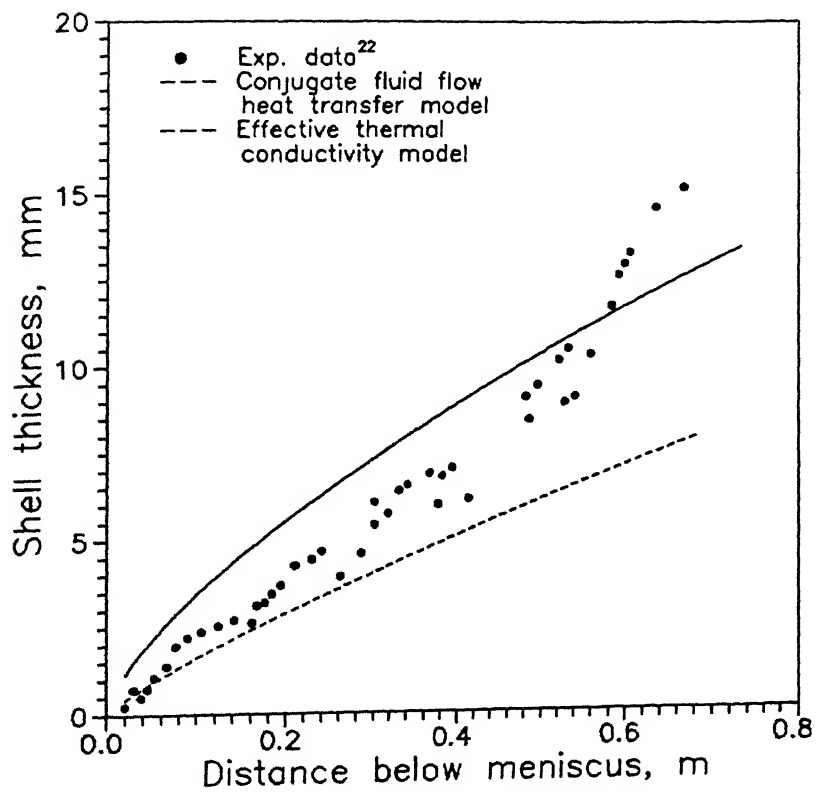
Fig. 3.20: Comparison between the present estimates of the shell profile and the corresponding experimental measurement of a typical square billet caster[22] (data set 2, Table 3.1).

casters considered is readily evident. Furthermore, for the sake of comparison, the corresponding predictions derived via artificial effective thermal conductivity based model (viz., Chapter 2) are also incorporated in Figs. 3.18 through 3.20. It may be noted that this latter model did not agree well with experimental data. This was already pointed out in Chapter 2, Sec. 2.5.7. Such comparisons readily demonstrate the superiority of the conjugate fluid flow heat transfer model over the artificial effective thermal conductivity model as applied to the analysis of heat flow phenomena during continuous casting of steel.

To illustrate the variations in results as shown in Figs. 3.18 through 3.20, predicted temperature profiles at identical axial locations by the two theoretical modelling approaches (viz., the artificial effective thermal conductivity model and the conjugate fluid flow and heat transfer model) are shown in Fig.3.21. It may be noted that the conjugate fluid flow and heat transfer model predicts nearly uniform temperature field within the liquid core, whereas, substantial temperature gradients exist in the mushy zone as well as in the solidified shell. Similarly, predictions derived via the artificial effective thermal conductivity model shows similar temperature distribution particularly in the central pool region, which is the natural outcome of assuming, a high value of thermal conductivity in the liquid region.

Nevertheless, a comparison between the two sets of predictions clearly indicate that energy transport from the liquid to the solid are considerably different for the two set of
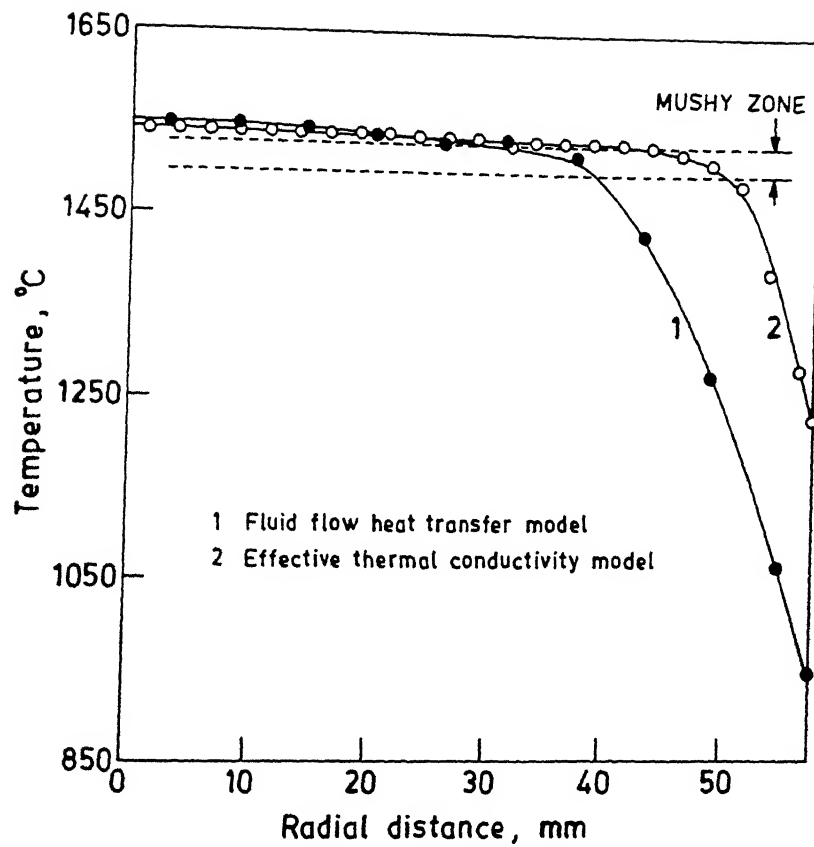
Fig. 3.21. Comparison between the temperature profiles
predicted by conjugate fluid flow heat transfer
model and effective thermal conductivity model
at the mould exit of a round billet caster.

predictions and this in turn appear to suggest that although a large thermal conductivity assigned to the liquid region leads to expected thermal gradients in the pool region nonetheless, cannot simulate the actual energy transport in the entire domain. Consequently, for investigating thermal phenomena of relevance to continuous casting, a mathematical model such as the one based on the concept of artificial effective thermal conductivity appears to be rather too simplistic and hence, a more sophisticated approach such as the one considered in the present study (viz., conjugate heat-fluid flow model) will be more appropriate.

Finally, in spite of the two dimensional nature of the model and several approximations involved in developing the model, it is evident from the predicted results and their subsequent comparison with the reported industrial measurements, that the computational procedure developed in the present study can be conveniently applied to the analysis of various thermal phenomena in industrial continuous casters.

It may be added here that some macrostructural and macrosegregation measurements, reported in chapter 4, were correlated successfully with predictions based on the model. It has been discussed fully in Sec. 4.5. This is taken as another confirmation of the reliability of the conjugate fluid flow-heat transfer model. It has also been proposed that this model may also be employed to predict equiaxial zone size in a CC billet.

3.6 SUMMARY AND CONCLUSIONS

In the present study a steady state, two dimensional (for the phenomena occurring at the mid face and on the central vertical plane) mathematical model based on the concept of conjugate fluid flow and heat transfer has been developed for continuous casting of steel. Two dimensional turbulent Navier Stokes equation has been considered for the simulation of fluid flow in the liquid pool and furthermore, a thermal buoyancy force term has been incorporated in the axial direction momentum balance equation to take into account the natural convection phenomena taking place in the liquid pool of the solidifying casting. The turbulence properties in the system was estimated via the Pun - Spalding formula, based on which the average effective viscosity was computed. Similarly, in the mushy zone, resistance to the flow produced by the solid matrix has been taken into account by increasing the viscosity to 20 times the molecular viscosity of liquid steel. In conjunction with these considerations, appropriate energy balance equation was considered, in which the latent heat of solidification was estimated from the solid fractions in the mushy zone assuming equilibrium solidification of steel.

The TEACH-T computer code, with considerable modifications, was used for the numerical solution of the governing fluid flow and heat transfer equations and thus, to deduce flow and thermal fields in continuously cast steel billets.

Prior to carrying out any comparison with experimental measurements, influence of various approximations applied to the mathematical model were analyzed computationally. Towards this,

the predicted shell thickness was found to be almost insensitive to the precise value of effective viscosity. This in turn revealed the exact modelling of turbulence in the pool is relatively less critical than has been originally anticipated. However, modelling of flow in the mushy zone was found to have some bearing on the predicted shell thickness, particularly in the lower pool region. Similarly, influence of buoyancy induced natural convection on the overall shell growth was found to be almost insignificant. In contrast, the buoyancy force was found to have significant influence on the nature of flow field within the liquid pool.

Velocity and temperature profiles were calculated for three different CC sections. The predicted velocity fields revealed that the flow of liquid steel in the pool was predominantly in the axial direction for most of the central regions, whereas, near the solidification front some reverse flow were seen. Furthermore, flow recirculation was found to be significant only in the upper pool region.

Comparison between predicted shell thickness and corresponding experimental measurements indicated reasonable agreement between the two. Similarly, comparison between the predictions of conjugate fluid flow and heat transfer model and those derived via the artificial effective thermal conductivity model demonstrated the superiority of the former over the latter. The present study has demonstrated that the conjugate fluid flow and heat transfer approach of modelling is relatively more accurate in simulating various relevant transport phenomena in continuous casting in comparison to an equivalent model based on

the concept of artificial effective thermal conductivity (viz.,
Chapter 2).

Table 3.1: Casting Conditions Considered for Numerical Simulation

Parameters	Data Set 1 [ref.22]	Data Set 2 [ref.22]	Data Set 3 [ref.33]
Cast geometry	square billet	square billet	round billet
Section size (m x m)	0.14	0.133	0.115
Pouring nozzle dia* (m)	0.025	0.025	0.02
Mould length (m)	0.51	0.685	0.5
Casting speed (m s^{-1})	0.0254	0.044	0.0317
Steel carbon (pct.)	0.1	0.1	0.1
Melt superheat* (^{o}C)	25	25	25
Solidus temp. (^{o}C)	1496	1496	1496
Liquidus temp. (^{o}C)	1529	1529	1529
Spray heat transfer coefficient (W m^{-2}C^{-1})	650*	650	1079.45**
Caster length simulated (m)	10	10	10

* - estimated
** - source ref. [11]

Table 3.2: Thermophysical properties of steel[*] used in the
numerical computations

Density of liquid steel	kg m^{-3}	7200.0
Viscosity of liquid steel	kg m^{-1} s^{-1}	5x10^{-3}
Coefficient of volumetric[†] expansion of liquid steel	^{0}C^{-1}	1x10^{-3}
Latent heat of solidification	J kg^{-1}	271954
Specific heat	J kg^{-1}C^{-1}	682.0
Thermal conductivity	W m^{-1}C^{-1}	34.60 & 15.89+0.011T

* - source: Ref.[54]

† - source: Estimated data Ref.[55]

CHAPTER 4

STUDY ON MORPHOLOGY AND MACROSEGREGATION IN CONTINUOUSLY CAST STEEL BILLETS

4.1 INTRODUCTION

Solidification of steel in continuous casting takes place with columnar and equiaxed dendritic structure. During solidification, segregation of solute elements (e.g. C,S,P, and Mn) occurs on both micro and macro scale[56-58]. Microsegregation results from freezing of solute enriched liquid in the interdendritic spaces. But it does not constitute a major quality problem. Mostly, the effects of microsegregation can be removed during subsequent soaking and hot working.

Macrosegregation, on the other hand, is nonuniformity of composition in the cast section on a larger scale. A high degree of positive segregation in the central region of a continuously cast section is commonly observed. Figure 4.1 presents one such typical carbon segregation pattern in a continuously cast slab[59]. It is established that macrosegregation occurs due to movement of solid and liquid phases in the mushy zone during final stages of solidification. The problem of axial or centreline segregation has been found to be more serious, particularly in high carbon steels cast at high speed and/or high tundish superheat[60]. Macrosegregation of solute elements, especially carbon, along the central axis of the cast section results in inconsistent transformation products (e.g., martensite, bainite) during
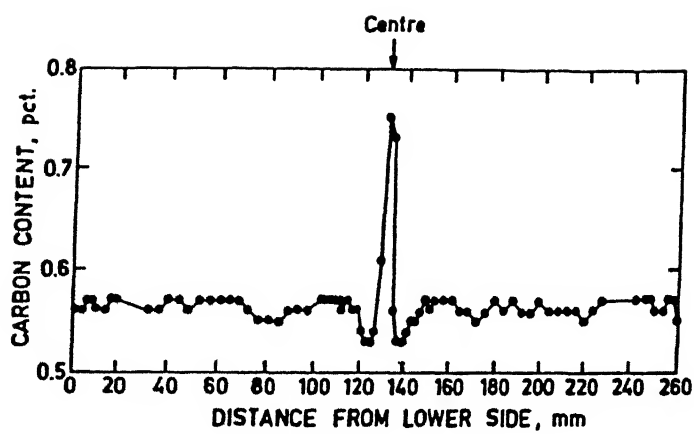
Fig. 4.1: Typical concentration profile as observed in continuously cast slabs[59].

subsequent hot working, and causes nonuniformity in mechanical properties of the finished product. Also, centreline segregation is known to be the prime source of sub-surface cracks and porosity in continuously cast products.

In longitudinal sections, the macrosegregation usually appears as regular V-shaped lines or bands. Also, the segregation profile is not smooth but is marked by random oscillations. In the recent years, there has been a growing concern for another type of segregation called 'semi-macrosegregation' or 'spot' segregation[61-63]. The spots are solute enriched regions of sizes larger than 100 microns and are in between micro and macrosegregation in size. Semi-macrosegregation spots are known to be the main source of hydrogen induced cracking in steels resistant to sour gas.

4.2 LITERATURE REVIEW

Macrosegregation in continuous casting of steels, especially the centreline segregation, has been reviewed in literature from time to time[56-58]. Hence, in this review, some of the features would be dealt with only in brief for the sake of completeness. Special emphasis would, however, be given on recent trends and developments as well as some features which are important, but have not been adequately covered before.

Segregation during solidification of alloys originates from the difference in solubility of solute elements between solid and liquid phases. Solubility of a solute in the solid state is lower as compared to that in the liquid state. As a result, solute atoms are continuously rejected by the solidifying dendrites

leading to constant enrichment of liquid at the solidification front with progress of solidification. Therefore, the liquid that solidifies in the final stage may contain significantly higher solute concentration than its original composition, and on solidification gives regions of high positive segregation. Rejection of solute by the solid and gradual enrichment of the former in the liquid at the solidification front has been termed as 'zone refining action'[56-58,64] since this phenomenon is utilized in zone refining of metals.

Redistribution of a solute element between solid and liquid phases during solidification under equilibrium conditions is given by the value of its equilibrium partition or distribution coefficient (k_0), defined as :

$$k_0 = \frac{C_S}{C_L} \qquad \qquad ...(4.1)$$

where C_S is the concentration of a solute in the solid in equilibrium with that in the liquid. The equilibrium partition coefficient is an important parameter for judging the segregation tendencies of solute elements in a given alloy system. The equilibrium partition coefficients are mostly less than 1. Table 4.1 presents some value of k_0 for Fe-binaries.

Under the condition of complete mixing in the liquid phase and no solid state diffusion of solute, the following solute redistribution equation, which is the well known Scheil's equation[57,64,65], is obtained.

$$C_L = C_0 (1 - f_s)^{k_0 - 1} \qquad \qquad ...(4.2)$$

where C_0 is the initial concentration of the solute in the liquid at the beginning of solidification, C_L is concentration in liquid during progress of solidification at fraction of solid, f_s. However, during real solidification, complete mixing in the liquid is hardly achieved. Also, there is always some amount of solid state diffusion. Moreover, Scheil's equation fails as solid fraction approaches 1 (i.e. complete solidification), since C_L approaches infinity[64,65].

Table 4.1:   Values of k_0 for solidification of iron[2,10]

Element	Solid phase	
	δ-Fe	γ-Fe
Al	0.92	–
C	0.24	0.36
Cr	0.95	0.85
H	0.32	0.45
Mn	0.84	0.95
Mo	0.80	0.60
Ni	0.80	0.95
N	0.28	0.54
O	0.02	0.02
P	0.13	0.06
Si	0.66	0.50
S	0.02	0.014
Ti	0.14	0.07
V	0.90	–

In spite of these limitations, Scheil's equation has been applied with limited success, in the analysis of micro and semi-macrosegregation during continuous casting[62,66]. In subsequent studies, Scheil's equation has been modified by Broady

and Flemings[67], and also by Clyne and Kurtz[68], who took into account the solid state diffusion in their model. However, the Clyne-Kurtz equation has been found to be more reliable for modelling microsegregation in continuously cast slab[66].

The zone refining action, mentioned above, which leads to continuous enrichment of liquid with progressive solidification can also be described by the Burton's equation[64,69], presented below. In derivation of this equation, incomplete mixing in the liquid phase has been considered in contrast to Eq.(4.2).

$$C_L = C_0 (1 - f_s)^{k_{eff}-1} \qquad \qquad \ldots (4.3)$$

in which, k_{eff} is effective partition coefficient defined by Burton et al[69] as follows :

$$k_{eff} = \frac{k_0}{k_0 + (1 - k_0) \exp(- R/k_m)} \qquad \ldots (4.4)$$

where, k_m is mass transfer coefficient, and takes into account the influence of bulk convection on segregation. R is the linear growth rate of the solidification front. k_{eff} is an important parameter for describing segregation during real solidification processes. Eqs.(4.3) and (4.4) predict that the degree of segregation increases with decreasing growth rate (R) and increasing k_m, which again increases with increasing intensity of bulk liquid flow. Under conditions of low R or high k_m, k_{eff} approaches k_0, and Eq.(4.3) reduces to Scheil's equation (i.e. Eq.(4.2)). At the other limit (i.e. high R and/or low k_m), k_{eff} approaches 1, and the steady state situation, where $C_s = C_L$ (i.e. no segregation) is obtained. Equation of Burton et al has been

found to be quite successful in modelling axial segregation resulting from turbulent convection in plane front growth[65]. However, this equation is more appropriate for microsegregation and semi-macrosegregation in ingots and continuous casting[70]. It is not possible to predict centreline macrosegregation from this equation alone, since macrosegregation is caused by microsegregation as well as large scale movement of segregated liquid and solid phases during solidification.

There are several causes leading to movement or transport of segregated liquid in the mushy zone[71,73]. These are suction due to solidification shrinkage, change in density of liquid due to composition change, natural and forced convection in the liquid pool, turbulent diffusion, movement of liquid and solid phases due to bulging. Settling of free crystals of steel, besides causing negative segregation, also induces flow in the bottom region of liquid pool[71]. Flemings et al[71,72] carried out theoretical analysis of macrosegregation in ingots resulting from flow in interdendritic channels of the mushy zone due to solidification shrinkage only. Solid state diffusion and other causes of flow were ignored. They considered the mushy zone as a porous medium and applied Darcy's law[73] to evaluate the flow through complex interdendritic channels, as follows:

$$v = \frac{\lambda}{\mu \, \gamma_L} \left(\nabla P + \rho_L g \right) \qquad \qquad \ldots (4.5)$$

in which, ∇P is pressure gradient in the mushy zone, g is acceleration due to gravity, ρ_L is density of liquid, and γ_L is volume fraction of liquid estimated by the following correlation:

$$\gamma_L = \frac{(1-f_s)/\rho_L}{f_s\rho_s + (1-f_s)\rho_L} \qquad \ldots(4.6)$$

λ in Eq.(4.5) is the permeability of the mushy zone, which has been assumed to be a function of γ_L and dendrite arm spacing (d_λ) as:

$$\lambda = d_\lambda \, \gamma_L^2 \qquad \ldots(4.7)$$

Finally, the investigators[71,72] proposed the following local solute redistribution equation for calculation of macrosegregation resulting from transport of solute-enriched liquid to feed the solidification shrinkage and thermal contraction.

$$\frac{\partial \gamma_L}{\partial C_L} = -\frac{1-\beta}{1-k_0}\left(1 + v\,\frac{\nabla T}{\varepsilon_0}\right)\frac{\gamma_L}{C_L} \qquad \ldots(4.8)$$

where, ∇T is temperature gradient, ε_0 is rate of temperature change, and β is volumetric solidification shrinkage, defined as:

$$\beta = \frac{\rho_s - \rho_L}{\rho_s} \qquad \ldots(4.9)$$

Flemings et al[72] calculated segregation profile of copper in Al-4.5 pct. Cu alloy ingot, and obtained reasonable agreement between their theoretical prediction and experimental data. The investigators, however, considered segregation due to interdendritic flow only, and influence of bulk flow was completely ignored.

Under steady state solidification with planar front moving with velocity R in X-direction Eq.(4.8) becomes[71,74]:

$$\frac{\partial \gamma_L}{\partial C_L} = - \frac{1-\beta}{1-k_0} \left(1 + \frac{v_x}{R} \right) \frac{\gamma_L}{C_L} \qquad \ldots (4.10)$$

where v_x is fluid velocity in a direction perpendicular to the solidification front. Eq.(4.10) reduces to the Scheil's equation when v_x and β both are equal to zero. In general, Eq.(4.10) can be integrated to the following form[74]:

$$\frac{C_L}{C_0} = (1-f_s)^{[(k_0-1)/\xi]} \qquad \ldots (4.11)$$

in which a parameter ξ has been introduced that takes into account the influence of fluid flow on macrosegregation during solidification[74].

Equation (4.11) has been termed as 'modified Scheil's equation' in the present investigation. For $\xi=1$, Eq.(4.11) becomes identical to the Scheil's equation (Eq.(4.2)). For $\xi > 1$, C_L becomes lower than the value calculated by Eq.(4.2), which indicates that negative segregation may occur. In the case of $0 < \xi < 1$ positive macrosegregation occurs. As mentioned already, complete mixing is practically not encountered during real solidification process. Therefore, the modified Scheil's equation is more realistic segregation model than the original Scheil's equation.

In a subsequent study, Ridder et al[75] considered the interaction between interdendritic flow and fluid flow in the liquid pool ahead of the liquidus isotherm in their macrosegregation model. Using experimentally determined temperature data on Sn-Pb alloys, it was reported that fluid flow

in the liquid pool, due to natural convection, had little effect on interdendritic fluid flow and the resulting macrosegregation. The investigators recommended their model for study of macrosegregation in continuous casting and electro-slag remelting. Besides the above-mentioned models, several other models have been reported. A good review on this subject is available[65].

In connection with centreline segregation in continuous casting of steel, Miyazawa and Schwerdtfeger[59] were the pioneers to model macrosegregation due to bulging. Miyazawa et al[59] obtained a reasonable agreement between theoretical predictions and experimental measurements. The investigators found bulging to be the main cause of centreline segregation in continuously cast slab. It was subsequently confirmed by other investigators. Role of bulging is well established.

In addition to the theoretical models, semi-empirical models of macrosegregation have also been proposed[74,76]. Takahashi et al[76] have proposed a semi-empirical model of macrosegregation for steel ingots. It is based upon the fact that bulk liquid flow affects morphology and segregation during solidification. Bulk liquid was assumed to penetrate the mushy zone of columnar region and sweep out the solute-enriched interdendritic liquid resulting in a negative segregation. This was called 'washing effect', and was thought to be the principal mechanism for the formation of 'white band', commonly observed in continuous casting with electromagnetic stirring (EMS)[74,76]. If the segregation level of bulk liquid is higher than that in the interdendritic liquid, the washing effect may lead to higher segregation. On the basis of

concept of washing effect, Takahashi et al[76] proposed the following correlation for the effective partition coefficient.

$$k_{eff} = 1 - B \frac{d_\lambda}{L} (1-k_0) (1-f_{sh}) \frac{v}{R} \qquad \ldots(4.12)$$

in which, B is an experimental constant, d_λ is primary dendrite arm spacing, L is thickness of solidifying zone (mushy zone), f_{sh} is the maximum solid fraction below which the washing effect acts, and v is velocity of liquid.

Takahashi et al[76] also carried out experiments with molten steel in the laboratory. Freezing was done on a water-cooled pipe rotating at known and variable RPM. On the basis of the results, they evaluated the constants and proposed the following correlation :

$$k_{eff} = 1 - 1.33 \times 10^{-4} (1 - k_0) (1 - f_{sh}) \frac{v}{R} \qquad \ldots(4.13)$$

Typical value of $f_{sh} = 0.67$, has been reported by the investigators[76]. As evident from Eq.(4.13), with decreasing growth rate (R), k_{eff} decreases and consequently extent of segregation increases. Takahashi et al obtained a reasonable correlation between their model predictions and experimental measurements. Eq.(4.13) was semi-empirically derived on the basis of controlled laboratory experiments. However, its application to continuous casting has been recommended by the investigators[74,76].

4.2.1   Influence of Morphology of Cast Structure on Macrosegregation

In general, segregation is closely related to morphology of the cast structure[56,64,74]. Any parameter that influences morphology will also influence the macrosegregation pattern. Structure of plain carbon continuously cast steel section has three zones, viz., chill zone, columnar zone, and equiaxed zone. Figure 4.2 presents a typical macrograph of CC billet. Growth of columnar crystals occurs due to constitutional supercooling associated with the rejection of solute at the solidification front leading to constant enrichment of residual liquid. Considerable information is available in literature[56,64,74] on theory of columnar-to-equiaxed transition. Studies are mostly with reference to ingot casting, sometimes unidirectionally solidified. Hence their applicability to continuous casting is to be always kept in mind. Some findings are applicable, some may not.

It has been generally accepted in the last two decades that equiaxed grains grow on seed crystals already floating in the melt[64,74]. Such crystals come either by detachment of crystals from chill zone or by remelting of dendrite tips and their consequent detachment in the columnar zone. Therefore, we are concerned with growth of crystals. Growth of equiaxed grains (as free dendrites) prevent further advance of columnar zone. Since columnar grains are also simultaneously growing, it is the competition between the growth rates of the two that governs columnar-to-equiaxed transition[74]. To what extent equiaxed grains should form prior to transition is being debated. However, some
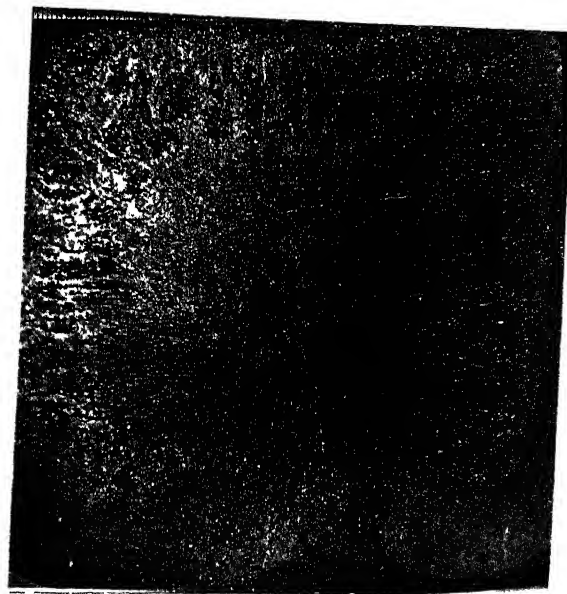
Fig. 4.2:   Macrostructure of a low carbon steel billet.

investigators have opinion that it requires reasonable quantity of equiaxed grains in order to bring in this transition.

Again equiaxed grains may be classified broadly into two types:

(i) *free crystals, randomly oriented*: these can move about; since they are purer and denser than the liquid they tend to settle downwards. Free crystals also are responsible for bands of negative segregation zones (V-shaped bands, white bands).

(ii) *equiaxed grains attached to columnar grains*: these would exhibit less random orientation.

The above discussions point out that the columnar-equiaxed transition may sometime be quite diffused depending upon the circumstances.

Formation of equiaxed crystals take place over wide region at a time. This tends to evenly distribute microsegregated region, and does not allow the zone refining action to aggravate. Therefore, a very effective method of minimization of axial segregation is to obtain a large equiaxed zone around the cast centre. This is a well-established fact, and hence does not require presentation of too many confirmatory evidences.

An equiaxed structure is preferred over columnar structure for other advantages such as easier mechanical working, prevention of internal cracks and centreline porosity. Hence a major objective in continuous casting of steel is to obtain as large an equiaxed zone as possible, and this is facilitated by[56,57,60]:

(i)   low superheat
(ii)   medium carbon steel
(iii)   electromagnetic stirring, particularly in-mould
(iv)   large section size.

4.2.2   Influence of Superheat

As stated earlier, the accepted mechanism is that growth of columnar zone stops when equiaxed zone starts forming. There always are innumerable tiny crystals (seed crystals) floating in the melt. When the superheat is dissipated these start growing thus forming equiaxed zone. Therefore, superheat should be as low as possible. It is also well established. A low tundish superheat has been found to enlarge the equiaxed zone and lower macrosegregation in the central region (Fig. 4.3).

Heat flow calculations, however, have revealed that during continuous casting the superheat is extracted almost completely in the mould and upper sprays[77]. Therefore, influence of superheat on columnar zone length has been attributed to the influence of superheat on the generation and survival of free crystals in the mould region, which, in turn, affect the cast structure many meters below the mould[78]. Consequently if the superheat is high most of the seed crystals remelt easily, and only a few of them survive and become available to bring about columnar-equiaxed transition in the lower pool region. Again, too low a casting temperature may result into nozzle clogging, difficulties of inclusion float-out, and poor surface quality of the casting. Thus, the casting temperature should be optimum.

4.2.3   Influence of Electromagnetic Stirring

Stirring helps in dissipation of heat of the liquid pool due to enhanced convective heat transfer, and helps in enlarging the equiaxed zone. This is the basis of
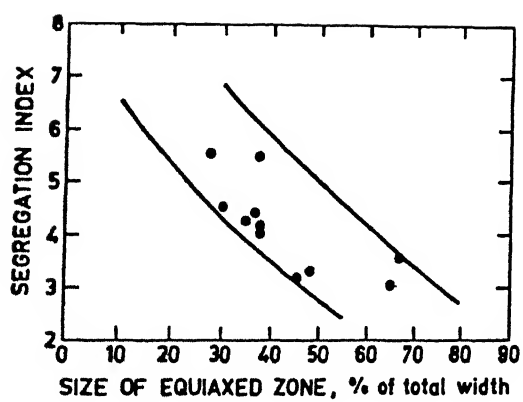
Fig. 4.3: Axial segregation index as a function of equiaxed zone size[57].

Electromagnetic stirring (EMS) in continuous casting which has been found to enhance equiaxed zone and cut down axial segregation.

It has been proposed that EMS also causes breaking and remelting of tips of columnar dendrites. Broken dendrite tips provide additional seed crystals for equiaxed zone to form (i.e. crystal multiplication process)[56]. The equiaxed structure formed due to EMS has been found to be finer than the one caused by low superheat and/or low speed casting[79]. Therefore, with EMS, a higher superheat can be tolerated in continuous casting without causing much harm to the internal quality of cast products due to centreline macrosegregation and centreline porosity.

However, it has been reported that high carbon steels exhibit some centreline segregation even with low superheat and/or EMS[56,60]. For these steel grades, combined in-mould EMS and EMS during the final stage of solidification (i.e. bottom region of pool) has been recommended[60,79]. Also, with EMS, a narrow band of negative segregation (white band) forms. Formation of white band has been attributed to the washing effect or sudden change in growth rate due to EMS[74,78]. Electromagnetic Stirring is more commonly applied to the slab caster as a measure to minimize the centreline segregation. For smaller cross-section (e.g. billets and blooms) it is less common. In the Western World use of EMS in billet casters[80] is limited to only 5 pct. There are also reports of some adverse effects of EMS, particularly in slabs. Agglomeration of inclusions and semi-macrosegregation have been reported to be aggravated in electromagnetically stirred slabs. Haida et al[63] found EMS to disperse the centreline

segregation into isolated semi-macrosegregation spots over a wider central region of a slab. Phosphorus segregation ratio as high as 1.7 in the semi-macrosegregation spots has been reported[63].

If section size is large then heat flux in the central region is low. Consequently there is less temperature gradient in the melt. This induces a large region to attain freezing temperature and hence larger equiaxed zone. So far as influence of carbon is concerned, it is well known that high carbon steels tend to produce a large columnar zone even with electromagnetic stirring. It is further aggravated by presence of alloying elements. It has been explained by the fact that with increase of carbon and also upon addition of some alloying elements (e.g. Cr), the freezing range (i.e. temperature difference between liquidus and solidus at fixed composition) increases. According to the theory of constitutional supercooling it helps growth of columnar zone.

From the above point of view a low carbon steel should exhibit largest equiaxed zone. It seems that is not borne by fact. The equiaxed zone is largest at medium carbon (0.3-0.4% C) and decreases as carbon content is lowered. The explanation for this is not clear cut. But it is claimed to be caused by transition from liquid$\rightarrow \gamma$-Fe to liquid$\rightarrow \delta$-Fe as the composition moves from medium carbon to low carbon steel.

4.2.4 Role of Peritectic Transformation

It has been observed that steels of chemical composition close to the peritectic point are prone to cracking

and have poor surface quality. This has been attributed to the $\delta \longrightarrow \gamma$ transformation[81] during solidification. Similarly, carbon content of steel has been found to have significant influence on the morphology of cast structure.

Mori et al[82] studied macrostructures in continuously cast steel billets. They found columnar zone length to increase in ascending order when carbon content of steel was changed from 0.3 pct. to 0.1 pct. to 0.6 pct. In other words, the columnar zone length was lowest at around 0.3 pct. carbon. In a subsequent study, Samarasekera et al[78], in spite of large scatter in data (Fig. 4.4(a)), reported minimum columnar zone length for CC billets containing 0.2 to 0.38 pct. carbon. This is almost similar to the findings of Mori et al[82]. For blooms, Miyahara et al[83] observed a sudden jump in columnar zone length at 0.42 pct. C. However, Irving et al[84] found a minimum equiaxed zone width at 0.3 pct. C which is in much contrast to that reported by Mori et al[82]. Again, Kitamura et al[85] have reported almost complete absence of equiaxed zone below 0.1 pct. C and above 0.45 pct. C for steel blooms. In spite of these somewhat differing claims by various investigators, there is a general agreement that equiaxed zone is maximum at the medium carbon range (0.3 - 0.4 pct.).

In addition to these, in a controlled laboratory experiment on iron carbon alloys and 8620 type steel ingots, Hurtuk and Tzavaras[86] measured mould heat flux, columnar zone length, and dendrite arm spacing. The investigators[86] also measured the values of $G/R^{1/2}$ (constitutional super cooling parameter) for each case. Their results indicated that, at 0.1 pct. C (lower limit of peritectic transformation: $\delta + L \longrightarrow \gamma$), the columnar
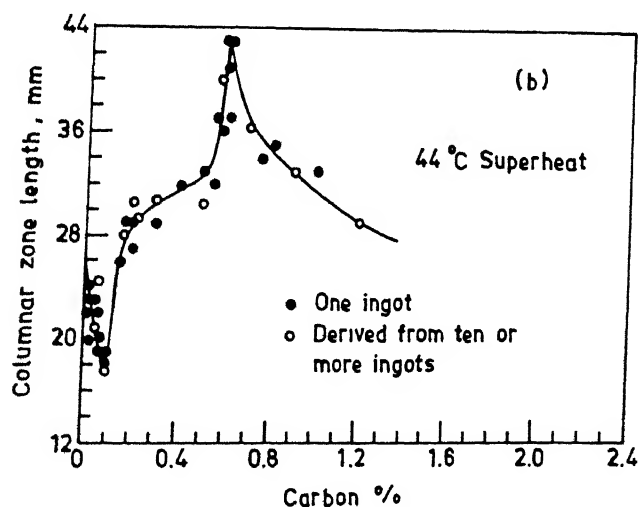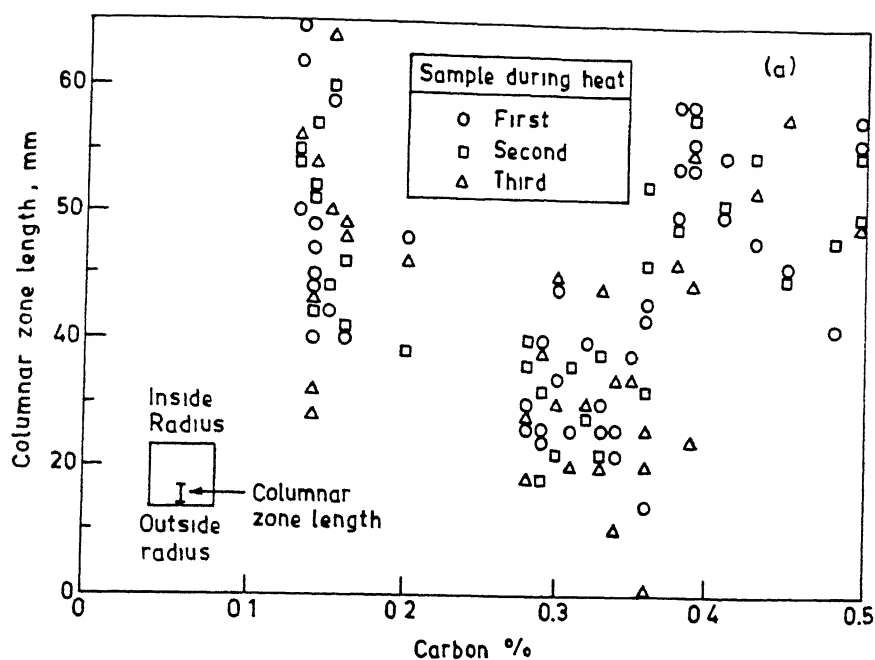
Fig 4.4 Influence of carbon content of steel on columnar zone
length (a) CC billets; Samarasekera et al.[78]
(b) 8620 steel ingots; Hurtuk and Tzavarus[86]

zone length, value of $G/R^{1/2}$, and mould heat flux were at their minimum, whereas, dendrite arm spacing was found to be maximum. Between 0.1 to 0.6 pct. carbon (approximately peritectic transformation range), columnar zone length, $G/R^{1/2}$, and mould heat flux were found to increase, and dendrite arm spacing found to decrease, with increasing carbon content. Close to the upper limit of peritectic transformation (0.6 pct. C), columnar zone length, $G/R^{1/2}$ and mould heat flux attained their maximum values. Variation of columnar zone length with carbon content in steel, as reported by Hurtuk and Tzavaras[86], is presented in Fig. 4.4(b). Since these are the data from controlled laboratory experiments, scatter was much less than in Fig. 4.4(a).

The investigators explained these by the $\delta \longrightarrow \gamma$ transformation associated with peritectic reaction. Hurtuk and Tzavaras[86] attempted to explain the influence of carbon content on the columnar zone length in terms of the influence of the former on the mold heat flux, as has been reported by Singh and Blazek[81] who observed a minimum heat flux at 0.1 pct C and attributed this to the maximum volumetric shrinkage at this carbon level during solidification. Consequently, in steels having carbon content close to 0.1 pct., $\delta \longrightarrow \gamma$ transformation occurs at the highest temperature or sooner after the solidification starts (i.e. close to meniscus). Therefore, the influence of solidification shrinkage on mould heat flux and in-mould solidification is maximum at 0.1 pct. carbon. As a result, reduced heat flux and columnar zone length was observed at this carbon level. However, with increasing carbon content, the ratio of δ / γ phases decreases leading to less shrinkage, increased heat flux and columnar zone

length. Also, the influence of constitutional super cooling becomes more predominant with increasing carbon[86].

On the other hand, Samarasekera et al[78] have attributed the role of carbon content of steel on morphology of cast structure during continuous casting, to the influence of peritectic reaction on generation and survival of free crystals in the molten pool of metal. According to them, at the lower carbon levels (below 0.17 pct. C) large volume shrinkage associated with $\delta \rightarrow \gamma$ transformation allow seed crystals to easily get separated from the mould wall leading to the generation of a large number of free crystals which are predominantly of δ- phase. These free crystals survive more easily due to the large melting range of δ-phase as compared to the γ-phase. Also, the peritectic reaction is diffusion controlled (slower process), and only a few δ-crystals may undergo peritectic transformation and form γ-phase. Whereas, at the higher carbon ranges, crystallites formed are predominantly of γ-phase having lower melting range and therefore remelt easily. So, at lower carbon range, these events lead to generation and survival of a large number of free crystals. As a result, in lower peritectic carbon range, due to large number of free crystals present, have shorter columnar zone (larger equiaxed zone) than steels in other carbon ranges when cast at the same superheat. However, Samarasekera et al[78] found minimum columnar zone length at 0.2 - 0.38 pct. C rather than at 0.1 pct. carbon, as expected. They attributed this discrepancy to the presence of Mn (0.46 - 1.39 pct.), which is a γ-stabilizer and could shift the limits of the peritectic transformation to the observed carbon concentrations[78].

4.2.5   Fluid Flow, Bulging and Centreline Segregation

As mentioned already, fluid flow in liquid during solidification plays an important role in the development of cast structure and macrosegregation. Solidification is accompanied by shrinkage in volume at the solidification front. This is one of the causes of fluid flow due to suction. The solidification front is never smooth and considerable longitudinal fluctuations occur in solidification front and concentration profile. As a result there are locations where columnar crystals come up to the centre and form bridges. This prevents feeding of shrinkage cavity from the pool and thereby resulting in the formation of mini-ingots (Fig. 4.5)[56,57]. It has following three consequences.

(i)   The impure liquid from interdendritic region of columnar zone gets sucked into the axial region increasing axial segregation.

(ii)   Zone refining action becomes more serious due to lack of feeding of fresh liquid.

(iii) Centreline porosity develops if feeding is incomplete.

In between the support rolls the strand shell may bulge outward due to the combined influences of solidification shrinkage, ferro-static pressure of the molten pool, and pressure (compression) of the support rolls. It has been established that bulging of the solid shell increases the centreline cavity leading to enhanced flow of residual segregated interdendritic liquid, and aggravate mini-ingotism. It, therefore, increases axial porosity and segregation. Miyazawa and Schwerdtfeger[59] mathematically analyzed bulging due to roll pressure and found it

DENDRITE GROWTH

GROWTH INSTABILITY

FORMATION OF BRIDGING

FORMATION OF PIPE

ACTUAL MACROSTRUCTURE
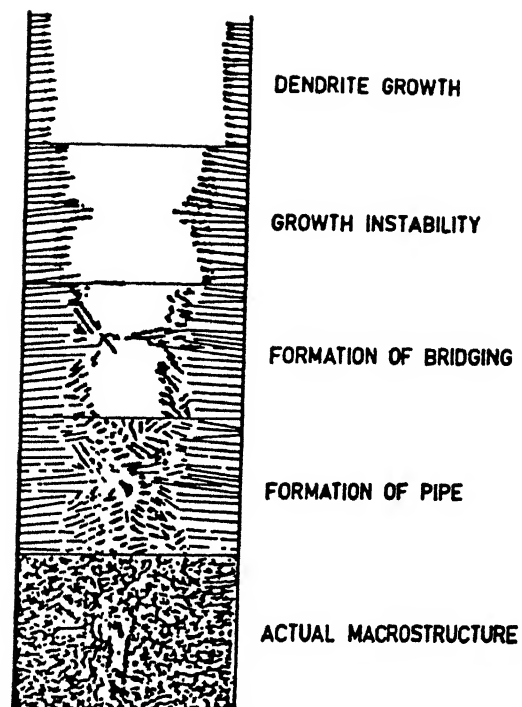
Fig. 4.5: Formation of mini-ingot in
continuous casting.
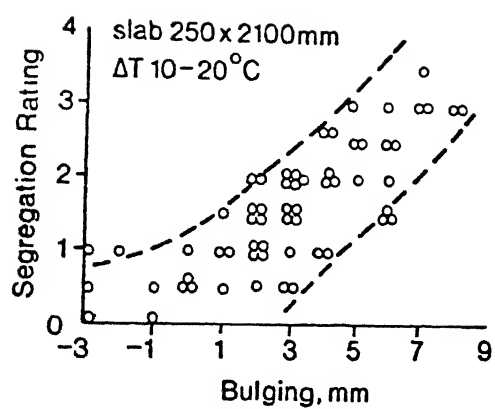
Fig. 4.6: Influence of bulging on centreline
segregation[24].
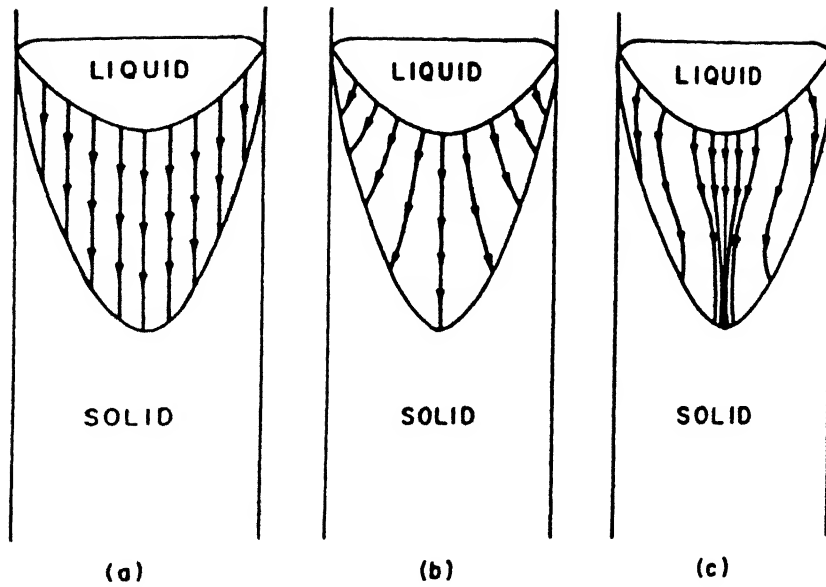
Fig. 4.7: Interdendritic fluid flow in continuous casting[64]

(a) limiting case, all flow vertical-no

segregation results;

(b) flow resulting in negative segregation at the

cast centre;

(c) flow resulting in positive segregation.

Improvement in centreline segregation through adjustment of roll gap taper has been reported in literature[61]. Adjustment of roll gap taper reduces the bulging before complete solidification, and thereby decreases the extent of macrosegregation. Also, soft reduction (SR) in the cross section of slab during the final solidification stage has been found to be quite effective in controlling the fluid flow in the mushy zone. Another new technique named 'controlled plane reduction (CPR)'[88], when applied on CC slabs, improved centreline segregation to such a degree as to eliminate macrosegregation. CPR seems to prevent bulging completely and at the same time compensate for the solidification shrinkage. Significant improvement in centreline segregation and semi-macro or spot segregation in slabs have been reported in literature[88].

Again, an enlarged equiaxed zone is of help, since equiaxed crystals do not interfere as much as columnar crystals with feeding of centreline cavities by the main pool, where the liquid does not have much segregation. In this connection fine network structure of equiaxed crystals is desirable. Treatment of molten metal with calcium or rare earth have been claimed to decrease extent of centreline segregation supposedly due to more fineness in equiaxed grain network structure.

4.2.7 Problems of Quantitative Measurement of Macrosegregation

In view of adverse effect of centreline segregation on product quality in the CC route, the author along with some others at the Indian Institute of Technology, Kanpur

carried out some investigations on the same. The various findings so far have already been reported elsewhere[58,89], and hence shall not be presented here as such. Only few remarks would be made.

In contrast to controlled laboratory measurements, industrial data are characterized by large scatters. In macrosegregation studies, non-uniformity of macrostructure and macrosegregation pattern introduce further scatter and uncertainty. Examples are:

(i)   Equiaxed zone size vs. tundish superheat

(ii) Columnar zone length vs. carbon content (Fig. 4.4)[78,86]

(iii) Fluctuating nature of segregation profile (Fig.4.1)

A transverse section, as shown in Fig. 4.2, consists of chill, columnar and equiaxed zones. Sizes of these zones would vary depending on the section being examined because of non-uniformity of structure along the longitudinal direction as revealed by segregation lines and bands, such as U-segregation band, V-segregation line and V-segregation band (as shown in Fig. 4.8). A major cause of these features is mini-ingot formation as discussed earlier (Fig. 4.5). In addition fluid flow pattern is also responsible. It is further illustrated in Fig. 4.9 by fluctuating nature of segregation profile along the centreline of a longitudinal section of CC billet.

Techniques of chemical analysis give rise to further difficulties in some cases. Fig. 4.9 illustrates this point. Goyal and Ghosh[89] carried out sulphur printing on longitudinal section of plain carbon steel billets. Sections had been cut through centreline of the billets so as to reveal the segregation patterns at and near the billet centreline. A dark spot on

U-segregation band

V-segregation lines

V-segregation bands
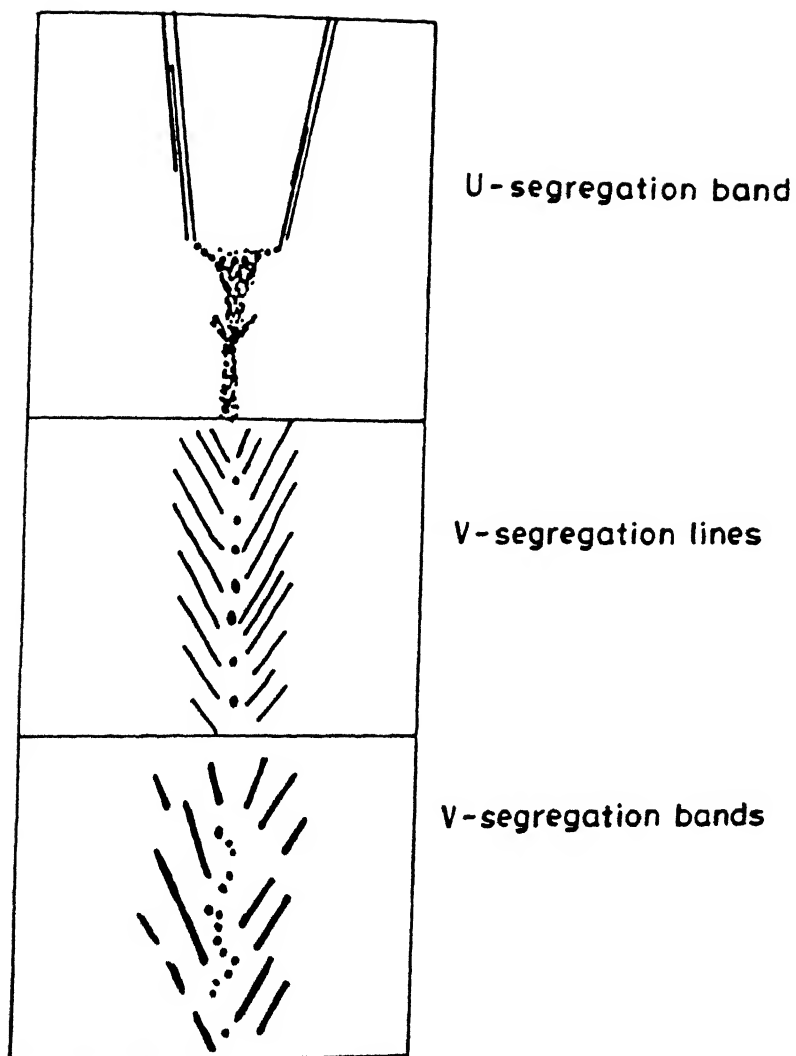
Fig. 4.8: Some features of macrosegregation in longitudinal section of CC products (schematic).
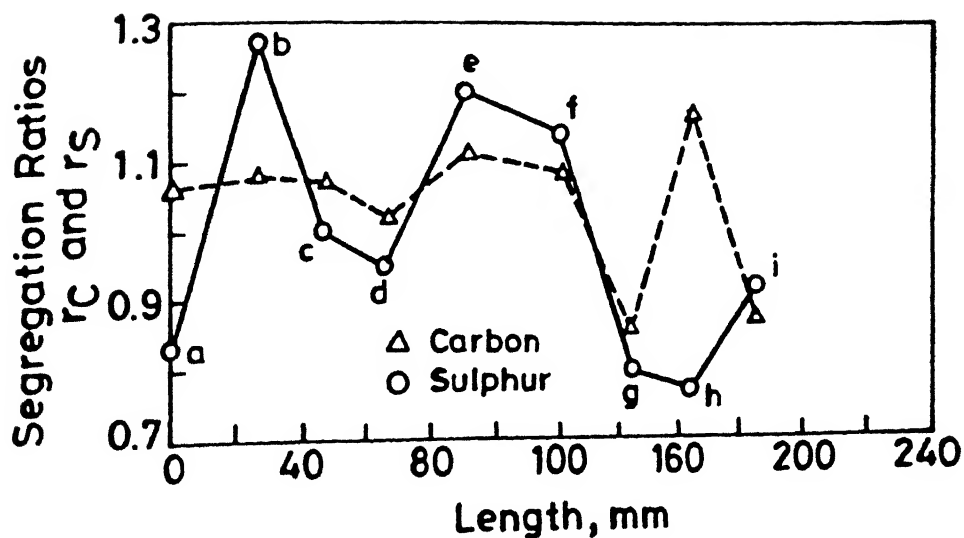
Location	Rating	Characteristics	Matching
a	2	faint dark spot with columnar bridge	N
b	3	predominantly white spot	N
c	3	predominantly white spot with columnar bridge	Y
d	3	predominantly white spot	Y
e	3	predominantly white spot at closed end of V-line	N
f	2	black spot with pipe	N
g	1	predominantly dark spot with columnar bridge	Y
h	1	predominantly dark spot	N
i	1	predominantly dark spot with columnar bridge	Y

Fig. 4.9: Segregation profiles of carbon and sulphur along the centreline of a typical steel billet[89].

sulphur print indicates region of high sulphur content and white spot low sulphur content. Then samples for analysis were collected by drilling with 8 mm dia. drills up to 8 mm depth at different locations on the axes of billets. Drillings were subsequently analyzed for carbon and sulphur by automatic carbon and sulphur determinator. A difficulty of chemical analysis is that analysis results would depend on choice of drill size[56].

A rating system was developed[89] for correlating chemical analysis with sulphur print. In this, 1 corresponds to the location predominantly dark, 3 predominantly white, and 2 in between 1 and 3. Matching is denoted by yes (Y) whenever 1 corresponded to peak, 3 corresponded with trough and 2 with middle position. No matching is denoted by N. It was found that both match and mismatch were there. One of the causes of mismatch lay in the fact that drilling had to be done to a finite depth to collect some sample. Due to non-uniformity it is very likely that the same drilling location has layers of alternate positively and negatively segregated regions. Non-destructive chemical analysis such as X-ray fluorescence or emission spectroscopy can remove this source of uncertainty. But to the best of author's knowledge the latter techniques cannot be employed for such large samples.

Previous studies[58,89] revealed that maximum segregation ratio for sulphur (i.e. ratio of centreline sulphur percent to estimated average sulphur percent in billet sample) in billet samples of Indian Steel Plants ranged between 1.2 to 1.8. Besides some variation in steel composition, the only other variable that was recorded was tundish superheat. Attempt was made to correlate maximum segregation ratio with superheat.

scatter in data did not allow revealing the expected trend. Study by Goyal and Ghosh[89] also indicated the value going up to approximately 2 or somewhat above for both carbon and sulphur.

4.2.8   Macrosegregation and New Measurement Techniques

As stated already in Section 4.1, semi-macrosegregation (or spot segregation) is drawing World-wide attention in recent years, and it is considered as a more serious defect in high grade continuously cast steels. Spot segregation is reported to form due to transport of segregated liquid in the mushy zone during the final stage of solidification[62,63]. The principal cause of transport has been found to be bulging of the strand between the support rolls[62,63]. The interesting feature of semi-macrosegregation is that it forms even with equiaxed solidification in the central region. As mentioned already, spot segregation has been found to be intensified by the application of electromagnetic stirring and soft reduction, even though the usual centreline macrosegregation is suppressed with these measures[63]. In steels for conventional application semi-macrosegregation has not been considered as a serious problem. However, in high grade steels for off-shore applications, even low level of segregation has been considered to be harmful. As a result of this, the permitted level of segregation in these steel grades has become more stringent.

This calls for the precise evaluation of segregation in continuously cast steel. Because of small size of segregation spots, semi-macrosegregation is difficult to evaluate by the conventional techniques such as: sulphur print, warm acid etching

and chemical analysis. Sulphur print technique also fails to detect macrosegregation in low sulphur and calcium treated steels[90]. Macroetching with hydrochloric acid has been found to be inadequate because of its poor resolving power[90]. The difficulties associated with the traditional method of sampling by drilling and chemical analysis, have been already discussed in the earlier section[56,80]. Too much sample is required for analysis.

In view of the above mentioned reasons, new evaluation techniques have come up. These include different types of electron probe micro analyzer (EPMA), etch print (EP) technique, and image analyzer[90]. Traditionally, EPMA has been used only for evaluation of dendritic microsegregation because of its inability to analyze large segregation spots. Nippon steel laboratory has developed a macroanalyser (MA) which is based on the same analytical principle as EPMA, but it can measure segregation on a relatively large area (i.e. 20 μm - 5 mm)[90]. Large samples (size 300 x 100 mm) can be accommodated in the instrument, and quantitative segregation maps of C, Mn and P can be obtained across the sample section. MA can also provide quantitative information on the fraction of segregated area and the size distribution of the segregation spots.

For rapid detection of segregation, etch-print technique has been developed[90]. It has been reported that etch print can reveal even extremely fine details (e.g. fine cracks, segregation spots) of cast structure. In some studies[79], etch print technique and image analyzer have both been employed. The combination of etch print and image analyzer facilitates measurement of total number

of spots, size distribution, and area fraction of semi-macrosegregation spots.

4.3 EXPERIMENTAL PROCEDURE

The present investigation on macrosegregation in transverse section of continuously cast billets involved the following program:

(i)   collection of samples from continuously cast billets, and corresponding shop floor data

(ii)   macrostructural examination of transverse sections of billet samples to evaluate various morphological features of billet casting

and (iii)   determination of composition of steel at the location of columnar-to-equiaxed transition boundary and at the centre in transverse sections, in order to evaluate macrosegregation and other characteristics of solidification.

4.3.1   Plant Data and Sample Collection

An important part of the present study was collection of billet samples and the corresponding data from the continuous casting shop of steel plant. On the basis of various aspects of solidification and macrosegregation phenomena during continuous casting, described earlier, the following factors have been taken into consideration during sample collection.

(i)   As mentioned already, industrial data are characterized by large scatter, and the continuous

casting process is no exception to these. The way to obtain a more conclusive pattern is to carry out investigations on a large number of samples.

(ii)   In Indian practice, there is no electromagnetic stirring. Hence, the size of equiaxed zone and centreline segregation are primarily controlled by the superheat of the liquid steel. Therefore, in order to establish correlation with superheat and morphology and/or macrosegregation, casting temperature should be measured as precisely as possible corresponding to each billet sample collected from the strand.

(iii) Casting of a particular heat in general continues for a long period, and there may be significant drop in temperature of liquid metal during continuous casting. Therefore, measurement of liquid steel temperature should be carried out at least twice, one at the beginning and another towards the end, and only the corresponding billet samples should be collected to study the influence of superheat.

(iv)   For a multistrand caster, each strand may have somewhat different characteristics. Therefore, all samples should be collected from one strand only, in order to keep the strand characteristics fixed and to make the comparative study more meaningful.

(v)   It is desirable to carry out investigation with different grades of steel, particularly those grades in which the problem of macrosegregation is

relatively more serious (e.g. high carbon steels). However, as described earlier, one of the objectives of the present study has been to correlate the actual columnar-equiaxed transition with the theoretical prediction of temperature field on the basis of heat transfer model developed in the present study (Ch.3). Also, another objective has been to study the applicability of various segregation models reported in literature, to macrosegregation in continuously cast billets. Such studies can be carried out even on a single grade of steel. Therefore, it was decided to collect all samples of same grade of steel.

Keeping the above points in mind, 21 low carbon steel billet samples of approximately 100 mm thick have been collected from the continuous casting shop of Tata Steel, Jamshedpur. The specification of the billet caster at Tata Steel is presented in Table 4.2. More details of the process adopted at Tata Steel are available elsewhere[91]. Additional comments on plant data collection are presented below.

(i)   All samples were collected from the strand number 4 which is one of the central strands.

(ii)   For each caster, two billet samples were collected, one at the beginning and another towards the end of casting.

(iii)   For the precise determination of superheat it is very desirable to measure the temperature of liquid steel in the mold or in the tundish-to-mold pouring stream. However, in industries the temperature of the liquid

steel is measured either in the ladle or in the tundish.

Hence, as a part of data collection program, special efforts were made to measure temperature in the mold or in the pouring stream. For this a Pt-Pt/10pct.Rh thermocouple assembly was designed and fabricated, and taken to the plant. However, it was not successful due to fluctuations in the output meter (i.e. millivoltmeter) and lack of sufficient life of thermocouple in the liquid metal. Hence, temperature was measured by the routine immersion thermocouple in the tundish only.

Another effort was made on temperature measurement by optical pyrometer. However, non-availability of a sophisticated two-color optical pyrometer did not allow satisfactory measurements. Hence, it was decided to estimate the casting temperature from the tundish temperature as closely as possible by some theoretical estimation procedure as the other alternative approach.

(iv) Subsequent correlation with superheat required that the samples be collected from a portion of billet which corresponded approximately to liquid steel whose temperature was measured.

This required knowledge of casting speed. In order to get it precisely, casting speed was independently calibrated several times. Table 4.3 presents the values of casting speed along with other data. These values are averages of 2-3 measurements in each heat. The casting speed, however, varied within a narrow range in all the heats.

Table 4.2: Characteristics of continuous casting machine at TATA STEEL[91]

Machine:

Supplier	CONCAST AG, W. Germany
Type	Curved Mould Billet caster
Radius	6 m
Number of Strands	6
Distance Between Successive Strand	1100 mm

Mould:

Material	Water Cooled Chrome Plated Copper
Length	0.8 m
Sizes	100x100 mm sq. and 125x125 mm sq.
Lubrication	Rape Seed Oil
Oscillation Frequency	100 to 150 Cycles Per min.
Water Flow Rate	504 m^3h^{-1}

Secondary Cooling Zone:

Total Length	7.45 m (Approx.)
Number of Zones	4
Water Flow Rate	324 m^3h^{-1}

Casting Speed: 3 m min.$^{-1}$ for 100 mm sq.
2.2 m min.$^{-1}$ for 125 mm sq. Billets

Metallurgical Length: 16.2 – 19.9 m

Tundish:

Capacity	12 tonnes
Nozzle Diameter	12 mm for 100 mm sq. and 15 mm for 125 mm sq. Billets
Refractory	Garnex Board; Nozzle-Zirconia

Ladle:

Capacity	130 tonnes
Nozzle Diameter	45 mm
Teeming Mode	Slide Gate Valve with no Turret Facility

Sequence Casting: 3 to 5 Heats

4.3.2   Macroetching of Transverse Section of Billets

The main objectives of macroetching in the present study have been the determination of area fractions of chill, columnar, and equiaxed zone, as well as determination of the position of columnar-to-equiaxed transition (CET) boundary in the transverse sections of the billet samples. For macroetching standard procedure described in literature, was adopted.

The billet samples were sectioned to the required size (50 mm thick samples), and subjected to the surface grinding before macroetching. Precautions were taken to avoid deep scratches and machining marks. After machining, sample surfaces were cleaned with acetone to remove dirt, oil and grease. Subsequent to this, samples were macroetched with warm 1:1 hydrochloric acid-water solution (by volume) to which about 10 ml hydrogen peroxide was added. During macroetching temperature of the etchant was maintained at $60-65^{\circ}C$, and the duration of etching was kept at 25 min. Also, in order to avoid the initial drop in the etchant temperature while dipping the sample into the etching solution, samples were preheated to the etching temperature (i.e. $60-65^{\circ}C$) in an oven. After etching, samples were washed with ammonium hydroxide solution in order to remove the acid completely from the macroetched surface, and final washing was carried out under tap water. Samples were then dried thoroughly in hot air blast and finally, kept in the oven maintained at $80^{\circ}C$ in order to protect the macroetched surface from rusting.

After macroetching, macrostructure of each billet sample was examined under magnascope (magnification 3X). Various features of the macrostructure were examined. All visible macrostructural

features of transverse sections of the billets were traced on transparent papers. These tracings were subsequently used for measurements of fractions of chill, columnar, and equiaxed zone as well as to ascertain the positions of CET boundaries using transparent graph papers. For checking the reproducibility of the macroetching procedure each billet sample was macroetched at least twice and the above mentioned procedure was followed for the measurements. Finally, macro photographs were taken for each section.

4.3.3   Chemical Analyses of Samples

Subsequent to the macrostructural examination, carbon and sulphur contents of steel at the CET boundary as well as at the centre of each billet section were determined. There are several methods for determination of carbon and sulphur in steel. In recent years, new evaluation techniques of segregation based on electron probe analyzer have also come up. However, due to non-availability of such sophisticated instruments, more frequently applied 'drilling technique' was adopted in the present study. It has been reported that the drilling technique may underestimate the actual segregation level due to some averaging effect in chemical analysis, if the drilled volume is large.

Therefore, a proper sampling/drilling scheme is crucial for a meaningful evaluation of segregation. In previous studies drill diameter varied from 3 to 8 mm and the drill depth were kept between 3 to 14 mm. Considering these factors samples were drilled out with a 3 mm diameter drill up to 5 mm drill depth at

the CET boundary in each billet sample. In order to generate sufficient quantity of sample, drilling was conducted at 6-8 locations along the CET boundaries, and then these were mixed. At the centre, most of the billets had centreline porosity. To generate sufficient samples, drillings were carried out with a larger (5 mm) diameter drill. Fig. 4.10 presents a sample photograph of a drilled surface.

Prior to drilling, the billet surface was macroetched and various locations of sampling in the macrostructure were marked with a punch. The surface was then cleaned. After drilling, samples were collected on plastic sheets. Finally, drillings were washed with acetone and distilled water, dried in oven, and stored in plastic envelop with proper identification marks.

Chemical analyses of the samples were carried out in the carbon-sulphur determinator at the National Metallurgical Laboratory (NML), Jamshedpur. The instrument was a CS-444 microprocessor-based determinator supplied by LECO, USA. The instrument is capable of doing measurements of carbon and sulphur contents of metals, ores, ceramics, and other materials. It is fitted with CS-444 determinator, the HF-400 induction furnace, a built-in balance, display monitor, printer Fig. 4.10
and key board.

Analysis of carbon and sulphur required 1 g sample weight and the duration of analysis was 1 min. During analysis of samples, the instrument was calibrated at different stages with LECO standard sample. For some samples, duplicate analyses were carried out in order to check the reproducibility of analysis.
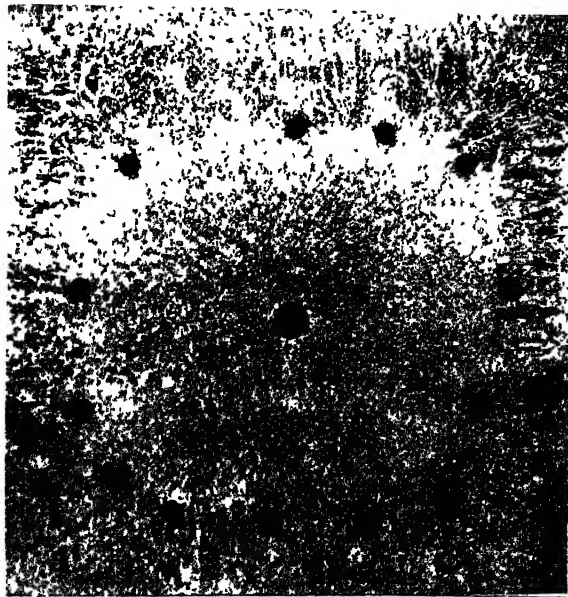
Fig. 4.10: Photograph of a drill surface.

4.4 RESULTS AND DISCUSSIONS

Table 4.3 presents the details of data collected from Tata Steel for the billet samples. The data consist of temperature of liquid steel in tundish, casting speed, chemical analysis of liquid steel (pct. C, Si, Mn, S, P etc), the grade of steel, and the time interval between temperature measurements in the tundish.

As stated in section 4.3, the casting speed was determined by the author for the present investigation in order to make it as precise as possible. Two billet samples were collected for each cast, one towards the beginning of casting and another after the time intervals indicated in Table 4.3. Temperature of molten steel in the tundish was measured by immersion thermocouple. The billet samples were so collected as to correspond approximately to liquid steel for which temperature were measured.

The overall tundish temperature variation in different heats were from 1525 to 1570 ^{o}C as noted in Table 4.3. All the grades of steel were of low carbon steel with carbon content varying from 0.08 to 0.2 pct. It has already been stated in section 4.3 that all samples were collected from strand 4 of the caster.

4.4.1 Results and Discussions on Macrostructural Examination

As stated in section 4.3, the macrostructure was examined on transverse section of billet only. The examinations were made under unetched and etched conditions both.

Table 4.4 presents macrostructural details of transverse

section of billet samples. In unetched condition 2 features were noted viz. rhomboidity and existence of pores especially near billet axis.

4.4.1.1   Measurement of equiaxed zone size

In the past the investigators employed either columnar zone width or equiaxed zone width or area of equiaxed zone for further correlation with superheat etc.[56,78,86]. In the present investigation it was decided to employ area of equiaxed zone for further correlation purposes. Table 4.4 presents data. It may be noted that areas of zones have been presented as pct. of cross-sectional area of billet.

As stated in section 4.2, each billet sample was polished and macroetched two to three times, and separate measurements were carried out after each macroetching in order to find out reproducibility of the entire procedure, and obtain more precise values. The reproducibility of measurements was ±5-20 pct. of average. This variation is attributed to the finite width of columnar-equiaxed transition zone. The transition is mostly not sharp and it was not possible to mark the transition boundary precisely. As discussed in Section 4.2, the columnar-equiaxed transition is expected to be diffused in nature. Hence, this observation is in agreement with what is expected and has been observed by others[56,74].

Table 4.3   Data on billet samples collected from Tata Steel

Sample code	Tundish temp. (°C)	Casting speed (m/min)	Nominal composition (pct.)					Time interval bet. temp measurements	Grade of Steel
			C	Si	Mn	S	P		
A1	1540	1.7	0.20	0.244	0.76	0.03	0.029		TMT50
A2	1535	1.8						50 min.	
B1	1530	1.7	0.18	0.229	0.71	0.025	0.029		TMT50
B2	1520	1.75						46 min.	
C1	1543	1.8	0.08	0.129	0.48	0.026	0.02		C1008
C2	1535	1.75						10 min.	expo.
D1	1557	1.8	0.11	0.158	0.69	0.034	0.026		10/13
D2	1545	1.7						1 hr.	Si-Ki
E1	1550	2.2	0.20	0.204	0.74	0.033	0.032	1 hr.	TC2
E2	1538	2.1						5 min.	
F1	1548	1.95	0.13	0.219	0.68	0.032	0.017	1 hr.	10/13
F2	1543	2.1							Si-Ki
G1	1543	1.75	0.13	0.185	0.69	0.033	0.023.		10/13
G2	1533	2.0						40 min.	Si-Ki
H1	1568	1.75	0.09	0.0106	0.50	0.029	0.024		C1008
H2	1555	1.95	Cr=0.01, Ni=0.016, Mo=0.01					48 min.	expo.
I	1563	1.75	0.18	0.20	0.73	0.03	0.027		-
J1	1545	1.6	0.14	0.25	0.70	0.025	0.030	1 hr.	-
J2	1528	1.65						10 min.	
K1	1550	1.7	0.11	0.125	0.43	0.033	0.011	1 hr.	-
K2	1535	1.6						10 min.	

Table 4.4 has a column indicating whether the equiaxed zone was symmetric or asymmetric around the geometric axis of the billet. From Table 4.4 it may be noted that equiaxed zone was asymmetric around both perpendicular directions parallel to edges (i.e. x and y directions) for 10 samples. There were 6 samples where it was symmetric around the centre. In rest 5 samples, it was symmetric with respect to only one axis. Figs. 4.11(a) - 4.11(c) show macrograph of billet sections. Figs. 4.12(a) - 4.12(c) present the sketches of corresponding CET boundaries. It may be noted that equiaxed zone is symmetric in Fig. 4.11(a), whereas, it is asymmetric in Figs. 4.11(b) and 4.11(c).

Samarasekera et al[78] have also reported asymmetric equiaxed zone in curved mold CC machine. The investigators observed longer columnar structure adjacent to the inside radius face than that next to the outside radius face. They attributed this to the preferential settling of free crystallites due to gravity at the columnar solidification front advancing from the outside radius face. These free crystallites subsequently, interfere with the columnar growth, and lead to asymmetric equiaxed structure in the solidified billet. The CC machine at Tata Steel is also a curved mold type. The observed asymmetry in structure here may also be partly due to the above explanation provided in literature. But it is not possible to make further statements about the exact cause of asymmetry here.

Table 4.4:   Measured Morphological Features in Transverse Section
of CC Billets

SAMPLE	C	Super heat (ΔT)	Features of unetched surface		Area percent of various zones on etched surface							
			Centre-line porosity	Rhomboi-dity	Chill				Equiaxed			
					Experiment sets				Experiment sets			
	pct.	°C			1	2	3	Avg.	1	2	3	Avg.
A1	0.2	28	4 mm dia	nil	7.7	9.2	8.0	8.0	20.0	18.0	23.0	20.0
A2	0.2	23	nil	nil	8.5	13.5	8.7	10.0	28.5	24.5	31.0	28.0
B1	0.18	20	nil	nil	11.0	9.0	9.0	10.0	28.0	24.0	32.0	28.0
B2	0.18	8	nil	nil	14.0	14.0	10.0	13.0	31.0	36.0	33.0	33.0
C1	0.08	20	nil	nil	9.0	14.0	-	11.5	4.0	2.3	-	3.0
C2	0.08	10	nil	nil	10.0	12.0	-	11.0	7.0	5.0	-	6.0
D1	0.11	35	small	1.03	10.0	11.0	8.0	10.0	2.5	5.5	4.0	4.0
D2	0.11	24	small	nil	8.0	9.0	7.0	8.0	9.0	8.0	11.0	9.0
E1	0.2	38	2 mm dia	1.01	13.6	12.5	-	13.0	24.8	21.5	-	23.0
E2	0.2	26	small	1.02	13.0	12.0	-	12.5	36.0	32.0	-	34.0
F1	0.13	28	small	1.03	12.0	15.0	-	13.5	30.0	26.5	-	28.0
F2	0.13	21	small	1.02	11.4	13.0	-	12.0	42.0	42.0	-	42.0
G1	0.13	24	nil	1.02	12.5	9.5	-	11.0	3.5	6.5	-	5.0
G2	0.13	13	nil	1.01	13.0	8.0	-	10.5	9.5	10.5	-	10.0
H1	0.09	42	3 mm dia	1.04	10.5	12.0	-	11.0	6.5	8.6	-	7.0
H2	0.09	27	small	1.03	11.0	11.5	-	11.0	15.5	12.8	-	14.0
I1	0.18	48	2 mm dia	1.06	10.0	8.0	-	9.0	9.0	13.0	-	11.0
J1	0.14	28	nil	1.01	9.0	10.0	-	9.5	7.2	5.0	-	6.0
J2	0.14	10	nil	1.02	8.0	10.0	-	9.0	13.9	10.6	-	12.0
K1	0.11	27	nil	1.03	10.0	-	-	10.0	19.0	-	-	19.0
K2	0.11	12	nil	1.05	10.0	11.0	-	10.5	22.4	18.0	-	20.0

Note: area pct. columnar zone = 100 - area pct. (chill + equiaxed) zone
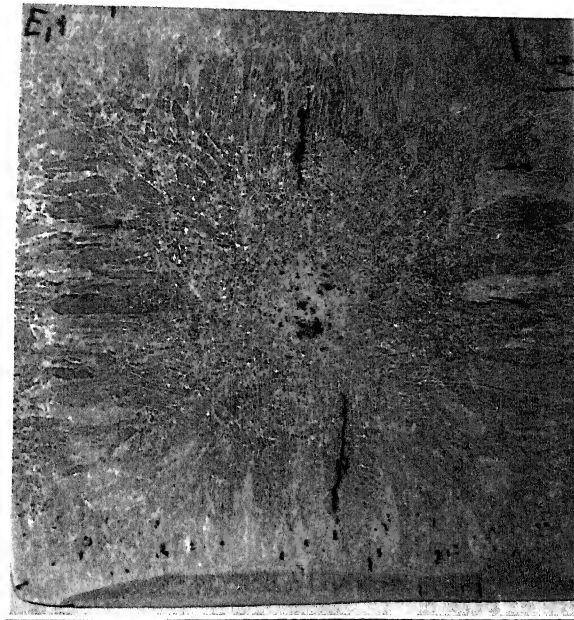
(a)
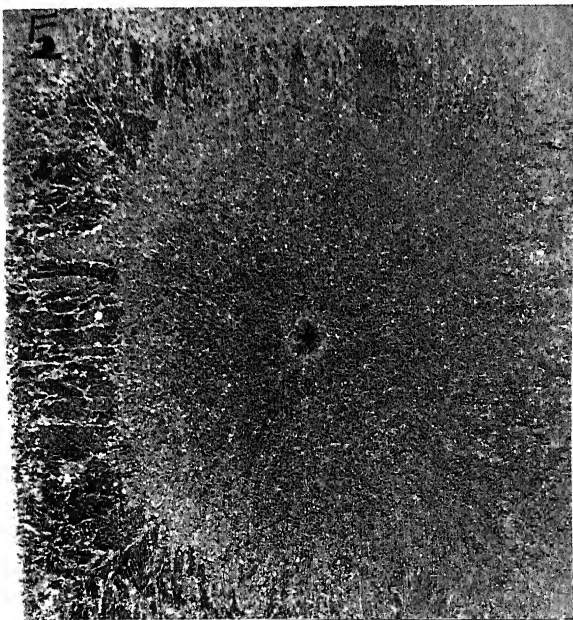
(b)
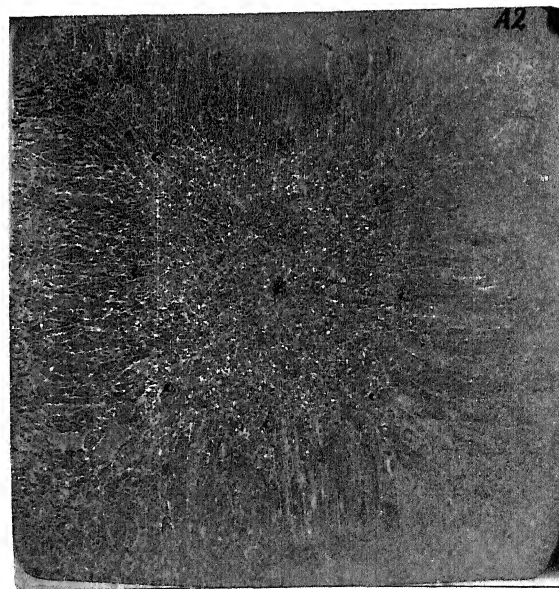
(c)

Fig.4.11: Photographs of macroetched surface of billet
samples with equiaxed zones as follows:

(a) symmetric (type I)

(b) asymmetric about one axis (type II)

(c) asymmetric about both axes (type III)
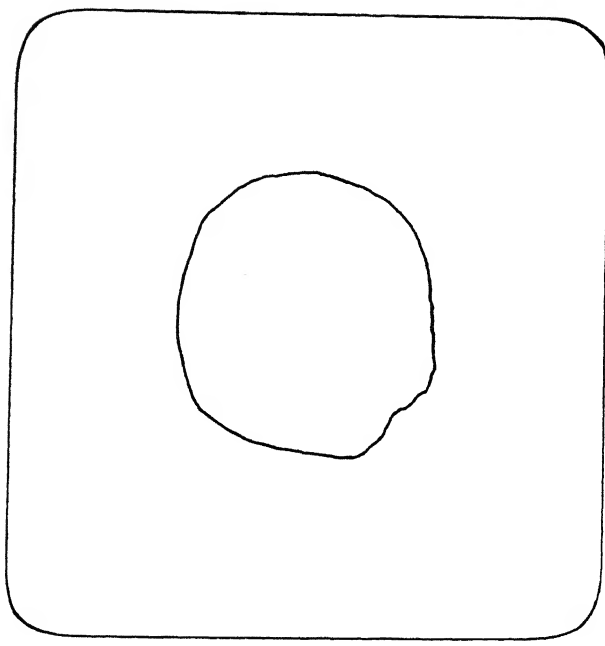
(a)
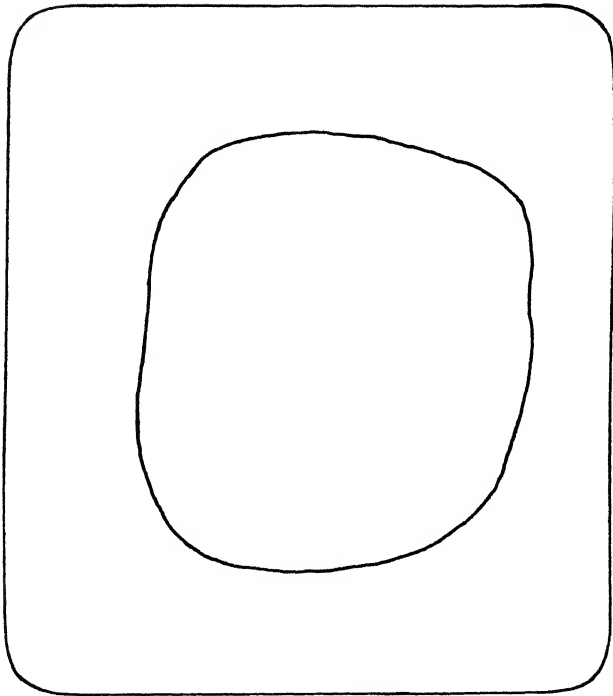
(b)
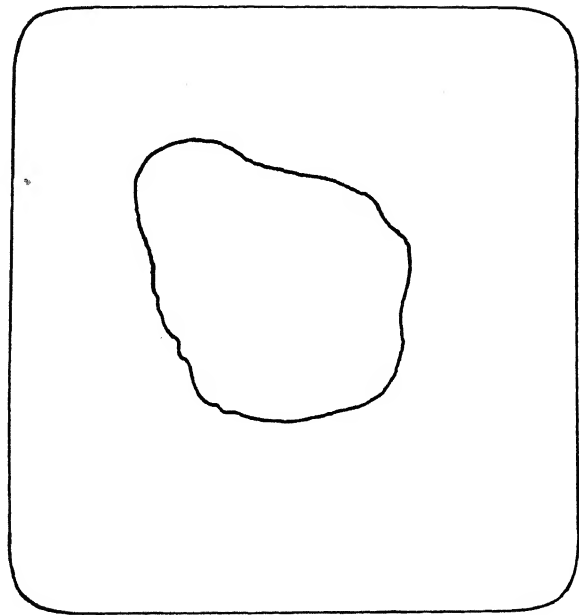
(c)

Fig. 4.12. Sketches of columnar-equiaxed transition boundaries for photographs in fig. 4.11

(a) symmetric

(b) asymmetric about one axis, and

(c) asymmetric about both axes

4.4.1.2 Influence of tundish superheat on equiaxed zone size

It has already been discussed in literature review (Sec. 4.2.2) that more the superheat, smaller would be the equiaxed zone size. It has been verified by many investigators. Fig. 4.13 shows the area of equiaxed zone in percent of total cross-sectional area as a function of tundish superheat (ΔT, in ^{0}C). ΔT is defined as:

$$\Delta T = T_0 - T_L \qquad \qquad ...(4.14)$$

Where T_0 is temperature of liquid steel in ^{0}C as measured in the tundish. T_L is liquidus temperature of steel in ^{0}C at its nominal composition (composition of liquid steel as collected from plant).

Steel is a multi-component alloy. Therefore, its liquidus temperature cannot be estimated precisely from the binary iron-carbon phase diagram. The standard approach of estimation of liquidus temperature of multi component alloys have been to sum the depressions which each component element would impose on the melting point of pure iron according to the respective binary phase diagrams. However, this approach is valid for dilute solutions, with negligible interactions amongst the solute elements, or 'quasibinary' alloys where only one of the elements is non-dilute and provided the solid phase is the same[92].

In literature[92-95], various correlations between the liquidus temperature and composition of steel have been proposed. A good review on this subject is available[92]. Thomas et al[93] have reported one of the correlations for liquidus temperature, which

is noted below:

$$T_L = 1537 - 88(\text{pct.C}) - 25(\text{pct.S}) - 30(\text{pct.P}) - 8(\text{pct.Si})$$
$$-5(\text{pct.Mn}) - 5(\text{pct.Cu}) - 2(\text{pct.Mo}) - 4(\text{pct.Ni})$$
$$-1.5(\text{pct.Cr}) - 18(\text{pct.Ti}) - 2(\text{pct.V})$$

$$\ldots(4.15)$$

In the present study, the liquidus temperature of steel has been estimated using various correlations reported in literature. Table 4.5 presents the results of calculations. It is to be noted from Table 4.5 that the values of T_L predicted from Eq.(4.15) match closely with those of Howe[92]. But there is some mismatch with others. Therefore, correlation of Thomas et al[93] (Eq.4.15) was selected for the subsequent calculations of the liquidus temperatures.

The calculated values of tundish superheat (ΔT) for various samples have been presented in Table 4.4. Fig.4.13 shows the variation of area pct. equiaxed zone with ΔT, and confirms the established literature finding that area of equiaxed zone decreases as the tundish superheat increases. Roy et al[58] earlier reported this on some Tata Steel billets. However their data were limited. In Fig.4.13 data collected by Roy et al[58] have also been included for the sake of completeness.

As may be noted from Fig.4.13 that there is lot of scatter in data points. The issue of scatter has already been discussed in Section 4.2, and it has been shown that such scatter is a characteristic feature of these industrial data as reported by others in literature. In order to establish the trend, linear regression analysis was done, and the best fit line is shown in

Table 4.5:   Estimated liquidus temperatures of billet samples using different correlations

Sample Number	Estimated Liquidus Temperature (°C)				
	Ref. 93	Ref. 94	Ref. 95	Ref. 96	Ref.92
A	1512.0	1515.2	1510.4	1515.1	1511.4
B	1514.3	1517.5	1512.7	1516.7	1513.8
C	1525.3	1527.7	1524.9	1524.3	1524.8
D	1521.0	1523.8	1520.3	1520.9	1520.3
E	1512.3	1515.6	1511.0	1515.5	1511.7
F	1519.1	1521.9	1517.7	1519.5	1518.5
G	1519.1	1522.1	1518.1	1519.7	1518.5
H	1524.9	1528.2	1525.4	1525.2	1524.6
I	1514.3	1517.7	1513.0	1516.9	1513.8
J	1517.7	1520.5	1516.2	1518.3	1517.0
K	1523.0	1526.0	1522.4	1523.2	1522.5
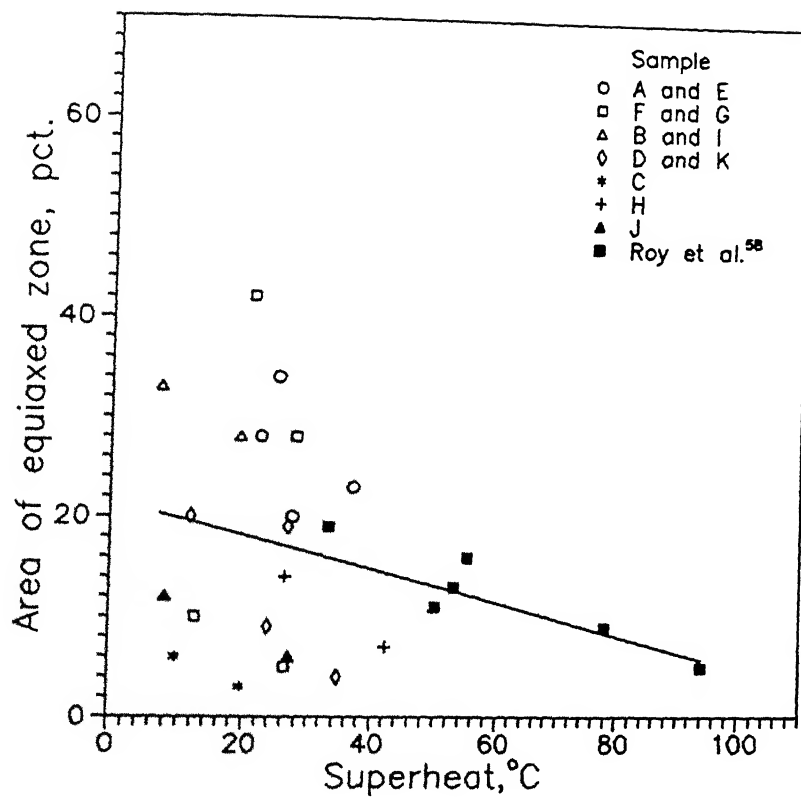
Fig. 4.13.: Influence of tundish superheat on the percentage of equiaxed zone area in billet samples.

Fig.4.13. The equation of best fit line is:

$$A_{Eq} = 21.45 - 0.17 \, \Delta T$$

...(4.16)

where, A_{Eq} = area of equiaxed zone as pct.of total cross-sectional area.

4.4.2   Results and Discussions on Macrosegregation Studies

4.4.2.1   Results

As stated in Section 4.3, the chemical analysis of liquid steel for each cast was provided by Tata Steel. The plant takes lollipop samples and analyze them in their Express Laboratory of steelmaking division by spectroscopic method. These have been designated as nominal composition and reported in Table 4.3.

For study of macrosegregation, drillings were collected from centreline as well as from columnar-equiaxed transition (CET) boundary. The samples were analyzed by LECO carbon-sulphur determinator at the National Metallurgical Laboratory with participation of the author. Table 4.6 presents the results of chemical analysis of all samples. Each analysis represents the average of a set of duplicate analyses.

The average reproducibility of carbon analysis as determined from the duplicate sets was ± 2 pct. of the value. For sulphur it was ± 6 pct. of the average value. The reliability of analysis was checked frequently by using standard samples. Moreover, few lollipop samples collected from the plant were also analyzed at the National Metallurgical Laboratory. They differed by few percent only of the value from those provided by the plant

Table 4.6: Analyses of carbon and sulphur at the centreline and CET boundaries of billet samples

Sample	Carbon			Sulphur		
	nominal	centre line	CET boundary	nominal	centre line	CET boundary
A1	0.2	0.232	0.218	0.03	0.0325	0.0203
A2	0.2	0.302	0.21	0.03	0.0616	0.0323
B1	0.18	0.18	0.197	0.025	0.0344	0.0326
B2	0.18	0.225	0.183	0.025	0.0361	0.0261
C1	0.08	0.096	0.105	0.026	0.0227	0.0265
C2	0.08	0.108	0.089	0.026	0.0266	0.0266
D1	0.11	0.102	0.11	0.034	0.0275	0.0323
D2	0.11	0.122	0.115	0.034	0.032	0.0354
E1	0.2	0.204	0.233	0.033	0.0336	0.0282
E2	0.2	0.237	0.227	0.033	0.0325	0.0392
F1	0.13	0.155	0.145	0.032	0.042	0.027
F2	0.13	0.134	0.139	0.032	0.042	0.027
G1	0.13	0.171	0.133	0.033	0.0378	0.0298
G2	0.13	0.159	0.126	0.033	0.0381	0.0333
H1	0.09	0.105	0.087	0.029	0.0255	0.027
H2	0.09	0.085	0.093	0.029	0.0275	0.0293
I	0.18	0.192	0.2	0.03	0.0285	0.024
J1	0.14	0.19	0.16	0.025	0.0337	0.0315
J2	0.14	0.183	0.166	0.025	0.031	0.0295
K1	0.11	0.231	0.183	0.033	0.0374	0.0297
K2	0.11	0.212	0.188	0.033	0.0374	0.0318

laboratory.

Extent of segregation is typically expressed by a parameter called 'degree of segregation', which is a measure of level of segregation defined as:

$$r_i = c_i/c_{io} \qquad \qquad ...(4.17)$$

where c_i = concentration of solute element i at the location under consideration

c_{io} = concentration of i in liquid steel (nominal concentration)

and r_i = degree of segregation of i.

Table 4.7 presents values of degree of segregation of carbon as well as sulphur (r_c and r_s respectively) for all samples from chemical analysis data.

4.4.2.2   Comparison of segregation levels at centreline and at columnar-equiaxed transition (CET) boundary

Fig.4.14 shows the data points of degree of segregation for sulphur (r_s) at the centreline vs. r_s at columnar-equiaxed transition (CET) boundary. As usual like other data, there is scatter. However most of the data points lie above the line with slope 1:1. This demonstrates that statistically speaking, level of segregation at the centreline was more than that at the CET boundary. As Fig.4.15 shows this was the feature of r_c as well. This observation is in agreement with what is expected from theoretical considerations i.e. segregation level at centreline should be more than that at any intermediate location on the billet section.

Table 4.7: Degree of segregation of carbon and sulphur at the centreline and CET boundaries of different billet samples

| Sample No.	Centreline			CET Boundary			
	r_c	r_s	$\ln r_s/\ln r_c$	f_s	r_c	r_s	$\ln r_s/\ln r_c$
A1	1.16	1.21	1.28	0.8	1.13	1.25	1.82
A2	1.51	2.28	2.0	0.72	1.08	1.2	2.37
B1	1.03	1.53	13.03	0.72	1.13	1.45	3.04
B2	1.3	1.6	1.79	0.67	1.05	1.16	3.04
C1	1.23	0.9	-0.51	0.97	1.35	1.02	0.06
C2	1.14	1.04	0.3	0.94	1.14	1.0	0
D1	0.96	0.94	1.52	0.96	1.04	1.06	1.48
D2	1.15	1.04	0.28	0.91	1.04	1.16	3.78
E1	1.05	1.28	5.1	0.77	1.2	0.95	-0.28
E2	1.22	1.17	0.79	0.66	1.17	1.33	1.82
F1	1.23	1.47	1.86	0.72	1.15	0.94	-0.44
F2	1.06	1.07	1.16	0.58	1.11	1.22	1.94
G1	1.35	1.27	0.8	0.95	1.01	1.00	0
G2	1.26	1.21	0.82	0.9	1.02	1.12	5.72
H1	1.2	0.98	-0.11	0.93	1.0	1.06	-
H2	0.96	1.07	-1.48	0.86	1.06	1.12	1.94
I	1.1	1.07	0.68	0.89	1.14	1.073	0.54
J1	1.4	1.5	1.21	0.94	1.16	1.4	2.24
J2	1.34	1.48	1.35	0.88	1.22	1.31	1.35
K1	2.16	1.26	0.3	0.81	1.73	1.17	0.3
K2	1.98	1.26	0.34	0.8	1.76	1.07	0.12
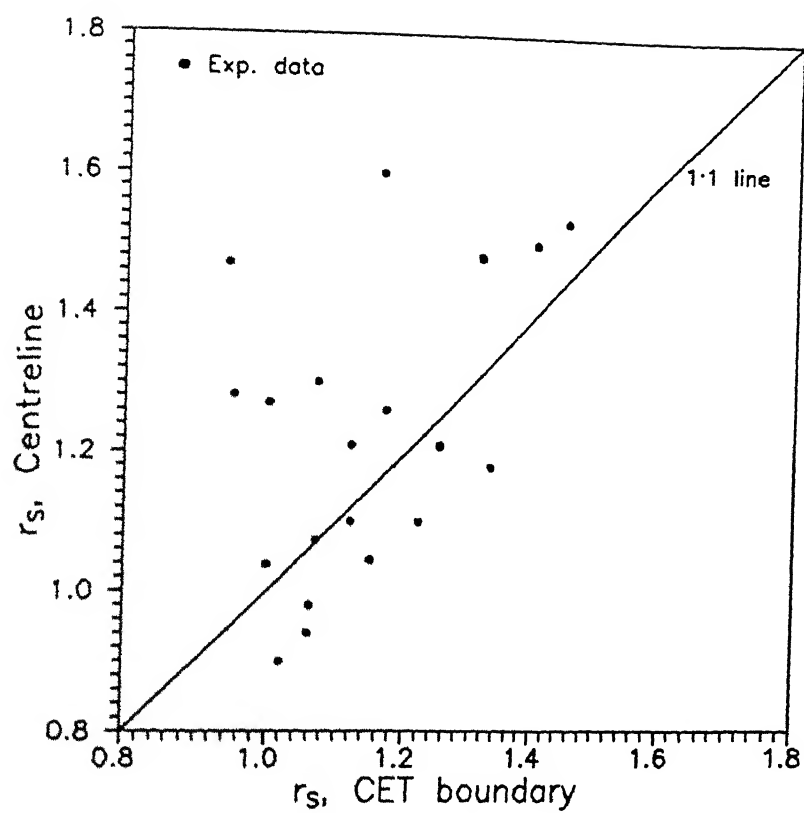
Fig. 4.14: Relationship between r_S at the centreline and columnar—equiaxed transition (CET) boundary.
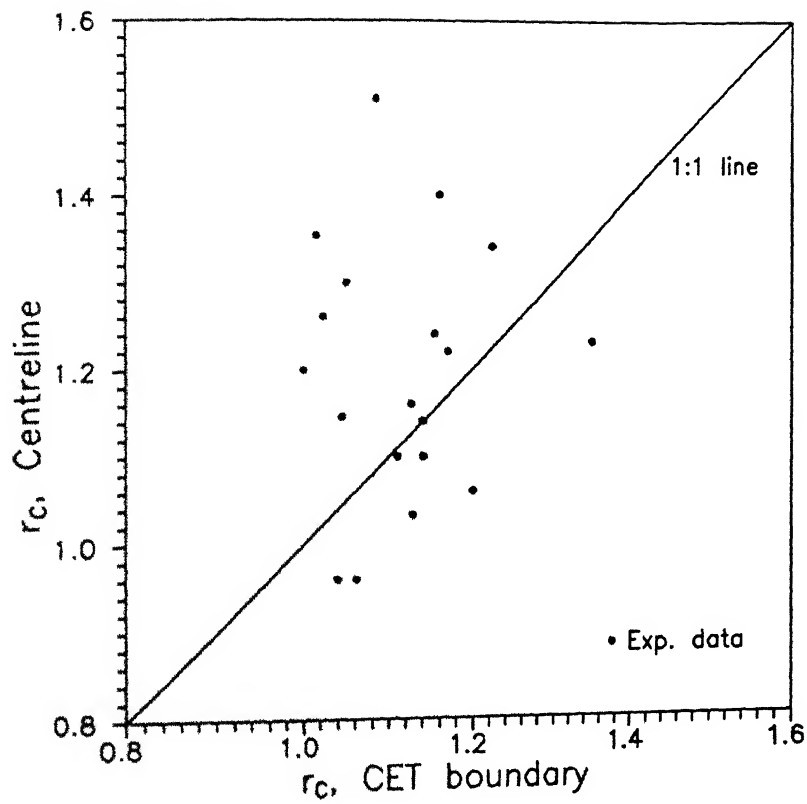
Fig. 4.15: Relationship between r_c at the centreline and CET boundary.

4.4.2.3   Quantitative relationship between r_s and r_c

As discussed in section 4.2, macrosegregation depends on (a) equilibrium partition coefficient (k_0) of solute elements and the parameter, R/k_m, (b) morphology, (c) movement of solid and liquid phases during solidification, and (d) extent of chemical reactions during freezing, i.e. formation of inclusions etc.. For a particular location, factors (b) and (c) are common for all solutes, but not (a) and (d). Hence, r_i values of various solutes at a given location would not be the same, but due to the common factors some correlations amongst them can be expected. Iwata et al[96] plotted the r_i values of S, Mn and P against that of carbon at the centreline by a linear plot. In spite of considerable scatter in data, investigators have reported some correlations of r_s, r_{Mn} and r_p with r_c. Moore[1] has described the advantages of this particular approach for determination of segregation ratios of C,S,P and Mn by knowing the segregation level of one of them. However, sulphur tends to form inclusions with Mn and other elements. Also, r_{Mn} does not show sufficient variation with r_c to provide an accurate assessment. Therefore, Moore[56] has recommended phosphorus to be the best element to use for determining the degree of segregation of carbon by using the above mentioned approach.

In the present study, also, it was decided to find out a quantitative relationship in a similar fashion mentioned above. Fig.4.16 presents data points on r_s vs. r_c plot for the centreline of all the billet samples along with the best fit line. The best fit line of Iwata et al[96] as well as that of Goyal and Ghosh[89] are also shown for comparison purposes. The equations
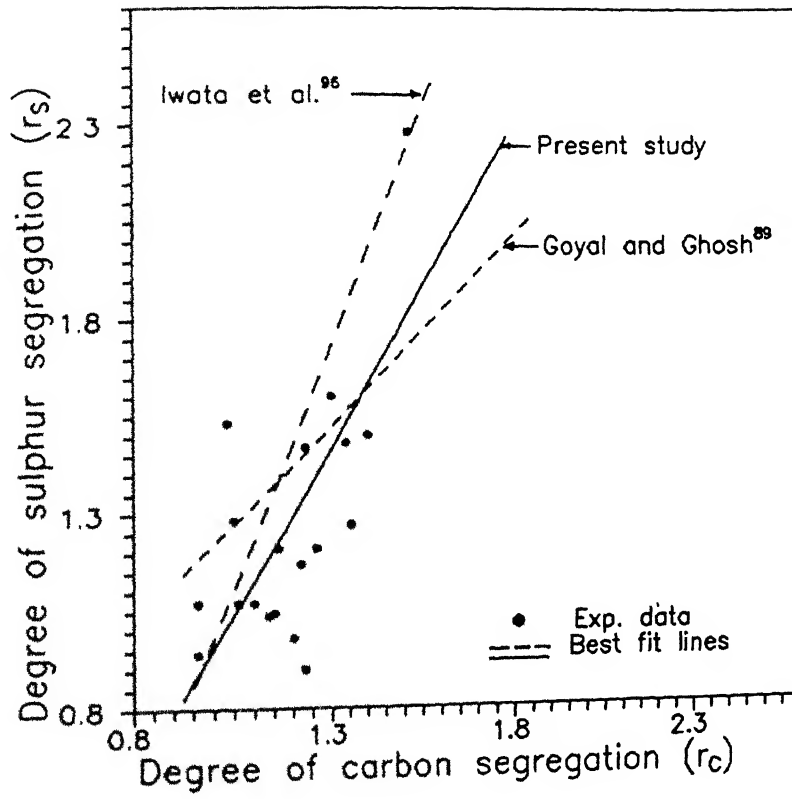
Fig. 4.16: Relationship between r_S and r_C at the centreline in billet samples.
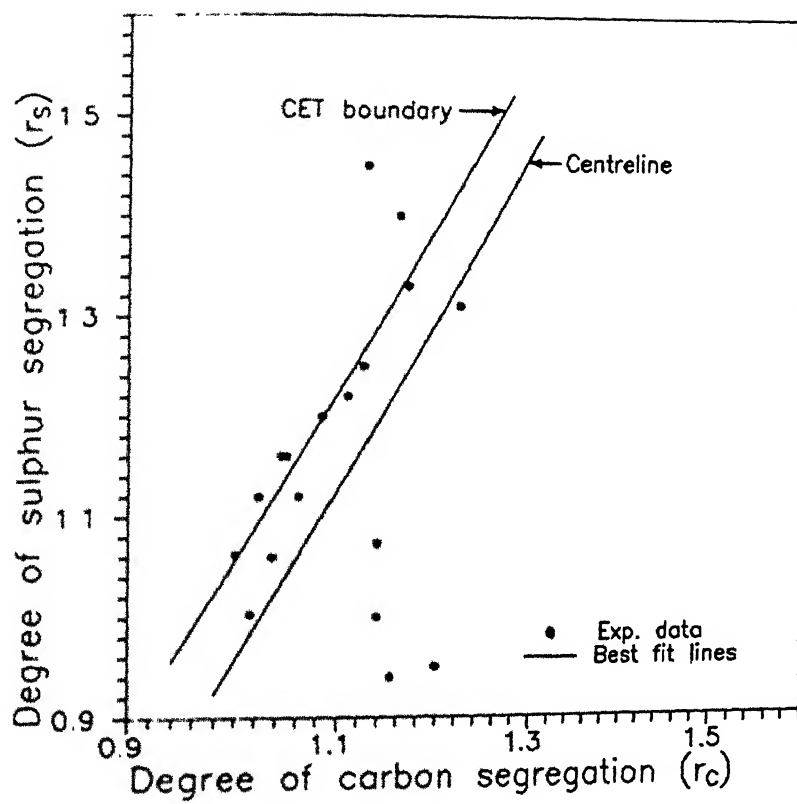
Fig. 4.17: Relationship between r_c and r_s at the CET boundary in billet samples.

different from that for centreline. However they are almost parallel.

As discussed in the next sub-section that no segregation equation predicts linear variation of r_s with r_c. It is a purely empirical approach. Hence no effort would be made to explain it further.

4.4.2.4   Correlation between r_s and r_c with the help of segregation equations

In the previous section r_s and r_c were correlated by linear regression analysis. It should be recognized that it is a purely empirical approach and does not have any segregation model as basis. Now, attempts would be made to see how segregation-models can be utilized for this purpose. It may be noted that the nature of data, both in literature[96] as well as in the present investigation, is characterized by scatter. Hence, the objective would be to attempt gross comparisons only. This is the only rational approach according to the author.

It may also be pointed out here that the segregation equations (Eqs.4.1 - 4.4 , in section 4.2) are applicable to simple situations such as plane front solidification or at best for dendritic solidification as encountered during columnar growth of crystals. Hence, they are more applicable at columnar-equiaxed transition boundary rather than at the centreline of the billet. However, a selective judicious application to centreline is not ruled out.

(A) Equilibrium solidification model[65]

The relevant equations are:

$$k_0 = C_S/C_L \qquad \qquad \ldots(4.1)$$

and
$$f_S + f_L = 1 \qquad \qquad \ldots(4.22)$$

The overall mass balance at the solidification front gives:

$$C_S f_S + C_L f_L = C_0 \qquad \qquad \ldots(4.23)$$

combining above equations:

$$k_0 C_L f_S + C_L (1 - f_S) = C_0 \qquad \qquad \ldots(4.24)$$

and
$$r = \frac{C_L}{C_0} = \frac{1}{1 + f_S (k_0 - 1)} \qquad \qquad \ldots(4.25)$$

Therefore, segregation ratios of carbon and sulphur would be:

$$\frac{1}{r_C} - 1 = f_S (k_0^C - 1) \qquad \qquad \ldots(4.25a)$$

and
$$\frac{1}{r_S} - 1 = f_S (k_0^S - 1) \qquad \qquad \ldots(4.25b)$$

At any location under consideration f_S is same for both carbon and sulphur.

Hence,
$$\frac{\left(\frac{1}{r_C} - 1\right)}{\left(\frac{1}{r_S} - 1\right)} = \frac{k_0^C - 1}{k_0^S - 1} = b = \text{a constant} \qquad \ldots(4.26)$$

From Table 4.1, the value of b=0.82. For CET boundary, values of $\left(\frac{1}{r_C} - 1\right)$ have been plotted against $\left(\frac{1}{r_S} - 1\right)$ for various samples in Fig 4.18. A line with slope b equal to 0.82 is also shown. It
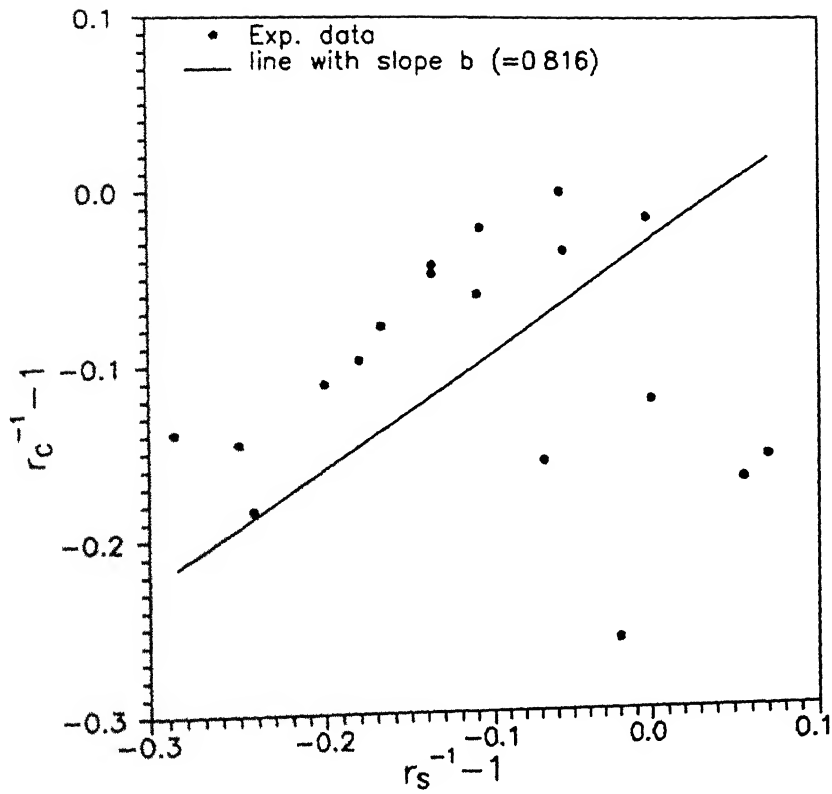
Fig. 4.18: Testing of applicability of equilibrium solidification model to segregation data of CET boundary.

is clear that there is no agreement of experimental data with prediction of equation (4.26). This is not surprising because the equilibrium solidification model is hardly applicable to continuously cast steel billets where solidification is fairly fast.

(B) Scheil's equation and modified Scheil's equation[64,74]

Scheil's equation and modified Scheil's equation are described in section 4.2 (viz., Eqs.(4.2) and (4.11)). From Scheil's equation, segregation ratio of solute element can be expressed as:

$$r = \frac{C_L}{C_0} = (1 - f_s)^{k_0 - 1} \qquad \ldots(4.2)$$

Whereas, the modified Scheil's equation gives the following equation of segregation ratio:

$$\frac{C_L}{C_0} = (1 - f_s)^{(k_0 - 1)/\xi} \qquad \ldots(4.11)$$

From Scheil's equation the segregation ratio of carbon and sulphur can be expressed as follows:

$$\ln r_C = (k_0^C - 1) \ln(1 - f_s) \qquad \ldots(4.27)$$

$$\ln r_S = (k_0^S - 1) \ln(1 - f_s) \qquad \ldots(4.28)$$

Therefore, at a fixed value of f_s common to both carbon and sulphur (i.e. at a particular location in the billet)

$$\frac{\ln r_s}{\ln r_c} = \frac{k_0^S - 1}{k_0^C - 1} = m = \text{a constant} \qquad \ldots (4.29)$$

It is evident from Eqs.(4.2) and (4.11) that the Scheil's and modified Scheil's equations are of identical forms. Hence, modified Scheil's equation would also give the same kind of correlation as in Eq.(4.29).

From the values of k_0^S and k_0^C (Table 4.1) the value of constant m (Eq.(4.29)) turns out to be 1.225. In Fig.4.19 the ratios of $\ln r_s/\ln r_c$ have been plotted against the corresponding billet sample numbers for the CET boundary as well as the centreline. The averages of $\ln r_s/\ln r_c$ data corresponding to CET and centreline are presented in the figure as solid lines. The line corresponding to Scheil's or modified Scheil's equation is also shown in Fig.4.19. The apparent value of constant m (i.e. m') in Eq.4.29 for the horizontal line is 1.235 for CET boundary. It may be noted that this matches fairly well with the value of m = 1.225 obtained from Eq.(4.29). On the other hand, m' = 0.72 for the centreline segregation, and it does not match at all with prediction of Eq.(4.29)

The agreement between m' corresponding to CET boundary with the prediction based on Scheil's/modified Scheil's equation has been attributed to the following factors:

(i) As mentioned in Sec. 4.2, unlike equilibrium solidification model, Scheil's or modified Scheil's equation does not assume uniformity of composition in the solid phase (i.e. no diffusion in solid). Also, the influence of fluid flow has been taken into account in these models up to some extent (e.g.
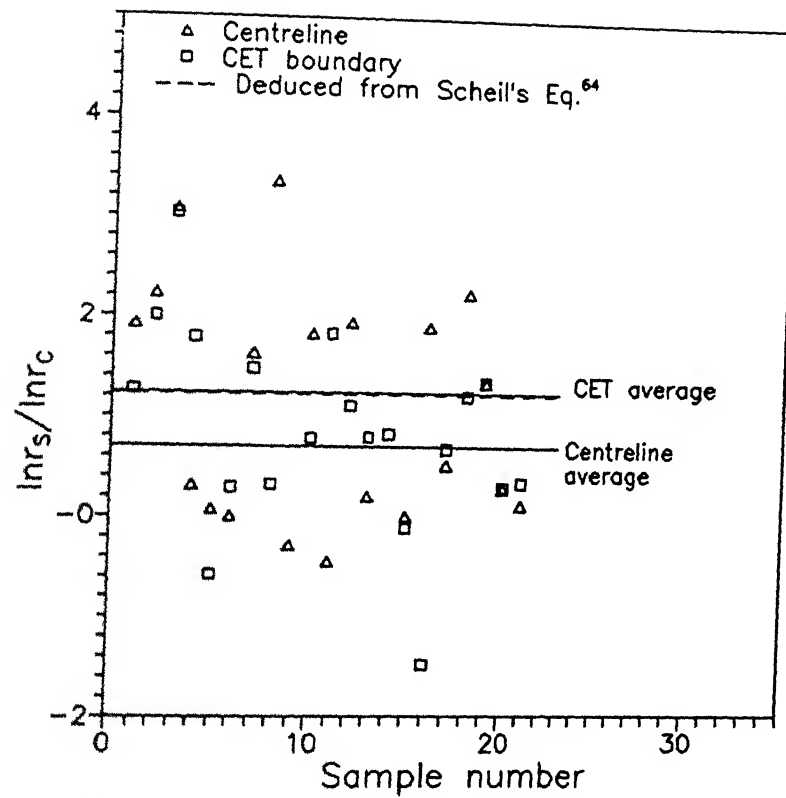
Fig. 4.19: lnr$_s$/lnr$_c$ values of billet samples for the centreline and CET boundary.

modified Scheil's equation). Hence, these models are fairly closer to the real situation than the equilibrium solidification model.

(ii) By considering the ratio of $\ln r_s / \ln r_c$, influence of fluid flow and other common factors get eliminated due to cancellation effect.

(iii) As mentioned already in the beginning of this section, that the Scheil's equation has better applicability in the columnar dendritic region than in the equiaxed region. In the columnar region solidification is predominantly unidirectional. Therefore, the CET boundary can be roughly assumed to be a plane front. On the other hand, the central equiaxed region has a more complex solidification characteristics. Therefore, simple segregation models would not be applicable to the centreline segregation in CC products. However, over a small segregated region such as spot segregation, Scheil's equation has been applied even in the equiaxed zone in some of the previous studies. Saeki et. al.[70] have adopted the approach similar to the present investigation and applied Scheil's equation in the analysis of semi-macrosegregation spots in slab. The Investigators have reported a reasonable agreement between model prediction and experimental data of P and Mn segregation in the semi-macrosegregation spots in slab.

However, the agreement with prediction based on Scheil's equation (i.e. Eq.(4.29)) at the CET boundary in the present study does not mean that these equations are fully applicable. This will be further discussed in the next subsection.

(C)   Equations using the concept of k_{eff}

Examples of these equations are that of Burton et al[69] (Eq.(4.3)) as well as by Takahashi et al[76] (Eq.4.12). As discussed in section 4.2, these two equations are based on entirely different models. Any way both of them yield composition variation with progress of solidification. As noted in Eq.4.4, k_{eff} depends not only on k_0 but on other kinetic parameters as well. These equations would lead to a relationship between r_s and r_c as follows:

$$\frac{\ln r_s}{\ln r_c} = \frac{k_{eff}^{S}-1}{k_{eff}^{C}-1} \qquad \ldots(4.30)$$

However, it was not possible to assign values of k_{eff}. Hence, it was not possible to test the applicability of Eq.(4.30) to the segregation data of the present investigation.

4.4.2.5   Relationship of r_s and r_c at CET boundary with fractional solidification (f_s)

As already stated, the values of f_s at the CET boundaries of different samples were calculated from the area fraction of equiaxed zone (Table 4.4). Values of f_s have been presented in Table 4.7. As may be noted from Sec. 4.2 that the segregation equations gave relationship between r (i.e. C_L/C_0) and f_s. For examining relationship between r and f_s it was decided to try only Scheil's or modified Scheil's equation, since only these could be satisfactorily employed for correlation between r_s and r_c at the CET boundary (Fig. 4.19).

As described earlier, from Scheil's model, the following correlations between r_s, r_c and f_s is obtained.

$$\ln r_s = (k_0^S - 1) \ln (1 - f_s) \qquad \ldots(4.31)$$

and
$$\ln r_c = (k_0^C - 1) \ln (1 - f_s) \qquad \ldots(4.32)$$

From the modified Scheil's equation, the correlations obtained are as follows:

$$\ln r_s = (k_0^S - 1)/\xi \left[\ln(1 - f_s) \right] \qquad \ldots(4.33)$$

and
$$\ln r_c = (k_0^C - 1)/\xi \left[\ln (1 - f_s) \right] \qquad \ldots(4.34)$$

Fig.4.20 presents $\ln r_s$ vs. $\ln(1-f_s)$ for all data points at the CET boundary, and the same for $\ln r_c$ is presented in Fig.4.21. Equations (4.31)-(4.34) show that with increasing $\ln(1-f_s)$ (i.e. decreasing f_s) both r_s and r_c should decrease. But the best fit lines in Figs. 4.20 and 4.21 have negative slope (i.e. with increasing f_s, r_s and r_c actually decreased). This finding runs counter to predictions of any of the segregation models mentioned above. However, they are in agreement with segregation data in transverse sections of continuously cast products as observed by several investigators[59,97].

A region of negative segregation around the high centreline positive segregation zone has been reported by many investigators[59,97]. Tako et al[97] have reported decreasing carbon concentration between f_s=0.64 to f_s=0.85 in a 0.8 pct. carbon steel billet (110 mm square). They observed this consistently in billets with both high as well as low superheat (27°C and 11°C).
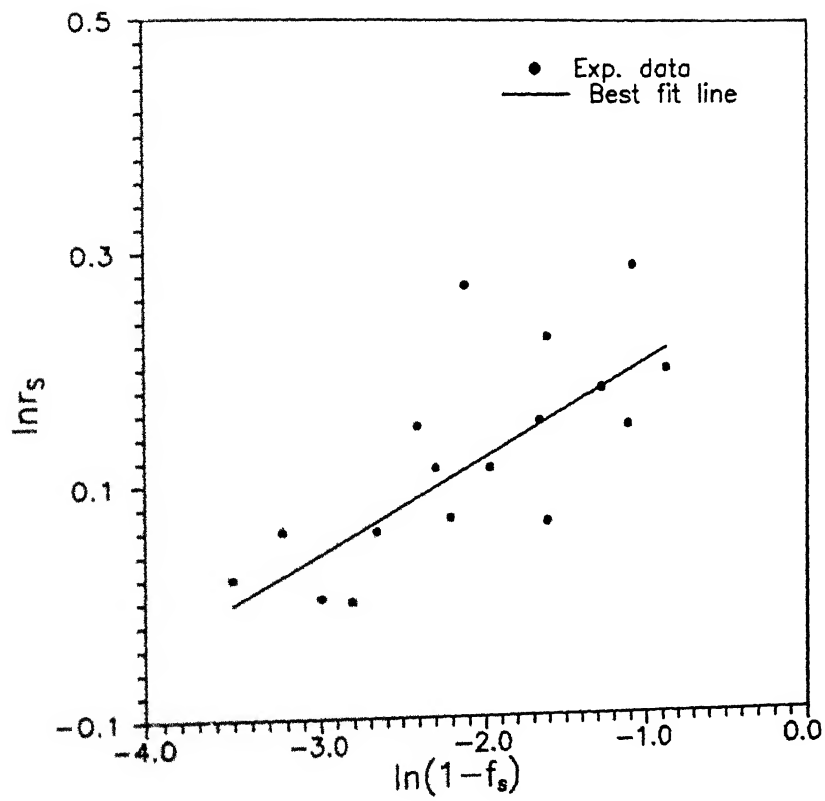
Fig. 4.20: Variation of $\ln r_s$ with $\ln(1-f_s)$ for CET boundary.
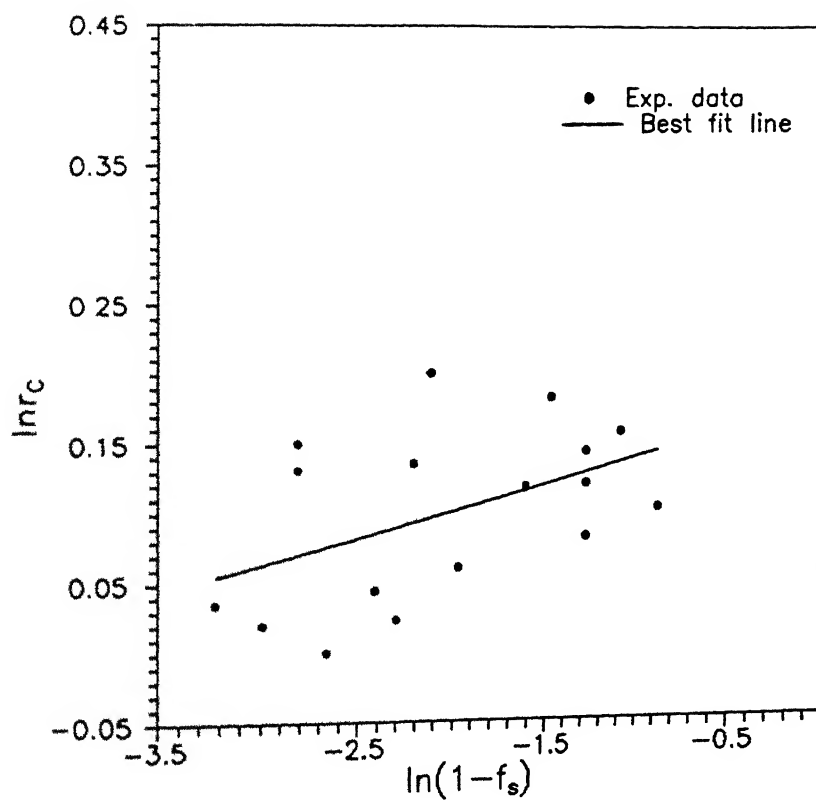
Fig. 4.21: Variation of $\ln r_c$ with $\ln(1-f_s)$ for CET boundary.

In another study, Miyazawa and Schwerdtfeger[59] observed a region of negative segregation around the centreline concentration peak at close to $f_s=0.95$ (Fig.4.1). In the present study f_s varied between 0.58 to 0.97. Therefore, from that point of view the present finding is consistent with that reported in literature.

In a controlled laboratory experiment involving solidification of liquid steel against a rotating water-cooled copper chill, Takahashi et al[76] observed that the concentration of liquid and solid phases remained unchanged regardless of the position. However, with rotation (i.e. fluid flow) solute concentration in solid phase decreased with position away from the chill, whereas, the liquid concentration increased (Fig.4.22). The investigators[76] attributed this to the washing effect due to bulk liquid flow. However, there is no clear cut explanation available in literature on the formation of zone of low or negative segregation. Miyazawa and Schwerdtfeger[59] attributed the flow of heated fluid with lower solute concentration in the mushy zone due to bulging to be the cause of negative segregation around the centreline positive macrosegregation. Moore[56] attributed this to the fluctuating nature of segregation profile. Settling of free crystals may also be one of the causes.
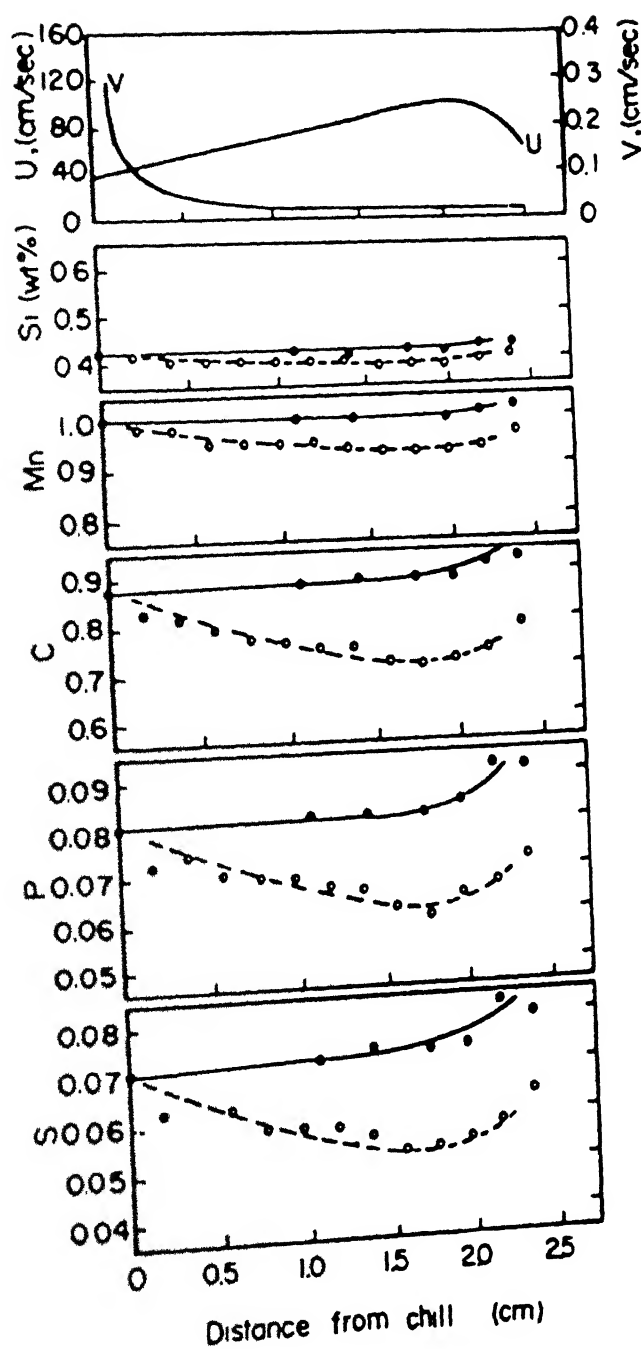
Fig. 4.22: Influence of bulk liquid flow (v) on the rate of solidification (R) and concentration profiles of different solute elements; as observed by Takahashi et al.[76] in a controlled laboratory experiment.

4.5 CORRELATION OF MACROSEGREGATION AND MORPHOLOGY DATA WITH PREDICTION OF HEAT TRANSFER MODEL

As stated in Chapter 1, section 1.3 that one of the objectives of the overall investigation was to try to correlate predictions based on mathematical modelling of heat transfer with the experimental observations on macrosegregation and morphology. Such an attempt was made for the columnar-equiaxed transition boundary. The procedure for this is outlined below:

1.   The chemical composition at the CET boundary of a billet section was employed to estimate the liquidus temperature at that location ($T_{L,CET}$) with the help of Eq. (4.15). Table 4.8 presents the estimated values of $T_{L,CET}$ for all samples.

2.   Measurements on a macroetched billet section allowed determination of the average distance of the CET boundary from the centre of the section. This is being designated as d_y, whose values for the samples are reported in Table 4.8.

3.   From the computer program for conjugate fluid flow-heat transfer model, as presented in Chapter 3, temperatures were calculated at various grid points corresponding to the casting condition for the sample (Table 4.3).

4.   From the computer print out of the above temperature field, the grid point corresponding to $T_{L,CET}$ was found out. This yielded the calculated value of the distance of the CET boundary from the centre of the billet section. This is being designated as d_x.

5.   The value of d_x as determined from the mathematical model would depend on the pouring temperature of liquid steel. As discussed in Section 4.3, attempts were made to experimentally

measure temperature of liquid steel in the CC mould or for the pouring stream from the tundish to the mould. However, these attempts failed because of experimental difficulties. Therefore, the temperatures of liquid steel as measured by immersion thermocouple in the tundish are available only.

6. Hence, in order to arrive at the correct pouring temperature, attempt was made to estimate the temperature loss from tundish to mould. Table 4.8 presents two values of d_x , viz. d_{X1} and d_{X2}. d_{X1} corresponds to uncorrected pouring temperature and d_{X2} corresponds to corrected tundish temperature as pouring temperature. Values of d_{X1} and d_{X2} have been reported in Table 4.8. Sub section 4.5.1 discusses about determination of the temperature loss from tundish to mould in continuous casting of steel.

4.5.1 Estimation of Correct Pouring Temperature of Liquid Steel

Correct pouring = Temperature measured in tundish
temperature   - Loss of temperature from
                    tundish-to-mould (ΔT_{Loss})

$$...(4.35)$$

Again, $\Delta T_{Loss} = \Delta T_{Loss,S} + \Delta T_{Loss,W}$ $...(4.36)$

in which $\Delta T_{Loss,S}$ = Loss of temperature due to pouring into mould

and $\Delta T_{Loss,W}$ = Loss of temperature in the tundish up to the tundish nozzle

$\Delta T_{Loss,S}$ (Eq.(4.36)) was calculated according to the procedure outlined by Ghosh[98]. $\Delta T_{Loss,S}$ is primarily due to radiation from the surface of the teeming stream. From the plant data $\Delta T_{Loss,S}$ was estimated as $0.35^{o}C$. This is not significant, and hence can be ignored. $\Delta T_{Loss,W}$ is much larger than $\Delta T_{Loss,S}$. In the literature few investigations could be located[99,100].

On the basis of measurements in the plant, Nemoto[99] determined mould superheat with varying tundish superheat (Fig. 4.23) .It shows that the ΔT_{Loss} which is the difference between tundish and mould superheat, ranges from approximately 10 - $30^{o}C$.

Robertson and Perkins[100] carried out an extensive investigation on temperature loss of liquid steel in ladle and in tundish. Their study consisted of measurements in plant, mathematical modelling as well as water modelling on tundish. The purpose of water model work of tundish was to essentially find out the residence time distribution for each nozzle separately.

One of the tundishes simulated was the centre-filled billet caster tundish of Temple borough plant of British Steel Corporation[100]. This was fitted with six nozzles for a six strand CC machine. This was similar both in shape and geometry to the six strand tundish at Tata Steel.

Robertson and Perkins[100] also carried out heat loss studies in the proto-type tundish in plant. Residence times were estimated from their water model data. In order to attempt an estimate of $\Delta T_{Loss,W}$ for liquid metal at Tata Steel, further information were obtained from the investigators through correspondence.
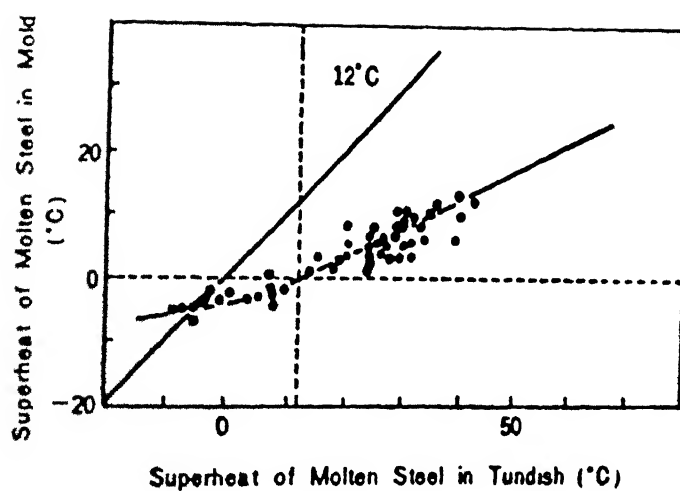
Fig. 4.23: Relationship between superheat of molten steel in the tundish and that in the mold[99].

Robertson and Perkins[100] proposed the following correlation for the average loss of temperature in tundish (i.e. $\Delta T_{LOSS,W}$)

$$\Delta T_{LOSS,W} = T_L - \bar{\tau}_r [\bar{Q}_s A_s + \bar{Q}_W A_W]/ M c \qquad \ldots(4.37)$$

Where $\bar{\tau}_r$ is the mean residence time of tundish. $\bar{Q}_s$ and $\bar{Q}_W$ are the average heat flux densities through the surface of liquid steel and through the walls respectively in the tundish. A_W and A_s are the surface areas of wall and bottom of tundish, and surface area of the melt surface respectively. M is tundish capacity and c is the specific heat of steel.

At the Tata Steel, residence time measurements had been carried out in tundish water model and $\bar{\tau}_r$ data have been reported elsewhere[101]. Relevant data for the estimation of average heat flux densities, $\bar{Q}_s$ and $\bar{Q}_W$, were obtained from Robertson and Perkins[100]. For the Tata Steel tundish, actual residence times were estimated from the residence times measured on water model by multiplying the latter by the scaling factor using the following expression[100]:

$$\text{Scaling Factor} = \frac{V_p Q_m}{V_m Q_p} \qquad \ldots(4.38)$$

Where V is the tundish capacity and Q is the liquid flow rate, and m and p refer to model and plant respectively.

For Tata Steel tundish, $V_p \cong 1.8$ m^3, $Q_p = 220$ l min^{-1}, $V_m \cong 0.37$ m^3, and $Q_m = 61.43$ l min^{-1}. Using these data the estimated residence time was found to be 41 sec. for strand 4 of the billet caster.

Using $\bar{\tau}_r$ = 41 sec, a sample calculation based on Eq. (4.37) gave a value of 8 ^{o}C drop in temperature in the tundish for strand 4, which matches with the temperature loss reported by Robertson and Perkins[100] for a similar tundish. However, the mean residence time data obtained from Perkins through correspondence was 3.5 min (=210 sec). Calculations based on this residence time yielded a fairly higher tundish temperature loss. Considering all these, finally it was decided to take ΔT_{LOSS} = 10 ^{o}C in all the subsequent calculations.

4.5.2 Comparison of Measured Location of CET Boundaries with Those Predicted from Mathematical Model

Table 4.8 presents the computed values of the distance of the CET boundary from centre of the billet section. Pouring temperature i.e temperature of liquid steel entering the mould, were either uncorrected (i.e. same as temperature of liquid steel in the tundish) or by taking ΔT_{Loss} = 10 ^{o}C as discussed in the previous sub-section.

Fig. 4.24 shows a plot of d_{X1} vs. d_y, where d_{X1} is the predicted value of the distance of the CET boundary from centre of the billet section when the pouring temperature was uncorrected. d_y represents the same measured experimentally from macrostructures. As the figure shows that the values of d_{X1} are somewhat higher than d_y. Table 4.8 presents the values of percent deviation of d_{X1} from d_y. It ranges from 1.5 to 30 pct.

Fig. 4.25 shows the plot of d_{X2} vs. d_y, where d_{X2} is the calculated value of the CET boundary from the model for corrected

Table 4.8: Results of correlation between measured CET boundary and those predicted by the mathematical model

| SAMPLE	$T_{L,CET}$ (°C)	Distance of CET boundary from centre of the billet (mm)			Deviation (pct.)	
		measured from macrostructure	computed with tundish temp.		$\dfrac{d_{x1}-d_y}{d_y}$	$\dfrac{d_{x2}-d_y}{d_y}$
		d_y	uncorrected d_{x1}	corrected d_{x2}		
A1	1509.4	28.0	28.4	27.2	1.4	2.9
A2	1510.2	33.0	34.8	33.3	5.1	0.6
B1	1511.8	33.0	35.1	32.9	6.0	0.6
B2	1513.3	36.0	38.0	36.1	5.9	0.6
C1	1522.4	11.0	14.2	10.4	29.1	5.5
C2	1524.0	15.0	18.0	15.9	17.6	4.0
D1	1520.5	12.5	16.2	13.1	29.6	4.8
D2	1520.3	18.0	19.3	18.5	7.0	2.8
E1	1508.4	30.0	30.5	30.6	1.7	2.0
E2	1509.0	36.4	37.8	37.2	3.8	2.2
F1	1517.2	33.1	34.0	33.4	2.7	0.9
F2	1517.5	40.5	41.3	40.6	1.9	0.2
G1	1519.0	14.0	16.5	14.5	17.8	3.6
G2	1518.7	20.0	22.3	20.2	11.5	1.0
H1	1524.9	16.5	17.6	16.8	6.7	1.8
H2	1524.3	23.4	24.0	22.3	2.6	-4.7
I	1512.0	21.0	24.5	20.9	16.7	-0.5
J1	1515.0	15.3	16.6	15.6	8.5	2.0
J2	1514.3	21.6	23.7	21.9	9.7	1.4
K1	1515.2	27.2	29.0	27.8	6.6	2.2
K2	1514.9	28.0	31.0	28.5	10.7	1.8
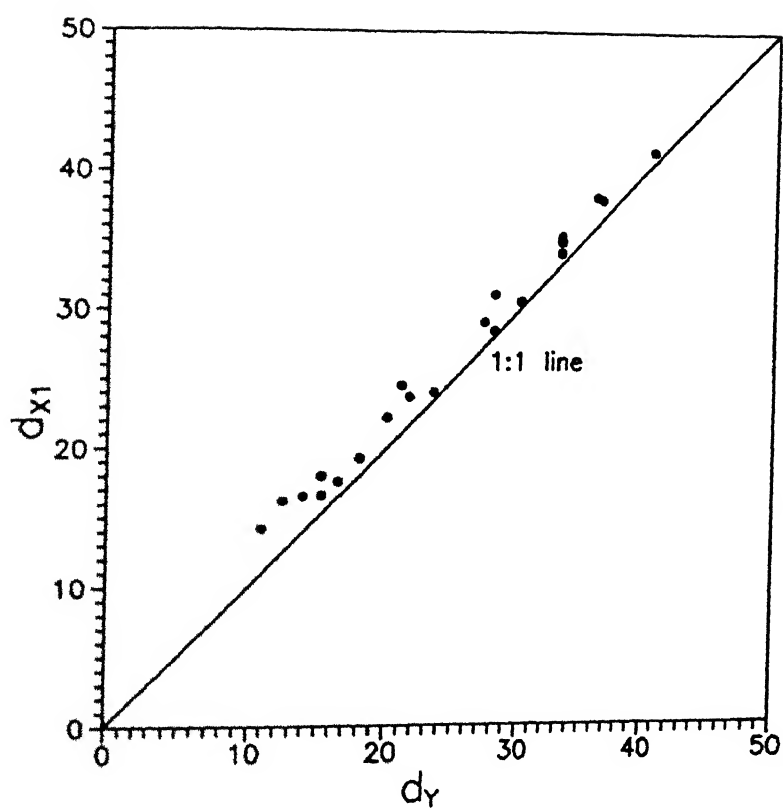
Fig. 4.24: Comparison between measured and computed positions of CET boundary from the centre of billet samples with uncorrected pouring temperature.
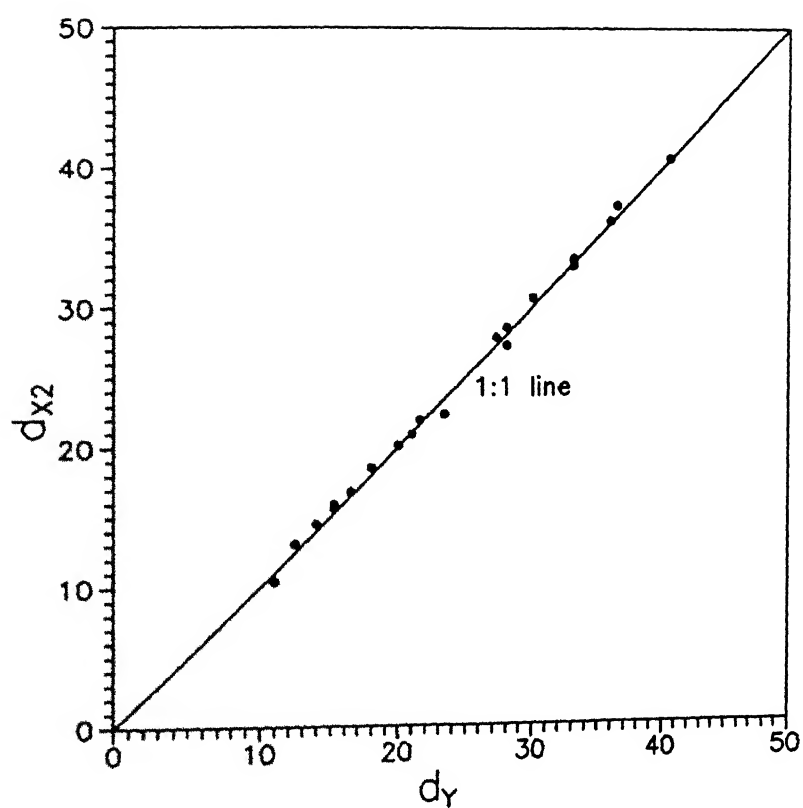
Fig. 4.25: Comparison between measured and computed positions of CET boundary from the centre of billet samples with corrected pouring temperature.

pouring temperature. It is evident from the figure that values of d_{x2} and d_y matches very well. This finding tends to confirm the reliability of both macrostructural measurements as well as the conjugate fluid flow-heat transfer model. Therefore, it is proposed that the same model may also be employed to predict the equiaxed zone size in continuously cast products.

4.6 SUMMARY AND CONCLUSIONS

Samples of 125 mm square billets of low carbon steel and the corresponding plant data were collected from strand no.4 of the continuous casting unit of Tata Steel, Jamshedpur. The samples were cut to a convenient size in order to carry out physical and chemical examinations of transverse sections of the billets. Ground and cleaned surfaces of billets were examined without etching as well as after macroetching by warm 1:1 hydrochloric acid-water solution with added hydrogen peroxide.

All visible macrostructural features of the transverse sections of the billets were traced on transparent papers. These were subsequently employed for measurements of fractions of chill, columnar equiaxed zone as well as to ascertain the positions of columnar-equiaxed transition (CET) boundaries.

Subsequent to the macrostructural examination, carbon and sulphur contents of steel at the CET boundary as well as at the centre of each billet section were determined. Samples were collected by drilling and analyzed in an automatic carbon-sulphur determinator.

Area percent of equiaxed zone (A_{Eq}) for transverse sections

ranged from 3 to 42 percent. Equiaxed zones were mostly asymmetric around the centres of the billet sections.

Temperature of molten steel was measured in the tundish twice during each cast. For determination of tundish superheat (ΔT), liquidus temperatures (T_L) were estimated for all the compositions by correlations of T_L with steel composition, proposed by several workers. On the basis of this exercise, the correlation of Thomas et al[93] was accepted. ΔT ranged from 7 to 50 ^{0}C. A_{Eq} was found to decrease with increase in ΔT in agreement with literature reports and the equation of the best fit line was:

$$A_{Eq} = 21.45 - 0.17 \, \Delta T$$

Degree of segregation of carbon and sulphur (r_c and r_s respectively) were calculated from analyses of drillings and from compositions of liquid steel as provided by the plant. Statistically speaking, r_c and r_s at the billet centres were higher than those at corresponding CET boundaries, as expected.

Both for the centre and the CET boundary, r_s was linearly correlated with r_c by the least square method. The best fit lines were compared with those available in literature.

Segregation equations based on various models were tested for their applicability at CET boundary. Equilibrium solidification model did not agree with experimental data. Predictions based on Scheil's equation or modified Scheil's equation yielded the relationship:

$$\frac{\ln r_s}{\ln r_c} = \frac{k_0^S - 1}{k_0^C - 1} = m = \text{a constant}$$

Theoretical value of m is 1.225, and at CET boundary

experimental data yielded an average value of 1.235 demonstrating good agreement. No agreement was found with the data for centre line.

The variations of r_s and r_c at CET boundary with fractional solidification (f_s) for the billet samples did not agree with predictions of above equations. However they were qualitatively consistent with observations reported in literature, and may be attributed to complex movements of liquid and free crystals in the solidifying pool of liquid steel.

Correlation of macrosegregation and morphological studies with heat transfer modelling was one of the objectives of the entire investigation reported here, and was attempted as follows. Experimental values of location of the CET boundaries were obtained from the macrostructures of billet sections. Conjugate fluid flow-heat transfer model was employed to calculate temperatures at various grid points. Location of CET boundaries were found from these corresponding to a liquidus temperatures at CET boundaries. These were carried out for both uncorrected and corrected pouring temperatures.

It has been demonstrated that predicted values of location of CET boundaries from the fluid flow heat transfer model agreed closely with the experimental values for corrected pouring temperatures of liquid steel.

The above agreement is being taken as an additional confirmation of the reliability of the conjugate fluid flow-heat transfer model. Therefore, It is proposed that the model may also be employed to estimate equiaxed zone size in continuously cast sections.

CHAPTER 5

SUMMARY AND CONCLUSIONS

The present study is concerned with continuous casting of steel, and consists of the following:

(i) mathematical modelling of heat transfer by the artificial effective thermal conductivity model

(ii) mathematical modelling by conjugate fluid flow - heat transfer model

(iii) macrosegregation and morphology study in continuously cast low carbon steel billets.

These have been presented in Chapters 2, 3, and 4 respectively. Each of these chapters has its own summary and conclusions. This chapter presents the same of the entire study in a consolidated fashion. It is a somewhat abridged version of the same from the above chapters.

5.1 MATHEMATICAL MODELLING BY ARTIFICIAL EFFECTIVE THERMAL CONDUCTIVITY APPROACH

(i) Based on the concept of artificial effective thermal conductivity approach, a steady state 3D heat flow model of continuous casting of steel was developed. Control volume based finite difference procedure has been employed for the numerical solution of the governing heat flow equation. A general computer program, which incorporates Tri Diagonal Matrix Algorithm for the solution of discretization equation, has been developed in

FORTRAN 77. The program is so written that computations in cartesian as well as in cylindrical polar coordinate systems can be performed in both 2-D and 3-D.

(ii) The present study has revealed that the axial conduction term has a minor role to play so far as the modelling of overall heat flow in CC is concerned. Numerical solution required the choice of grid configurations so as to make it grid independent. Procedures applied to model heat flow in the mushy zone as well as the surface boundary condition in the mould were also found to affect the predictions somewhat.

(iii) In order to select a proper K_{eff} value and test its sensitivity to computed results, values of K_{eff} were varied over a wide range. Finally, it was decided to take K_{eff} = 7K for further computation.

(iv) Model predictions have been assessed against three sets of experimental data from literature for round and square billet casters. However, in most of the cases the overall agreement between predictions and experimental measurements of shell thickness were not found to be satisfactory.

(v) It appears that the concept of artificial effective thermal conductivity, as applied to the liquid pool to account for the effect of fluid convection and turbulence on heat transfer, is not adequate enough to describe various thermal phenomena in continuous casting of steel realistically.

5.2 Mathematical Modelling by Conjugate Fluid Flow - Heat Transfer Approach

(i) A steady state, two dimensional mathematical model based on the concept of conjugate fluid flow and heat transfer has been developed for continuous casting of steel.

(ii) Two-dimensional turbulent Navier Stokes equation has been considered for the simulation of fluid flow in the liquid pool and furthermore, a thermal buoyancy force term has been incorporated in the axial direction momentum balance equation to take into account the natural convection phenomena taking place in the liquid pool of the solidifying casting.

(iii) The turbulence properties in the system was estimated via the Pun - Spalding formula, based on which the average effective viscosity was computed. Similarly, in the mushy zone, resistance to the flow produced by the solid matrix has been taken into account by increasing the viscosity to 20 times the molecular viscosity of liquid steel.

(iv) In conjunction with these considerations, an appropriate energy balance equation was considered, in which the latent heat of solidification was estimated from the solid fractions in the mushy zone assuming equilibrium solidification of steel.

(v) The TEACH-T computer code, with considerable modifications, was used for the numerical solution of the governing fluid flow and heat transfer equations and thus, to deduce flow field, temperature field and pool profile in continuously cast billets.

(vi) Prior to carrying out any comparison with experimental

measurements, influence of various approximations applied to the mathematical model were analyzed computationally. Towards this, the predicted shell thickness was found to be almost insensitive to the precise value of effective viscosity. This in turn revealed that the exact modelling of turbulence in the pool is relatively less critical than has been originally anticipated. However, modelling of flow in the mushy zone was found to have some bearing on the predicted shell thickness, particularly in the lower pool region. Similarly, influence of buoyancy induced natural convection on the overall shell growth was found to be almost insignificant.

(vii) Velocity and temperature fields were calculated for three different CC sections. The predictions of velocity field revealed that the flow of liquid steel was predominantly in the axial direction for most of the central regions. Whereas, near the solidification front some reverse flow were seen. Furthermore, reverse flow was found to be significant only up to few meters below the meniscus.

(viii) Comparison between predicted shell thickness and corresponding experimental measurements reported in literature indicated reasonable agreement between the two. Similarly, comparison between the predictions of conjugate fluid flow and heat transfer model and those derived via the artificial effective thermal conductivity model demonstrated the superiority of the former over the latter.

5.3   STUDY ON MACROSEGREGATION AND MORPHOLOGY

(i)   Samples of 125 mm square billets of low carbon steel and the corresponding plant data were collected from strand no.4 of the continuous casting unit of Tata Steel, Jamshedpur. The samples were cut to a convenient size in order to carry out physical and chemical examinations of transverse sections of the billets. Ground and cleaned surfaces of billets were examined without etching as well as after macroetching by warm 1:1 hydrochloric acid-water solution with added hydrogen peroxide.

(ii)   Area percent of equiaxed zone (A_{Eq}) for transverse sections ranged from 3 to 42 pct.. Equiaxed zones were mostly asymmetric around the centres of the billet sections. Temperature of molten steel was measured in the tundish twice during each cast. Tundish superheat (ΔT) ranged from 7 to 50 ^0C. A_{Eq} was found to decrease with increase in ΔT in agreement with literature reports.

(iii) Subsequent to the macrostructural examination, carbon and sulphur contents of steel at the columnar-equiaxed transition boundary (CET) as well as at the centre of each billet section were determined. Samples were collected by drilling and analyzed in an automatic carbon-sulphur determinator.

(iv) Degree of segregation of carbon and sulphur (r_c and r_s respectively) were calculated from analyses of drillings and from compositions of liquid steel as provided by the plant. Statistically speaking, r_c and r_s at the billet centres were higher than those at corresponding CET boundaries, as expected. Both for the centre and the CET boundary, r_s was linearly correlated with r_c by the least square method. The best fit lines

were compared with those available in literature.

(v) Segregation equations based on various models were tested for their applicability at CET boundary. Equilibrium solidification model did not agree with experimental data. Predictions based on Scheil's equation or modified Scheil's equation yielded the relationship:

$$\frac{\ln r_s}{\ln r_c} = \frac{k_0^s - 1}{k_0^c - 1} = m = \text{a constant}$$

Theoretical value of m is 1.225, and at CET boundary experimental data yielded an average value of 1.235 demonstrating good agreement. No agreement was found with the data for centre line.

(vi) The variations of r_s and r_c at CET boundary with fractional solidification (f_s) for the billet samples did not agree with predictions of above equations. However they were qualitatively consistent with observations reported in literature, and may be attributed to complex movements of liquid and free crystals in the solidifying pool of liquid steel.

5.4 CORRELATION OF MACROSEGREGATION AND MORPHOLOGICAL STUDIES WITH HEAT TRANSFER MODELLING

(i) This was one of the the objectives of the entire investigation reported here, and was attempted as follows. Experimental values of location of the CET boundaries were obtained from the macrostructures of billet sections. Conjugate fluid flow-heat transfer model was employed to calculate

temperatures at various grid points. Location of CET boundaries were found from these corresponding to liquidus temperatures at CET boundaries. These were carried out for both uncorrected and corrected pouring temperatures.

(ii) It has been demonstrated that predicted values of locations of CET boundaries from the fluid flow heat transfer model agreed closely with the experimental values for corrected pouring temperatures of liquid steel.

(iii) The above agreement is being taken as an additional confirmation of the reliability of the conjugate fluid flow-heat transfer model.

(iv) It is proposed that the model may also be employed to estimate equiaxed zone size.

5.5 SUGGESTIONS FOR FURTHER WORK

(i) In the present conjugate fluid flow - heat transfer model, a somewhat simplified modelling approaches have been adopted to take into account the turbulence phenomena in the liquid pool, for the reasons already described in Chapter 3. Therefore, it would be desirable to carry out further a comparative study between the present approach and that by application of standard turbulence model.

(ii) Improved treatments for fluid and heat flow in the mushy zone has been reported in literature. Inclusion of some of these treatments in the model would be desirable. Similarly, for the estimation of solid fraction in the mushy zone, nonequilibrium solidification models are available which if included in the model would make the conjugate fluid flow-heat

transfer model further closer to the real situations.

(iii) In the present study, blockage ratio/cell porosity method have been adopted to take into account the influence of solidified shell on the velocity field and to assign the prescribed velocity (i.e. the casting speed) in the completely solidified region. Alternative approach to this is the high viscosity method. A comparative study between these techniques from the view point of convergence and the accuracy of prediction is desirable.

(iv) Extension of the present conjugate fluid flow-heat transfer model to three dimension is desirable. Also, in the present study pouring of liquid steel through straight nozzle has been considered. However, in industries, particularly in slab casting submerged entry nozzles are commonly employed. Therefore, the present study should be extended to the submerged pouring condition also.

(v) Mathematical modelling in conjunction with in-plant measurements is desirable.

(vi) A mathematical model involving coupled fluid flow, heat transfer, as well as mass transfer phenomena can provide the complete description of continuous casting process.

(vii) The key findings in macrosegregation and morphological studies at the CET boundary, viz. some agreement with Scheil's equations, as well as agreement with heat transfer model ought to be established by carrying out more experiments. Measurement of temperature of liquid steel in mould or teeming stream should be an integral part of such study.

REFERENCES

1. R.D. Phelke: 'Metals Hand Book', 9th Ed., Vol.15, ASM International, 1988, p.308.

2. R.H. Tupkary: 'Modern Steelmaking', Khanna Publishers, New Delhi, 1980, p.343.

3. Klaus Wünnenberg: 'Proc. 6th Int. Iron and Steel Congress'. Nagoya, Japan, 1990, p.364.

4. Osamu Tsubakihara et al: Trans. ISIJ, $\underline{25}$ (1985), p.687.

5. Metal News: The Indian Institute of Metals, $\underline{15}$, No.2, April (1993), p.17.

6. Metal News: The Indian Institute of Metals, $\underline{15}$, No.1, Feb. (1993), p.19.

7. A.W.D. Hills: J. Iron Steel Inst., $\underline{203}$ (1965), p.18.

8. E.A. Mizikar: Trans. Met. Soc. AIME, $\underline{239}$ (1967), p.1747.

9. J.K. Brimacombe, J.E. Lait, and F. Weinberg: 'Proc. Conf. Math. Models in Ironmaking and Steelmaking': The Metals Soc., 1975, p.174.

10. J.K. Brimacombe: Canadian Met. Quart., $\underline{15}$ (1976), p.163.

11. S. Asai and J. Szekely: Ironmaking and Steelmaking, $\underline{3}$ (1975), p.205.

12. P.J. Flint, Q.L. He, R.B. Mahapatra, and J. Herbertson: 'Proc. 10th PTD Conf., Toronto, Canada, ISS-AIME, (1992), p. 279.

13. R.B. Bird, W.E. Stewart, and E.N. Lightfoot: 'Transport Phenomena', Wiley, New York, 1966.

14. J.J. Gautier, Y. Morillon, and J.Dumont-Fillon: J. Iron and Steel Inst., $\underline{208}$ (1970), p.1053.

15. D. Mazumdar and Ravi Verma: Trans. IIM, $\underline{42}$ (1989), p.447.

16. R. Alberny: 'Information Symposium on Casting and Solidification of Steel', Commission of the European Communities, Guilford, U.K., IPC Sci. and Tech. Press Ltd., Vol 1 (1977), p.278.

17. A. Perkins and W.R. Irving: 'Proc. Conf. Mathematical Process Models in Ironmaking and Steelmaking', Metals Soc., London, (1975), p.187.

18. R.D. Phelke: Metals Eng. Quart., $\underline{4}$ (1964), p.42.

19. J. Savage: J. Iron and Steel Inst., <u>200</u> (1962), p.41.

20. J. Savage and W.H. Pritchard: J. Iron and Steel Inst., <u>178</u> (1954), p.267.

21. E.A. Mizikar: Iron and Steel Engineer, <u>6</u> (1970), p.53.

22. J.E. Lait, J.K. Brimacombe and F. Weinberg: Ironmaking and Steelmaking, <u>2</u> (1974), p.90.

23. J.E. Lait, J.K. Brimacombe and F. Weinberg: Ironmaking and Steelmaking, <u>1</u> (1974), p.35.

24. Ed. J.K. Brimacombe, I.V. Samarasekera, and J.E. Lait: 'Monograph on Continuous Casting', Vol.2, ISS-AIME, (1984)

25. R.S. Laki, J. Beech and G.T. Davies: Ironmaking and Steelmaking, <u>12</u> (1985), p.163.

26. R.S. Laki, J. Beech and G.J. Davies: Ironmaking and Steelmaking, <u>11</u> (1984), p.283.

27. M.J. Mundim, J.L. Pimenta, C.A.G. Valadares, and P.F. Perira: 'Proc. Conf. Continuous Casting of Steel', 1985, London, Metals Soc., p.50.1.

28. A.K. Lahiri: 'Proc. Int. Sympo. on Modern Developments in Continuous Casting', New Delhi, Indian Inst. of Metals, (1989), p.145.

29. D. Mazumdar, ISIJ International, <u>29</u> (1989), p.524.

30. S.V. Patankar, 'Numerical Heat Transfer and Fluid Flow', Hemisphere Pub. Co. Inc., 1980, New York.

31. N.C. Markatos, Ironmaking and Steelmaking, <u>16</u> (1989), p.266.

32. S.V. Patankar: Unpublished work, University of Minnisota, USA, 1980.

33. K. Ushijima, Tetsu-to-Hagane, <u>48</u> (1962), p.747.

34. B.G. Thomas, L.J. Mika, and E.M. Najjar, Met. Trans., <u>21B</u> (1990), p.387.

35. J. Szekely and V. Stank, Met. Trans., <u>1</u> (1970), p.119.

36. J. Szekely and R.J. Yadoya, Met. Trans., <u>4</u> (1973), p.1879.

37. J. Szekely and R.J. Yadoya, Met. Trans., <u>3</u> (1972), p.2673.

38. J. Szekely and R.J. Yadoya, 'Proc. Math. Process Models in Ironmaking and Steelmaking', Metals Society, London, (1975), p.165.

39. A.N. Kolmogorov, Tzvest Akad. Nauk, USSR, (1942), Ser. Fiz.6, p.56.

40. L. Prandtl, Nachri. Akad, Wiss Gottingen, Math.-Phy.-Chm. Abt., (1945), p. 6.

41. C.R. Swaminathan and V.R. Voller: 'Materials Processing in the Computer Age', TMS, Warrendale, PA, (1991), p. 259.

42. V.R. Voller and C. Prakash: Int. J. Heat and Mass Transfer, 30 (1987), p. 1709.

43. A.D. Gosman and F.J.K. Ideriah: A General Computer Program for Two Dimensional, Turbulent Recirculating Flows, "Fluids Section Report", Mech. Engg. Dept. Imperial College, London (1976).

44. B.E. Launder and D.B. Spalding: 'Math. Model of turbulence', (1972), London and New York, Academic Press.

45. W. Rodi: 'Turbulence Models and Their Application in Hydraulics': A State of Art Review, University of Karlsruhe, West Germany, (1980).

46. W.M. Pun and D.B. Spalding: Proc. Int. Astronomical Congress, Pergamon Press/PWN - Polish Scientific Publishers, 3 (1967), p.3-21.

47. A.D. Gosman, W.M. Pun, A.K. Runchal, D.B. Spalding and M. Wolfshtein: 'Heat and Mass Transfer in Recirculating Flows', Academic Press, London and New York, (1969).

48. T. DebRoy, A.K. Mazumdar, and D.B. Spalding: 'Applied Math. Modelling', 2 (1978), p.146.

49. J. Szekely, N. El-Kaddah, and G.J. Grivit: 'Proc. Int. Conf. on Injection Metallurgy', Lulea, Sweden, (1980), p.5.1.32.

50. R.N. Basfield and J.A. Kitchener: J. Iron Steel Inst., 180 (1955), p.324.

51. W.M. Pun and D.B. Spalding, 'A General Computer Program for Two Dimensional Elliptic Flows', Mech. Engg. Dept., Imperial College, London, U.K., (1976).

52. S.V. Patankar and D.B. Spalding: Int. Jr. Heat and Mass Transfer, 15 (1972), p.1787.

53. A. Moult, D.B. Spalding, and N.C. Markatos: Trans. of Institution of Chemical Engineers, 57 (1979), p.200.

54. 'Physical Constants of Some Commercial Steels at Elevated Temperatures', Ed. The British Iron and Steel Research Association , Butterworths Scientific Pub., London 1953.

55. Ed. Y.S. Touloukian et.al.,'Thermophysical Properties of Matters (Thermal Expansion)', TRC Data Series, Vol. 12.

56. J.J. Moore: 'Continuous Casting', vol. 2, ISS-AIME, (1984), p. 185.

57. Ahindra Ghosh: 'Principles of Secondary Processing and Casting of Liquid Steel', Oxford IBH Pub. Pvt. Ltd., New Delhi, (1990), p. 174.

58. T.K. Roy, S.K. Choudhary, and A. Ghosh: Tool and Alloy Steels, December (1992), p. 365.

59. K. Miyazawa and K. Schwerdtfeger: Arch. Eisenhüttenwes, 52 (1981), p. 415.

60. J.P. Birat, M. Bobedilla, J.L. Jacquot, M. Martinot, J. Rour, L. Backer and J.M. Bastin: 'Proc. Continuous Casting', Institute of Metals, London, (1985), p. 18.1.

61. J.E.Haggart, A.W. Hardie, D.W. Bruce: Ironmaking and Steelmaking, 17 (1990), p. 130.

62. Y. Tsuchida, M. Nakada, T. Sugawara, S. Miyahara, K. Murkakami, and S. Tokushige: Trans. ISIJ, 24 (1984), p. 899.

63. O. Haida, H. Kitaoka, Y. Habu, S. Kakihara, H. Bada and S. Shiraishi: Trans. ISIJ, 24 (1984), p. 891.

64. M.C. Flemings: 'Solidification processing', Mc Graw Hill Book Co., New York, (1974), p. 34.

65. T.P. Battle: International Materials Review, 37 (1992), p. 249.

66. T. Matsumiya, H. Kajioka, S. Mizoguchi, Y. Ueshina, and H. Esakai: Trans. ISIJ, 24 (1984), p. 873.

67. H.D. Brody and M.C. Flemings: Trans. TMS-AIME, 236 (1966), p. 615.

68. T.W. Clyne and W. Kurz: Met. Trans., 12A (1981), p. 965.

69. J.A. Burton, R.C. Prim, and W.P. Slichter: J. Chem. Phy., 21 (1953), p. 1987.

70. T. Sakai, H. Oonishi, H. Niimi, E. Miwa, T. Yoshida, S. Igari and S. Kitamine: Trans. ISIJ, 24 (1984), p. 907.

71. M.C. Flemings and G.E. Nero: Trans. TMS-AIME, 239 (1967), p. 1449.

72. M.C. Flemings: 'Proc. Elliott Symp.', ISS-AIME, (1990), p. 216.

73 S.D. Ridder, F.C. Reyes, S. Chakravorty, R. Mehrabian, J. Nauman, J.H. Chen, and H.J. Klein: Met. Trans., 9B (1978), p. 415.

74. I. Ohnaka: 'Metals Handbook', ISS-AIME, 15 (1988), p. 136.

75. S.D. Ridder, S. Kou, and R. Mehrabian: Met. Trans., 12B (1981), p. 435.

76. T. Takahashi, K. Ichikawa, M. Kudou, and K. Shimahara: Trans. ISIJ, 16 (1976), p. 283.

77. X. Huang, B.G. Thomas, and F.M. Nazzar: Met. Trans., 23B (1992), p. 339.

78. I.V. Samarasekara, R. Bommaraju and J.K. Brimacombe: 'Electric Furnace Proc.', Toronto, ISS-AIME, 42 (1984), p. 249.

79. K.S. Oh, I.R. Lee, Y.K. Shin, Y.S. Koo, I.J. Lee, and D.Y. Lee: 'Proc. 6th Iron and Steel Congress', Nagoya, ISIJ, 1990, p. 256.

80. P.K. Sung, D.R. Poirier, B. Yalamachili and G.H. Geiger: Ironmaking and Steelmaking, 17 (1990), p.424.

81. S.N. Singh and K.E. Blezek: 'Open Hearth Conf. Proc.', St. Louis, AIME, 59 (1976), p. 264.

82. M. Mori, N. Tanaka, N. Sato and M. Hirai: Trans. ISIJ, 2 (1972), p. 103.

83. S. Miyahara, H. Tsuchita, M. Suzuki, S. Kawa and A. Shiroyam: Tetsu-to-Hagane, 65 (1979), p. S273.

84. W.R. Irving, A. Perkins and M.C. Brooks: Ironmaking and Steelmaking, 11 (1984), p.152.

85. M. Kitamura et al: 'Proc. 4th Iron and Steel Congress', London, Metals Society, (1982).

86. D.J. Hurtuk and A.A. Tzavaras: Journal of Metals, 2 (1982), p. 40.

87. H.S. Marr: Proc. Int. Symp. on Continuous Casting and Solidification of Steel, Commission of European Communities, IPC Science and Tech. Press Ltd., Guildford, U.K., Vol. 1 (1977), p. 338.

88. H. Hittori et al.: 'Proc. Steelmaking', ISS-AIME, Vol.72 (1989), p. 91.

89. R.K. Goyal and A. Ghosh: Trans. IIM, 45 (1992), p. 303.

90. K. Miyamura, T. Taguchi and H. Soga: Trans. ISIJ, 24 (1984), p. 883.

91. Govindrajan and Amit Chatterjee: 'Monographs on Continuous Casting at Tata Steel', 1991.

92. A.A. Howe: Ironmaking and Steelmaking, 15 (1988), p.134.

93. B.G. Thomas, I.V. Samarasekera, and J.K. Berinacombe: Met. Trans., 18B (1987), p.119.

94. M. Wolf: Proc. Concast Metallurgical Seminar, Zurieh, 1982.

95. A. Kagawa and T. Okamoto: Mater Sci. Tech.; 2 (1986), p.997.

96. H. Iwata, K. Yamada, T. Fuzita, and K. Hayashi: Trans. ISIJ, 16 (1975), p. 374.

97. K. Takeo and H. Iwata: Wire Journal, Aug. (1971), p. 32.

98. Ahindra Ghosh: 'Principles of Secondary Processing and Casting of Liquid Steel', Oxford IBH Pub. Pvt. Ltd., New Delhi, (1990), Ch. 4, p.84.

99. H. Nemoto: Trans. ISIJ, 16 (1976), p. 51.

100. T. Robertson and A. Perkins: Ironmaking and Steelmaking, 13 (1986), p. 301.

101. S. Govindrajan, S.K. Ajmani, A. Chatterjee, and T. Mukherjee: 'Proc. Int. Sympo. on Modern Developments in Continuous Casting', 15-16 Nov. 1988, New Delhi, organized jointly by The Indian Inst. of Metals and Steel Authority of India Ltd., p. 153.

MME-1783-D-CHo-STU